FACHBEREICH PHYSIK - UNIVERSITÄT DORTMUND

NEUTRINOS ON THE ROCKS

On the phenomenology of potential astrophysical neutrino sources

Dissertation zur Erlangung des Doktorgrades

vorgelegt von

Julia K. Becker

Dortmund, März 2007

CONTENTS

Introduction

The field of astroparticle physics is currently developing rapidly, since new experiments challenge our understanding of the investigated processes. Three messengers can be used to extract information on the properties of astrophysical sources. Historically, the optical observation of objects such as planets, stars, galaxies, supernovae, etc. was the first, and most obvious way of analyzing astrophysical phenomena. New wavelength bands have been explored successively, and today, photons from the radio band up to the highest energies (TeV) are observed with different detection methods. In the non-thermal Universe, photons mirror the acceleration process of charged particles in the sources. Charged particles coming from outer space have been observed since 1912, when Viktor Hess accomplished measurements of the ionization of the atmosphere, a phenomenon caused by the interaction of Cosmic Rays with the atmosphere. However, the charged particles do not carry directional information, since their direction is scrambled by intergalactic magnetic fields. The third messenger is the neutrino, still providing information on their origin just as the photon. Due to the low interaction probability of the neutrinos, they can even be used to examine the fundamental processes within the sources of Cosmic Rays. While the low interaction probability is considered as an advantage for measuring the source's properties, it is a disadvantage for the detection. Since neutrinos barely interact with matter, huge volumes have to be instrumented in order to observe these particles. So far, neutrinos from the sun and from a supernova in 1987 have been observed [Hel87]. Experiments such as IceCube and KM3NeT are being built with the primary aim to detect neutrinos from various galactic and extragalactic sources, e.g. Active Galactic Nuclei, Gamma Ray Bursts, etc. These sources are of high interest, since their energy output in photons implies the acceleration of protons to the highest energies ($\sim 10^{21}$ eV).

The understanding of the connection between photon emission, Cosmic Rays and neutrinos is crucial for the interpretation of the underlying processes in astroparticle physics, since none of the messengers alone is able to give a complete picture. In this thesis, parts of the connection between the three messengers are examined in detail, with the focus on the neutrino emission. Measurements of Cosmic Rays and photons help to develop acceleration models with different neutrino output. Neutrino flux models for different source types are derived, and already existing models are investigated with respect to newly set limits by the AMANDA experiment.

After a summary of the state of the art in Chapter 1, the source catalogs used throughout this thesis are presented in Chapter 2. This is necessary since neutrino astrophysics needs to make use of the photon information in order to identify possible sources. Acceleration processes in astrophysical sources are considered in Chapter 3 by using simulations of collision-less shocks and discussing the shape of the Cosmic Ray spectrum. A correlation between the sources' boost factor and the spectral behavior is presented and examined in detail. In Chapter 4, the neutrino emission from Active Galactic Nuclei and the detection rates are discussed. Gamma Ray Bursts are examined with respect to the expected neutrino signal in Chapter 5. Here, the focus lies on the fluctuation of single source spectra with the individual intrinsic properties of the object. The AMANDA experiment at the geographic South Pole currently provides most restrictive limits to neutrino flux models from extraterrestrial sources. In Chapter 6, different models are examined with respect to their consistency with the limits, and conclusions about the underlying physics are drawn. In addition, source catalogs of Active Galactic Nuclei are investigated concerning the source distribution in the sky. In that context, the prospects of the next generation neutrino telescopes ICECUBE and KM3NET are examined. In Chapter 7, the results of this thesis are summarized. In the appendix, additional pieces of information on the different chapters are presented. In particular, an organization scheme of this thesis is presented in appendix A, in which the connections of the introductory chapters to one specific chapter are given. A summary of the definitions of the different particle fluxes can be found in appendix D.1. At the end of this thesis the index of key words and astroparticle physics experiments are listed.

Einleitung

Das Feld der Astroteilchenphysik entwickelt sich momentan dank neuer Experimente und den sich daraus ergebenden neuen theoretischen Erkenntnissen mit extremer Geschwindigkeit. Drei Botenteilchen - das Photon, die geladene kosmische Strahlung und das Neutrino - werden zur Zeit genutzt, um Informationen über die Eigenschaften astrophysikalischer Quellen zu extrahieren. Historisch gesehen war die optische Beobachtung von Planeten, Sternen, Galaxien, Supernovae etc. der erste und offensichtlichste Weg zum Studium astrophysikalischer Phänomene. Neue Wellenlängenbereiche wurden sukzessiv erschlossen. Heute werden Photonen von Radiowellen bis hin zu hochenergetischen Ereignissen (TeV-Energien) mit verschiedenen Meßmethoden beobachtet. Die Photonen spiegeln Beschleunigungsprozesse geladener Teilchen wider. Solche geladenen Teilchen aus astrophysikalischen Quellen werden seit Anfang des 20. Jahrhunderts beobachtet, als Viktor Hess Messungen der Ionisation der Atmosphäre durchführte - ein Phänomen, welches von Wechselwirkungen der kosmischen Strahlung mit der Atmosphäre hervorgerufen wurde. Diese geladenen Teilchen können jedoch keinen Aufschluß über ihren Ursprung geben, da ihre ursprüngliche Richtung durch intergalaktische Magnetfelder verwirbelt wird. Die dritte Sorte der Botenteilchen ist das Neutrino, welches seine ursprüngliche Richtung bei der Propagation beibehält, ähnlich wie es bei den Photonen der Fall ist. Aufgrund der geringen Wechselwirkungswahrscheinlichkeit von Neutrinos können sie Aufschluß über fundamentale Prozesse im Inneren der Quellen kosmischer Strahlung geben. Diese hier als positiv gewertete Eigenschaft der Neutrinos stellt sich bei der Detektion eher als nachteilig dar: Da Neutrinos kaum mit Materie wechselwirken, muß auf sehr große, natürliche Wechselwirkungsmedien zurückgegriffen werden. Große Volumina müssen zum Nachweis instrumentiert werden, um die Detektionswahrscheinlichkeit zu erhöhen. Bisher war es möglich, Neutrinos von der Sonne und von einer Supernova aus dem Jahr 1987 zu beobachten [Hel87]. Experimente wie ICECUBE und KM3NET werden momentan gebaut, um Neutrinos von verschiedenen galaktischen und extragalaktischen Quellen, wie z.B. von Aktiven Galaktischen Kernen, Gamma Ray Bursts usw. zu detektieren. Insbesondere werden die genannten

Quellklassen als potentielle Neutrinoemitter in Betracht gezogen, da deren totale elektromagnetisch emittierte Energie auf die Emission von Hochenergie-Protonen ($E_p \sim 10^{21}$ eV) schließen läßt, was wiederum die Produktion von Neutrinos zur Folge hat.

Die Untersuchung des Zusammenhangs zwischen der Beobachtung von Photonen, kosmischer Strahlung und Neutrinos ist essentiell für die Interpretation grundlegender Prozesse in der Astroteilchenphysik, weil keines der drei Botenteilchen alleine die physikalischen Fragen komplett beantworten kann. In dieser Arbeit werden die Verbindungen zwischen Emissionsprozessen der drei Botenteilchen im Detail phänomenologisch untersucht. Der Fokus ist hier auf die resultierenden Neutrinoflüsse gerichtet. Messungen der kosmischen Strahlung und der Photonflüsse verschiedener Quellen dienen der Entwicklung von Beschleunigungsszenarien, welche, abhängig von den Bedingungen in der Quelle selbst, verschiedene Neutrinoflußvorhersagen ergeben. Neutrinoflußmodelle werden für verschiedene Quelltypen hergeleitet, und existierende Modelle werden im Hinblick auf die aktuellen Neutrinoflußgrenzen des AMANDA-Experiments untersucht.

Nach einer Zusammenfassung des aktuellen Forschungsstands in Kapitel 1 werden in Kapitel 2 die Quellkataloge, die in dieser Arbeit verwendet werden, präsentiert. Es ist notwendig, auf Quellkataloge elektromagnetischer Strahlung in verschiedenen Wellenlängen zurückzugreifen, um mögliche Neutrinoquellen zu identifizieren. Beschleunigungsprozesse in astrophysikalischen Quellen werden in Kapitel 3 untersucht. Hier werden Simulationen von kollisionsfreien Schocks verwendet, um das Spektralverhalten verschiedener Quelltypen zu bestimmen. Der Zusammenhang zwischen dem Lorentzfaktor der Quellen und dem Spektralverhalten wird im Detail analysiert. In Kapitel 4 werden Neutrinoflüsse von Aktiven Galaktischen Kernen betrachtet sowie die erwarteten Detektionsraten diskutiert. Des weiteren wird das erwartete Neutrinosignal von Gamma Ray Bursts in Kapitel 5 abgeschätzt. Hier liegt der Fokus auf den Fluktuationen der Einzelquellspektren, die sich durch individuelle, intrinsische Variationen der beobachteten Ereignisse ergeben. In Kapitel 6 werden verschiedene Modelle in Hinsicht auf die Konsistenz bezüglich der oberen Neutrinoflußgrenzen untersucht, die vom AMANDA-Experiment bestimmt wurden. Die Konsequenzen für die grundlegende Physik wird dargelegt. Zudem wird die Verteilung von Quellen verschiedener Kataloge Aktiver Galaktischer Kerne untersucht. In diesem Zusammenhang werden die Aussichten der Neutrinoteleskope der zweiten Generation, IceCube und KM3NeT, diskutiert. In Kapitel 7 werden die Ergebnisse dieser Arbeit zusammengefaßt. Im Anhang werden zusätzliche Informationen zu den einzelnen Kapiteln präsentiert. Insbesondere wird in Anhang A die Verbindung der einleitenden Kapitel zu den einzelnen folgenden Kapiteln in einer schematischen Darstellung veranschaulicht. Eine Zusammenfassung der Definition der verschiedenen Teilchenflüsse ist in Anhang D.1 gegeben. Am Ende dieser Arbeit stehen zwei Stichwortverzeichnisse, in welchen auf Schlüsselwörter und Experimente der Astroteilchenphysik verwiesen wird.

CHAPTER 1

The Cosmic Ray, photon & neutrino connection

Non-thermal photon spectra as observed in astrophysical shock environments are in hadronic acceleration scenarios directly linked to the emission of charged Cosmic Rays and to neutrinos. In this chapter, the possible sources of Cosmic Rays are discussed with respect to their emission properties for all three messengers - protons, photons and neutrinos.

1.1 Cosmic Rays

Charged Cosmic Rays (CRs) have been observed from energies of $E_{CR} \sim 10^9$ eV up to $E_{CR} \sim 10^{20}$ eV. The spectrum is altered by the Solar wind for energies below about $E_{CR} \sim 20 \cdot Z$ GeV, where Z is the charge of the nucleus. At higher energies, the energy spectrum follows a powerlaw with two, possibly three breaks. The powerlaw structure can in general be explained by shock acceleration in astrophysical sources. In this section, the observed spectrum with its features is discussed as well as the acceleration mechanism built on stochastic acceleration of test particles at magnetic field inhomogeneities in astrophysical shocks. Chapter 3 will then deal with the interpretation of charged particle spectra from astrophysical shocks and their appearance in extragalactic sources.

1.1.1 Observation of charged Cosmic Rays

Already in the early 20th century, it was discovered that the Earth is exposed to a continuous flux of charged particles from outer space, see e.g. [Hes12, Koh13]. Hess and others performed balloon flights proving that the ionization of the atmosphere increases with height. This contradicted the hypothesis that the flux of ionizing particles arises from radioactive matter in the Earth's rocks exclusively.

Today, the spectrum dN_{CR}/dE_{CR} of charged CRs has been examined over a wide range of energies E_{CR}, using balloon experiments and satellites for low energies ($E_{CR} < 10^{14}$ eV) and Earth-bound experiments for high energies ($E_{CR} > 10^{14}$ eV). The all particle energy spectrum of CRs is shown in Fig. 1.1. The spectrum is weighted by E_{CR}^2 in order to have a flatter representation of the very steep spectrum. The powerlaw behavior of the spectrum is clearly visible,

$$\frac{dN_{CR}}{dE_{CR}} \propto E_p^{-\alpha_{CR}} \,. \tag{1.1}$$

Two kinks can also be seen, referred to as *knee* and *ankle*. The spectral indices for the different parts of the spectrum are [WBM98, V$^+$99]

$$\alpha_{CR} \approx \begin{cases} 2.67 & \text{for} \qquad\quad \log(E_{CR}/\mathrm{eV}) < 15.4 \\ 3.10 & \text{for } 15.4 < \log(E_{CR}/\mathrm{eV}) < 18.5 \\ 2.75 & \text{for } 18.5 < \log(E_{CR}/\mathrm{eV})\,. \end{cases} \tag{1.2}$$

A second knee around $E_{CR} \sim 4 \cdot 10^{17}$ eV is discussed today, with an even steeper behavior up to the ankle, see e.g. [Hör03, HKT07] and references therein. The general spectral powerlaw-like behavior can be explained by stochastic particle acceleration in collision-less plasmas. This will be dealt with in Section 1.1.2.

Charged Cosmic Rays below $E_{CR} < Z \cdot 10^{17}$ eV do not point back to their origin, since they are scrambled by interstellar magnetic fields. The strong connection between non-thermal emission from astrophysical sources and particle acceleration can, however, be used to establish a model for different sources and source types to explain the Cosmic Ray spectrum. Sources within our Galaxy can produce the Cosmic Ray spectrum up to the ankle. Events at higher energies have to be extragalactic:

(a) no galactic source class is energetic enough for the production of particles at such high energies and

(b) the particles' gyroradius becomes too large and they escape from the galaxy already at lower energies.

(c) At energies as high as $E_{CR} \sim 10^{20}$ eV, the particle diffusion is low compared to the traveling length through the Galaxy [Hil84]. The observed particles point in this case back to their original source. The observed events are isotropically distributed, which is only possible for traveling lengths longer than the diameter of the galaxy.

This leaves extragalactic or exotic sources as the origin of the highest energy events, for which acceleration up to $E_{CR} \sim 10^{21}$ eV is possible.

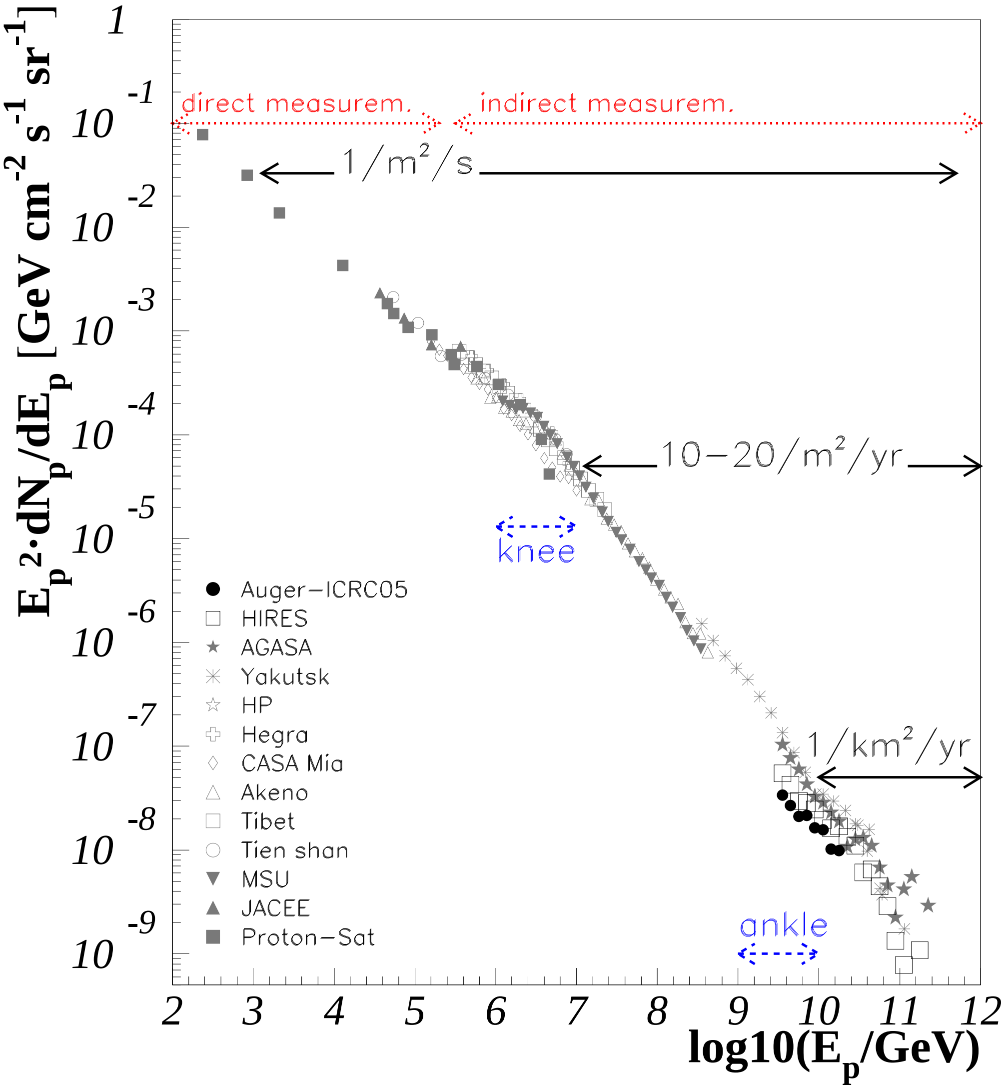

Figure 1.1: All particle Cosmic Ray spectrum [Sta06, Som05]. Data points come from the experiments as listed in the bottom left corner.

The Greisen Zatsepin Kuzmin cutoff

Protons effectively lose energy by interactions with the Cosmic Microwave Background (CMB) on their way to Earth:

$$p\,\gamma_{CMB} \longrightarrow \begin{cases} \Delta^+ \\ p\,e^+\,e^- \end{cases} \tag{1.3}$$

which happens most effectively at $E_{CR} > 5 \cdot 10^{19}$ eV [Gre66, KZ68]. This effect is named "Greisen Zatsepin Kuzmin (GZK) cutoff".

At the highest energies of $E_{CR} > 5 \cdot 10^{19}$ eV, a discrepancy between the CR fluxes as observed by two experiments, AGASA[1] and HiRes[2] was found. AGASA data are represented by stars and HiRes is shown as open boxes in Fig. 1.1. While AGASA detected several events above $5 \cdot 10^{19}$ eV, HiRes observed a decay of the spectrum. Given the GZK cutoff, the result from HiRes is expected, while the AGASA events need to be explained by exotic phenomena. A surface array for the measurement of the charged component of the showers was used by AGASA [Y+95] while HiRes [HiR04] consisted of telescopes measuring the emission of the showers' fluorescence light. At these energies, there are quite large uncertainties in the calibration of the spectra due to the low statistics and large systematic errors. Taking this into account, it is possible to interpret the two results in a way which would still fit a single theory, see [C+06b]. The Auger experiment is being built among other things to resolve the issue of the highest energy events, see e.g. [DA+06]. With Auger, the two different techniques as used by AGASA and HiRes are combined in a hybrid array. This allows for the investigation of systematic uncertainties. The size of the array ensures sufficient statistics. Auger has now instrumented more than 2/3 of a 3000 km^2 surface array and all four telescopes for fluorescence measurements are operating as of March 2007. The hybrid array is expected to be completed by the end of 2007 [DA+06]. The Auger array can be expected to solve the question of the high energy events.

1.1.2 Acceleration mechanism

Astrophysical environments are often characterized by the collision of different plasmas. As an example, a supernova explosion is observed for typically more than 1000 years, since the shell of matter is accelerated and encounters the interstellar medium. A second example is the collision of two galaxies due to gravitational interaction. A shock front is produced, when a gas encounters other gas or a wall, with a velocity faster than any signal velocity. Such phenomena are not only observed in astrophysical environments, but also in other media, for instance in the atmosphere, such as supersonic movement of planes or bullets in air. The plane or bullet moves faster than the characteristic speed of the medium, the speed of sound, and produces a shock wave, the Mach cone [MW84, MW85, Mac98]. In astrophysical shocks, the characteristic speed of the plasma is the speed of magnetic waves.

Non-thermal emission of electromagnetic radiation is believed to originate from shock-accelerated electrons. If a hadronic component is accelerated, the high

---

[1] **A**keno **G**iant **A**ir **S**hower **A**rray

[2] **Hi**gh **Res**olution Fly's Eye Detector

energy component of electromagnetic emission up to TeV energies can also arise from protons. Protons can lose energy by synchrotron radiation or by proton-photon and proton-proton interactions, the latter leading to photon emission from π^0 decays.

Test particle acceleration

In order to calculate the particle spectrum resulting from shock acceleration, it is useful to work with a test particle population entering and leaving the shocked region without influencing the shock conditions. Calculations of stochastic shock acceleration for test particles in collision-less plasma shock discontinuities have been done for the first time analytically by Fermi [Fer49, Fer54]. Stochastic shock acceleration results in a powerlaw spectrum of primary charged particles. The theory of acceleration has been refined later in the 1970s by Bell [Bel78a, Bel78b], Krymskii [Kry77], Blandford & Ostriker [BO78] and Axford, Leer & Skadron [ALS78]. While Bell worked out a microscopic approach, in which individual particles are traced, Krymskii, Blandford & Ostriker and Axford worked on the macroscopic description of astrophysical shocks, neglecting any individual movement of particles. One important consequence of acceleration theory is that the maximum energy depends on the magnetic field and the size of the acceleration region as derived by Hillas [Hil84].

As discussed by Fermi [Fer49, Fer54] and also by Darwin [Dar49], stochastic particle acceleration can be described by following a particle entering an acceleration region with an energy E through the acceleration process, until it exits the region again. It is assumed that particles are accelerated at moving magnetic field inhomogeneities, and in each encounter, an energy of $\Delta E = \xi \cdot E$ is gained. The momentum gain ξ comes from the movement of the magnetic field inhomogeneities.

There are two basic configurations for stochastic acceleration. The first approach was to consider a moving, partially ionized gas cloud as shown in Fig. 1.2. In the figure, E_1 , p_1 and θ_1 are the energy and momentum of the incident particle, and E_2, p_2 and θ_2 are the energy, momentum and angle of the outgoing particle. For instance, magnetized gas clouds in the interstellar medium move with a velocity of ~ 15 km/s [Pro98]. In this configuration, particles are scattered off magnetic field inhomogeneities which are bound to the cloud, see Fig. 1.2. The direction of the Cosmic Rays is randomized in the cloud, since the particles escape from the cloud in any direction. The momentum gain ξ in this case proportional to the squared cloud velocity, $\xi \propto V_c^2$, as discussed in e.g. [Pro98]. This mechanism is referred to as *second order Fermi acceleration.* The energy gain is positive, independent of the velocity direction, but it is of second order and thus, not very efficient ($V_c < 1$).

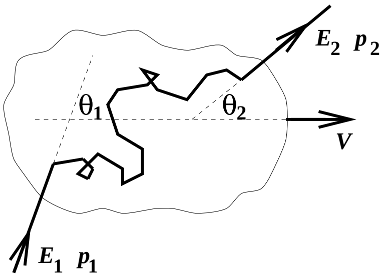

Figure 1.2: The original Fermi theory (Second order Fermi acceleration). Interaction of a cosmic particle of energy E_1 in a cloud moving with speed V. Figure from [Pro98].

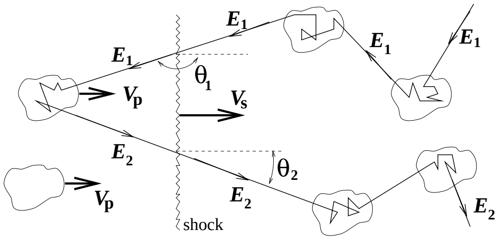

Figure 1.3: First order Fermi acceleration. The shock front is considered to be plane, moving with a velocity of V_S. Figure from [Pro98].

In comparison, *first order Fermi acceleration* is considering a plane, infinite shock front, see Fig. 1.3. In the figure, it is visualized that particles gain energy by crossing the shock front. A particle with an initial energy E_1 only changes its energy by crossing the shock, where it is accelerated at moving magnetic field inhomogeneities to an energy E_2. Again, the incident angle is defined as θ_1 in the figure and the angle of the returning particle towards the shock front is θ_2. Here, first order effects are dominant for the momentum gain of the particle. For strong shocks with a density jump of ~ 4 at the discontinuity, the energy gain is $\xi \sim 1/2 \cdot u_u$ in each direction. The total momentum gain for one cycle of acceleration is then $\xi \sim u_u$, since the signs of the velocity directions cancel for a particle crossing the shock front. A review of first and second order Fermi acceleration is given in [Pro98].

Guiding center approximation While early results were analytical treatments, more precise results are achieved today by Monte Carlo studies. To trace the particle, the guiding center approximation can be used. The helical motion of the particle due to gyration is considered to be small compared to the general drift of the particle and is hence neglected. The guiding center is defined as

$$\vec{r}_{gc} := \vec{r} - \vec{r}_g \, , \tag{1.4}$$

with $\vec{r}$ as the vector from the observer to the particle's location and $\vec{r}_g$ as the gyroradius as measured from the center of the helix. The plasma is considered as collision-less, which means that binary particle interactions are much weaker than the influence of the external magnetic field. The particles are thus scattered and accelerated at moving inhomogeneities of the external field rather than by particle collisions. The scattering process can happen at small or large angles towards the direction of the magnetic field. Small angle scattering is also referred to as *pitch angle diffusion*. Particles gyrate along the magnetic field line, if their velocity is parallel to the magnetic field direction. The angle α between the particle velocity and the magnetic field lines is referred to as the *pitch angle.* For $\alpha \neq 0$, the particles diffuse on the scale of the pitch angle. For relativistic shocks, this angle is connected to the boost factor of the shock Γ, $\alpha \leq 1/\Gamma$. Generally, this is the most realistic approach to highly-relativistic shock phenomena. The small angle diffusion case arises because most field perturbations modeled cannot turn particles more than $\alpha \approx 1/\Gamma$ before shock return. Concentrated, high fields scatter centers acting in a fraction of the distance between scatter centers are needed for *large angle scattering.* This configuration can occur in non- to mildly-relativistic shocks. For high magnetic fields in combination with small acceleration regions, large angle scattering is justified.

Rankine-Hugoniot relations The description of astrophysical shocks is done in the framework of magnetohydrodynamic (MHD) fluid theory. The macroscopic behavior of fluids is investigated in the presence of strong magnetic fields. A collection of particles is treated as a fluid, matter which can be deformed in the continuum. The individual identity of the particles is ignored as the motion of an ensemble of particles is considered. When a fast moving plasma collides with a slower plasma, a shock discontinuity is formed. The shockfront is a thin transition layer between *upstream*, representing the unshocked plasma, and *downstream*, the shocked plasma. The geometry is displayed in Fig. 1.4 and will be discussed in more detail later in this section. For a detailed review of space plasma physics, see e.g. [Par04, JE91].

At the shock discontinuity, three physical conditions have to be fulfilled,

$$\begin{aligned} \frac{\partial}{\partial x}(\rho\, u) &= 0\,, && (1.5)\\ \frac{\partial}{\partial x}\left(\rho\, u^2 + P\right) &= 0\,, && (1.6)\\ \frac{\partial}{\partial x}(\rho\, u^3 + \frac{\gamma_g}{\gamma_g - 1} u\, P) &= 0 && (1.7) \end{aligned}$$

in order to obey the conservation laws of mass, momentum and energy. In the above equations, ρ is the mass density, u is the flow velocity along the x-axis and P is the pressure of the gas. The ratio of specific heats for a monochromatic gas is given by γ_g. The jump conditions at the shock border are then given by the Rankine-Hugoniot relations:

$$\begin{aligned} \rho_u\, u_u &= \rho_d\, u_d\,, && (1.8)\\ \rho_u\, u_u^2 + P_u &= \rho_d\, u_d^2 + P_d\,, && (1.9)\\ u_u \cdot \left(\frac{1}{2}\rho_u \cdot u_u^2 + \frac{\gamma_g}{\gamma_g - 1} \cdot P_u\right) &= u_d \cdot \left(\frac{1}{2}\rho_u \cdot u_d^2 + \frac{\gamma_g}{\gamma_g - 1} \cdot P_d\right)\,. && (1.10) \end{aligned}$$

The index d stands for "downstream", while u stands for "upstream" values. These fundamental conditions serve as the basis for Monte Carlo studies of astrophysical shocks.

The velocity compression ratio r is defined as $r := u_u/u_d$ and is an important parameter for shock simulations[3]. For adiabatic shocks ($\gamma_g = 5/3$), non-relativistic sources typically have compression ratios near $r \sim 4$. For relativistic, purely hydrodynamic shocks and an ultra-relativistic equation of state, the compression ratio is typically assumed to be $r \sim 3$, see [BM76].

Shock geometry

Figure 1.4 shows the geometry of a shock in its own restframe. This implies that the shock front is stationary at $x = 0$ in this representation. The shock normal n and the magnetic field B_u are connected via the angle ψ. Magnetic fields and flow velocities change at the discontinuity, both in strength as in direction. It can be useful to work with different frames of reference in order to simplify the geometry. This will be discussed in the next paragraph.

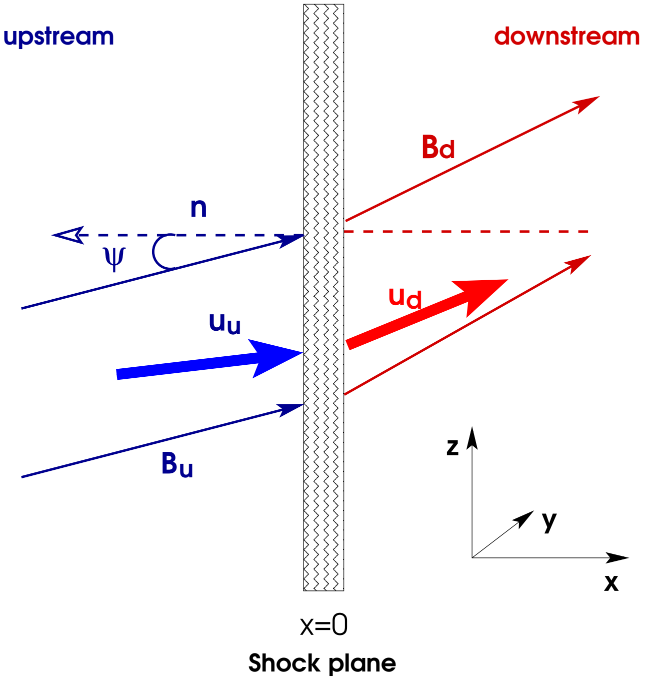

Figure 1.4: Geometry of an astrophysical shock in its restframe. A velocity transformation of the shock parallel to its surface is done to get from the lab frame to the shock restframe. A plasma of velocity u_u meets a plasma of velocity u_d with $u_u > u_d$. A shock front builds up at $x = 0$ between the upstream and downstream region. The shock front stays stationary in this frame. Magnetic fields B_u and B_d have an angle towards the shock normal n. The angle between B_u and the shock normal is labeled ψ.

---

[3] Note that the velocity compression ratio r corresponds to the pressure compression ratio r_p in the non-relativistic case, $r_p = r$, but that the two differ for relativistic shocks, $r_p \neq r$.

The shock geometry is defined by the upstream magnetic field strength and its inclination angle towards the shock normal ψ. While *parallel shocks* have $\psi = 0°$ and *perpendicular shocks* are given for $\psi = 90°$, most shocks are *oblique* with $0° < \psi < 90°$. Shocks with $0° < \psi < 45°$ are referred to as *quasi-parallel* and a $45° < \psi < 90°$ configuration is named *quasi-perpendicular*. Oblique shocks occur in many astrophysical phenomena. The best-studied case is the Earth's bow-shock where the solar wind meets the Earth's magnetic field. The observation of this shock structure was the first verification for the occurrence of collision-less shocks in space, see [JE91] and references therein. Bow-shock observations are quasi-parallel and prove that collision-less shocks can accelerate particles. A second example for the unambiguous observation of collision-less shocks are solar flares and interplanetary traveling shocks.

Reference frames

Due to the lack of symmetries, particle acceleration in the laboratory frame is very difficult to handle. Thus, transformations in different frames are used to simplify matters.

Shock frame In Fig. 1.4, the *shock restframe* is used, working with a stationary shock front at $x = 0$. A transformation of velocity V_S is done to go from the laboratory frame to a frame in which the shock velocity is zero. Upstream and downstream fluids have velocities of u_u and u_d in the shock frame, and the corresponding magnetic fields are B_u and B_d. Magnetic fields can generate electric fields E_u and E_d via

$$\vec{E} = -\frac{\vec{u} \times \vec{B}}{c}\,. \tag{1.11}$$

de Hoffmann-Teller frame As pointed out by de Hoffmann and Teller [HT50], electric fields which can arise from the magnetic current complicate calculations. Thus, the de Hoffmann-Teller (HT) frame uses a velocity transformation of velocity $\vec{V}_{HT}$ such that the resulting upstream velocity is parallel to the magnetic field,

$$\vec{V}_{\|} = \vec{u}_u - \vec{V}_{HT}\,. \tag{1.12}$$

Here, $\vec{u}_u$ is the upstream velocity before transformation. In this case, the electric field vanishes,

$$\vec{E} = -\frac{\vec{V}_{\|} \times \vec{B}}{c} = \vec{0}\,. \tag{1.13}$$

The transformation into the HT frame can be done by going to the shock frame first. The correlation between the z-component of two velocities is

$$V_{HT}^{z} = \frac{B_z}{B_x} \cdot V_S^{z}\,. \tag{1.14}$$

This configuration results in a plasma flow parallel to the magnetic field both upstream and downstream.

The transformation to the HT frame is only possible for inclination angles fulfilling the condition $\tan\psi \leq 1$ with ψ given in the shock frame. The HT speed is described by $V_{HT} = V_S \cdot \tan\psi$, since $B_z/B_x = V_{HT}^z/V_{HT}^x = \tan\psi$. The HT speed cannot exceed the shock velocity and therefore, the condition $\tan\psi > 1$ is unphysical. No transformation into the HT frame is possible in this case. Shocks are classified as *subluminal*, if they transform into the HT frame, while they are referred to as *superluminal* if such a transformation is not possible.

Fluid frames Apart from the shock reference frames, there are two plasma fluid frames.

- In the upstream frame, the upstream flow is at rest.
- In the downstream frame, the downstream velocity is zero.

1.1.3 Primary spectra and radiation fields

In this section, the correlation between accelerated primaries and secondary radiation effects will be examined. The focus lies on the synchrotron emission, since its observation reveals the spectral behavior of the primaries as discussed in the following.

Total synchrotron power

The total radiated power P_{tot} is proportional to m^{-4} with m as the mass of the particle. Since the electron-proton mass ratio is $m_e/m_p \sim 5 \cdot 10^{-4}$, the radiated energy from electrons is a factor $\sim 10^{13}$ higher than for protons. Protons only lose energy to synchrotron radiation for extremely high energies and large magnetic fields, since the power increases with the squared product of the external magnetic field B and particle's energy E, $P_{tot} \propto (B \cdot E)^2$. Electrons undergo synchrotron losses at moderate energies already.

Synchrotron radiation and the spectral shape

For non-thermal spectra, the spectral index of the primary shock-accelerated particles can be expressed in terms of the synchrotron spectral index of a source. Electrons and protons follow the same distribution, i.e. the spectral index of the electrons is the same as for the protons, α_p. The following calculation follows the one of Rybicki and Lightman [RL79]. The power $P(\omega)$ per unit frequency $d\omega$ for a particle accelerated by an external magnetic field B can be written in terms of a function $F(x)$, which only depends on the dimensionless variable $x := \omega/\omega_c$:

$$P(\omega) \propto F(\frac{\omega}{\omega_c}) . \tag{1.15}$$

The critical frequency ω_c of the synchrotron spectrum is given as

$$\omega_c = \frac{3q\,B\,\sin\alpha}{2\,m\,c} \cdot \gamma^2 , \tag{1.16}$$

giving a measure for the maximum frequency of acceleration for the particle spectrum. In this expression, q is the charge, m the mass and γ is the boost factor of the accelerated particles. The latter can be expressed in terms of the energy, $E = \gamma\,m\,c^2$.

Since shock-accelerated primaries follow a powerlaw distribution,

$$\frac{dN_p}{dE_p}\,dE_p \propto {E_p}^{-\alpha_p}\,dE_p , \tag{1.17}$$

the total radiated power $P_{tot}(\omega)$ can be expressed as

$$P_{tot}(\omega) \propto \int_{{E_p}^1}^{{E_p}^2} P(\omega)\,E_p^{-\alpha_p}\,dE_p \propto \int_{{E_p}^1}^{{E_p}^2} F(\frac{\omega}{\omega_c})\,E_p^{-\alpha_p}\,dE_p . \tag{1.18}$$

Using $E_p \propto \omega_c^{1/2}$ (see Equ. 1.16), γ can be substituted for $x := \omega/\omega_c(\gamma)$ and the total power can be written as

$$P_{tot} \propto \omega^{-(\alpha_p-1)/2} \cdot \int_{x_1}^{x_2} F(x) \cdot x^{(\alpha_p-3)/2}\,dx . \tag{1.19}$$

Since the integral only gives a constant value, the frequency dependency is given as

$$P_{tot} \propto \omega^{-(\alpha_p-1)/2} . \tag{1.20}$$

The total synchrotron spectrum follows therefore a powerlaw with a spectral index s

$$P_{tot} \propto \omega^{-s} . \tag{1.21}$$

This leads to a linear correlation between synchrotron and particle spectral index,

$$s = \frac{\alpha_p - 1}{2} . \tag{1.22}$$

The differential spectral index which will be used in the following is $\alpha_\gamma = -s - 1$ with $dN_\gamma/dE_\gamma \propto {E_\gamma}^{\alpha_\gamma}$ as it is discussed in Section 1.2. The flatness of the synchrotron spectra is limited by the theory of synchrotron radiation. Since a single electron produces a spectrum with $\alpha_\gamma = -2/3$, the total synchrotron spectrum of an electron population cannot be flatter than $\alpha_\gamma \leq -2/3$. This phenomenon is referred to as the *line of death*[4] [P$^+$98].

It becomes important, for instance, in the case of Gamma Ray Burst (GRB) spectra, which are typically explained by synchrotron emission of electrons. In some cases, the burst spectra are flatter than the maximum values, which indicates that other phenomena like absorption due to high optical depth need to play a role in the radiative processes in GRBs as well. This will be discussed in Chapter 3.

Electron cooling

The calculations above assume that the dynamical timescale of the system is much shorter than the cooling time of electrons due to radiation losses. This is called the *slow cooling regime*, see [Kar62]. In the *fast cooling regime* of long dynamical timescales compared to radiative cooling, the photon spectrum is flatter by 1/2,

$$s = \frac{p}{2}\,. \tag{1.23}$$

For the prompt emission in GRBs, for example, the dynamical time scale is short compared to the cooling time and slow cooling has to be considered.

Further radiation effects

Note that the synchrotron spectrum is in many cases altered by further radiation effects. The synchrotron field can interact with the electron population, leading to the *Inverse Compton* (IC) effect, which boost photons to higher energies. This scenario is called *Synchrotron Self Compton* (SSC). Processes like optical depth effects, extinction by dust, pair production or bremsstrahlung can additionally alter the observed spectrum. At the highest energies ($E_\gamma \sim$ TeV), the decay of π^0 particles resulting from proton-proton and proton-photon interactions can also dominate the spectrum. The last process competes with the SSC model. TeV emission in such hadronic models are referred to as *Proton-Induced Cascades* (PIC), see [Rac00] for a discussion of the emission features. The question whether high energy photon signals originate from hadronic (π^0-decays) or leptonic (SSC) processes is one of the most striking these days. In some cases, TeV photon emission can also be explained by proton synchrotron radiation.

---

[4] In the integral representation, $S \propto \nu^{-s}$, the spectrum behaves as $S \propto \nu^{1/3}$. While in GRB physics, it is more common to use the differential representation, the integral form is more common to use in the case of AGN spectra.

1.2 Astrophysical Photons

In this section, the most energetic sources in the sky are discussed with respect to their observation in photons, and the possible contribution to the spectrum of charged Cosmic Rays which is displayed in Fig. 1.1. The observed photon spectra are essential for the prediction of neutrino fluxes, since photons are the only messengers giving direct evidence on the properties of the sources. Galactic sources are supernova remnants (SNRs) as likely sources for the production of Cosmic Rays up to the knee as well as X-Ray Binaries (XRBs), in particular microquasars, and pulsars which are candidates for the production of Cosmic Rays above 100 TeV [Gai90]. The most energetic, extragalactic sources are Active Galactic Nuclei (AGN) as permanent sources in the sky as well as Gamma Ray Bursts (GRBs) as transient eruptions. Considering the abundance of the different source types and their individual electromagnetic output, leads to the expectation that galactic sources can produce the Cosmic Ray Spectrum up to the ankle while extragalactic sources are responsible for the CR flux above the ankle. The power of electromagnetic output mirrors the power in Cosmic Rays, since electromagnetic radiation originates from the charged particles in the source. Table 1.1 lists source classes with their intrinsic luminosity and possible contribution to the Cosmic Ray spectrum.

Source class	typical electromagnetic output	possible contribution in energy range:
GALACTIC	SOURCES	
SNR	10^{42} erg/s	10^{10} eV$< E_p < 10^{15}$ eV
SNR-wind	10^{44} erg/s	10^{10} eV$< E_p < 10^{18}$ eV
X-ray binaries	10^{38} erg/s	10^{14} eV$< E_p < 10^{18}$ eV
Pulsars	10^{37} erg/s	10^{14} eV$< E_p < 10^{18}$ eV
EXTRAGALACTIC	SOURCES	
Galaxy clusters	$\sim 10^{44}$ erg/s	$3 \cdot 10^{18}$ eV$< E_p < 10^{21}$ eV
AGN	$10^{44} - 10^{47}$ erg/s	$3 \cdot 10^{18}$ eV$< E_p < 10^{21}$ eV
GRBs	$10^{49} - 10^{51}$ erg/s	$3 \cdot 10^{18}$ eV$< E_p < 10^{21}$ eV

Table 1.1: Source classes possibly contributing to the Cosmic Ray spectrum.

In this thesis, the focus lies on extragalactic sources, since the presently most sensitive neutrino telescope, AMANDA-II[5], is located at the geographic South Pole [AI$^+$06a] and the successor, ICECUBE, is being built there as well [AI$^+$04]. This gives only little access to galactic sources, since the main field of view is the northern hemisphere. However, with the starting construction of ANTARES[6] [AA$^+$97, Mon03] and the plan of building KM3NET [KM3a, KM3b] in the

---

[5] **A**ntarctic **M**uon **A**nd **N**eutrino **D**etector **A**rray-**II**

[6] **A**stronomy with a **N**eutrino **T**elescope and **A**byss environmental **RES**earch

Mediterranean, galactic sources become more and more interesting for high energy neutrino physics.

1.2.1 Active Galactic Nuclei

A class of galaxies with a particularly bright core has been detected for the first time in 1962. An object, appearing star-like in the sky, showed extreme radio-emission features and could therefore not be classified as a star. The interpretation that this object, today known as 3C 273, was indeed a distant galaxy with a very bright core, was suggested for the first time one year after the detection by Maarten Schmidt [Sch63]. This class of objects was referred to as Quasi Stellar Objects (QSOs).

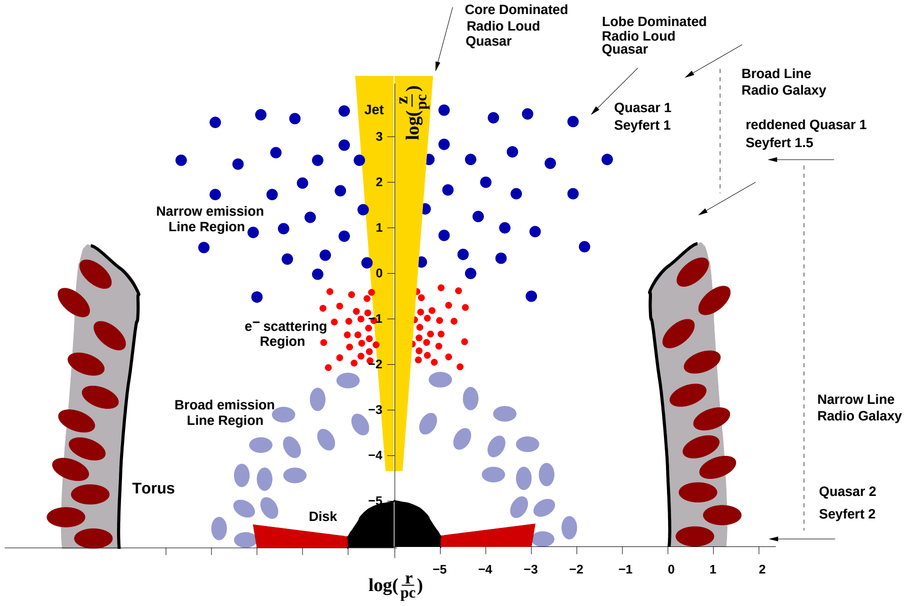

Figure 1.5: Scheme of a cylindrically symmetric AGN shown in the r-z-plane, both axes logarithmically scaled to 1 pc. It is indicated which objects are believed to be seen from which direction [ZB02].

Today, it is known that QSOs fit into the general classification scheme of Active Galactic Nuclei (AGN), objects which are believed to be powered by a rotating supermassive black hole in the center of the galaxy. A schematic view of the general picture of AGN is shown in Fig. 1.5. The core is “active” due to the accretion disk which forms around the central black hole and radiates strongly at optical frequencies. The disk is fed by matter from a dust torus. Perpendicular to the accretion disk, two relativistic jets are emitted, transporting matter in form of lobes. Knots and hot spots along the jets emit radio emission, leading to the strong observed radio signal of AGN. It is expected that these knots and hot spots represent shock environments in which particles are accelerated to high energies, in the case of hadrons up to proton energies of $E_p \sim 10^{21}$ eV, see [BS87]. This is discussed in more detail in Chapter 3. In this section, a general classification scheme for AGN is presented as well as spectral and temporal properties of the sources.

AGN unification scheme

Three main criteria can be used for the unification scheme of Active Galactic Nuclei which is indicated schematically in Fig. 1.6:

1. The activity of the source at radio wavelengths yields a division into radio loud and radio weak objects. About 90% of all AGN are radio weak and are usually hosted in spiral galaxies, while radio loud nuclei are located in the centers of elliptic galaxies.

2. The luminosity of the object is a further classification criterion. Radio weak sources are subdivided into optically strong and optically weak sources, which can be distinguished by considering the features of the emission lines. Optically strong sources usually lack narrow emission lines which are present in the optically weak case. Both source types appear to have broad emission lines. Radio loud sources with extended jets ($\sim$ 100 kpc) are subdivided at radio wavelengths into low luminosity and high luminosity objects at a critical luminosity of $L_\nu = 2.5 \cdot 10^{26}$ W/Hz. The jets of compact objects such as GHz-Peaked Sources (GPS) and Compact Steep Sources (CSS) are believed to get stuck in matter.

3. The third classification criterion is the orientation of the AGN towards the observer. AGN are axisymmetric along the jet axis. In the branch of radio loud AGN, an object is classified as a blazar if one of the jets is pointed directly towards the observer. Flat Spectrum Radio Quasars (FSRQ) are the high luminosity population of the blazars while BL Lacs form the corresponding low luminosity population. So called Faranoff Riley (FR) galaxies are being looked at from the side, so that jets and torus are usually clearly visible. The high luminosity FR-II galaxies show a very strong radio emission at the outermost end of the jets, while the radio emission of the low luminosity class FR-I happens in knots throughout the jet.

   For radio weak AGN, the objects are called radio weak quasars in the optically strong case and Seyfert-I galaxies in the optically weak case when looked at the gap between jet and AGN torus. The radio weak equivalent to FR galaxies are Radio Intermediate Quasars (RIQ) and Seyfert-II galaxies, where the observer's view is directed towards the torus.

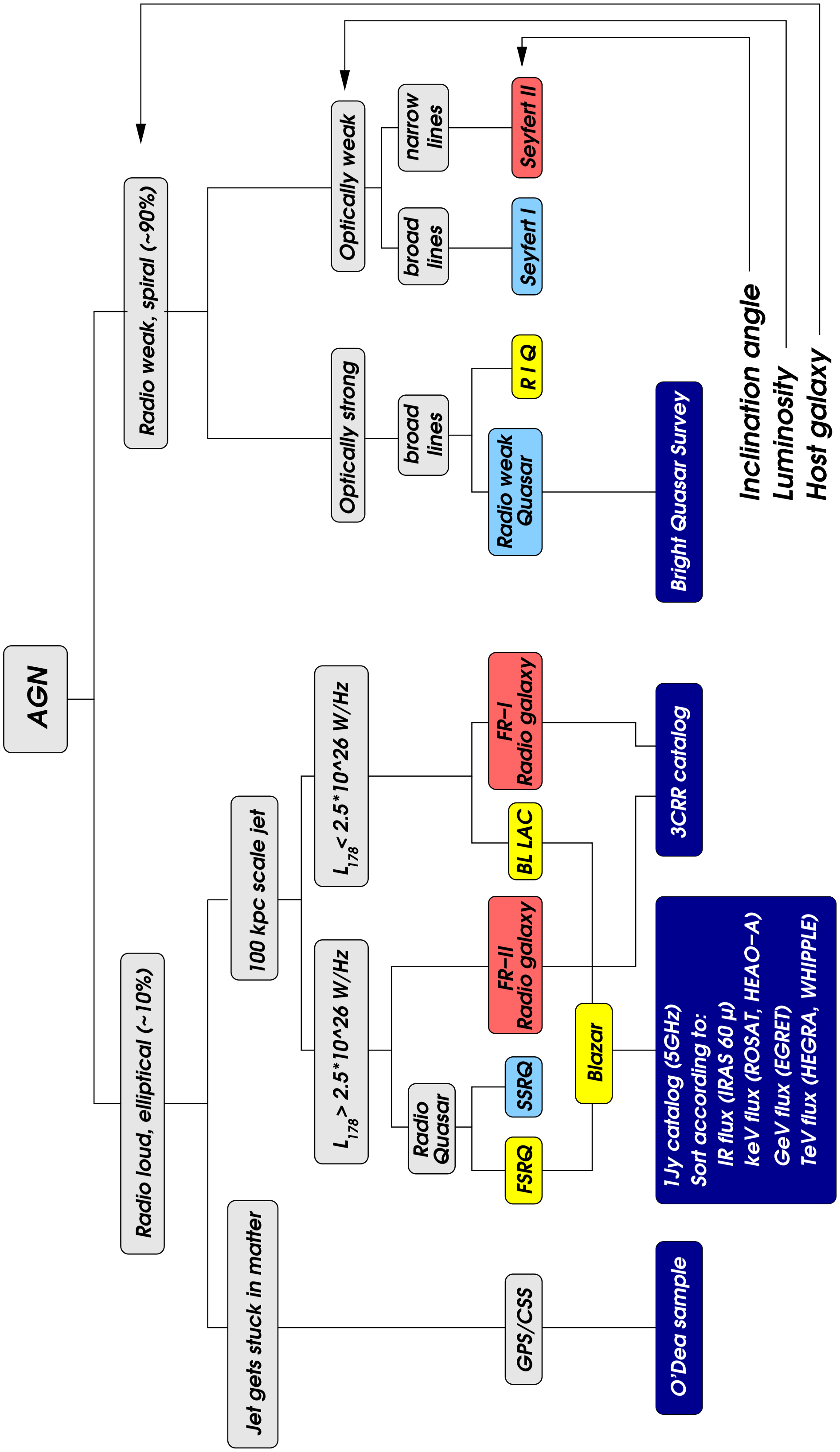

Figure 1.6: AGN classification scheme, figure from [Gro06].

Multiwavelength observations of AGN

AGN have been observed in all frequency bands, ranging from radio observations up to TeV measurements. As an example, the lightcurves of the BL Lac object 1ES 1959+650 is shown in Fig. 1.7, taken during the multiwavelength campaign between May 18, and August 14, 2002 [K$^+$04d]. The bandpasses shown are TeV emission as detected by WHIPPLE (stars) and HEGRA[7] (circles), X-ray emission as measured by RXTE[8], optical emission in the Violett, Red and Infrared band as well as radio measurements from UMRAO[9] at frequencies of 14.5 GHz and 4.8 GHz. As can be seen from the example, AGN are highly variable objects at all wavelengths. In multiwavelength campaigns as the presented one, the correlation between the temporal behavior in the different bandpasses is examined. Such campaigns are relevant to determine the origin of the radiation. In the case of the observation of 1ES 1959+650, a so-called *orphan flare* has been observed, representing a rapid increase in intensity only at TeV energies. Since SSC models necessarily predict the correlated emission of TeV photons and X-rays, this scenario can be excluded for the observed flare. A hadronic scenario in which the TeV photons come from the decay of π^0 particles produced in proton-photon interactions is favored in this case. Orphan flares are very interesting in the context of neutrino emission, since they are a strong hint for hadronic acceleration.

Recent results from [AhH$^+$06a] could restrict the temporal variability at TeV energies to less than 2 days. This implies scales of the order of the Schwarzschild radius of M 87, indicating that the TeV signal originates from the core of the object and not from the jets.

The spectral energy distribution (SED) of AGN typically shows two main bumps apart from dust radiation, which can also lead to a bump in the spectrum, see e.g. [C$^+$89]. The lower energy hump is believed to arise from synchrotron radiation of electrons. Different radiation processes can be responsible for the second hump at higher energies (GeV-TeV): in the Synchrotron Self Compton scenario, the synchrotron photons are up-scattered to high energies by the primary electrons by the Inverse Compton effect. This implies the direct correlation of the two humps in the case of an intensity variation. A second possible scenario is the production of TeV photons in π^0-decays. Neutral pions are produced in hadronic interactions with photon fields or with each other in the source. Such a hadronic scenario leads to the coincident production of high-energy neutrinos. It does not necessarily imply the coincident variation of the lower and higher energy hump, since the two emission signatures are not directly linked. A third component which can contribute at TeV energies is the synchrotron radiation of protons. The latter radiate in the case of high magnetic fields in the acceleration region.

---

[7] **H**igh **E**nergy **G**amma-**R**ay **A**stronomy

[8] **R**ossi **X**-ray **T**iming **E**xplorer

[9] **U**niversity of **M**ichigan **R**adio **A**strophysical **O**bservatory

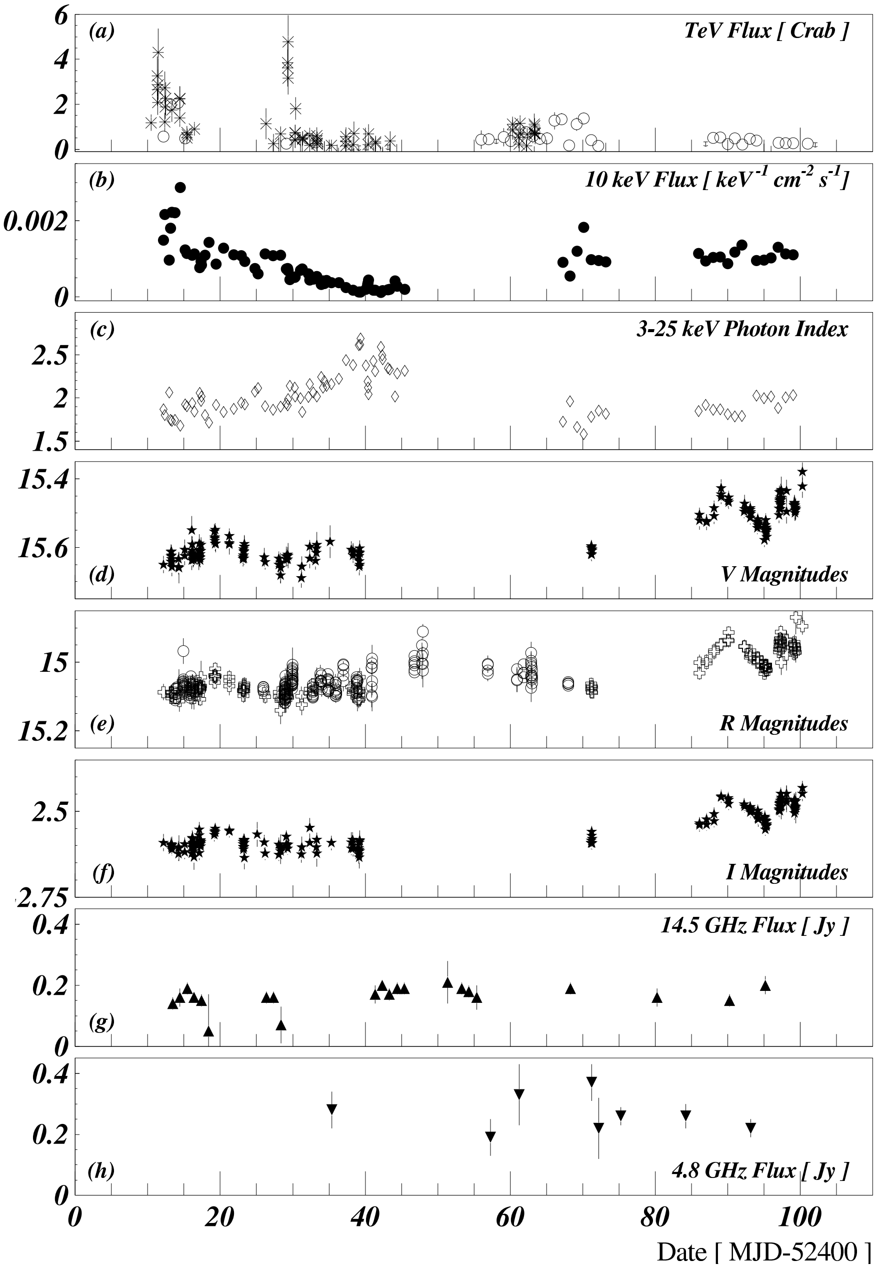

Figure 1.7: Lightcurve of 1ES 1959+650 between May 18, and August 14, 2002. Figure from [K$^+$04d]; Data (from the top): (a) TeV detection by WHIPPLE (stars) and HEGRA (circles); X-ray measurements from RXTE, (b): 10 keV, (c): spectral photon index between (3 – 25) keV; Optical results, (d), (e) and (f): *V* and *I* magnitudes from BOLTWOOD and *R* magnitude from BOLTWOOD (Swiss crosses) and ABASTUNAMI (circles); (g) and (h): radio measurements at frequencies of 14.5 GHz and 4.8 GHz from UMRAO.

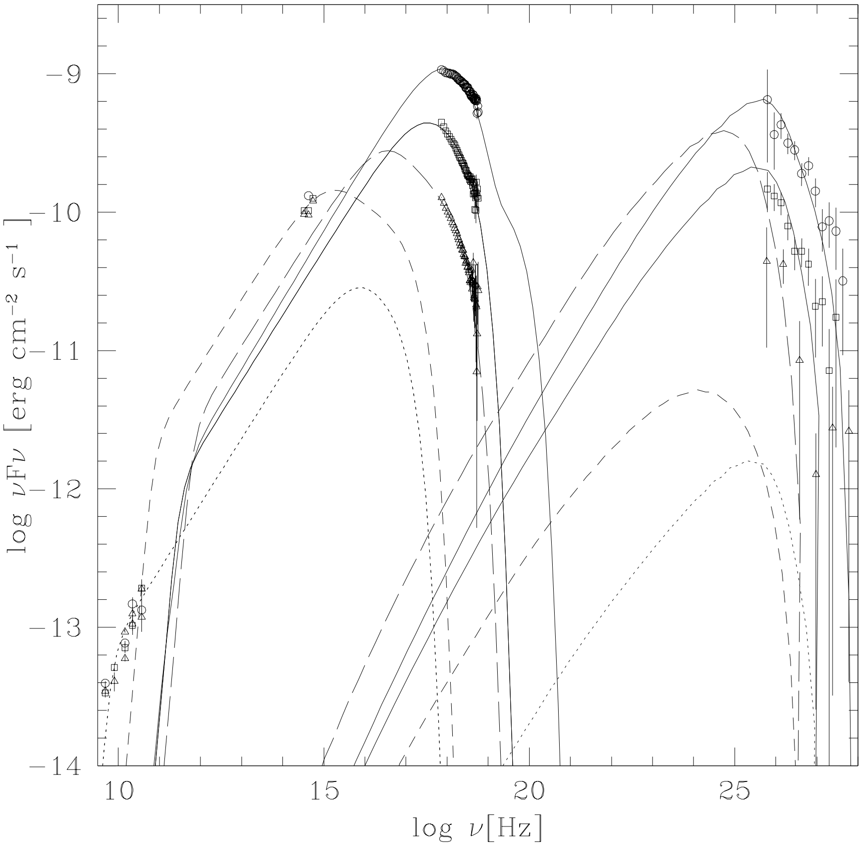

Figure 1.8: Photon spectrum of Mkn 421 [B^+05a].

Depending on the energy range of the second hump in the SED, BL Lac objects can be divided into a further sub-class of *High-peaked BL Lacs (HBLs)* and *Low-peaked BL Lacs (LBLs)*. If the peak occurs at TeV energies, sources are called HBLs, while they are referred to as LBLs at peak energies in the GeV range. As an example for a high-peaked BL Lac, the SED of the BL Lac object Mkn 421 is given in Fig. 1.8. It shows photon emission over 18 orders of magnitude. The spectrum is characterized by two peaks, one in the keV and one in the GeV to TeV region.

1.2.2 Gamma Ray Bursts

Photon eruptions of unknown origin were detected in the 1960th by both America and Soviet military satellites. While it was immediately clear that these events were not man made, but originated from outer space, the publication of the first observation in 1967 did not happen before 1973 in the case of the VELA SATELLITES [KSO73] and only a few months later in the case of the Soviet KOSMOS-461, and the American OSO-7[10] and IMP-6[11] satellites [W$^+$73, CD73, MGI74]. Systematic studies of these Gamma Ray Bursts (GRBs) were done with BATSE[12] on board of the CGRO[13] which was taking data for 9 years, between April 1991 and June 2000 [P$^+$99]. During that time, 2704 GRBs in the energy range of (20, 2000) keV were detected[14].

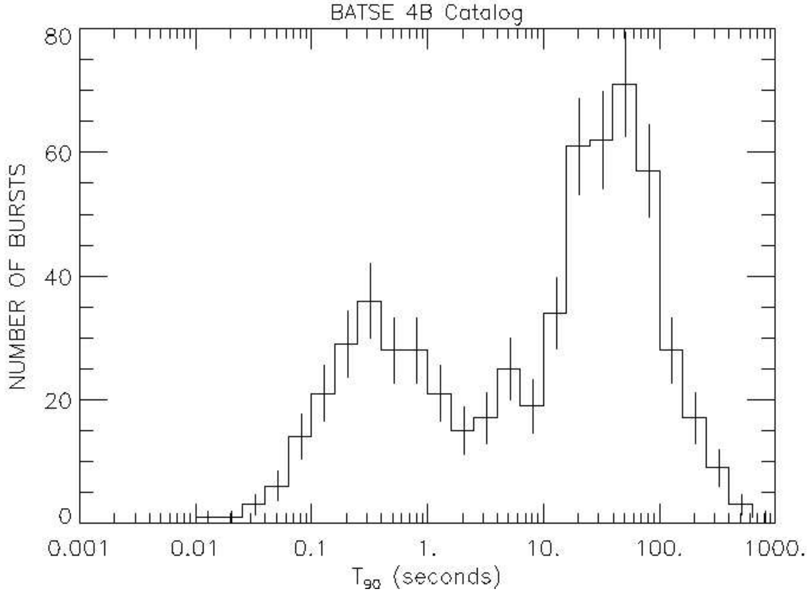

Figure 1.9: Distribution of t_{90} for 1234 GRBs in the BATSE 4B Catalog [P$^+$99, BAT06]. Events with $t_{90} < 2$ s are classified as short bursts, GRBs with $t_{90} > 2$ s are called long bursts. Figure courtesy NASA/CGRO BATSE team.

Figure 1.9 shows the distribution of the duration of the bursts t_{90} [BAT06, P$^+$99], defined in the way that 90% of the signal was received during that time. Two populations of bursts can be identified, classified as "short" ($t_{90} < 2$ s) and "long" ($t_{90} > 2$ s) bursts. The spatial distribution of GRBs in galactic coordinates as observed by the BATSE experiment is displayed in Fig. 1.10. The bursts distribute isotropically with no visible clustering in the galactic plane or anywhere else. This indicates an extragalactic origin of the events. However, scenarios of a galactic halo with so far unknown sources of GRBs were also proposed, see e.g. [H$^+$94, PRR95, FS96]. A first indication of a cosmological origin was given by the spatially non-Euclidean distribution of the source luminosity. Details on

---

[10] **O**rbiting **S**olar **O**bservatory-**7**

[11] **I**nterplanetary **M**onitoring **P**latform-**6**

[12] **B**urst **a**nd **T**ransient **S**ource **E**xperiment

[13] **C**ompton **G**amma **R**ay **O**bservatory

[14] In the following, the detection energy range of all quoted instruments is given in the notation ($E_{\min}$, $E_{\max}$) *keV* for simplicity.

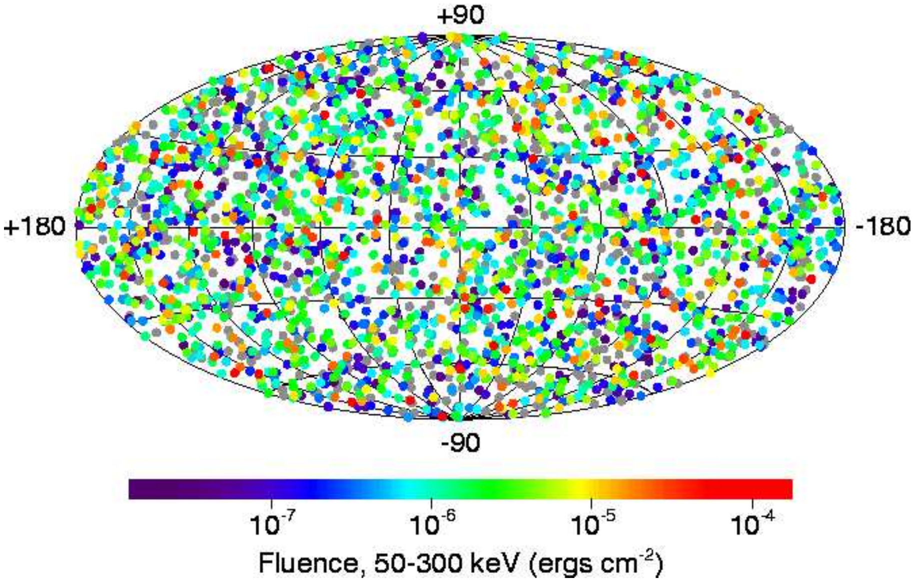

Figure 1.10: Spatial distribution of 2704 GRBs in the BATSE Catalog [P^+99, BAT06] in galactic coordinates. The distribution is isotropic. Figure courtesy NASA/CGRO BATSE team.

the spatial evolution of source class distributions can be found in Chapter 6. The final proof of the cosmological distance of GRBs was only given in 1997 by the first afterglow observation by the BeppoSax[15] satellite, see e.g. [WRM97]. While the prompt emission is mainly detected in the keV-MeV band, the so-called afterglow continues until long after the prompt emission and is seen in basically all wavelength-bands, from the radio band up to GeV-energies. From the afterglow-observation, host galaxies can be identified, or absorption and emission lines can be measured to determine the redshift at which the GRB occurred. These redshifts are cosmological, so that GRBs are known to happen outside of our Galaxy. The reason for the intense discussion of a galactic origin was that the photon fluence F_γ in the (20, 2000) keV energy band as measured by BATSE scatters around

$$F_\gamma \sim 10^{-6}\ \mathrm{erg/cm}^2\,. \tag{1.24}$$

The term "fluence" is used here as opposed to flux, since the units are erg/cm^2, while a flux is typically measured per area and time interval. For extragalactic distances, the total luminosity L_{GRB} of a GRB event lies around

$$L_{GRB} \sim 10^{51}\ \mathrm{erg/s} \tag{1.25}$$

for isotropic emission, but a little bit lower in the case of beamed emission favored

---

[15] **Beppo** stands for Guiseppe Occhialini, and "SAX" is an acronym for **S**atellite per **A**stronomia **X**

currently. This tremendous output lies more than four orders of magnitude higher than the typical output of AGN, the most luminous source class in the sky,

$$L_{AGN} \sim 10^{44} - 10^{47}\mathrm{erg/s}\,. \tag{1.26}$$

While GRBs emit only for a short time of a few seconds, AGN are active over long periods, so that the time integrated output is comparable, $\sim 10^{62}$ erg. In the past decades, different models have been developed to explain the output from GRBs and AGN. Many of the classical arguments for the description of GRB physics are borrowed from supernova remnants [Wol72, Cox72, CS74] or AGN models [Ree70], since the phenomena are similar, although on different spacetime-scales. Both AGN and GRBs show a variable time structure. supernova remnants as well as long GRBs are produced in the explosion of stars. In all three objects, shock fronts are responsible for particle acceleration and therefore, the non-thermal electromagnetic spectrum can explained by synchrotron radiation of electrons, Inverse Compton scattering and also by proton-photon interactions. The favored model which is able to explain most of the phenomena connected to a GRB is the fireball model, explaining the huge electromagnetic emission by shock formation of relativistic plasma shells, see e.g. [Pir99, Pir05a, ZM04]. Alternatively, the Cannonball model tries to explain GRBs by colliding plasma balls, see e.g. [DR04, Dar06]. The latter meets, however, observations difficult to match the predictions in this model, e.g. the prediction of apparent motion for the radio emission, which is not observed for GRBs. Thus, only the fireball model will be discussed in more detail in the following paragraph.

Fireball model

A schematic view of the fireball model is shown in Fig. 1.11. It is based on the model of stellar outbursts as described in [Sed58] and has been enhanced including relativistic effects in order to match GRB observations. The fireball model does not give any constraint on the progenitor. It yields a phenomenological description of the actual burst observations. The basic idea is that a large amount of mass is ejected within a short time interval by a central engine. The plasma is ejected successively in shells. At some point, the outer shells slow down and are caught by inner shells and a shock front is built up, accelerating electrons and baryons in the plasma up to high energies. While protons can be accelerated basically loss-free up to energies as high as 10^{21} eV [Vie95, Wax00], electrons lose their energy to synchrotron radiation, escaping from the shocks as soon as the region becomes optically thin. This is observed as prompt emission from GRBs. Those shocks resulting from collisions of shells are called *internal shocks*. So-called *external shocks* result from collisions of the shells with the interstellar medium leading to afterglow emission as described in the following paragraph. While the prompt emission occurs mainly at energies of $E_\gamma > 100$ keV, afterglow emission is observed in almost all wavelength bands. Reviews on the details of the underlying physics are given in e.g. [Pir99, Pir05a, ZM04].

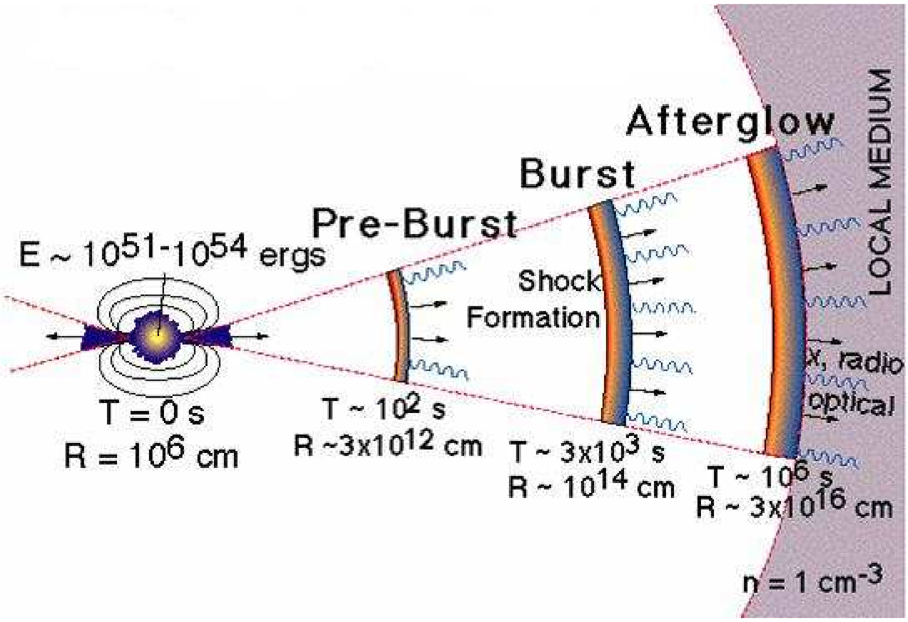

Figure 1.11: Schematic view of the fireball scenario [Swi06b].

GRB experiments after BATSE

After the BATSE era, many GRB satellites were taking data, each covering a much smaller field of view and thus providing much less statistics than BATSE. Additionally, many of the satellites were not able to give directional information. For the determination of the GRB spatial origin, it is necessary to have at least three detectors. BATSE had four energy channels and could localize GRBs. The precision was between approximately 10° and a few degrees. Other satellites have only one or two instruments on board. To improve the localization of GRBs, the INTERPLANETARY NETWORK was created already in the 70s as an interconnection of all GRB satellites. The currently active third INTERPLANETARY NETWORK, IPN3, was formed with the launch of ULYSSES in 1990 [H$^+$92, Uly06]. Since the beginning, more than 25 spacecraft missions have participated. The CGRO joined in 1991 when it was launched. Today, HETE-II[16] [S$^+$05a, HET06], INTEGRAL[17] [Win04, M$^+$05b], RHESSI[18] [RHE06], MARS ODYSSEY [H$^+$06c, Mar07], ULYSSES [H$^+$92, Uly06], KONUS WIND [M$^+$05a, Kon06] and SWIFT form the IPN3. The most important GRB experiments with some of their individual properties are listed in table 1.2. With information of more than two instruments, GRB positions of a accuracies up to several square-arcminutes can be reconstructed. Before the launch of BEPPOSAX in 1996, this was the only possibility of arcminute precision measurements. HETE-II and INTEGRAL are

---

[16] **H**igh **E**nergy **T**ransient **E**xplorer-II

[17] **INTE**rnational **G**amma-**R**ay **A**strophysics **L**aboratory

[18] **R**amaty **H**igh **E**nergy **S**olar **S**pectroscopic **I**mager

able to localize GRBs without additional information from IPN3. Konus is very sensitive to short GRBs and a catalog of ~ 130 short GRBs is examined in the context of neutrino emission, see Chapter 5.

GRB Sat.	Launch-Demise	FoV***	E-range [keV]	Localiz. Precision	Reference
Vela 5B	05/1969-06/1979	$6.1^\circ \times 6.1^\circ$	(3, 750)	-	[KSO73]
Kosmos-641	12/1971-09/1972	$\sim 2\pi$ sr	(28, 1000)	-	[MGI74, Pal07] [M$^+$75]
Ulysses*	10/1990-now	$< 75^\circ$	(5, 150)	-	[H$^+$92] [Uly06]
BATSE	04/1991-06/2000	$\sim 2\pi$ sr	(20, 2000)	degree	[P$^+$99] [BAT06]
BeppoSax	04/1996-04/2002	$0.5^\circ - 1.3^\circ$	(0.1, 300)	arcmin	[B$^+$97a] [Bep06]
Mars Od.*	04/2001-now	62°	(50, 10000)	-	[H$^+$06c] [Mar07]
NEAR	02/1996-02/2001	60°	(1, 10000)	-	[NEA06]
Konus W.*	11/1994-now	$\sim 2\pi$ sr	(10, 10000)	-	[Kon06]
RHESSI*	02/2002-now	1°	(3, 20000)	-	[RHE06]
INTEGRAL*	10/2002-now				[M$^+$05b]
SPI		16°	(18,8000)	-	
IBIS		$9^\circ \times 9^\circ$	(15, 10000)	arcmin	
HETE-II*	10/2000-now	$1.5 - 3$ sr	(0.5, 400)	arcmin	[HET06] [S$^+$05a]
Swift*	11/2004-now				[Chi06]
BAT		2 sr	(15, 150)	arcmin	[Swi06a]
UVOT**		$17' \times 17'$	(170, 650)	arcsec	
XRT		$23.6' \times 23.6'$	(0.2, 10)	arcsec	

Table 1.2: Some GRB Satellites and the basic properties of the main instruments for the detection of prompt emission. FoV= Field of View. /* : Current member of IPN3. /**: the energy range for UVOT is given in terms of wavelength, in units of nano-meters (nm). /***: FoV for BATSE and Kosmos-641 is actually 4π sr, but here it is assumed that $\sim$ half a hemisphere is occulted by the Earth.

The Swift satellite was launched in November 2004 - for a review see e.g. [Chi06] and references therein. Swift is a dedicated GRB satellite with four instruments on board. The main purpose of the BAT[19] detector is the discovery of prompt emission from GRBs. The main sensitivity is in the energy range of (15, 150) keV and the field of view is about 2 sr. About 100 GRBs per year are detected with BAT. The XRT[20] covers an energy range of (0.2, 10) keV and serves afterglow observation. The UVOT[21] is an instrument for the detection of the optical afterglow at (170, 650) nm wavelengths.

---

[19] **B**urst **A**lert **T**elescope

[20] **X**-**R**ay **T**elescope

[21] **UV**/**O**ptical **T**elescope

The advantage of a satellite carrying both prompt emission and afterglow instruments is that the afterglow can be followed almost starting from the prompt emission phase. This has already lead to the discovery of unexpected temporal behavior directly after the prompt emission, see e.g. [Més06] for a review. The basic features of the early afterglow are shown in Fig. 1.12. While the afterglow appearance at $t \sim 10^4$ s after the prompt emission had been known before, the temporal behavior at earlier times was unexplored until the launch of SWIFT. Two main features are found. Firstly, a break in the temporal decay structure t^{α_t} is observed. The decay index changes from $\alpha_t \sim -3$ to ~ -0.5 at around 100 s to 1000 s after the prompt emission and it changes back to the previously observed $\alpha_t \sim -1.3$ behavior at 10^4 s to 10^5 s. Secondly, X-ray flares are detected during the early afterglow, indicated by the dashed triangle in the curve. X-ray flares occur only in a fraction of the observed bursts. Different models to explain both the changes in the decay index and the X-ray flares have been developed which are reviewed in e. g. [Més06].

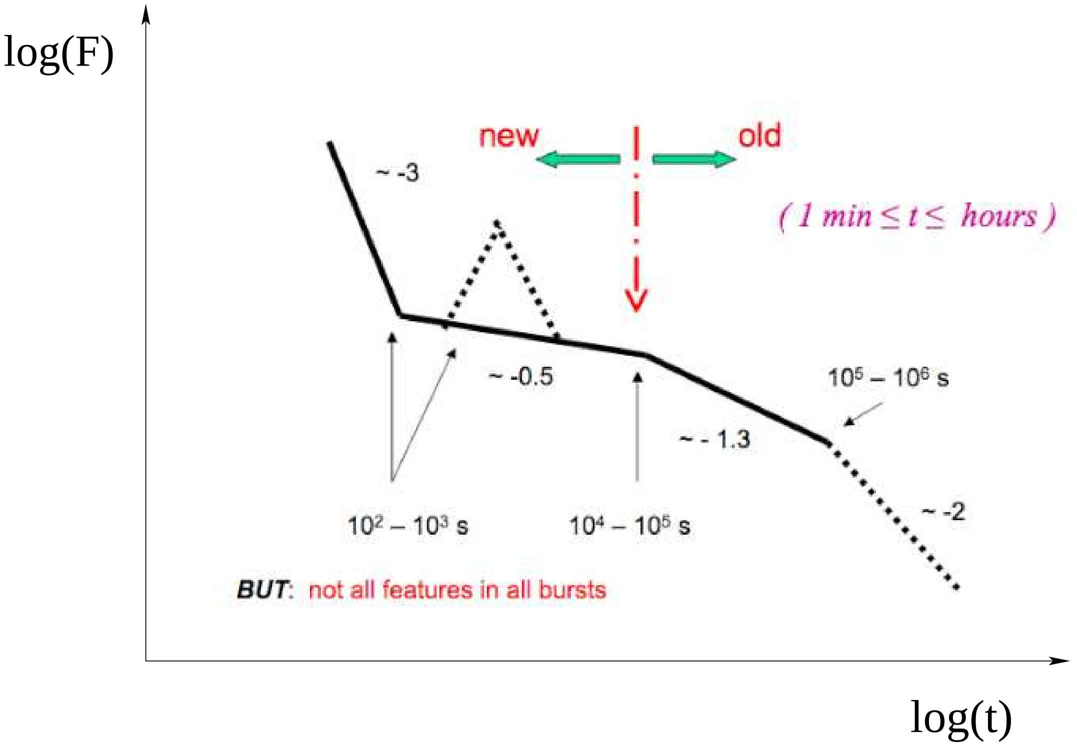

Figure 1.12: Early afterglow - temporal intensity behavior. The scale is double logarithmic and the temporal behavior follows t^{α_t} with different decay indices α_t for different time periods as indicated in the figure. Figure from [Més06].

Prompt GRB spectra

The prompt GRB photon spectrum, $dN_\gamma/dE_\gamma(E_\gamma)$, is usually given by a Band function [B$^+$93],

$$\frac{dN_\gamma}{dE_\gamma}(E_\gamma) = \begin{cases} A\left(\frac{E_\gamma}{100\ \mathrm{keV}}\right)^{\alpha_\gamma} e^{(-E_\gamma/E_0)} & E_\gamma \leq (\alpha_\gamma - \beta_\gamma)\,E_0 \\ A\left(\frac{E_\gamma}{100\ \mathrm{keV}}\right)^{\beta_\gamma} \left[\frac{(\alpha_\gamma-\beta_\gamma)E_0}{100\ \mathrm{keV}}\right]^{\alpha_\gamma-\beta_\gamma} e^{(-(\alpha_\gamma-\beta_\gamma))} & E_\gamma > (\alpha_\gamma - \beta_\gamma)\,E_0\,. \end{cases} \tag{1.27}$$

Here, E_γ is the photon energy, E_0 is the reference energy with $(\alpha_\gamma - \beta_\gamma)\cdot E_0 = \epsilon_\gamma^b$ as the break energy in the photon spectrum. The energy range of detection may not cover both parts of the spectrum and many spectral fits use simpler approximations. The samples used in this section are based on three different fit methods. Each model represents a simplified version of the Band function:

1. *Model 1* is a single powerlaw fit with an exponential cutoff in the spectrum,
$$\frac{dN_\gamma}{dE_\gamma} \propto E_\gamma^{\alpha_\gamma}\cdot\exp(-E_\gamma/E_0)\,. \tag{1.28}$$
2. *Model 2* is a single powerlaw fit with no cutoff,
$$\frac{dN_\gamma}{dE_\gamma} \propto E_\gamma^{\alpha_\gamma}\,. \tag{1.29}$$
In that case, the cutoff lies out of the detector's range. Thus, a lower limit of the cutoff is given by the maximum detection energy and Equ. (1.28) can be used.
3. *Model 3* is a broken powerlaw,
$$\frac{dN_\gamma}{dE_\gamma} \propto \begin{cases} E_\gamma^{\alpha_\gamma} & \text{for } E_\gamma < \epsilon_\gamma^b \\ E_\gamma^{\beta_\gamma} & \text{for } E_\gamma \geq \epsilon_\gamma^b\,. \end{cases} \tag{1.30}$$

The break energy for the photon spectrum is given as $\epsilon^b_{\gamma,MeV} = E_0/\mathrm{MeV}$ for model 1 and 2, and $\epsilon^b_{\gamma,MeV} = (\alpha_\gamma - \beta_\gamma)\cdot E_0/\mathrm{MeV}$ for model 3.

The spectrum is presumably produced by synchrotron radiation of electrons in the internal shock fronts of the jet, see e.g. [HaHo02] and references therein. There are two approaches to explain the break in the spectrum at a break energy of typically $\epsilon_\gamma^b \sim 250$ keV. The most common explanation is the steepening of the spectrum by one power due to cooling of electrons at high energies, see for example [ZM04, Pir05a] as a review. The break can also be explained by assuming an Inverse Compton scattering scenario, see e.g. [DR04] and references therein. Throughout this thesis, all given energies for GRB spectra are in the observer's frame at Earth unless declared otherwise. For a regular GRB, the spectral indices are usually distributed around average values of $\alpha_\gamma \sim -1$ and $\beta_\gamma \sim -2$. These values scatter over a wide range. Short GRBs tend to have harder spectra with $\alpha_\gamma \sim 0$ and $\beta_\gamma \sim -1$. Assuming hadronic acceleration in the jet, a prompt neutrino flux that is correlated to the photon spectrum results from photo-hadronic interactions in the source.

Observed Redshifts from GRBs and GRB progenitors

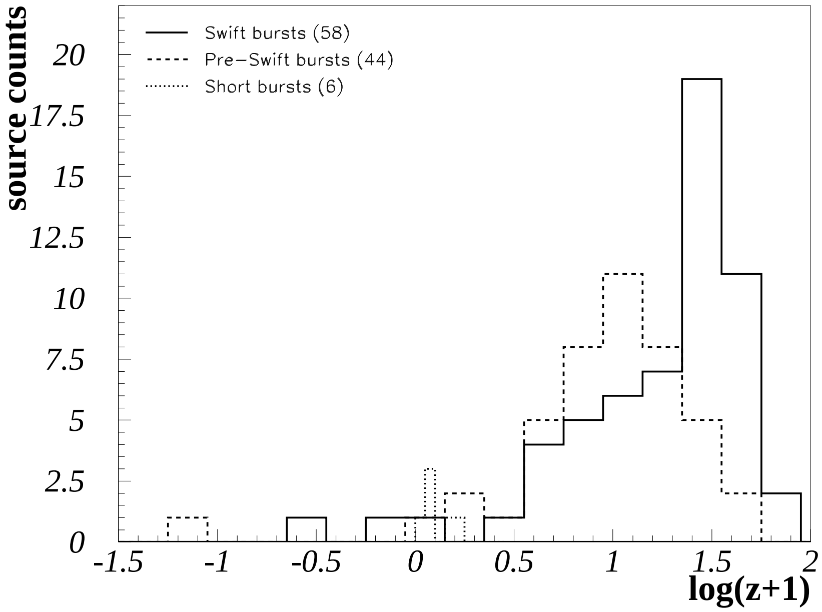

Figure 1.13: Observed bursts with measured redshifts. The solid line represents long bursts with redshifts from the SWIFT time, the dashed line shows long GRBs in the pre-SWIFT era. There is a clear shift of the distributions. Bursts in the pre-SWIFT era (mostly BATSE measurements) have lower redshifts on average. The dotted line shows the distribution of short bursts with measured redshifts in the SWIFT era. There were no redshift detections of short bursts before the launch of SWIFT.

The first afterglow observation by BEPPOSAX for GRB970228 also implied the first measurement of the redshift of a GRB. Between 1997 and November 2004 - the time of the launch of SWIFT - redshifts of 44 GRBs have been detected. Since the launch of SWIFT, 58 long and 6 short GRB redshifts were measured as of March 12 2007. Figure 1.13 shows the redshift distribution of those GRBs. The solid line represents SWIFT bursts while the dashed line shows pre-SWIFT measurements of redshifts. The mean of the distributions is shifted, SWIFT observations show a higher contribution of very distant bursts. One reason for this is the better sensitivity of SWIFT compared to pre-SWIFT instruments. Bursts at high redshifts have typically a weaker fluence and may have been missed by instruments of lower sensitivity. The systematically higher redshift behavior of SWIFT-era bursts is shown in Fig. 1.14, where the measured redshifts are shown versus time, the data points coded according to the instrument of prompt emission detection.

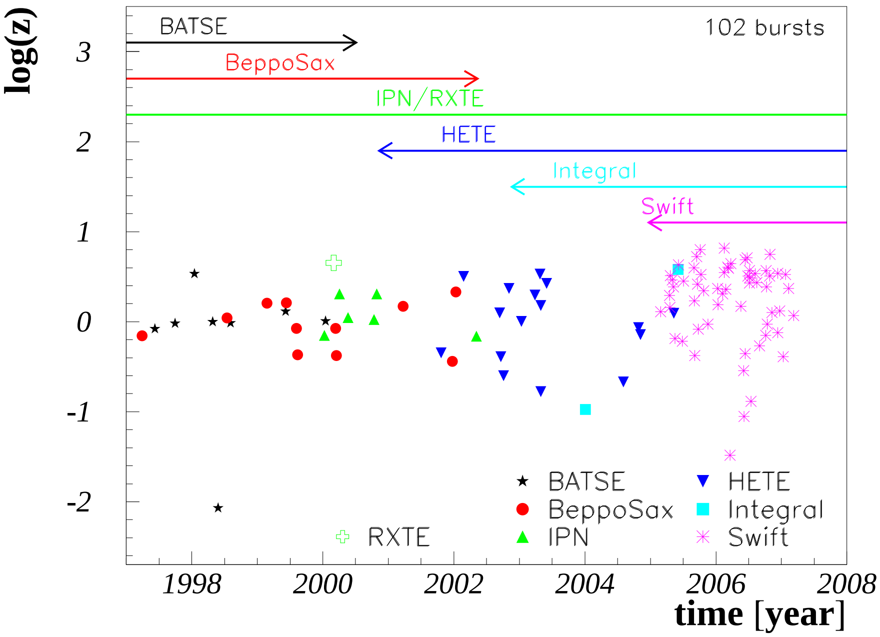

Figure 1.14: GRB redshift versus time. SWIFT bursts (starlets) typically have a higher redshifts than bursts detected by other experiments due to differences in the sensitivity and energy range of detection.

The higher statistics relies on the possibility of early afterglow observation of the SWIFT instruments XRT and UVOT. The increase of redshift measurements with time since the launch of SWIFT is displayed in Fig. 1.15, where the number of bursts with measured redshifts is displayed versus time. The number of bursts increases linearly with time, but changes to a different slope with the launch of SWIFT.

It has been known since 2003 that long GRBs are connected to supernova explosions of type Ic, which follow the death of Wolf-Rayet stars [M$^+$03a]. Two scenarios of producing jets in exploding stars have been discussed:

1. the core collapse from the center of a flattened, fast rotating star, see [Sak71, Möl76];

2. the magnetorotational core collapse with an initial dipole magnetic field configuration as suggested in [Bis70, Bis71].

Short bursts have been proven in 2005 to originate from the merging of two neutron stars or a neutron star and a black hole in a binary system [H$^+$05, V$^+$05c,

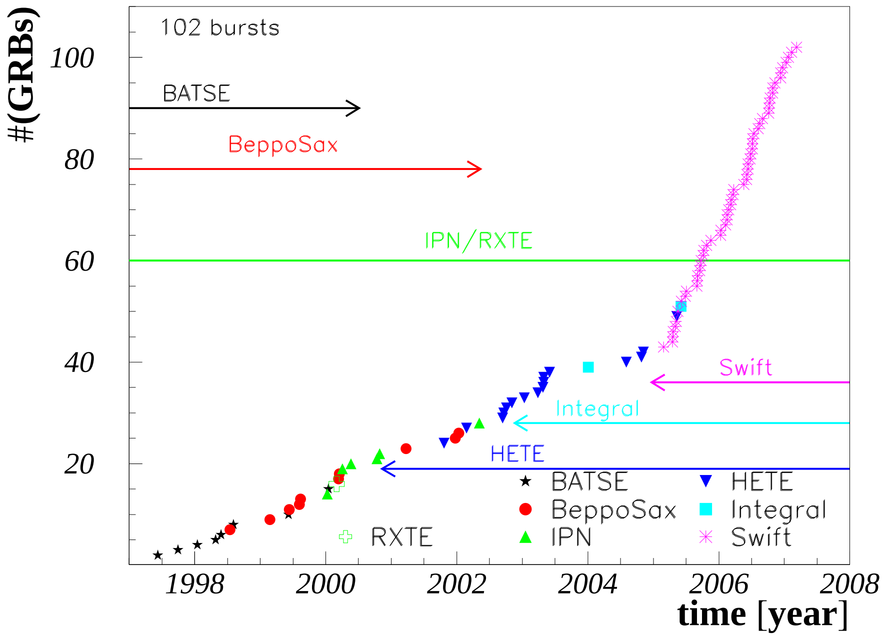

Figure 1.15: Number of bursts with known redshift versus time. There is a clear kink in the curve, at the time where Swift started taking data. The increased measurement of redshift depends on the fast response of the Swift XRT, which allows an arcmin localization within less than a minute.

G$^+$06b]. The differences in the observed events lie not only in the duration of the bursts, but are also seen in the redshift distribution. While long GRBs are most likely to follow the star formation rate and are located in starforming regions, short bursts happen in regions of rather low star formation rate and at small redshifts ($z \sim 0.1$).

New results from the Swift satellite show, however, that this scheme is still too simple: there are exceptional bursts which do not fit into this scheme (e.g. GRB060218, GRB060614) [C$^+$06a, G$^+$06a]. Also, Swift does not see the strong extinction between short hard and long soft bursts as it was observed by BATSE [SaSw06]. This indicates that the classification scheme is more complex than it can be determined yet and needs to be refined in the future.

Redshift estimators

Due to the lack of information on actual GRB redshifts, different estimator methods have been developed. The aim is to use secondary properties which can be measured for most GRBs and which are directly correlated to the redshift. In the following, three estimators will shortly be discussed. Two of them will be used in Chapter 5 to determine the neutrino flux from the sources with pseudo redshifts. Redshifts of 568 bursts have been determined by [G$^+$04] using the *variability method* and redshifts from 292 bursts have been found by applying the *lag method*.

All redshift estimators are based on correlations between a certain observable and the burst luminosity. The methods are analogous to distance measurements based on the selection of standard candles setting up the astronomical distance ladder. The redshift can easily be obtained from the luminosity, since the latter is correlated with the observed fluence via the luminosity distance $d_l(z)$,

$$L(z) = \frac{F_\gamma}{t_{90}} \cdot 4\,\pi\, d_l(z)^2 \cdot (1+z)\,. \tag{1.31}$$

Thus, knowing the luminosity yields the possibility of redshift determination.

Variability method Each GRB lightcurve shows a certain “spikiness“ on short time scales. Defining a “variability“ of the flux as a measure of the spikiness, this can be correlated with the luminosity of the bursts [FR00]. Smooth bursts seem to be intrinsically less luminous. Finding the exact correlation for bursts with known luminosities, it can be applied as a redshift estimator for bursts with no observed redshifts. A measure for the variability V is defined in [FR00]. The variability V is defined in a certain energy interval $[E_{lower}, E_{upper}]$, $V := V(E_{lower}, E_{upper})$, since the different energy channels of BATSE, see e.g. [P$^+$99, BAT06], will be used to calibrate the relation as will be seen in the following. Defining $Y := (1+z)/(1+z_b)$ with a baseline redshift of $z_b = 2$ (since most GRBs are located at high redshifts, i.e. $z > 1$), another parameter,

$$C_x := \frac{V(Y\,E_{lower}, Y\,E_{upper})}{V(E_{lower}, E_{upper})} \tag{1.32}$$

can be defined. For $Y = 2$, C_x can be estimated using that BATSE energy channels 1 and 2 are shifted by a factor 2 (channel 1: (25, 50) keV, channel 2: (50, 100) keV). Analyzing BATSE data, it is found that

$$C_x(Y=2) = 0.85\,. \tag{1.33}$$

Under the assumption that the relation is invertible, i.e.

$$\left(\frac{V(Y\,E_{lower}, Y\,E_{upper})}{V(E_{lower}, E_{upper})}\right)^{-1} \approx \frac{V(Y^{-1}\,E_{lower}, Y^{-1}\,E_{upper})}{V(E_{lower}, E_{upper})}\,, \tag{1.34}$$

it is known that

$$C_x(Y = 2^{-1} = 0.5) = (0.85)^{-1}\,. \tag{1.35}$$

The average pulse width of a GRB as a function of energy behaves as a powerlaw, and thus, following Fenimore & Ramirez [FR00], a relation between Y and C_x can be derived as follows:

$$C_x(Y) \propto Y^{-0.24}\,. \tag{1.36}$$

Seven bursts with known redshift and variability have been analyzed and it has been found that the correlation between the luminosity per solid angle $d\Omega$ is

$$L/d\Omega = \begin{cases} 5.9 \cdot 10^{60} \cdot V^{5.8}\,\mathrm{erg/s} \\ 2.4 \cdot 10^{54} \cdot V^{2.2}\,\mathrm{erg/s}\,. \end{cases} \tag{1.37}$$

There are two powerlaws suggested by [FR00], since the data still scatter relatively widely. SWIFT [Chi06] is already able to contribute many bursts with measured redshift, so that in the future, a better description of the correlation between intrinsic luminosity and variability is expected.

Temporal lag Another method of estimating redshifts is a correlation between an observed temporal lag τ_{lag} in BATSE energy channels 1 and 3 and the intrinsic luminosity of the bursts L_γ [Nor02]. The method is described in detail by Norris et al. [Nor02]. The result is that the luminosity is correlated to the temporal lag as

$$L_\gamma^{52} \approx \begin{cases} 13\,\left(\frac{\tau_{lag}}{0.01\mathrm{s}}\right)^{-1.14} & \text{for } 0.003\text{ s} < \tau_{lag} < 0.35\text{ s} \\ 78\,\left(\frac{\tau_{lag}}{0.01\mathrm{s}}\right)^{-4.7} & \text{for } \tau_{lag} > 0.35\text{ s}\,. \end{cases} \tag{1.38}$$

Peak energy As it has been pointed out by e.g. [Att03, Y$^+$04, PH06], the peak energy in each GRB seems to be correlated with the redshift of the source. Using the exact description of the GRB spectrum through the Band function as described previously, the peak energy of the spectrum E_{peak} can be derived as

$$E_{peak} = (2 + \alpha_\gamma)\,E_0\,,$$

under the assumption that $\alpha_\gamma > -2$ and $\beta_\gamma < -2$ [Y$^+$04]. For bursts with measured redshifts, the peak luminosity can be calculated using the total flux Φ_γ, $L_p = 4\,\pi\,d_l^2\,\Phi_\gamma\,k_c$. k_c is a correction factor taking into account cosmological redshifting as described in [A$^+$02]. A correlation between E_{peak} and L_p has been developed from these pieces of information and it is given as [Y$^+$04]

$$\frac{L_p}{10^{52}\mathrm{erg/s}} = (2.34^{+2.29}_{-1.76}) \cdot 10^{-5}\,\left[\frac{E_{peak}\,(1+z)}{1\text{ keV}}\right]^{2.0\mp0.2} \tag{1.39}$$

with 1σ errors given.

Currently, it seems that this method of determining GRB redshifts is the most reliable of the three methods [Sch04]. There is no sample available from this method at the moment.

Classification of GRBs

In order to explain the observation of the prompt emission in GRBs, a boost factor of $\Gamma > 100$ for the shock fronts is necessary. For lower boost factors, the shock region is optically thick to pair production processes. On the other hand, the boost factor must not exceed $\Gamma \sim 1000$, since protons would lose most of their energy due to synchrotron radiation in that case [HaHo02]. The peak energy of the GRB, E_{peak} is directly correlated to the boost factor and lies around $E_{peak} \sim (100,\ 1000)$ keV for regular GRBs. Typically, a boost factor of $\Gamma = 300$ is assumed. The two main sub-classes of GRBs are long and short ones. The differences do not only lie in the duration of the events, but also in the hardness of the spectra. Short bursts typically have much harder spectra than long GRBs which is why they are usually referred to as Short Hard Bursts (SHBs).

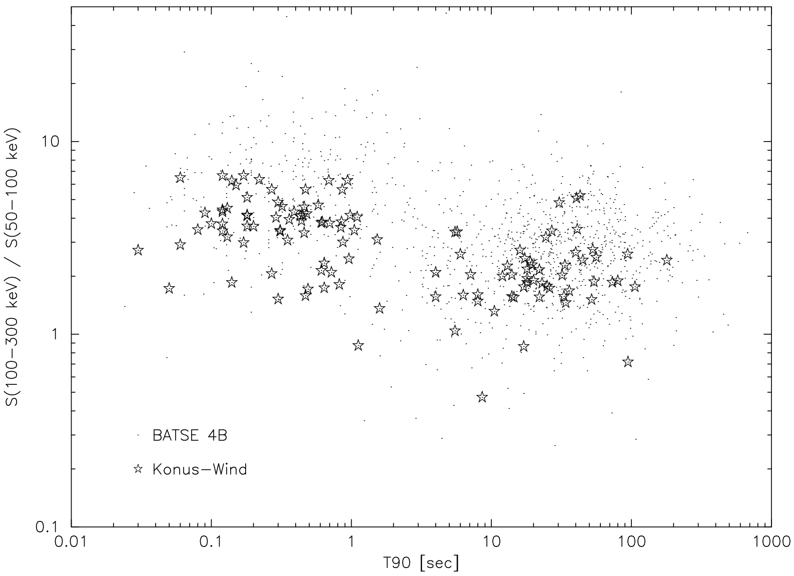

Figure 1.16: Hardness ratio of BATSE (dots) and Konus (stars) GRBs versus t_{90}. Short bursts with $t_{90} < 2$ s tend to be harder than long ones. Figure from [SaSw06].

A measure for the hardness is the ratio of soft to hard emission,

$$\text{hardness ratio} := H := \frac{S(\text{hard})}{S(\text{soft})}\,. \tag{1.40}$$

with S as the photon flux. In the case of BATSE, which had four energy channels, channel 3 with an energy range of (100, 300) keV and channel 4, (50, 100) keV were used to determine the hardness ratio. The result is shown in Fig. 1.16 where the duration of the bursts are displayed versus the hardness ratio $H_{32} = S(100,\ 300)/S(50,\ 100)$. BATSE bursts are marked as dots. Bursts with $t_{90} < 2$ s are generally harder than long bursts ($t_{90} > 2$ s). It should be noted, though, that follow-up experiments like HETE-II, KONUS and SWIFT do not see equally hard short bursts. In Fig. 1.16, stars display KONUS bursts. The short bursts are still harder, but typically not as hard as BATSE bursts. For more details, see [SaSw06].

Detailed studies by HETE-II have shown that apart from the regular, long GRBs, there are bursts having peak energies in the X-ray regime [S+05a]. For the classification of events in terms of the energy band of emission, the hardness ratio for the flux at (30, 400) keV and (2, 30) keV was examined:

$$H_{HETE} = \frac{S(30,\,400)}{S(2,\,30)}\,. \tag{1.41}$$

Regular GRBs have $H > 1$. About 2/3 of the 45 HETE-II bursts have, however, $H < 1$. This class of GRBs peaking in the X-ray regime, has further been subdivided into X-Ray Rich bursts (XRRs) with X-ray and soft γ-ray emission, $0.3 < H < 1$, and X-Ray Flashes (XRFs) with only X-ray emission, $H < 0.3$. The ratio between these three burst classes as observed by HETE-II is

$$(\text{GRB:XRR:XRF}) = (1:1:1)\,. \tag{1.42}$$

A schematic view of the classification of GRBs into long and short events and the further subdivision of the long events into regular GRBs, XRRs and XRFs is shown in Fig. 1.17. The ratio of long to short GRBs is indicated of 2 : 1 as detected by BATSE [P+99]. However, HETE-II rather detects a ratio of 3 : 1. The detection ratio should be considered as dependent on the instrument properties[22]. For the analysis of the GRB-XRR-XRF relation, however, it is stated that not many GRBs are missed relative to XRR and XRF events due to any observational effects [S+05a], so that a 1:1:1 ratio seems to be reasonable.

One interpretation of the strong variation of the peak energy is based on variations in the baryonic load of the shocks, which is an important parameter for the development of the boost factor [DCB99]. With a high baryonic load in the evolving jet, the system cannot be accelerated to high energies due to the high mass of the baryons. Thus, a this *dirty fireball* has boost factors of an order of magnitude less than a regular GRB, $\Gamma \sim 10$. Since the peak energy evolves with Γ, the typical values for dirty fireballs are $E_{peak} \sim (1,\,100)$ keV and XRRs or XRFs are observed. GRBs as typically observed by BATSE are classified as *regular fireballs. Clean fireballs* have a very low baryonic load and thus, a high gamma of around $\Gamma \sim 1000$, leading to peak energies of $E_{peak} >$ MeV. The duration of such short high energy bursts (SHE) would be small, since the lack of heavy baryons enables the jet to evolve more rapidly, so that $t_{90} \sim 0.1$ s. Such events have, however, not been observed yet. With the launch of GLAST[23], the detection of

---

[22] SWIFT for instance detects only one short GRB for 18 long ones. This is also due to the fact that SWIFT detects at relatively low energies $E < 150$ keV, while the emission for short GRB rather happens at higher energies as discussed before.

[23] **G**amma-Ray **L**arge **A**rea **S**pace **T**elescope

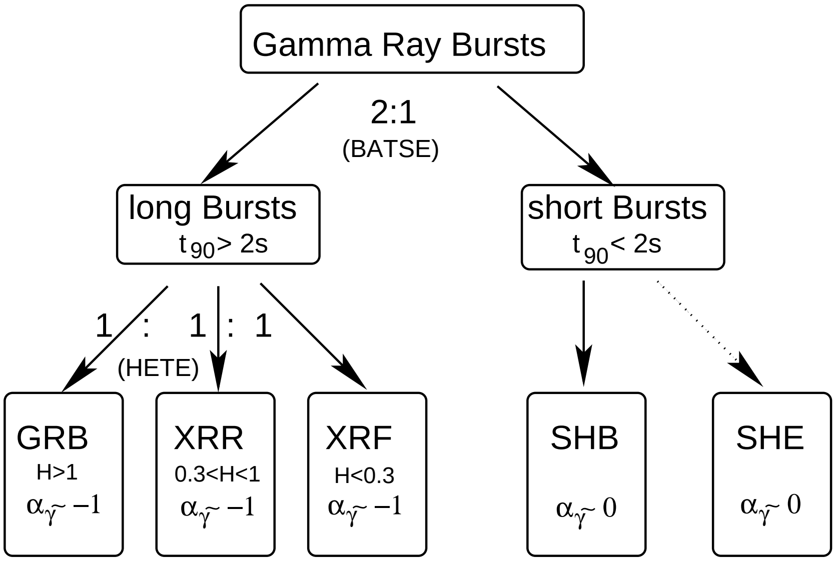

Figure 1.17: Classification scheme of GRBs.

such phenomena will be possible [GM99]. A summary of the different burst types and their basic parameters is given in table 1.3. The fact that most bursts occur as regular fireballs shows that a certain fraction of baryons needs to be present in the jet which inevitably leads to the production of neutrinos in proton-photon interactions. The question about the intensity of such a neutrino signal has still to be solved.

parameter	clean	dirty (XRR/XRF)	regular (GRB)
Γ	~ 3000	~ 30	~ 300
E_{peak} [keV]	> 1000	$1 - 100$	$100 - 1000$
t_{90} [s]	0.1	~ 10	~ 10

Table 1.3: Basic parameters of clean/dirty and regular fireballs.

The classification scheme as presented here needs to be refined including a more detailed view on the matter in the future: today, there are several bursts which fall out of the scheme, e.g. GRB060218 and GRB060614, and SWIFT seems to detect a different sub-class of short bursts as compared to BATSE [SaSw06]. A review of the observation of the different sub-classes (XRF/GRB/short) with SWIFT is given in [Z$^+$07]. In [Z$^+$07], the detection of the shallow decay of the early afterglow as recently observed in many SWIFT bursts as energy injection features. Such a scenario disfavors the interpretation of XRFs as low$-\Gamma$ GRBs. SWIFT will help to improve the current classification scheme. For now, the scheme as presented above is still useful, since it can describe the majority of bursts.

1.2.3 Galactic sources

In this section, the electromagnetic output of galactic sources of non-thermal emission will be used to estimate their contribution to the Cosmic Ray spectrum. More detailed reviews on the subject can be found in e.g. [Gai90, Sta04, Aha04a].

The Cosmic Ray luminosity can be written as

$$L_{CR} = \frac{4\,\pi}{c} \cdot j_E(E_{\min}) \cdot \frac{V_{GD}}{\tau_R} \tag{1.43}$$

assuming the production of Cosmic Rays in the Milky Way with a residence time $\tau_R \approx 6 \cdot 10^6$ yr in the volume of the galactic disk $V_{GD} \approx 10^{67}$ cm^3. Here,

$$j_E(E_{\min}) = \int_{E_{\min}} \frac{dN_p}{dE_p}\, E_p\, dE_p \tag{1.44}$$

is the Cosmic Ray energy flux. The Cosmic Ray luminosity depends on the minimum energy which is produced. The calculation can only be valid at energies below the ankle, $E_{CR} < 3 \cdot 10^{18}$ eV: at the highest energies ($E_{CR} > 3 \cdot 10^{18}$ eV), the observed spectrum is too isotropic to be of galactic origin. Figure 1.18 shows the Cosmic Ray luminosity versus minimum energy. Three potential source classes are indicated as filled/hatched areas below the curve. In the following, the different source classes will be reviewed with their potential contribution to the Cosmic Ray luminosity. Here, it is assumed that the luminosity in Cosmic Rays produced by a source class must be less than the total electromagnetic output of the same class, $L_{CR}^{class} < L_{em}^{class}$.

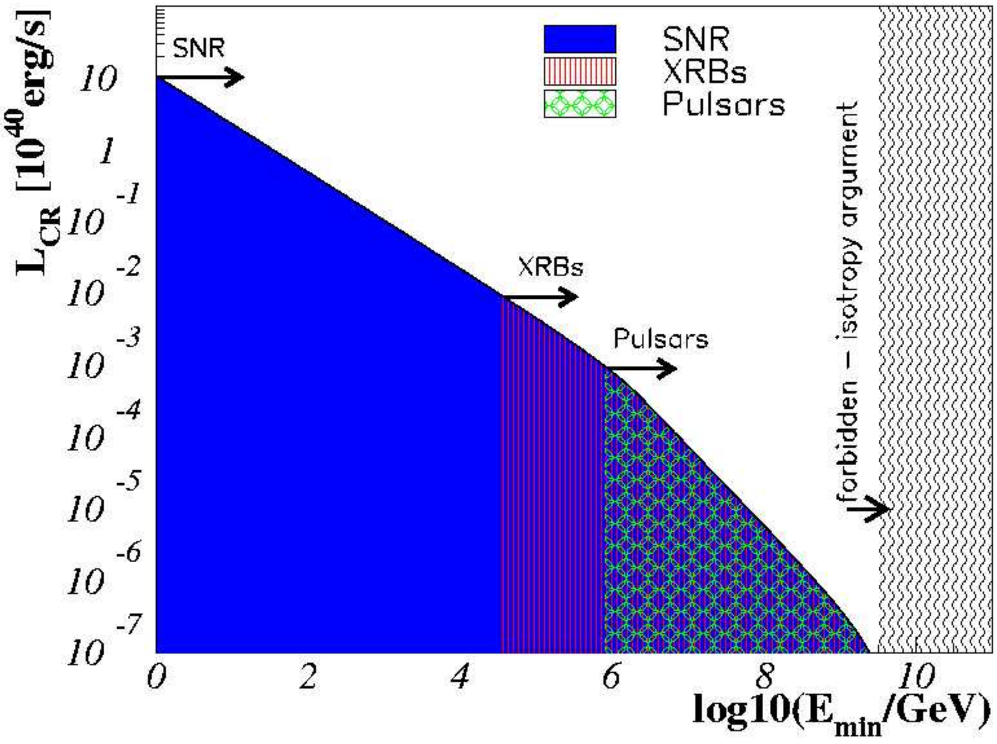

Figure 1.18: Cosmic Ray luminosity from the Milky Way and possible sources given their electromagnetic output. The upper bound of the curve indicates the Cosmic Ray luminosity for energies $E_p > E_{\min}$. Cosmic Rays above the ankle, i.e. $E_p > 3 \cdot 10^{18}$ eV, cannot have a galactic origin, since the observed signal is too isotropic. Since supernova remnants in our Galaxy can produce a luminosity of $L_{SNR} \sim 10^{42}$ erg/s, they can be responsible for Cosmic Ray production starting at the lowest energies, i.e. $E_p \sim 1$ GeV (blue filled area). X-ray binaries ($L_{XRB} \sim 10^{38}$ erg/s) and pulsars ($L_{pulsar} \sim 10^{37}$ erg/s) can only be responsible for the Cosmic Ray flux above $10^{4.5}$ GeV (XRBs, red hatched area, lines) resp. $10^{5.8}$ GeV (pulsars, green hatched area, circles). Alternatively, supernova winds can be responsible for the contribution above the knee, since higher energies can be reached in winds as opposed to SN explosions into the interstellar medium.

Supernova remnants

The CR spectrum at energies below the knee is commonly believed to be produced by the shock fronts in expanding shells of supernova remnants (blue filled area). When a star perishes in a supernova (SN) explosion, the emitted material encounters the interstellar medium (ISM), building a shock front of typical velocities $V_S \sim 10^5$ m/s. With the typical rate of SN explosions in a galaxy, $dN_{SN}/dt \sim 3/(100\text{ yr})$, and a mean ejected mass of $M_{SN} \sim 10\,M_\odot$ per SN, the supernova remnant's shock front is active for about $\Delta t_{SNR} \sim 1000$ yr. The luminosity of a single SNR, $L_{SNR} \sim 10^{41}$ erg/s, can then be converted into the total luminosity of SNRs in the Milky Way,

$$L_{tot}^{SNR} \approx \frac{dN_{SN}}{dt} \cdot L_{SNR} \cdot \Delta t_{SNR} \approx 3 \cdot 10^{42}\text{ erg/s}\,. \tag{1.45}$$

Given the integral luminosity required for the production of Cosmic Rays at $E_p > 10^9$ eV,

$$L_{CR}(E_p > 1\text{ GeV}) \approx 10^{41}\text{ erg/s}\,, \tag{1.46}$$

SNRs are good candidates for the production of Cosmic Rays. It is, however, difficult to explain the break in the spectrum at $E_p \sim 10^{15}$ eV. One possibility is that leakage of particles out of the Milky Way becomes important, leaving only heavy elements at the higher energies. This can lead to a steepening of the spectrum. Another possibility is that SN explosions into their own winds can be able to accelerate particles to higher energies, since higher mass numbers (Helium up to iron) are produced. SN explosions of type Ib and Ic lose their hydrogen (for Ic also the helium) envelope before collapsing. This leads to a higher density of particles when the shock forms and thus to different shock conditions. Regular SNRs can in this scenario produce CRs up to the knee and SNR-Winds are responsible for the spectrum between the knee and the ankle.

Pulsars, X-ray binaries and microquasars

As an alternative explanation for the contribution above the knee, systems including neutron stars or black holes are considered.

Neutron stars can be observed due to their emission of electromagnetic radiation along the magnetic field axis. Since the rotational axis of the objects does not align with the magnetic field axis, they are observed as pulsars: the emission is only seen when the particle jet points towards Earth. Pulsars have periodic signals ranging from several seconds down to milliseconds. The Crab as the most prominent, since most luminous, example is a millisecond pulsar. It is a neutron star which was presumably produced in a SN explosion observed on July 04, 1054. For a review of historical SNe see [GS03]. The remnant has been observed at all wavelengths. From radio energies up to UV light, the supernova remnant is seen, while the pulsar itself is visible at X-ray and higher energies. The observed TeV signal from the Crab is non-thermal, an indication for particle acceleration in a shock environment, see e.g. [AhH+06b]. The main reason why pulsars are good candidates for particle acceleration are the very high magnetic fields of around $B \sim 10^{12}$ G. Pulsars have luminosities around 10^{37} erg/s and can therefore not be responsible for the CR flux below the knee. They can, however, contribute to the region between knee and ankle (see Fig. 1.18, green hatched area, circles).

Magnetars, which are observed as Anomalous X-ray Pulsars (AXPs) or Soft Gamma Repeaters (SGRs), represent pulsars with even higher magnetic fields of $B \sim 10^{15}$ G. For a review on AXPs and SGRs see e.g. [WT04]. Five SGR candidates have been observed in the Milky Way so far. These reveal themselves by randomly emitting γ radiation from time to time. The smaller eruptions have usually thermal spectra, while giant bursts of non-thermal emission are observed from time to time. Famous events are the outbursts of SGR 1806-20 on January 7, 1979 and on December 27, 2004 as well as the giant emission of SGR 1900+14 on August 27, 1998. Flare luminosities of SGRs range from $\sim 10^{38}$ erg/s up to $\sim 10^{44}$ erg/s. AXPs show similar phenomena, but with emission at X-ray energies rather than γ rays. The original definition of AXPs was the steady emission of X-rays. About half of the AXPs today are known to be variable in X-rays, though. Eight AXP candidates have been observed in the Milky Way so far. The eruptions from magnetars are believed to come from star quakes, exciting the surface of the magnetar which leads to the emission of high energy radiation. The energy output from AXPs lies at around $10^{33} - 10^{36}$ erg/s.

Binary systems including a neutron star or a black hole are good candidates for shock acceleration as well. Low-Mass X-ray Binaries (LMXBs) consist of a white dwarf feeding the neutron star, while neutron stars in High Mass X-ray binaries (HMXBs) are fed by a blue star (O/B star). In the case of HMXBs, once the neutron star companion exceeds the Roche volume of the binary system, it starts to feed the compact object with matter. The neutron star or black hole in turn emits the gained energy in a jet along the magnetic axis. Such systems can lead to particle acceleration up to the ankle at most. The typical electromagnetic energy of such X-ray binary systems is $\sim 10^{38}$ erg/s. This is much lower than the total energy required to explain the CR luminosity for $E_p > 10^{10}$ eV. But considering only events at higher energies, i.e. $E_p > 10^{13.5}$ eV leads to a much lower CR luminosity due to the steeply falling spectrum (see Fig. 1.18, red hatched area, lines). For a summary of the XRB and CR connection, see e.g. [Gai90].

A special case of an X-ray binary is the so-called microquasar. There are two types of sources which are classified as microquasars. For once, a heavy Be-star accompanied by a neutron star leads to a periodic emission of high energy photons: Be-stars are massive stars with a circumstellar disk. The path of the neutron star around the Be-star is highly elliptic. This leads to the accretion of matter by the neutron star from the massive star only near the periastron, the point of closest distance of the two stars. A periodic emission of TeV photons has been observed from two systems in the Milky Way, LS 5039 has been detected by the H.E.S.S.[24] experiment [AhH$^+$06c], while LS I 61+303 was seen by MAGIC[25] [AM$^+$06a]. In both cases, a Be-star/neutron star binary is suggested to explain the emission of TeV photons. Another appearance of microquasars is the emission of photons along two co-linear jets. Such a phenomenon has for instance been observed in GRS 1915+105 [MR94]. It is believed to be caused by instabilities in the accretion disk of the system. A burst is caused every time a particularly large amount of matter is accreted from the accompanying star. This burst is seen at the accretion disk itself in X-rays. It then propagates outwards along the jets in form of radio to optical emission. For a recent summary of microquasar physics, see [Mir06].

---

[24] **H**igh **E**nergy **S**tereoscopic **S**ystem

[25] **M**ajor **A**tmospheric **G**amma **I**maging **C**herenkov Telescope

1.3 Astrophysical neutrinos

Until today, two sources of astrophysical neutrinos are confirmed. Neutrinos have been observed from the sun, leading to the detection of neutrino oscillations by SuperKamiokande[26] and SNO[27] [FK+98, SNO02]. The second astrophysical object seen in neutrinos is the supernova explosion 1987A. Within 13 s, 24 events were observed by five different experiments, see e.g. [Hel87]. An overview of the neutrino spectrum expected over the wide range from meV up to EeV is shown in Fig. 1.19.

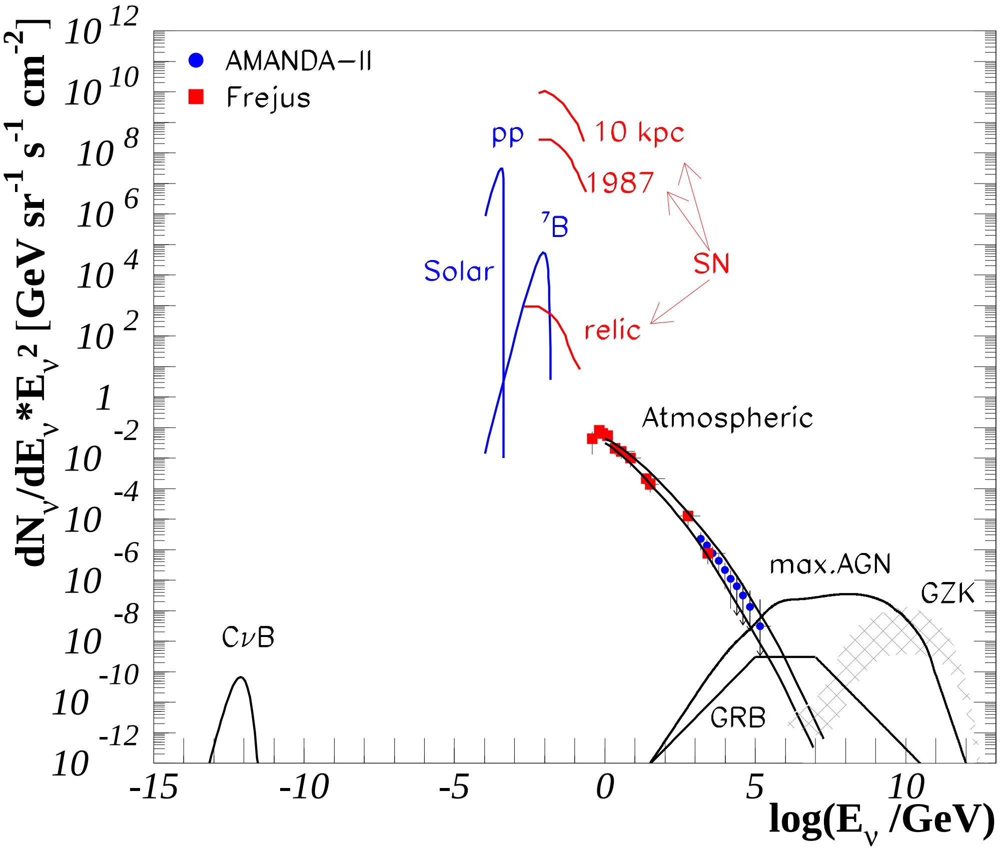

Figure 1.19: The astrophysical neutrino spectrum including different source predictions ranging from meV up to EeV energies. Point source fluxes have been scaled by $1/(4\,\pi)$ in order to be comparable to diffuse spectra. Figure after [Rou00].

---

[26] Super **K**amioka **N**ucleon **D**ecay **E**xperiment

[27] **S**udbury **N**eutrino **O**bservatory

The Cosmic Neutrino Background (CνB) is an isotropic neutrino flux having decoupled in the Early Universe, only 1 s after the Big Bang. It is the neutrino equivalent of the cosmic microwave background. Since it decoupled very early, the temperature of the blackbody spectrum corresponds to ~ 1.9 K today, and the flux peaks at milli-eV energies. While this background is essentially predicted in the standard model of cosmology, it was not possible to test it experimentally yet. The sun emits neutrinos in different fusion processes in the MeV range. In the figure, neutrinos from $p\,p$ interactions and the ^{7}B spectrum is shown. Massive stars ($M \sim 10^{20} \cdot M_{\odot}$) are expected to emit neutrinos at ~ 1 MeV due to Silicon burning [OMK04, MOK06]. At slightly higher energies lies the neutrino spectrum from SN 1987A. The expected flux from a SN at a distance of 10 kpc is indicated. Such a close supernova will be observed by todays neutrino telescopes. The flux from SNRs ("relic"), however, is about four orders of magnitude lower and could not be tested yet. At energies > 0.1 GeV, the measured spectrum of atmospheric neutrinos is indicated, squares are measurements from FRÉJUS [Ber87, D$^+$95] and dots are AMANDA measurements from the year 2000 [M$^+$05d]. At the highest energies, a generic spectrum from GRBs is indicated [WB97, WB99], as well as the maximum contribution from AGN [MPR01] and the expected neutrino flux from the absorption of protons by the GZK effect [YT93]. These sources have not been observed yet due to the high atmospheric background and limited sensitivities of the detectors. Figure 1.20 shows the various neutrino spectra at the highest energies, $E_\nu > 100$ GeV. Many sources are expected to contribute to the neutrino spectrum at high energies. The different source classes are discussed in more detail in the following paragraphs.

1.3.1 Neutrino production scenario

Neutrinos are produced in astrophysical shock fronts in proton-photon and/or proton-proton interactions via pion-production. The dominant channels are here

$$p\gamma \longrightarrow \Delta^+ \longrightarrow \begin{cases} p\,\pi^0 & \text{, fraction } 2/3 \\ n\,\pi^+ & \text{, fraction } 1/3 \end{cases} \tag{1.47}$$

$$p\,p \longrightarrow \begin{cases} p\,p\,\pi^0 & \text{, fraction } 2/3 \\ p\,n\,\pi^+ & \text{, fraction } 1/3\,. \end{cases} \tag{1.48}$$

The same processes occur for incident neutrons instead of protons, leading to the production of π^- particles. At higher energies, kaons can also contribute to the spectrum [Rac00].

While the resulting neutrons are likely to interact before decaying, charged pions decay and produce neutrinos,

$$\pi^+ \rightarrow \mu^+\,\nu_\mu \rightarrow e^+\,\nu_e\,\overline{\nu}_\mu\,\nu_\mu \tag{1.49}$$

$$\pi^- \rightarrow \mu^-\,\overline{\nu}_\mu \rightarrow e^-\,\overline{\nu}_e\,\nu_\mu\,\overline{\nu}_\mu\,. \tag{1.50}$$

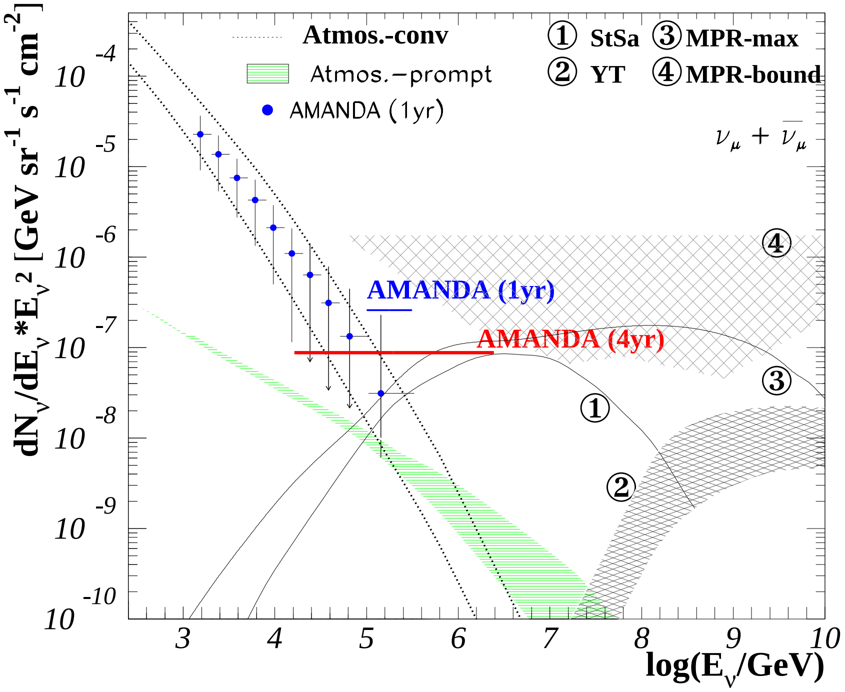

Figure 1.20: Diffuse neutrino flux predictions. Data points are measurements with AMANDA, year 2000, including the limit for one year [M$^+$05d]. The four year limit arises from the analysis of the highest energy events with AMANDA. Model (1) represents the neutrino flux expected from MeV-photon emitting blazars [Ste05]. Model (2) describes the neutrino flux arising when protons are absorbed by the GZK effect [YT93]. The uncertainties come from different source evolution scenarios. Model (3) represents the maximum contribution from TeV blazars [MPR01]. An upper bound for optically thin (lower line) and optically thick (upper line) sources is derived in this context (model (4)).

Assuming that pions of negative and positive charge occur equally, the production flavor ratio of neutrinos at the source is

$$(\nu_e : \nu_\mu : \nu_\tau) = (\overline{\nu}_e : \overline{\nu}_\mu : \overline{\nu}_\tau) = (1 : 2 : 0)\,. \tag{1.51}$$

This implies that tau neutrinos are not produced in astrophysical sources. However, since neutrinos have non-vanishing mass eigenvalues, they oscillate on their way to Earth. For path lengths exceeding the size of the solar system, the flavor ratio approaches

$$(\nu_e : \nu_\mu : \nu_\tau) = (\overline{\nu}_e : \overline{\nu}_\mu : \overline{\nu}_\tau) = (1 : 1 : 1)\,. \tag{1.52}$$

Thus, equal numbers of electron, muon and tau neutrinos are expected to be observed at Earth.

Given that the existence of high-energetic protons in astrophysical environments is bound to neutrino production, the observed flux of charged Cosmic Rays can be used to estimate the neutrino intensity expected from the sources of Cosmic Rays, see e.g. [Hal06] and references therein. The Cosmic Ray energy density above the ankle $j_E(E_{\min} = 3 \cdot 10^{18}\text{ eV}) = \int_{E_{\min}=3\cdot 10^{18}\text{eV}} dN_p/dE_p\, E_p\, dE_p$, is expected to be proportional to the neutrino energy density,

$$j_E(E_{\min}) = x_{\nu/p} \cdot \int \frac{dN_\nu}{dE_\nu}\, E_\nu\, dE_\nu\,. \tag{1.53}$$

The constant of proportionality $x_{\nu/p}$ depends on the optical thickness of the source to proton-photon interactions and on the fraction of energy transferred to the charged pion. The fraction of energy going into the neutron does not contribute to neutrino production.

Due to the second channel in which π^0 particles are produced, the neutrino flux is expected to be accompanied by a high-energy photon flux:

$$\pi^0 \rightarrow \gamma\,\gamma\,. \tag{1.54}$$

The resulting photons are produced at > TeV energies. Thus, optically thin sources emit TeV photons in coincidence with high-energy neutrinos and the energy densities are proportional:

$$\int_{E_{\min}} \frac{dN_\gamma}{dE_\gamma}\, E_\gamma\, dE_\gamma = x_{\nu/\gamma} \cdot \int_{E_{\min}} \frac{dN_\nu}{dE_\nu}\, E_\nu\, dE_\nu\,. \tag{1.55}$$

The constant of proportionality $x_{\nu/\gamma}$ depends on the fraction of energy going into pion production. For optically thin sources, in the case of $p\,p$ interactions, 1/3 of the proton energy goes into each pion flavor and the energy in $\nu_\mu + \overline{\nu}_\mu$ corresponds to the energy in photons, $x_{\nu/\gamma} \sim 1$. For $p\,\gamma$ interactions, $x_{\nu/\gamma} \sim 1/4$. If the source of neutrino emission is optically thick to TeV photons, the TeV signal avalanches to lower energies until it reaches a level at which it can escape the source. Thus, sources of GeV to sub-MeV emission can be sources of neutrino production as well, assuming an optically thick environment. Equation (1.55) holds with different values for $x_{\nu/\gamma}$ and modified integration limits.

1.3.2 Neutrinos from AGN

In some hadronic acceleration models it is assumed that for each class of AGN, the electromagnetic emission is correlated to a neutrino signal. Apart from individual normalization factors, the corresponding cosmological integrations are basically mathematically identical. In this section, the correlation between the emission of neutrinos and photons at different wavelengths will be reviewed according to neutrino flux models which are currently being discussed in the literature. Table 1.4 summarizes the different models with their very basic assumptions.

source class	Normalization wavelength	ν correlation to wavelength	origin	model(s)
blazars	CRs	proton flux, responsible for $p\gamma$ in source	jet	[MPR01] [M$^+$03b]
	$>$ 100 MeV	cascaded π^0 signal connected to $\pi^{+/-}$ production ($\Rightarrow$ νs)	jet	[MPR01] [M$^+$03b] [Man95]
	$>$ MeV	cascaded π^0 signal connected to $\pi^{+/-}$	jet	[Man95] [Ste05]
FSRQs	radio	jet-disk correlation radio $\sim$ total power	jet	[BBR05]
FR-II	radio	jet-disk correlation radio $\sim$ total power	jet	[BBR05]
radio quiet AGN	X-ray	cascaded π^0 signal	disk	[StSa96] [NMB93] [AM04]

Table 1.4: Neutrino models for Active Galactic Nuclei. The models are developed for different AGN sub-classes, using different signal hypotheses. Each model uses either charged Cosmic Rays or non-thermal photon emission from the given source class to normalize the neutrino spectrum. The correlation between charged Cosmic Rays and neutrinos is present, since the CR flux gives evidence for proton acceleration. Some protons interact with the photon field to produce neutrinos. The correlation between neutrinos and MeV-GeV photons can be present if the photons arise from π^0-decays which imply the coincident production of charged pions, the latter decaying to leave neutrinos. The normalization to the radio signal from AGN can be used, since the radio power is connected to the total power of the AGN via the jet-disk model. A fraction of the total power goes into neutrinos. X-rays originate from the foot of AGN jets. In the cited models, these X-rays are assumed to be produced in π^0 decays, the signal cascading in an optically thick environment from TeV-energies to X-ray wavelengths.

TeV photon sources and Cosmic Rays

Sources of electromagnetic TeV emission can be interpreted as optically thin to photon-neutron interactions, $\tau_{\gamma n} \ll 1$ [M$^+$03b, MPR01] in hadronic acceleration models. In such a scenario, charged Cosmic Rays (CRs) are produced in the vicinity of the source through the decay of the escaping neutrons. In this case, the resulting neutrino energy density would be proportional to the extragalactic CR component measured at Earth. A theoretical upper bound of such a contribution to the diffuse neutrino flux has been derived by Mannheim, Protheroe and Rachen (in the following referred to as the *MPR bound*), see [MPR01]. Within the framework of the proton-blazar model, the neutrino flux from High frequency peaked BL Lacs (HBLs) has been calculated using the connection between Cosmic Rays and neutrino emission, see [M$^+$03b].

Normalization to the diffuse EGRET and COMPTEL spectrum

In the case of optically thick sources ($\tau_{\gamma n} > 1$), the photons interact with nucleons in the source before escaping at lower energies leading to the emission of sub-TeV photons. Therefore, the diffuse extragalactic background measured by the EGRET[28] experiment [SMR05] ($E_\gamma > 100$ MeV) can be interpreted as an avalanched TeV signal from blazars and can thus be used to normalize the neutrino flux from EGRET or COMPTEL[29]-type sources. Again, an upper bound to the contribution from such sources is given in [MPR01], which is much less restrictive than the optically thin case. Apart from the bound, a calculation of the maximum contribution from blazars is given in [MPR01]. In addition to the contribution from HBLs within the framework of the proton-blazar model, a contribution from the optically thick Low-frequency peaked BL Lacs (LBLs) can be calculated using the EGRET diffuse extragalactic background for a normalization of the neutrino spectrum, see [M$^+$03b]. A model of proton-photon interactions in AGN and collisions of protons from the core with protons of the host galaxy is derived in [Man95]. This model will be referred to as *M95-A*. Alternatively to optically thin sources with photon emission above 100 MeV, the environment can be optically thick allowing only photons below 100 MeV to escape. In that case, the neutrino signal can be normalized to the diffuse extragalactic contribution measured by COMPTEL at energies in the range of (0.8, 30) MeV [K$^+$96]. This would enhance the contribution of neutrinos from proton-photon interactions by almost an order of magnitude as shown in [Man95]. We will refer to this model as *M95-B* in the following.

A model by [StSa96] was originally using the diffuse cosmic X-ray background and has recently been modified in a way that it is using the COMPTEL diffuse background to normalize the neutrino spectrum [Ste05]. This reduces the formerly very high contribution by a factor of 10. In addition, oscillations have been taken into account which leads to a further reduction by a factor of 2.

The ROSAT X-ray background as normalization option

The measurement of the diffuse extragalactic contribution in X-rays by ROSAT[30] has raised the question whether it is produced by radio-weak AGN. Assuming that

---

[28] **E**nergetic **G**amma **R**ay **E**xperiment **T**elescope

[29] **COM**pton **TEL**escope

[30] **RO**entgen **SAT**ellite

the X-ray emission comes from the foot of the jet, the X-ray signal would be accompanied by a neutrino flux. A model by [NMB93] and an approach by [StSa96] have been presented. An alternative scenario would be the up-scattering of thermal electrons via the Inverse Compton effect. In that case, the X-ray component would not be accompanied by a neutrino signal, see e.g [MSR95]. Until today, about 75% of the diffuse X-ray signal has been resolved by ROSAT [BH05], with the help of CHANDRA and XMM-NEWTON[31] data, this number can be updated to 90%, see [BH05] and references therein. More than 70% of the diffuse background could be connected to the X-ray emission of Active Galactic Nuclei most of which are radio weak. Measurements of a diffuse neutrino flux with AMANDA did not yield a significant signal and restricts these models strongly.

Correlated radio and neutrino emission

Detailed examination of multi-wavelength observations have shown a correlation between the disk and jet power of Active Galactic Nuclei, see [FMB95, FB95, FB99]. This correlation can be used to estimate the diffuse neutrino flux from FR-II galaxies and flat spectrum radio quasars within the framework of the jet-disk symbiosis model [BBR05]. The neutrino flux has been assumed to follow an ${E_\nu}^{-2}$ spectrum which leads to a relatively high neutrino flux at energies above $E_\nu \sim$ TeV. Assuming on the other hand a correlation between the radio spectral index and the index of the proton spectrum leads to an ${E_\nu}^{-2.6}$ neutrino spectrum. Since the flux is normalized at low energies, the contribution decreases significantly at higher energies with an increasing spectral index.

1.3.3 Neutrinos from GRBs

A summary of neutrino emission from GRBs is shown in Fig. 1.21. For a review, see [MRZ04]. Three phases of neutrino emission are expected, i.e. precursors hours prior to the GRB [RMW03a], emission during the prompt phase [WB97, WB99] as well as afterglow emission [WB00]. The lower row shows the neutrino energy spectra for the three phases while the upper row displays the corresponding electromagnetic output schematically.

- A *precursor model* has been developed in [RMW03a]. The basic idea is that just when the shocks reach the progenitor's surface, while the burst is still opaque to photon emission, the shock environment yields a good target for neutrino production by shock-accelerated protons interacting with thermal X-rays in the sub-stellar jet cavity. The shocks happen at smaller radii than the prompt emission and at lower boost factors Γ. The neutrino signal could also be accompanied by a signal in the far infrared. The low energy part of the neutrino spectrum arises from neutrino production in pp interactions

---

[31] **X**-ray **M**ulti-**M**irror Mission **Newton**

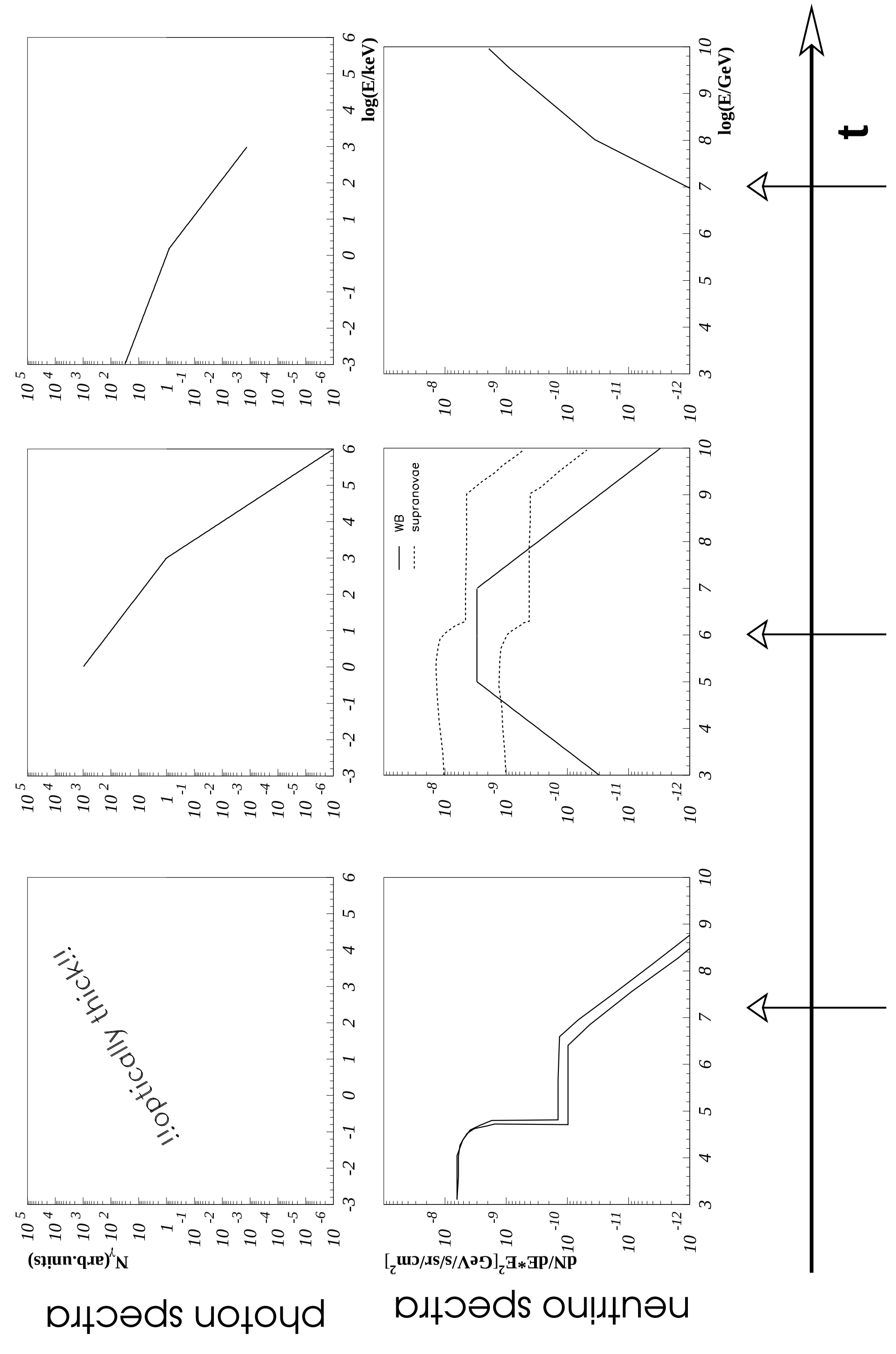

Figure 1.21: Overview of different neutrino production scenarios during the three different phases of a GRB. The corresponding electromagnetic output is indicated schematically as well. The different flux models are described in the text.

and is ${E_\nu}^{-2}$-shaped. The flux at energies $E_\nu > 10^5$ GeV originates from proton-photon interactions. The two lines in the lower left panel of Fig. 1.21 represent different shock/jet radii and envelope mass settings. For more details, see [RMW03a].

- The *prompt* photon *emission* from GRBs is expected to be directly correlated to a neutrino output. The energy in the prompt photon spectrum is inversely correlated to the neutrino energy. Furthermore, the total flux in the keV-range is expected to be proportional to the neutrino flux intensity, due to a connection between the electron synchrotron emission and the neutrino emission. Such a correlation exists when assuming energy equipartition of protons and electrons in the GRB, where the neutrinos are produced in proton-photon interactions. The resulting flux is shown as the solid line in the lower middle plot of Fig. 1.21. The details of this models are explained in Chapter 5.

  Additionally, a neutrino component induced by the precursor supernova of long GRBs (so-called "supranovae") is expected [RMW03b] as displayed in the middle of Fig. 1.21 (dashed lines). Protons are accelerated by the supernova which happens up to months before the GRB. These protons are injected into the internal shock of the GRB which leads to neutrino production through proton-proton and proton-photon interactions. The upper line represents the flux in the case that all supernovae produce GRBs while the lower line shows the output if only 10% of all supernovae contribute.

- *Afterglow neutrinos* are produced when the internal shocks from the original fireball hit the interstellar medium and produce external shocks [WB00]. As for the prompt emission, the synchrotron emission of electrons gives evidence for the existence of relativistic charged particles which in turn implies neutrino production by the baryonic component of the jet and the photon field. In the case of afterglow emission, Waxman and Bahcall [WB00] predict the acceleration of ultra-high energy protons ($E_p > 10^{20}$ eV) in reverse shocks occurring when the internal shocks hit the interstellar medium and are reflected at the boundary surface [MR97]. These shocks are mildly relativistic. The acceleration of protons to such high energies always implies the production of neutrinos in proton-photon interactions. As for the prompt emission, the neutrino spectrum is directly correlated to the photon spectrum. Synchrotron radiation of the afterglow is observed at X-ray energies. The characteristic synchrotron energy lies at ~ 1 MeV for the prompt emission, but at only a few keV for the afterglow. Since photon and neutrino energy are inversely correlated, the observed neutrinos would be emitted at higher energies than during the prompt phase which is also seen in Fig. 1.21.

A general question is the timing of photon and neutrino emission. Depending on the environment of the astrophysical shock, neutrinos are not exactly emitted at the same time as the photons. This is important in the case of temporal selection of data in high energy neutrino experiments. It is typically still assumed that flaring sources emit the neutrinos during the same time interval, but the time window is often chosen to be slightly larger than the photon emission time to account for this effect. Transient astrophysical shocks in the context of temporal evolution are described in [RM98].

1.3.4 Galactic neutrino sources

The basic assumptions for neutrino production in galactic sources are the same as for extragalactic neutrino sources: in the case of optically thin sources, TeV emission can be directly correlated to neutrino emission in the case of a hadronic acceleration scenario. In addition, the emission at lower energies can be interpreted as an avalanched high energy signal. One striking difference between galactic and extragalactic neutrino spectra is the maximum energy, since galactic sources produce maximum energies of $E_p < 3 \cdot 10^{18}$ eV which is mirrored in the neutrinos' relatively low maximum energy. Candidates for neutrino emission are microquasars, see e.g. [Bed05, TRM05], soft gamma repeaters and anomalous X-ray pulsars, see e.g. [HLM05], and supernova remnants, see e.g. [K$^+$06]. Molecular clouds as they have been observed by H.E.S.S. [AhH$^+$06d] are good candidates for neutrino emission: TeV emission is observed, since an astrophysical accelerator hides behind the clouds. The protons are absorbed by the dense clouds ($n_H \sim 250/\text{cm}^3$) and produce TeV photons and high energy neutrinos through proton-proton and proton-photon interactions. Recently, MILAGRO[32] detected diffuse TeV emission from the Cygnus region [GM$^+$06]. This is a good candidate for a neutrino production site as well.

So far, only the outer part of the galactic plane can be observed thoroughly, since the most sensitive instruments, AMANDA and ICECUBE are located in the southern hemisphere. This only gives a clear view of the northern hemisphere (see Section 1.3.6). With KM3NET to be built in the northern hemisphere, the galactic center will be observable.

1.3.5 Cosmogenic neutrinos

High energy protons interact with the Cosmic Microwave Background (CMB) on their way to Earth via Bethe-Heitler pair production,

$$p\,\gamma_{CMB} \rightarrow p\,e^+\,e^- \tag{1.56}$$

and via the Δ-resonance,

$$p\,\gamma_{CMB} \rightarrow \Delta^+\,. \tag{1.57}$$

---

[32] **M**ultiple **I**nstitution **L**os **A**lamos **G**amma **R**ay **O**bservatory

In the latter process, neutrinos are produced in the decay of the Δ-resonance via the channel of charged pion production, see Section 1.3.1. The resulting diffuse neutrino flux has been calculated by various authors, see e.g. [YT93, RB93, ESS01, YK06]. It is usually referred to as the flux of *cosmogenic neutrinos* or *GZK neutrinos*. The neutrino flux ranges from approximately $E_\nu \sim 10^{16}$ eV up to $E_\nu \sim 10^{21}$ eV. The signal strength depends strongly on the distribution of the proton-producing sources in the sky. Typically, it is assumed that ultra-high energy protons are produced in AGN or GRBs. These objects follow the evolution of star formation and the redshift behavior is assumed as $\rho \sim (1+z)^m$ up to a redshift $z = z_{\max}$, with $m > 0$. At high redshifts, $z > 3$ to 4, the source number counts become small and the exact behavior of for example the distance distribution of AGN has long been difficult to determine. For a long time, it has been assumed that the source density is constant at $z > z_{\max}$, $\rho \sim (1 + z_{\max})^m$. Today, there are indications that there is negative evolution at high redshifts $(1+z)^m$, $m < 0$. In [YT93], the evolution is assumed as

$$\rho \propto \begin{cases} (1+z)^m & \text{for } z < z_{\max} \\ (1+z_{\max})^m & \text{for } z > z_{\max}\,. \end{cases} \tag{1.58}$$

The results are given for different parameter sets $(m, z_{\max})$ to account for the uncertainties in the source density. In [YK06], a more detailed representation of the source density is used,

$$\rho \propto \begin{cases} (1+z)^m & \text{for } z < z_{\max} \\ (1+z)^{m'} & \text{for } z_{\max} < z < z_{\max,2} \\ (1+z)^{m''} & \text{for } z > z_{\max,2}\,. \end{cases} \tag{1.59}$$

The parameter set $(m, m', m'', z_{\max}, z_{\max,2})$ is varied depending on the scenario, i.e. if protons come from GRBs or AGN. In the case of GRB protons, recent results from SWIFT have been used to model the star formation scenario for these sources. The evolution turns out to be much stronger than in the case of AGN.

1.3.6 High energy neutrino detection methods

When a neutrino ν interacts with a nucleon N via charged current interactions, a lepton l is produced,

$$N\,\nu_l \rightarrow X\,l\,. \tag{1.60}$$

Here, X indicates the hadronic product of the interaction, leading to a hadronic cascade. Charged particles in a medium emit Cherenkov light if traveling faster than the speed of light in the medium. The Cherenkov effect is described in detail in [Jac06]. The blue Cherenkov light can be detected by photomultiplier tubes and both the incidental direction and the neutrino energy are reconstructible. The signatures for electrons, muons and tauons are very different. While electrons produce an electromagnetic cascade within the detector, since interacting with the electrons of the medium, muons only undergo radiation losses. The track of the muon can be reconstructed, since the Cherenkov signal is emitted in form of a directed cone. Tauons also leave cascade-traces. A first cascade is produced in the first $\nu_\tau N$ interaction, where a τ and a hadronic cascade is produced. The τ in turn decays, producing a second cascade in which a further τ is generated. Thus, tau neutrinos have the unique property to regenerate themselves. In the case of neutral current interactions, a further neutrino is produced,

$$N\,\nu_l \rightarrow X\,\nu_l \tag{1.61}$$

and a hadronic cascade X can be observed.

The primary detection technique is the measurement of neutrino-induced muon tracks in water or ice. To guarantee that the observed muons are neutrino-induced, the Earth is used as a filter. While muons produced in the atmosphere are absorbed by the Earth, neutrinos traverse the Earth and the signature is unique. After the filtering of atmospheric muons, the remaining signal mainly consists of neutrinos produced in hadronic showers in the atmosphere. Different analysis methods have been developed to separate this background from a potential signal from extraterrestrial sources. In addition to the neutrino-induced lepton, a cascade produced at the interaction vertex contributes to the signal. While the muon leaves an optical track, the cascade events produce a radio and an acoustic signal apart from the optical emission. Thus, three different detection methods - optical, radio and acoustic detection - are reviewed here. The focus will lie on the description of optical detection. This method has been proven by BAIKAL and AMANDA already. AMANDA limits of different detection strategies are reviewed, since those are used in later chapters.

Atmospheric neutrino background

The main background in the search for extraterrestrial neutrinos is the background of atmospheric muons and neutrinos. When primary CRs interact in the upper atmosphere, a shower develops. If the primary is a hadron, e.g. a proton, secondary mesons and muons are produced while the shower propagates through the atmosphere. Secondary mesons like charged pions and kaons produce neutrinos when decaying. The neutrino spectrum follows an $E^{-3.7}$ behavior. This is about one power steeper than the primary spectrum, $\sim E^{-2.7}$, since a considerable fraction of pions and kaons ($\tau \sim 10^{-8}$ s) interact again before decaying. Neutrinos from pion and kaon decays are usually referred to as *conventional atmospheric neutrinos* as opposed to *prompt atmospheric neutrinos* from heavier hadrons.

$\cos(\theta)$	1	0.6	0.4	0.3	0.2	0.1	0.05	0
$E_\pi(\theta)$ [GeV]	121	202	298	392	572	886	1060	1190
$E_{K^\pm}(\theta)$ [GeV]	897	1500	2190	2900	4220	6540	7820	8760
$E_{K^0}(\theta)$ [GeV]	194	324	473	628	915	1410	1690	1890
$a(\theta)$	-1	-0.355	-0.687	-0.619	-0.384	-0.095	0.0	0.083
$b(\theta)$	0.0	-0.23	-0.01	-0.007	-0.09	-0.165	-0.186	-0.215

Table 1.5: Angle distribution parameters [Vol80].

Conventional atmospheric neutrinos An analytic description of the muon neutrino spectrum at $E_\nu > 100$ GeV is given in [Vol80] as

$$\left.\frac{dN}{dE_\nu d\Omega}\right|_{\nu_\mu}(E_\nu,\theta) = \begin{cases} 0.0285 \cdot E_\nu^{-2.69} \cdot \\ \left[\frac{1}{1+6E_\nu/E_\pi(\theta)}\right. \\ \left. + \frac{0.213}{1+1.44E_\nu/E_{K^\pm}(\theta)}\right] & 100 \text{ GeV} \le E_\nu < 5.4 \cdot 10^5 \text{ GeV} \\ \\ 0.48 \cdot E_\nu^{-4.04} \cdot \\ \left[E_\pi(\theta) + 0.89 E_{K^\pm}(\theta)\right] & E_\nu \ge 5.4 \cdot 10^5 \text{ GeV} \end{cases} \tag{1.62}$$

and the electron neutrino spectrum is given as

$$\left.\frac{dN}{dE_\nu d\Omega}\right|_{\nu_e}(E_\nu,\theta) = \begin{cases} 0.0024 \cdot E_\nu^{-2.69} \cdot \\ \left[\frac{0.05}{1+1.5E_\nu/E_{K^\pm}(\theta)} + \frac{0.185}{1+1.44E_\nu/E_{K^0}(\theta)} + \right. \\ \left. \frac{11.4E^{\zeta(\theta)}}{1+1.21E_\nu/E_\pi(\theta)}\right] & 100 \text{ GeV} \le E_\nu < 3.7 \cdot 10^5 \text{ GeV} \\ \\ 0.0071 \cdot E_\nu^{-4.045} \cdot \\ \left[E_{K^\pm}(\theta) + 3.7 E_{K^0}(\theta)\right] & E_\nu \ge 3.7 \cdot 10^5 \text{ GeV}\,. \end{cases} \tag{1.63}$$

E_π, $E_{K^\pm}$ and E_{K^0} are angle distribution parameters, depending on the zenith angle θ. ζ is energy dependent as

$$\zeta(\theta) = a(\theta) + b(\theta) \cdot \log(E_\nu)\,. \tag{1.64}$$

The values of E_π, $E_{K^\pm}$, E_{K^0}, $a(\theta)$ and $b(\theta)$ are listed in table 1.5. At lower energies, $E_\nu < 100$ GeV, the description is given numerically by [H$^+$95].

The ratio of neutrinos to anti-neutrinos is energy dependent. In [Wei93] it is given as

$$\begin{aligned} R_{atm}(E_\nu) &= \left(dN_\nu/(dE_\nu d\Omega)\right)_\nu / \left(dN_\nu/(dE_\nu d\Omega)\right)_{\overline{\nu}} = \\ &\begin{cases} 1 & E_\nu \le 1 \text{ GeV} \\ 1 + 0.3 \cdot \log\left(E_\nu/GeV\right) & 1 \text{ GeV} < E_\nu \le 100 \text{ GeV} \\ 0.6 + 0.5 \cdot \log\left(E_\nu/GeV\right) & 100 \text{ GeV} < E_\nu \le 1000 \text{ GeV} \\ 1.2 + 0.3 \cdot \log\left(E_\nu/GeV\right) & E_\nu > 1000 \text{ GeV}\,. \end{cases} \end{aligned} \tag{1.65}$$

The spectrum of conventional atmospheric neutrinos in the parameterization of [Vol80] is shown in Fig. 1.20 (dashed lines). The spectrum is one power steeper than the spectral behavior of the primaries, since the probability that pions and kaons interact before decaying increases with the energy [Gai90]. The upper line represents the horizontal neutrino flux, while the lower line shows the vertical flux. The intensity of the spectrum increases with the angle of the neutrino towards the zenith angle. The larger the angle, the lower the density gradient of the atmosphere and therefore, more pion decays are possible for horizontal events as opposed to vertical events.

Prompt atmospheric neutrinos When heavy hadrons with charm and beauty content are produced in the atmosphere, the resulting neutrino spectrum appears flatter than the one of conventional atmospheric neutrinos. Due to short lifetimes ($\sim 10^{-12}$ s) these hadrons do not interact before decaying for energies up to $E_\nu < 10^9$ GeV. Therefore, the spectrum of the prompt neutrinos follows the primary index, $\propto {E_\nu}^{-2.7}$. One parameterization of the prompt neutrino flux is given in [MRS03] as shown in Fig. 1.20 (green, hatched area). The indicated region includes uncertainties in the interaction models.

General detection method

An estimate of the detection rate of neutrino-induced muons/cascades R can be given by folding the expected neutrino flux at Earth with the probability of the detection of the neutrino,

$$R(E_{\min}, \theta) = \int_{E_{\min}} P_{\nu \to l}(E_\nu, E_{\min}) P_{shadow}(\theta, E_\nu) \frac{dN_\nu}{dE_\nu} dE_\nu \,. \tag{1.66}$$

Here, $P_{\nu \to l}(E_\nu, E_{\min})$ is the probability that a neutrino interacts with a nucleus to produce either a muon - $l = \mu$ - or an electromagnetic or hadronic cascade - $l =$ cascade - which is detectable in a large volume neutrino detector. It can be written as

$$P_{\nu \to l} = N_A \int_{E_{\min}}^{E_\nu} dE_l \, \frac{d\sigma}{dE_l} r_l(E_l, E_{\min}) \,, \tag{1.67}$$

where N_A is Avogadro's constant, r_l is the range of the produced muon within detection range and $d\sigma/dE_l$ is the differential cross section for $N\,\nu$ interactions. In the case of a muon signal, the pure charged current cross section is used, in case of cascades, charged and neutral currents contribute.The energy threshold of the detector for an event detection is given as $E_{\min}$. The cross section is determined using the parton distribution functions given by [CER], where the model of [GRV92] is chosen.

P_{shadow} is the probability that the neutrino traverses the Earth without interaction. It is given as

$$P_{shadow} = \exp\left(-X(\theta)/\lambda\right) \,. \tag{1.68}$$

The thickness $X(\theta)$ of the Earth to the neutrino is dependent on the angle of the incoming neutrino towards the nadir, θ. It is determined by the distance which the neutrino travels through the Earth and the Earth's density using [DA81]. The atmosphere's density of the US standard atmosphere model is included as well. For a description of $X(\theta)$ and λ see for example [Gai90].

Three main signatures can be detected from neutrino-nucleon interactions. The main detection method is the optical detection of the Cherenkov light. Here, detectors in water and ice have been and are being built. The main differences between the detector performance in ice and water lie in the scattering and absorption lengths in water and ice. While ice absorbs only little of the light, water has better scattering properties. In water, there are two additional background components, bioluminescence from bacteria populations in the sea water, and light from ^{40}K decay.

Additionally, the neutrino-induced cascades can be detected at radio wavelengths and also as an acoustic pulse. These cascades are detectable over long distances and therefore, radio and acoustic arrays do not need to be instrumented as densely as optical detectors. On the other hand, larger volumes need to be deployed, since the radio and acoustic detection methods become effective at high threshold energies, $E_{\rm min} \sim 10^7 - 10^8$ GeV, at which the expected neutrino flux is already very low. In the following, the current status of the three detection methods will be reviewed shortly.

Optical detection in ice

The largest currently operating, completed high energy neutrino detector is AMANDA-II. The low neutrino-nucleon cross section demands the instrumentation of large volumes to achieve a significant rate of events. AMANDA is located in the Antarctic ice, between 1500 m and 2000 m below the surface and covers a geometric volume of ~ 0.016 km^3. The detector consists of 19 strings with a total of 677 PhotoMultiplier Tubes (PMTs). AMANDA can detect neutrinos with energies of a lower threshold energy of $E_{\rm min} \geq 50$ GeV.

AMANDA's successor ICECUBE is currently being built around the AMANDA experiment in 1500 m to 2500 m depth. The final configuration will include a geometric volume of 1 km^3 with $70 - 80$ strings, carrying 60 PMTs each. During the past three polar seasons (each year between October and February the following year), a total of 22 strings has already been deployed (1 string in 04/05, 8 strings in 05/06 and 13 strings in 06/07). The array is expected to be completed around 2011. Since the spacing between the PMTs and also between the strings is larger than in AMANDA, the lower energy threshold is slightly higher, $E_{\rm min} \sim 100$ GeV. With the increased volume, higher energy events are easier to identify (the light deposition and the path lengths are increased with increasing energy) and better sensitivities can be achieved.

Analysis strategies in AMANDA/IceCube In order to keep the analysis blinded to avoid experimenters bias, analysis cuts are optimized using off-source samples created by scrambling the right ascension of events or excluding the time window of transient emissions under investigation. Diffuse flux analyses are optimized on a low energy sample, where the signal is expected to be negligible.

AMANDA has a twofold strategy for searching for steady point sources. In a first method, a source catalog of 32 sources was established and spatial cuts were determined based on the position of the potential neutrino emitters. The second technique searches for the spatial clustering of events. Neither of the two point source searches has shown a significant excess of events. The mean sensitivity in the northern hemisphere to an ${E_\nu}^{-2}$ neutrino flux from a point source, Φ^{PS}, is

$$E_\nu^2 \Phi^{\mathrm{PS}} = 5.9 \cdot 10^{-8}\,\mathrm{GeV\ cm^{-2}\,s^{-1}} \tag{1.69}$$

for 5 years of data taking.

The search for single point sources was complemented by stacking classes of sources according to the direct correlation between the photon output and the potential neutrino signal. This was done for 11 different AGN samples that were selected at different wavelength bands, see [AI$^+$06e]. The optimum sensitivity was typically achieved by the stacking of around 10 sources. A method to interpret stacking limits as diffuse limits is presented in Chapter 6. The method is applied to the results from the AMANDA stacking analysis and conclusions about current neutrino flux limits are drawn.

The search for GRBs with AMANDA is almost background free. All bursts in the northern hemisphere during the operation time of AMANDA have been analyzed by temporal and spatial selection in the data. This leaves a vanishing amount of atmospheric neutrinos in the sample. The background is estimated by choosing a 2 hour time window around the burst duration. A similar analysis has been done for cascade events where also the southern hemisphere can be analyzed. Additionally, AMANDA searches for GRBs which are too weak to be detected in photons but have a potentially strong neutrino signal. Here, the data are analyzed according to density fluctuations in the temporal structure. No signal above the atmospheric neutrino background was detected in any of the searches. Limits on the neutrino flux from GRBs could be set for each of the searches as indicated in Fig. 1.22. A Waxman-Bahcall spectrum has been assumed where each burst is parameterized the same way [WB97, WB99]. The search for up-going muons gives limits on the muon neutrino flux (Fig. 1.22(a)), while the cascade analysis gives all-flavor limits (Fig. 1.22(b)). Analyses are now underway which use individually parameterized spectra for each GRB. For more details on each of the GRB analysis methods of AMANDA, see [AI$^+$05]. While the AMANDA sensitivity is not high enough to reach the sensitivity of the flux predictions, IceCube is at the level of the diffuse signal prediction. Also, for individual parameterizations of GRB spectra, the strongest bursts would contribute with about ~ 1 event/km^3. This is investigated in more detail in Chapter 5.

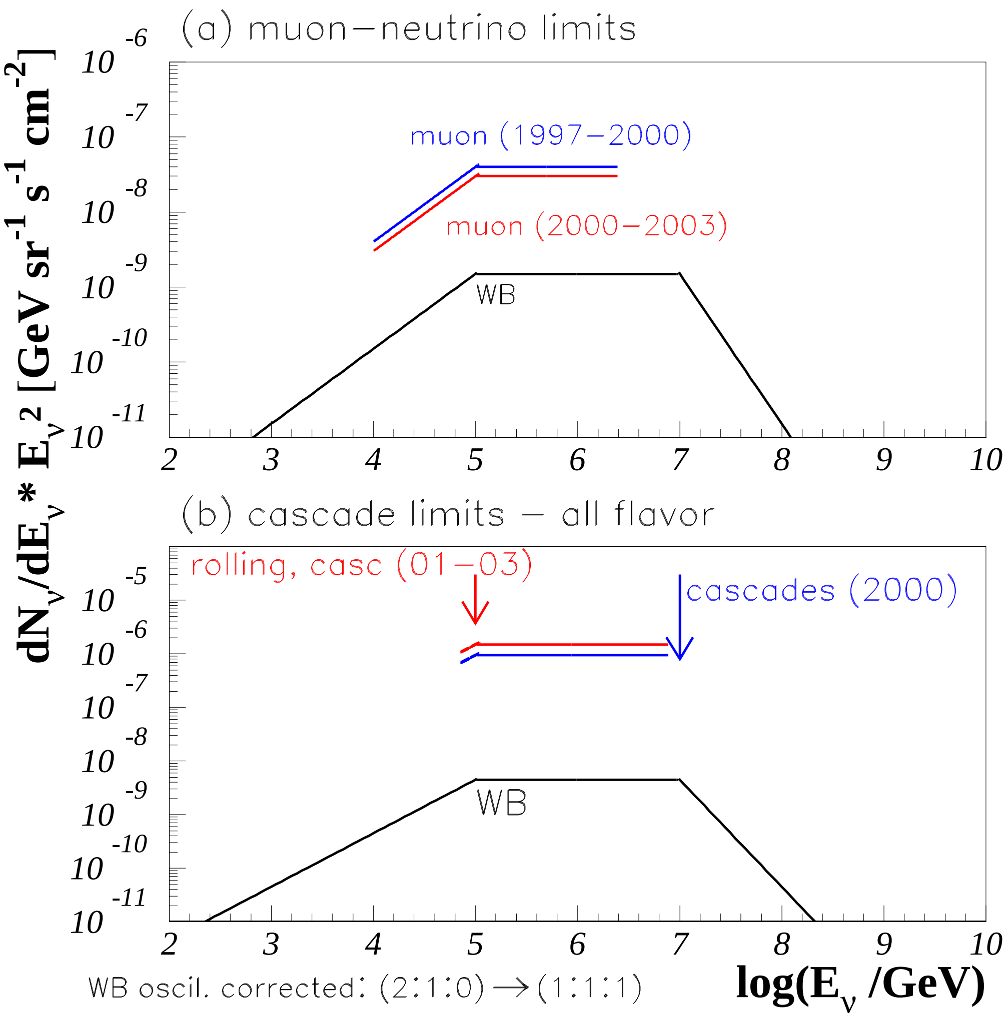

Figure 1.22: Diffuse neutrino flux prediction by [WB97, WB99] and limits to the flux prediction for different channels [AI+07]. (a) results based on the detection of neutrino-induced muons; (b) cascade measurements.

In the diffuse analysis high energy (HE) events from all directions are examined with respect to the spectral energy behavior of the sample. A flattening of the total neutrino spectrum is expected when a flat, astrophysical component ($dN_\nu/dE_\nu \sim {E_\nu}^{-2}$) overcomes the steep atmospheric background ($dN_\nu/dE_\nu \sim {E_\nu}^{-3.7}$). The reconstructed energy spectrum for one year of data (year 2000) is shown in Fig. 1.20. It follows the atmospheric prediction (dashed lines). The most restrictive limit $\Phi^{\mathrm{DL}} = {E_\nu}^2\, dN_\nu/dE_\nu$ from the diffuse analysis for the years 2000 to 2003 is given as

$$\Phi^{\mathrm{DL}} = 8.8 \cdot 10^{-8}\,\mathrm{GeV\ cm^{-2}\,s^{-1}\,sr^{-1}} \tag{1.70}$$

in the energy range of $4.2 < \log(E_\nu/\mathrm{GeV}) < 6.4$.

The results were obtained by optimizing the analysis cuts on ${E_\nu}^{-2}$ spectra. Nonetheless the dependency of the response function of the detector to different spectra was considered and limits were set for different spectral shapes (e.g. ${E_\nu}^{-3}$) or specific models. Varying the spectral index in the simulation shows that the event distribution simulated for AMANDA peaks at very different energies depending on the assumed spectral index. While, for an ${E_\nu}^{-2}$ spectrum, 90% of the signal lies between $4.2 < \log(E_\nu/\mathrm{GeV}) < 6.4$ as discussed above, an ${E_\nu}^{-3}$ spectrum shows an event distribution located about an order of magnitude lower in energy while an ${E_\nu}^{-1}$ spectrum shifts the sensitivity to higher energies. This shows that it is useful to model the spectra according to the predicted shape. This is discussed in detail in [AI$^+$06b]. The diffuse neutrino flux limits are interpreted in Chapter 6 with respect to current neutrino flux models.

Optical detection in water

The optical detection of neutrinos via the Cherenkov effect has already been probed by lower energy detectors like SUPERKAMIOKANDE and SNO as discussed above. In the case of high-energy neutrinos, natural water reservoirs are used for detection. The first generation detector BAIKAL detects neutrino-induced muons in lake Baikal [AB$^+$06, Wis06]. The advantage of this lake is that it is deep enough to deploy $\sim$ 80 m long strings in depths of $\sim$ 1100 m and that the detector can be reached in winter due to the thick ice layer covering the lake. BAIKAL is taking data with the NT-200 detector since 1998. In April 2005, the detector was enlarged to NT-200+, enclosing 0.005 km^3 of water. The sensitivity to a diffuse flux lies around $\Phi^{\mathrm{DS}} \sim 2 \cdot 10^{-7}\,\mathrm{GeV\ cm^{-2}\,s^{-1}\,sr^{-1}}$.

Currently, different experiments are under construction in the Mediterranean sea. In the ANTARES project, 300 m long strings are being deployed up to a depth of $\sim$ 2500 m [AA$^+$97, ANT07]. As of February 2007, 5 lines were deployed and the first muon tracks could already be identified. The final detector configuration will consist of 12 strings with an instrumented volume of $\sim$ 0.03 km^3. A second array is being constructed near the coast of Italy, the NEMO[33] detector [Sap06, NEM07], at a depth of ~ 3500 m. Such a high depth has two main advantages: the flux of atmospheric muons from above is lower in the detector, and also the bioluminescence background is low at high depths. The first tower has been deployed in 2006. In a second phase, the deployment of one or more additional towers are planned. NESTOR[34] is a third experiment, being deployed near the coast of Greece at a depth of 3800 m [AN+05, NES07]. The first phase of the detector was deployed in March 2003, and first results are presented in form of the measurement of horizontal atmospheric muons [AN+05].

The primary aim of the three arrays described above is to explore different sites and techniques for neutrino detection in sea water in order to build a 1 km^3 detector, choosing the optimal location and design, namely KM3NeT [KM3a]. This detector will be complementary to IceCube, detecting mainly muon neutrinos from the southern hemisphere. With both arrays, a view of the complete sky is possible. The view on the southern hemisphere enables KM3NeT the observation of the galactic center, which is not visible from the South Pole. In Chapter 6, different extragalactic source catalogs are investigated with respect to their contribution in the northern and southern hemisphere. It will be shown which classes are better to observe from the north or from the south.

Acoustic and radio detection

Current neutrino experiments are able to measure the atmospheric neutrino spectrum up to 100 TeV without observing a significant contribution from extragalactic sources. Successor experiments like IceCube aim at the detection of neutrinos at 100 TeV up to 100 PeV. The detection of a signal at even higher energies is restrictedly also possible with IceCube, but to achieve a good detection possibility of the cosmogenic neutrino flux, new methods are being developed which are complementary to optical detection. Acoustic and radio neutrino detection aims at the measurement of neutrinos at Extremely High Energies (EHEs), i.e. $E_{\mathrm{min}} \sim 10^8$ GeV.

Radio detection As it was discussed for the first time by Askaryan [Ask62], the Cherenkov effect is not only present at optical and UV wavelengths, but has a strong component in the radio. The electromagnetic shower at radio wavelengths has an extension of about 10 cm. The Askaryan effect has been observed in sand [S+01], salt [G+05] and also in ice [GA+06]. It is used for the purpose of neutrino detection in the RICE[35] experiments which aims at the detection of the radio signal from neutrino-induced cascades at energies of $(10^{15}, 10^{18})$ eV in the ice below the geographic South Pole [K+03]. A geometric volume of 0.008 km^3

---

[33] **NE**utrino **M**editerranean **O**bservatory

[34] **N**eutrino **E**xtended **S**ubmarine **T**elescope with **O**ceanographic **R**esearch

[35] **R**adio **I**ce **C**herenkov **E**xperiment

is instrumented with dipole receivers at a depth of 100 m to 300 m below the surface. The advantage of the high energy threshold is that the atmospheric background of muons and neutrinos can be neglected. The challenge is the very small signal rate at such high energies. So far, no neutrino signal could be identified yet. Most recent studies concerned the search for individual GRBs, with limits to GRB afterglow neutrino emission models given in [BRAH07]. A second detector trying to measure the radio signal from neutrino-induced cascades is the ANITA[36] balloon-borne experiment [BA$^+$06], sensitive in the energy range of ($10^{18.5}$, $10^{23.5}$) eV. Radio emission arising from neutrino interactions with nucleons in the Antarctic ice sheet is measured from above. First limits come from test-flights of ANITA-LITE, the first full ANITA flight was successfully done in December 2006, with 3.5 circles around Antarctica, with no results published yet. ANITA is expected to investigate the model of GZK neutrinos, either confirming a positive signal, or setting limits which will restrict source evolution scenarios for the production of ultra-high energy protons, see Section 1.3.5.

Next generation detectors of radio emission from neutrino-induced cascades are planned in salt and in ice. In ice, the AURA[37] experiment [GME93] will be succeeding RICE. The final aim is the instrumentation of about 10 km^2 in Antarctica. A new project using radio antennas on top of the Ross Ice Shelf at the Antarctic coast is ARIANNA[38] [Bar06], making use of neutrino-induced radio emission in the ice shelf. Salt is a good target material, since it has about 2.3 times the density of water and ice, and therefore also provides more than 2 times more nucleons within the same volume. The neutrino effective interaction volume is hence increased. The SalSA[39] experiment is planned, where parts of a salt dome is supposed to be instrumented for the purpose of neutrino detection. First tests are already being done in salt domes [V$^+$05b].

Another method of detecting neutrino-induced radio emission is to observe the moon with radio telescopes. The moon yields a good target for neutrino interaction and therefore, an enhanced radio signal is expected from the direction of the moon. Projects investigating this effect are planning to use the WSRT[40] or SKA[41]. The latter is planned to be used in the context of the LUNASKA[42] project [LUN07]. For an overview of the status of neutrino radio detection methods, see e.g. [Sal06].

---

[36] **AN**tarctic **I**mpulsive **T**ransient **A**ntenna Experiment

[37] **A**skaryan **U**nderice **R**adio **A**rray

[38] **A**ntarctic **R**oss **I**ceshelf **AN**tenna **N**eutrino **A**rray

[39] **Sal**t dome **S**hower **A**rray

[40] **W**esterbork **S**ynthesis **R**adio **T**elescope

[41] **S**quare **K**ilometre **A**rray

[42] **L**unar **U**ltra-high-energy **N**eutrino **A**strophysics using **SKA**

Acoustic detection The first array for acoustic neutrino detection was deployed in water, i.e. in the ocean. The SAUND[43] [VGL05] array makes use of a military basis in the Bahamas. The array is located between depths of 1570 m and 1600 m, spread over a surface of $\sim$ 250 km^2. First results were presented in [VGL05]. The acoustic technique in the ocean is also tested at the ANTARES site with the AMADEUS[44] detector, currently being deployed along with the ANTARES strings [N$^+$06]. The main aim of these prototype detectors is the study of the background and general water properties. For the detection of an EeV neutrino signal, an extremely large array ($\sim$ 10 km^2) needs to be deployed. In addition to water, ice and salt are good environments occurring naturally for the installation of a large volume acoustic neutrino detector. In the SPATS[45] project [B$^+$05b, AI$^+$06b], first hydrophones were deployed at together with one IceCube string in January 2007 in order to test the acoustic properties of the Antarctic ice. The final aim is again the construction of a $\sim$ 10 km^2-wide array for the detection of EeV neutrinos. For a summary of the current status of acoustic neutrino detection arrays, see [Van06].

Hybrid arrays The three techniques as described above provide complementary information on the neutrino-induced showers. Therefore, the best reconstruction of neutrino events will be possible, if all three detection methods are combined in a hybrid array. First simulations of a combined array of acoustic, radio and optical array have been done for ice [BI$^+$05]. Here, the IceCube configuration has been used together with a further outer ring of strings for optical detection, as well as an acoustic and radio array with a diameter of 10 km around IceCube. A scheme of the configuration and of the effective volumes of the three arrays and the combined array is given in [V$^+$05a]. In the simulated configuration, about 10 GZK events per year are expected independently from the acoustic and radio array, using the flux as derived in [ESS01].

---

[43] **S**tudy of **A**coustic **U**ltra-high-energy **N**eutrino **D**etection

[44] **ANTARES** **M**odules for **A**coustic **DE**tection **U**nder the **S**ea

[45] **S**outh **P**ole **A**coustic **T**est **S**etup

CHAPTER 2

Photon catalogs in the context of neutrino emission

It is crucial to investigate the potential neutrino output of astrophysical sources by analyzing different source classes and their photon output. Neutrinos are produced in proton-photon and proton-proton interactions. No such extragalactic neutrinos have been observed yet. It is therefore necessary to make use of observations of other particles which according to theory can be connected to neutrino emission. There are three different assumptions which can be made: The connection of neutrino emission to

1. the observation of the CR flux,
2. the observation of photon field which are the target for proton-photon interactions, or
3. to the observation of photon fields which are secondaries of electron populations in the sources. The electromagnetic output of these secondaries can be related to the total energy in primary electrons which in turn is proportional to the total energy in baryons in the source. The baryon total energy is then again correlated to the neutrino total energy via a simple constant of proportionality.

In each of the three cases, the energy density of the observed particles (case (1): protons; cases (2) and (3): photons) is related to the neutrino energy density as discussed in Section 1.3.

In this section, different source classes are considered with respect to their electromagnetic output (cases (2) and (3)). The advantage in comparison to scenario (1) is that the sources of the particle emission are identified. They can be modeled individually, without having to rely on average parameters. The directional information of the signal can be used to select data in order to optimize the analysis for the search of a signal from specific sources in high energy neutrino telescopes.

2.1 Active Galactic Nuclei

As discussed in Chapter 1, according to the unified model, AGN divide into sub-classes with respect to their intrinsic morphology and luminosity, and to the orientation angle of the jet towards the observer at Earth. In this section, different source classes and catalogs are discussed. They are used to investigate the possibility of neutrino observation from each source class.

2.1.1 Radio classes

Generally, AGN are subdivided into *radio loud* and *radio quiet* object, where the former are connected to elliptical galaxies and the latter are observed in spiral galaxies. About 90% are radio quiet, only $\sim 10\%$ are radio loud. Radio loud sources are divided by their luminosity, which is connected to a change in morphology. AGN with many radio-emitting knots along the jet have luminosities of $L_{radio} < 10^{26.5}$ W/Hz, while AGN with only one large radio-lobe at the outer end of the jet have high luminosities, $L_{radio} > 10^{26.5}$ W/Hz. The 3CRR catalog lists radio-loud AGN with fluxes at Earth of $S > 1$ Jy [LRL83]. Studies of higher sensitivity, i.e. $S < 1$ Jy are the 7CRS [MR90, L$^+$99a] and 6CE [REL01] catalogs. This classification was first introduced by Faranoff and Riley (FR) [FR74]. FR-I and FR-II galaxies refer to low- and high-luminosity AGN as seen from the side, i.e. the jet morphology can be resolved. These sources have steep radio spectra, $S \sim \nu^{-0.8}$ and are therefore also referred to *steep spectrum sources.* A sample of 356 steep spectrum sources is presented and analyzed in [W$^+$01], subdividing it into a sample of FR-I and FR-II galaxies.

Radio loud AGN are classified as blazars when the jet is oriented towards Earth. High-luminosity objects are referred to as *Flat Spectrum Radio Quasars* (FSRQs) due to their flat spectra. They are defined to have spectra flatter than $S \sim \nu^{-0.5}$, and typically, they are as flat as $S \sim \nu^{0}$. A sample of 171 FSRQ is given in [Pea85], selected from the Parkes selected regions sample, the Parkes $\pm 4^{\circ}$ zone [Pea85, W$^+$82], the 'northern-sky' survey of [PW81] and the 'All-Sky' survey of [WP85]. Low-luminosity objects are called *BL Lacs* after the first detected object of this kind in the constellation Lacerta. The class of blazars has been studied in more detail at high photon energies, $E_{\gamma} >$ MeV. Most of the high-energy measurements come from instruments on board of the CGRO which was taking data between April 1991 and June 2000, with OSSE[1] at (15, 150) keV, COMPTEL at > MeV and EGRET at > 100 MeV.

---

[1] **O**riented **S**cintillation **S**pectrometer **E**xperiment

2.1.2 X-ray AGN

In the 1990s, ROSAT provided the highest-resolution all-sky survey at X-ray energies. It measured a diffuse X-ray background, 70% of which could be assigned to resolved X-ray emitting AGN. With the launch of CHANDRA in July 1999 and XMM-NEWTON in December 1999, the general sensitivity and resolution of X-ray surveys was improved significantly in such a way that 95% of the diffuse X-ray background could be identified as AGN. A sample of > 1000 AGN from ROSAT, CHANDRA and XMM-NEWTON data is presented in [HMS05]. This large sample of AGN has been used for detailed studies of the luminosity evolution and the distance distribution. A luminosity-dependent distance distribution is presented, showing a behavior of

$$\rho = A \cdot \begin{cases} (1+z)^m & \text{for} z < z_1 \\ (1+z_1)^m & \text{for} z_1 < z < z_2 \\ (1+z_1)^m \cdot 10^{k\cdot(z-z_2)} & \text{for} z < z_1 \,. \end{cases} \tag{2.1}$$

Different parameter sets (z_1, z_2, m, k) are found for different luminosity bins,

$$(z_1, z_2, m, k) = \begin{cases} (0.7, 0.7, 4.0 \pm 0.7, -0.32) & \text{for } 10^{42.5} \text{ erg/s} \\ (1.2, 1.2, 3.4 \pm 0.5, -0.32) & \text{for } 10^{43.5} \text{ erg/s} \\ (1.7, 2.7, 5.0 \pm 0.2, -0.43) & \text{for } 10^{44.5} \text{ erg/s} \\ (1.7, 2.7, .1 \pm 1.0, -0.43) & \text{for } 10^{45.5} \text{ erg/s} \,. \end{cases} \tag{2.2}$$

This distance distribution comprises the largest, probably most complete, sample of AGN and will therefore be used in Chapter 3 for the description of the distribution of the sources of Cosmic Rays.

Hard X-ray measurements have been done at $(0.2, 25)$ keV by the HEAO-A[2] satellite in the 1970s, with the results listed in [W+84]. A more complete, but still small catalog is given by INTEGRAL with 15 sources identified at an energy range of (20, 40) keV.

2.1.3 AGN at soft γ-ray energies

A first catalog of blazars [M+95] and later of Seyfert galaxies [J+97] at soft γ-ray energies, i.e. (15, 150) keV, was presented by OSSE. Recently, a catalog of 42 AGN at soft gamma ray energies, (20, 100) keV has been presented from the INTEGRAL satellite [B+06], confirming many of the OSSE sources and presenting new sources at soft γ-ray energies.

---

[2] **H**igh **E**nergy **A**stronomy **O**bservatories-**A**

2.1.4 AGN at >MeV energies

COMPTEL provides the single catalog of AGN at > MeV energies [K$^+$96]. This catalog of 10 blazars can be extended with future experiments of higher sensitivity and better resolution. A possible successor experiment is MEGA[3] [K$^+$04a].

2.1.5 AGN at GeV energies

The detailed examination of photon emission at energies of $E_\gamma > 100$ MeV has been done by EGRET. The catalog comprises 67 identified AGN. It is expected to be significantly improved by GLAST measurements. GLAST provides a higher sensitivity and a better resolution. Therefore, more sources will be resolved. GLAST's launch is planned for the end of 2007.

2.1.6 AGN at TeV energies

Since 2003, the second generation of Imaging Air Cherenkov Telescopes (IACTs) is taking data, with leading results from H.E.S.S. and MAGIC. So far, 15 HBLs have been detected. HBLs represent AGN with the second peak in the spectrum at ∼ TeV energies. LBLs have the second bump at ∼ GeV energies. Most recently, the first LBL, BL Lacertae, has been identified at TeV energies by the MAGIC experiment [Alb07]. In addition, M 87 as a misaligned blazar, or a FR-I galaxy, is identified at energies of $E_\gamma > 100$ GeV. The AGN identified at TeV energies and their basic properties are listed in table 2.1.6. The difficulty in detecting extragalactic objects at TeV energies is the absorption of photons at the highest energies by the Extragalactic Background Light (EBL), comprised of the infrared background as the trace of star formation, the cosmic microwave background and other photon fields in the Universe. For a lower energy threshold of ${E_\gamma}^{th} \sim 100$ GeV, sources up to $z \sim 0.2$ can be observed. Lowering the energy threshold to ∼ 20 GeV allows for a view of the Universe up to $z \sim 1$. For source populations following the star formation rate, it is expected that most sources are located between $z \sim 1 - 2$. Therefore, one of the primary aims of IACTs is to lower the energy threshold in order to increase the number of observed sources.

While IACTs are very sensitive to point sources, water Cherenkov detectors instrument a large area with photomultipliers, being able to observe both photons, electrons and muons from electromagnetic showers. This technique allows for the observation of 2π sr at once, however, with a relatively low sensitivity. MILAGRO succeeded with the observation of Mkn 421 and the Crab nebula. In addition, diffuse emission regions in the Cygnus region were found, which is not possible with IACTs due to the small field of view. The next generation water

---

[3] **M**edium **E**nergy **G**amma-ray **A**stronomy

Source	type	redshift	α_{gamma} $dN_\gamma/dE_\gamma \propto {E_\gamma}^{\alpha_\gamma}$	first detection
M 87	FR-I	0.004	-2.9	HEGRA
Mkn 421	HBL	0.031	-2.2	WHIPPLE
Mkn 501	HBL	0.034	-2.4	WHIPPLE
1ES 2344+514	HBL	0.044	-2.9	WHIPPLE
Mkn 180	HBL	0.045	-3.3	MAGIC
1ES 1959+650	HBL	0.047	-2.4	TEL. ARRAY
BL Lacertae	LBL	0.069	-3.6	MAGIC
PKS 0548-322	HBL	0.069	n/a	H.E.S.S.
PKS 2005-489	HBL	0.071	-4.0	H.E.S.S.
PKS 2155-304	HBL	0.116	-3.3	MARK VI
H 1426+428	HBL	0.129	-3.3	WHIPPLE
1ES 0229+200	HBL	0.139	n/a	H.E.S.S.
H 2356-309	HBL	0.165	-3.1	H.E.S.S.
1ES 1218+304	HBL	0.182	-3.0	MAGIC
1ES 1101-232	HBL	0.186	-2.9	H.E.S.S.
1ES 0347-121	HBL	0.188	n/a	H.E.S.S.
PG 1553+113	HBL	?	-4.0	H.E.S.S./MAGIC

Table 2.1: AGN of TeV emission. Table adapted from [Tes06]. Sources are sorted by redshift. The redshift of PG 1553+113 is still unknown. The sources with no spectral index announced (n/a) are preliminary.

Cherenkov telescopes, including the planned HAWC[4] experiment [SSM05, S^+06], are expected to give more information on diffuse emission due to a higher sensitivity.

---

[4] **H**igh **A**ltitude **W**ater **C**herenkov

2.2 Starburst galaxies

The radio emission observed in distant galaxies is typically due to synchrotron emission of electrons. In many cases, it is observed to be spatially structured, showing an increased emission of compact sources such as young supernova remnants. Such SNRs are typically found in regions of high star formation. Starburst galaxies represent galaxies with high star formation rate, implying that many supernova explosions happen within this galaxy type compared to regular galaxies. Far-infrared photons are emitted when the light of primarily young stars heats the dust in a galaxy and therefore, a correlation between the radio and far-infrared band is expected. This correlation turns out to be a simple proportionality at reference wavelengths of $\lambda = 60\,\mu$m and $\lambda = 100\,\mu$m for the far-infrared and frequencies of $\nu = 1.4$ GHz and $\nu = 5$ GHz. In addition, a correlation between far-infrared and X-rays is found [C$^+$87].

With the IRAS[5] catalog of infrared sources, a detailed, full-sky coverage survey is available, while radio data are only available for a selection of radio sources. Selective catalogs of Starburst sources have been presented by different authors. A more complete catalog is being developed [Dre09] using data bases and catalogs [WB92, WO90, HW64, BWE91, D$^+$96, C$^+$96, BWH95, C$^+$98, L$^+$05, M$^+$90, S$^+$03]. Combining the previously mentioned catalogs yields a preliminary source sample of the ~ 200 strongest sources. The completed catalog will most likely comprise a much larger sample, including weaker sources which have only been detected by IRAS with no radio counterpart. The correlation between radio and infrared can then be used to estimate the radio output of the corresponding source.

2.3 Gamma Ray Bursts

Catalogs of prompt emission from GRBs are presented in this section. These catalogs are typically organized by experiments. Each GRB satellite has different properties concerning the detection rate of GRBs and the spectral measurements. The bandpass and the field of view vary with each detector and lead therefore to different selection effects as it has been discussed in Section 1.2.2. Between 2000 and 2004, many satellites contributed to the localization of GRBs with the IPN3, but the individual satellites only observed small numbers per year due to small fields of view. For this time, no homogeneous sample can be presented.

---

[5] **I**nfra**R**ed **A**stronomical **S**atellite

2.3.1 The BATSE catalog

The BATSE experiment on board of CGRO detected 2704 bursts during about 10 years of operation (1991-2000). The BATSE 4B catalog consists of a sample of 1234 [P+99] with given duration. Not all of the 1234 GRBs sufficient spectral information. Two sub-samples have been developed from the BATSE catalog, applying spectral fits to the data.

- Spectral band fits for 568 bursts are given in [G+04], including a redshift estimate using the variability method as described in Section 1.2.2. This catalog will be referred in the following as the *variability sample*.
- 292 bursts have been fitted using the Band function, see [GSF05]. For each of the bursts, a redshift has been estimated using the lag method as described in Section 1.2.2. This sample is referred to as the *lag sample*.

2.3.2 The Konus catalog of short bursts

The KONUS experiment published a catalog of 130 short GRBs between 1994 and 2002 [M+05a]. Of the 130 events, 99 have fitted energy spectra. In comparison to the BATSE sub-samples, the KONUS spectral fits use simplified single powerlaw fits, or in some cases broken powerlaw fits, since the energy range is not wide enough to have information on the spectral break or on the behavior at higher energies.

2.3.3 The Swift catalog

Since November 2004, SWIFT is successfully taking data. As of March 12, 2007, 228 bursts were detected of which 201 have spectral information. These 201 bursts divide into 188 long and 13 short events were detected. Data are available online at [Swi06a]. Due to the relatively small bandpass of (15, 150) keV, SWIFT only observes the lower part of the Band function. Therefore, single powerlaw fits are given instead.

CHAPTER 3

Cosmic Rays from relativistic shock environments

In this chapter, recent results of Monte Carlo simulations of oblique, relativistic shocks will be discussed with respect to GRB and AGN spectra.

Shocks are divided into two categories, sub- and superluminal, as discussed in Chapter 1. Both cases will be examined with respect to their contribution to the Cosmic Ray Spectrum. The bulk Lorentz factor Γ will be varied in order to simulate the conditions in extragalactic sources such as AGN and GRBs. Both AGN and GRBs have been suggested as the sources of UHECRs and their contribution to the CR spectrum within the framework of oblique shocks will be examined.

As it turns out, only subluminal shocks are able to accelerate particles to the highest energies, see Section 3.3. Superluminal shocks only reach maximum particle energies of around $\sim 10^5$ GeV and can therefore be excluded as sources of Cosmic Rays above the ankle. The case of subluminal shocks is investigated further, since these sources are able to accelerate particles up to 10^{21} eV as discussed in Section 3.1. The primary spectra are discussed in Section 3.3. A correlation between the spectral index of the primary spectrum and the boost factor is examined for the case of subluminal shocks. Further, in Section 3.4, the phenomenological results obtained in previous sections are discussed in the context of GRB observations. In Section 3.5, the single source spectra as derived in Section 3.3 are used to calculate the diffuse spectrum expected at Earth, using shock configurations as they occur in AGN and GRBs.

3.1 Maximum energy

The acceleration of particles is limited by the size of the acceleration region and the magnetic field, as it has for the first time been pointed out by Hillas [Hil84]. Once the gyration radius exceeds the source radius, the particles escape. The maximum energy is then given as

$$E_{\max}^{18} = \beta_s \cdot Z \cdot B_{\mu G} \cdot R_{kpc} \,. \tag{3.1}$$

Here, $E_{\max}^{18} := E_{\max}/(10^{18}\text{ eV})$ is the maximum energy which can be achieved, $\beta_s = V_s/c$, Z is the charge of the accelerated particle in units of the charge of the electron, e. Furthermore, $B_{\mu G} := B/(1\,\mu\text{G})$ is the magnetic field of the acceleration region in units of $1\,\mu$G and $R_{kpc} := R/(1\text{ kpc})$ is the size of the acceleration region in units of 1 kpc. The equation is visualized in Fig. 3.1. Different astrophysical objects are indicated with their typical magnetic field configuration on the y-axis and their extension on the x-axis. The acceleration of protons ($Z = 1$) in relativistic shock environments ($\beta_s = 1$) is possible for sources which lie above the dashed line. The solid upper line indicates the same configuration for $\beta_s = 1/300$. The solid lower line assumes $\beta = 1$ and iron nuclei ($Z = 26$). It can be seen from the figure that AGN cores and radio galaxy lobes, as well as hot spots, are promising candidates for the acceleration of the highest energy events, but that also neutron stars are in principle able to accelerate protons up to 10^{21} eV. However, a second criterion for particle acceleration as discussed by Hillas is the velocity of the magnetic field inhomogeneities. This is directly connected to the energy threshold for synchrotron losses of charged particles and to the magnetic field strength. Radio galaxy hot spots allow the acceleration of particles up to 10^{21} eV and in radio galaxy lobes, energies of 10^{19} eV can be produced. All other sources are not able to produce particles of such high energies, since the synchrotron time scale is shorter than the acceleration time scale [Hil84]. Today, it is known that also GRBs are able to accelerate protons to 10^{21} eV without significant synchrotron losses as is discussed in the following.

1. *Particle acceleration in AGN:*
   AGN are typically assumed to accelerate particles in relativistic shocks. The boost factors are typically assumed to be around $\Gamma \sim 10$, although in special cases, the boost factor can reach up to $\Gamma \sim 30-40$. It can, however, be possible that the shock itself happens in a relativistic environment. This implies that the plasma flow is relativistic itself and not necessarily the shock. Here, we will still assume the relativistic movement of the shock-front. The magnetic field is $B \sim 10^{-3}$ G in the jet at a radius of, $r \sim 1$ kpc and the field typically decreases with the radius. This allows for particle acceleration up to the highest energies, i.e. $E_{\max}^{AGN} \sim 10^{21}$ eV as indicated in Fig. 3.1.

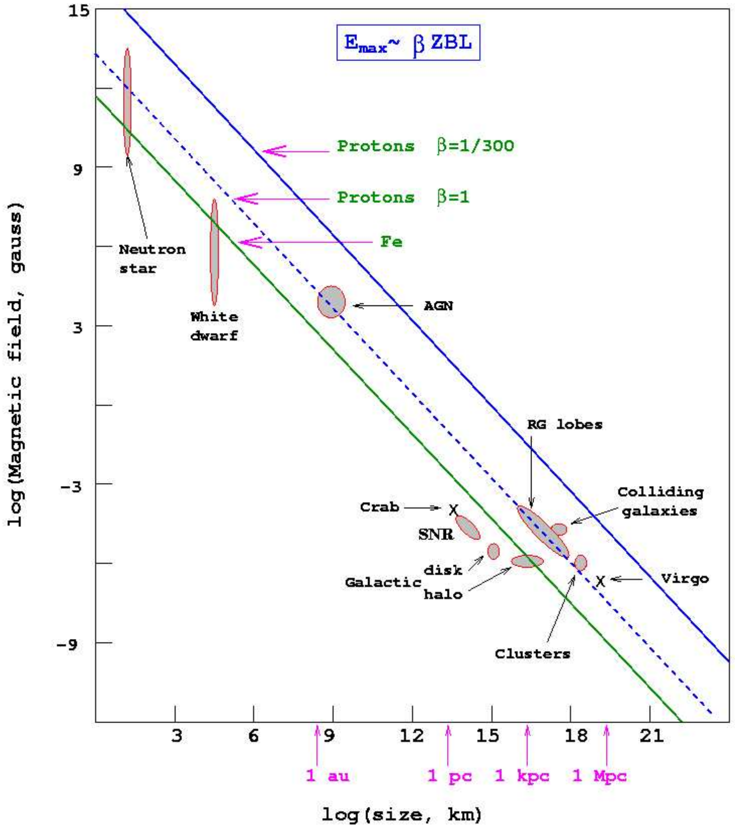

Figure 3.1: The Hillas plot showing various objects. The logarithm of the magnetic field of the sources is shown versus the size of the objects. The lines represent proton acceleration (upper: $\beta_s = 1/300$ and middle: $\beta_s = 1$) and iron acceleration with $\beta_s = 1$. Objects below the lines cannot accelerate the corresponding nucleon to energies above the GZK cutoff ($E > 5 \cdot 10^{19}$ eV) [Arg00].

2. *Particle acceleration in GRBs:*
The prompt emission of GRBs happens at a radius $r \sim 10^{12} - 10^{13}$ cm from the center. The exact magnetic field strength of GRBs can only be estimated so far. For instance, in [LW06a], a lower limit of the magnetic field at the order of $B_{\rm min} \sim$ mG has been determined, the exact value depending on the density of the medium. This gives a lower limit of the maximum energy around 10^{20} eV for protons, with slightly higher magnetic fields, 10^{21} eV can be reached. The hypothesis that GRBs are candidate sources for the acceleration of Cosmic Rays to the highest energies has already been established in [Wax00, Vie95].

3.2 Spectral behavior

The primary particle spectra follow a powerlaw distribution with an upper cutoff: after one acceleration cycle, the particles are swept away from the acceleration region and have only limited chance of returning back to the shock. The chance of undergoing a second acceleration cycle is, however, not vanishingly small, so that some particles do return to the shock region. In this case, the spectrum continues up to higher energies and a bump is visible at the point where most particles leave the acceleration region. The part at higher energies is produced by particles undergoing two acceleration cycles. These features are also visible in the Monte Carlo spectra discussed in the following.

The spectral index of the primary particle spectrum, α_p, is found to vary with the boost factor. Some simulations indicate that the spectral index approaches a canonical value of $\alpha_p \rightarrow 2.23$ for $\Gamma \rightarrow \infty$, see e.g. [K$^+$00, BO98, OB02]. It is pointed out in [Bar04], however, that this is a rather special case which applies for parallel shocks with velocity compression ratios of $r := u_u/u_d = 3$ with pitch angle diffusion. For lower compression ratios, the spectrum becomes steeper and it gets flatter for higher ratios. Also, spectra tend to get flatter in the case of second cycle acceleration. The evolution of the spectral index with the boost factor will be examined in more detail for oblique, subluminal, relativistic shocks in the following sections.

3.3 Primary protons

Sub- and superluminal particle spectra have been calculated in Monte Carlo simulations [Mel06]. This section reviews the primary particle emission of relativistic shocks. In the simulation, pitch angle diffusion is used for $\sim 10^5$ particles injected upstream [Mel06]. The velocity compression ratio is chosen to be $r = 3$. The spectra are presented downstream, for protons. The spectra at the source as they are calculated here are labeled $d\Phi/dE_p$, while propagated spectra at Earth are as before given by dN_p/dE_p.

The spectra at the source are investigated in the context of the maximum energy obtained from the Monte Carlo and the spectral behavior. The calculations for subluminal shocks are presented in more detail, since early results showed that superluminal shocks are only efficient up to $E_p \sim 10^5$ GeV and can therefore not be considered as sources of UHECRs at $E_p > 3 \cdot 10^{18}$ eV [MQB05]. At lower energies, these spectra cannot be visible, since galactic Cosmic Rays dominate the spectrum.

3.3.1 Superluminal spectra

Superluminal shocks have been simulated for the oblique condition $\psi = 76°$ given in the shock frame for different boost factors[1]. Since a transformation into the HT frame is not possible, the particles were followed in the appropriate fluid frame and the results are presented in the shock frame to ensure the consistency of the results. More details on the simulation of these shocks are given in [MQB05].

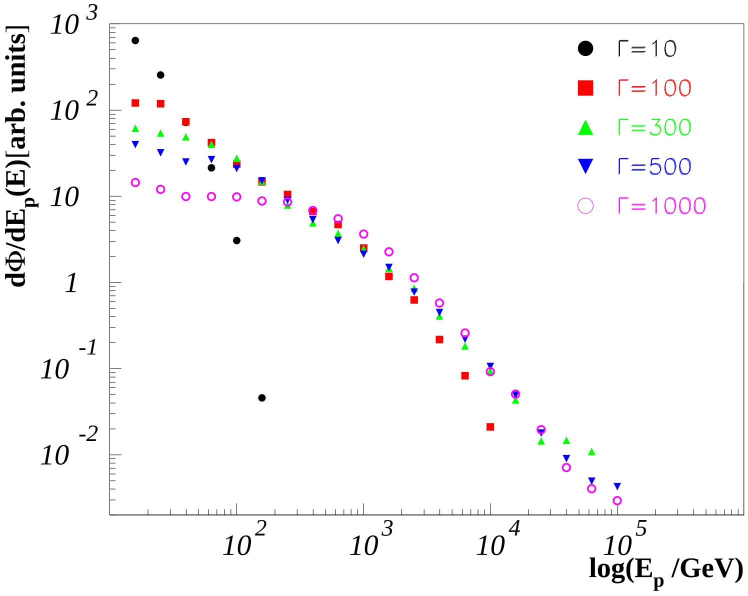

Figure 3.2: Superluminal, relativistic spectra at $\psi = 76°$. Boost factors are varied between $\Gamma = 10, 100, 300, 500, 1000$.

The resulting particle spectra for $\Gamma = 10, 100, 300, 500$ and 1000 are displayed in Fig. 3.2. For mildly-relativistic shocks ($\Gamma = 10$), the shock is efficient only at the lowest energies $E_p < 100$ GeV. Highly-relativistic shocks ($\Gamma \geq 100$) can produce particles up to $E_p < 10^5$ GeV. The observed spectrum of charged Cosmic Rays is dominated by non-relativistic galactic sources up to energies of $E_p < 3 \cdot 10^{18}$ eV. Therefore, it can be concluded from these calculations that superluminal, relativistic shocks do not contribute to any observed effects. The situation is different for subluminal relativistic shocks, as will be explained in the following section.

---

[1] The result is basically independent of ψ, if superluminal and oblique, and is therefore only done for one, arbitrarily chosen, angle configuration, here $\psi = 76°$.

3.3.2 Subluminal spectra

Particle spectra emitted from relativistic, subluminal shocks have been calculated for three different angles in the shock frame, $\psi = 23^\circ$, 33° and 43°. The spectra are presented in Figures 3.3, 3.4 and 3.5. In each figure, the particle spectrum is shown for nine different boost factors, $\Gamma = 10, 20, 30$ in the first row from the left, $\Gamma = 100, 300, 500$ in the middle row and $\Gamma = 700, 900, 1000$ in the lower row. Each graph shows the logarithm of the proton spectrum $d\Phi/dE_p$ in arbitrary units versus the protons' energy in units of GeV. Note that the spectrum can more generally be expressed in terms of the particle's boost factor $\gamma = E_p/(m_p c^2)$. Therefore, the results are also valid for nuclei with higher mass. Here, protons are considered only.

The bumps in most of the spectra at the lowest energies are due to the monochromatic injection of the particles. The powerlaw approximation has in each case been applied at higher energies. That way, artificial injection features are excluded from the calculations. The bump at higher energies is a physical feature: especially at high boost factors, particles can be accelerated in a second cycle. The lower energy part of the spectrum is dominated by particles undergoing one acceleration cycle, while the second bump in the spectrum represents particles having done two cycles. The upper limit for the powerlaw approximation is 10^{21} eV.

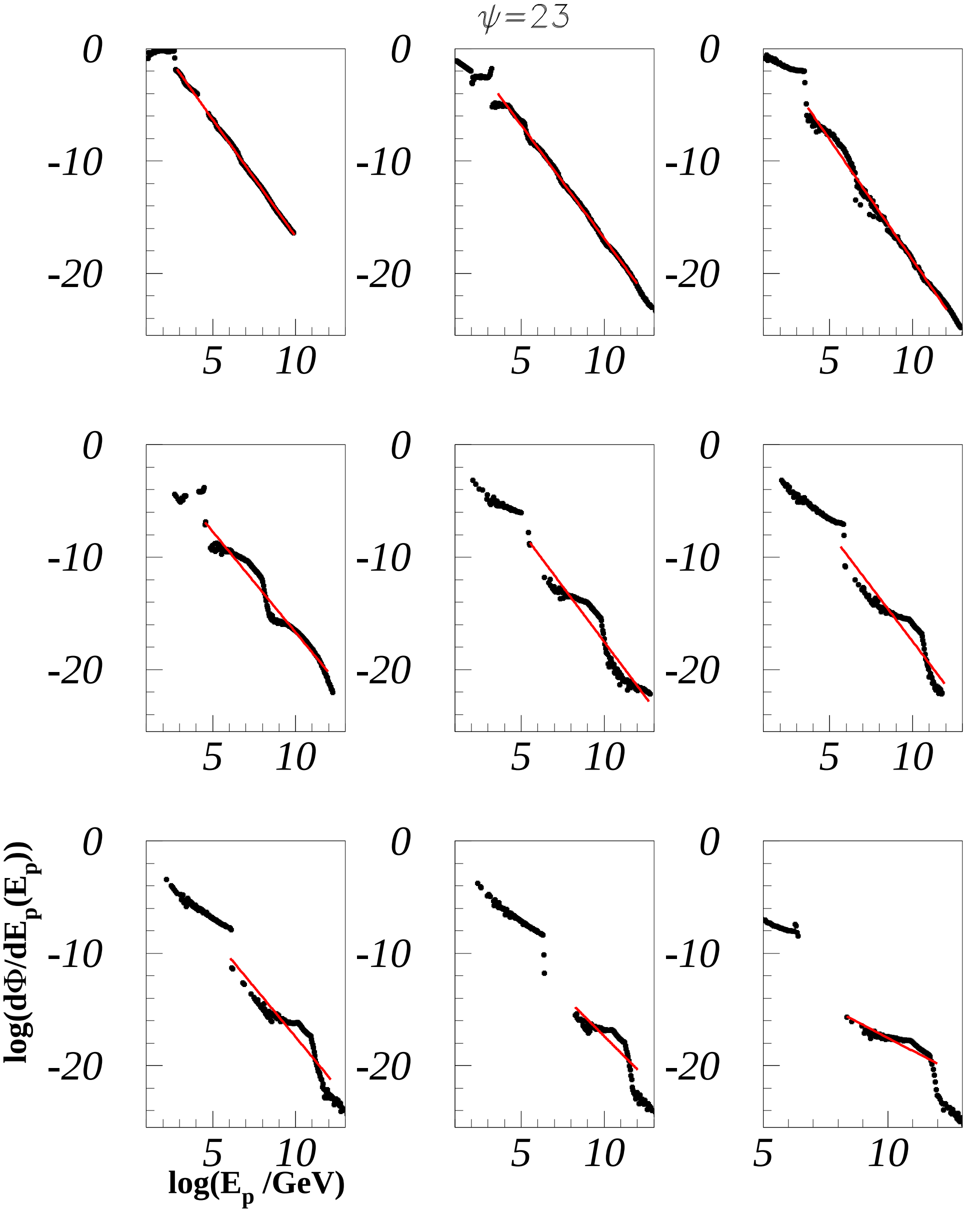

Figure 3.3: Subluminal spectra for $\psi = 23°$ and different Γ: $\Gamma = 10, 20, 30$ is displayed in the first row, in the middle, $\Gamma = 100, 300, 500$ is shown and $\Gamma = 700, 900, 1000$ is the bottom row.

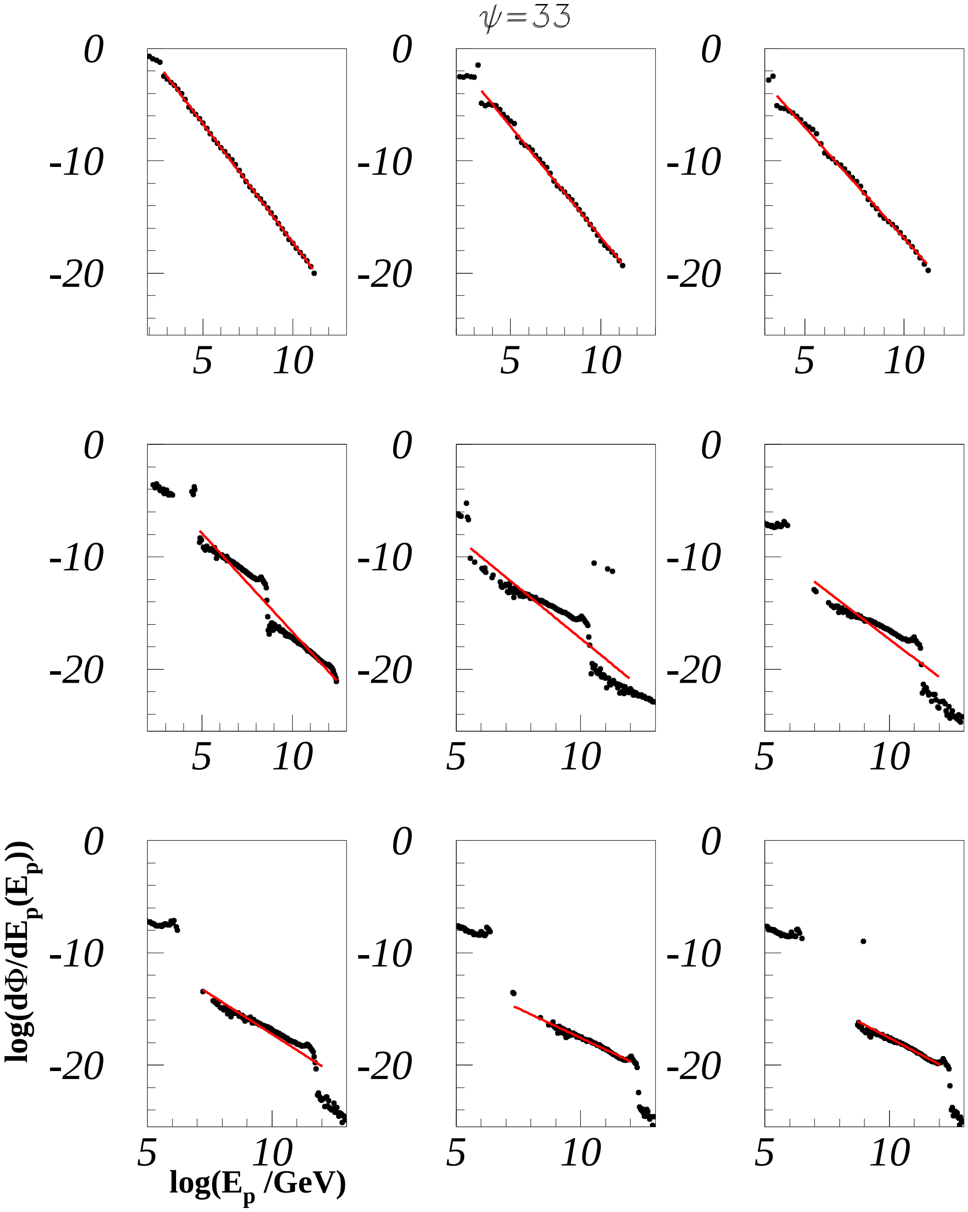

Figure 3.4: Subluminal spectra for $\psi = 33°$ and different Γ, as in Fig. 3.3.

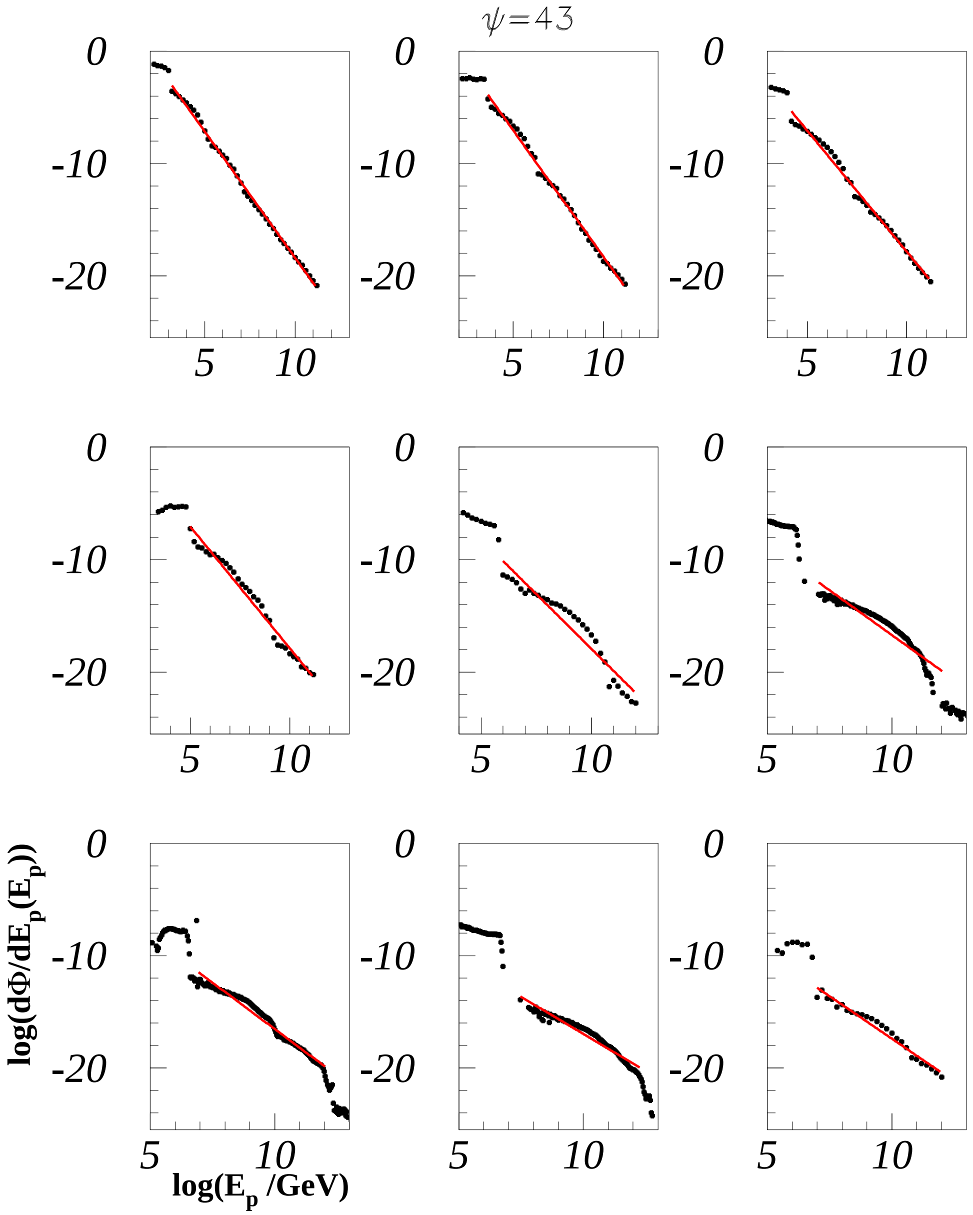

Figure 3.5: Subluminal spectra for $\psi = 43°$ and different Γ, as in Fig. 3.3.

The aim of the single powerlaw approximation of the spectra is to examine the variation of primary spectra with the boost factor. The spectra themselves are difficult to compare, since the structure gets more complex with increasing boost. With a simple approximation, the spectral indices can be compared for varying Γ. Figures 3.6, 3.7 and 3.8 show the spectral index versus the boost factor for the three angles $\psi = 23°, 33°, 43°$. In each case, the spectra get harder with increasing boost factor. The correlation appears to be linear and is best for highly oblique shocks $\psi = 33°$ and $43°$. Linear fits yield

$$\alpha_p(\Gamma, \psi = 33°) = 2.1 - 0.7 \cdot 10^{-3} \cdot \Gamma \tag{3.2}$$

$$\alpha_p(\Gamma, \psi = 33°) = 2.0 - 0.9 \cdot 10^{-3} \cdot \Gamma \tag{3.3}$$

$$\alpha_p(\Gamma, \psi = 43°) = 2.2 - 0.9 \cdot 10^{-3} \cdot \Gamma \tag{3.4}$$

This confirms that the resulting spectrum is relatively independent of the angle ψ. Figures 3.6, 3.7 and 3.8 also indicate, that the results seem to get more stable with higher obliquity. These results deviate from investigations by e.g. Kirk [K$^+$00] and Ostrowski & Bednarz [BO98, OB02], which show a saturation of the hardening of the spectra with the boost factor, $\alpha_p \rightarrow 2.33$ for $\Gamma \rightarrow \infty$. In these calculations, even going up to boost factors of $\Gamma \sim 1000$ does not show any sign of saturation of the spectral index. It has, however, been pointed out by Baring [Bar04] already, that in the calculations of [K$^+$00, BO98, OB02], shock configurations are very specific, assuming parallel shocks with $r = 3$ and pitch angle diffusion. Baring points out that the spectra tend to get flatter with decreasing velocity compression ratio and steeper for higher values of r. The spectra become much flatter with increasing spectral index due to the obliquity of the shock.

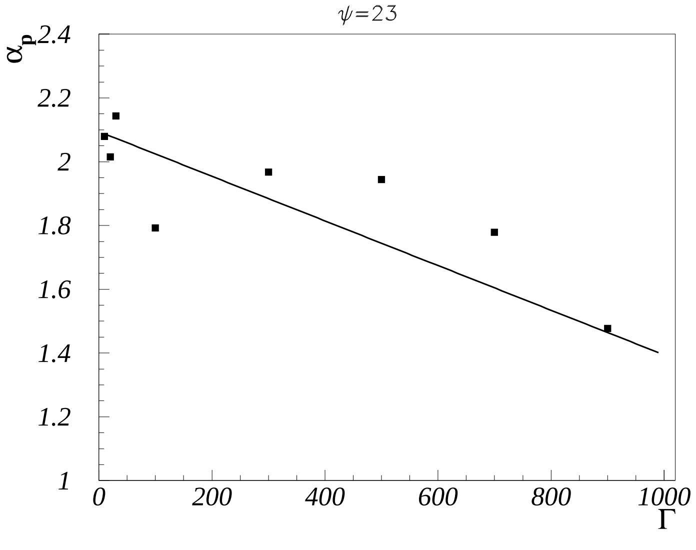

Figure 3.6: Correlation between primary spectral index α_p and boost factor Γ for $\psi = 23°$.

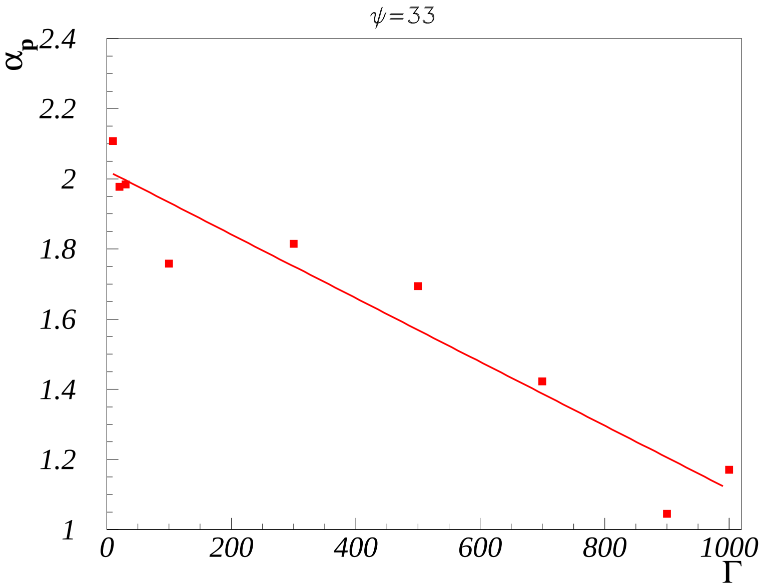

Figure 3.7: Correlation between primary spectral index α_p and boost factor Γ for $\psi = 33°$.

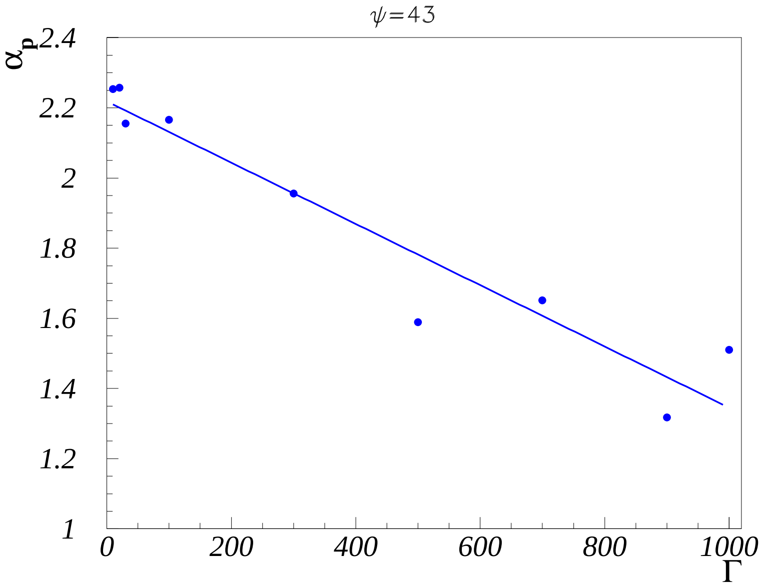

Figure 3.8: Correlation between primary spectral index α_p and boost factor Γ for $\psi = 43°$.

3.4 Subluminal shocks in GRBs

Subluminal, relativistic shocks were shown to accelerate particles up to 10^{21} eV. It is the aim of this section to apply the shock acceleration results from above to astrophysical phenomena. Observational data are used and combined with the phenomenological relations found above.

In particular, the particle spectra are compared to Gamma Ray Burst data in this section. In order to do this, the correlation between the observed photon spectrum and the actual boost factor of the GRB shock is reviewed in Section 3.4.1. One specific burst, namely GRB941017, is examined in Section 3.4.2. This burst is chosen, since it has a temporally resolved energy spectrum, reaching up to photon energies of $E_\gamma >$ MeV. The evolution of the primary spectrum is discussed using the correlation between boost factor and particle spectral index. Furthermore, a sample of GRBs from the BATSE era is examined in Section 3.4.3. Prompt spectra of 568 bursts were fitted with a broken powerlaw in [G$^+$04]. The spectral fits are compared to the particle spectral index. This in turn is compared to the synchrotron model for Gamma Ray Bursts.

3.4.1 Discussion of the boost factor

It has been pointed out by [Wax00, G$^+$04] that the GRB boost factor can be determined by observational data. Given the energy spectrum of the prompt emission from a GRB, the boost factor is determined via the break energy ϵ_γ^b. For a classical GRB of $\epsilon_\gamma^b \geq 0.5$ MeV, the boost factor is assumed to be close to its minimum value which occurs for pair production optical depths close to one, and thus at the maximum observed energy of prompt emission $E_\gamma^{\max}$,

$$\Gamma \sim 250 \cdot \left[L_{\gamma,52} \cdot t_{v,-2} \cdot \left(\frac{E_\gamma^{\max}}{100\ \mathrm{MeV}} \right) \right]^{1/6} . \tag{3.5}$$

Here, $L_{\gamma,52} := L_\gamma/(10^{52}\ \mathrm{erg/s})$ is the GRB luminosity L_γ in units of 10^{52} erg/s and $t_{v,-2} := t_v/(0.01\ \mathrm{s})$ is the GRB's variability time in units of 0.01 s. As a few bursts have been observed by EGRET, the maximum photon energy is chosen as $E_\gamma^{\max} = 100$ MeV. The parameters in Equ. (3.5) are described in more detail in Chapter 5.

Since the approximation of the minimum Lorentz factor can only be used for high break energies, it only applies for $\epsilon_\gamma^b \geq 0.5$ MeV. For bursts with lower break energies, the boost factor is estimated through the break energy directly,

$$\epsilon_\gamma^b = \epsilon_B \cdot \epsilon_e \cdot \frac{L_{\gamma,52}^{1/2}}{\Gamma_{2.5} \cdot t_{v,-2}} , \tag{3.6}$$

with $\Gamma_{2.5} = \Gamma/10^{2.5}$. ϵ_B and ϵ_e are the equipartition fractions of the magnetic and electric field, chosen to be $\epsilon_B = \epsilon_e = 0.1$.

Both equations are simple approximations. The redshift of GRBs can in most cases only be estimated, which translates into uncertainties in the burst luminosity. The variability time is equally difficult to estimate and will be fixed at $t_{v,-2} = 1$. In addition, parameters as the equipartition fractions and the maximum energy of a GRB are not well-determined. This shows that the estimate of the boost factor in this section can only be considered as an estimate. Another difficulty is that the boost factor can be underestimated due to a misaligned jet or due to substructures of the jet. However, since the boost factor is expected to lie between $100 < \Gamma < 1000$ and the results above yield a distribution peaking at $\Gamma \sim 300$, it still seems to be a reasonable approximation.

Beaming and off-axis effects From the observation of jet-breaking in various GRB afterglow observations, it has been confirmed that the particle emission in GRBs happens in jets and not isotropically, see [Pir05b] and references therein. Jet-breaking is observed when the jet opening angle θ exceeds $1/\Gamma$, which is the maximum opening angle for relativistic radiation, which is isotropically emitted in the restframe of the radiation source, see e.g. [RL79]. Relativistic radiation is beamed with at least $1/\Gamma$, and when the jet's opening angle exceeds this limit, a break in the intensity of the afterglow lightcurve is observed. For the calculation of the intrinsic luminosity of a GRB, it is necessary to account for the beaming effect. An isotropically emitting source has a luminosity L_{iso} connected to a fluence F_γ, a distance d_L and a duration t_{90}, of

$$L_{iso} = \frac{4\pi d_L^2}{t_{90}} \cdot (1+z) \cdot F_\gamma \,. \tag{3.7}$$

If the source emits a cone of radiation only, the luminosity is smaller by a factor of $\theta^2/2$,

$$L_{beam} = \frac{2\,\pi \cdot \theta^2 d_L^2}{t_{90}} \cdot (1+z) \cdot F_\gamma \,. \tag{3.8}$$

In all calculations throughout this thesis, is assumed that this jet points directly towards the observer. It should be noted, however, that a slightly misaligned jet can lead to significant changes in the observed spectrum in comparison to a jet directly pointed at the observer. In particular, misalignment can lead to the misinterpretation of of the boost factor. Similar effects have already been investigated in the case of AGN, which have a similar geometry. In addition to effects concerning the boost factor, the photon spectrum as seen by the observer varies with the angle of misalignment. This has been investigated in [DAK07], with the conclusion that it is not possible to reconstruct the aligned emission easily. This effect needs to be studied more extensive experimentally and theoretically in the future in order to have a more precise description of GRB spectra. At this stage, these effects need to be neglected.

3.4.2 Temporal evolution of GRB941017

The combination of BATSE and COMPTEL data for GRB941017 allows the examination of the temporal evolution of the GRB in the energy range of (0.03, 200) MeV. GRB941017 was observed by BATSE for a duration of $t_{90} = 77\,\mathrm{s}$. The total energy fluence as measured by BATSE was $F_\gamma = 1.6 \cdot 10^{-4}\,\mathrm{erg/cm^2}$, among the 20 brightest events ever seen by BATSE. As it has been analyzed in [Gon04], the photon energy spectrum softens with the evolution of the bursts, meaning a shift of the break energy towards lower energies. The break energy and the first photon spectral index of the fits are given in table 3.1. Here, the break energy is used to determine the boost factor of the shock front, applying Equ. (3.6). The evolution of the boost factor with time is shown in Fig. 3.9. As expected, the shock becomes more relativistic with time. At the beginning, the shock moves with $\Gamma = 143$. This is reasonable, since the minimum boost factor needed for the source to become transparent to pair production is $\Gamma \sim 100$. In its final stage, the burst reaches boost factors of $\Gamma \sim 912$ where $\Gamma \sim 1000$ is the maximum expected value. It should be noted, however, that for the last time bin, the peak energy and the first photon spectral index are fixed. For the fit procedure, only β and the normalization of the spectrum were determined. Therefore, the last value may be biased due to the lack of experimental observation.

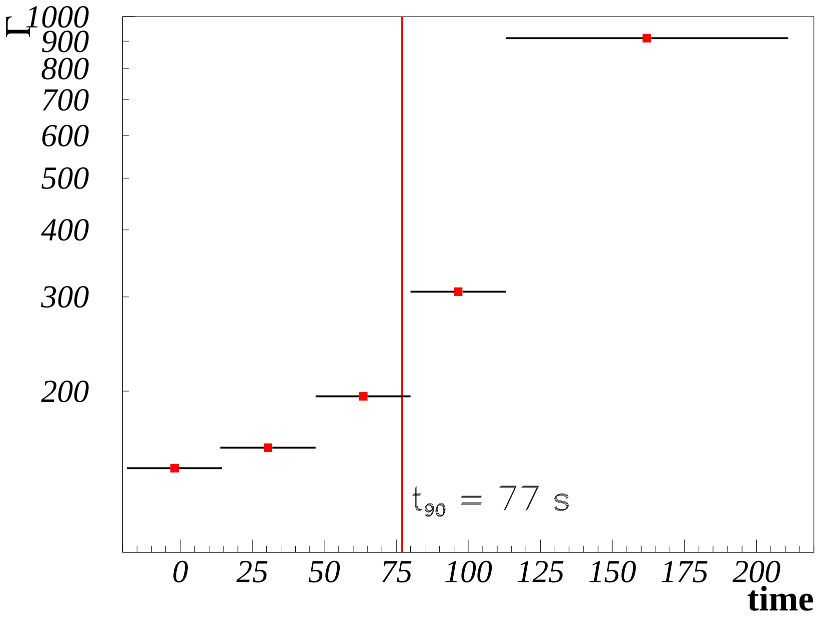

Figure 3.9: Evolution of the boost factor Γ with time for GRB941017.

The relation between the boost factor Γ and the spectral index of the primaries α_p is applied now as developed in Section 3.3. Equation (3.4) can be used for the parameterization of highest obliquity, $\psi = 43°$. Since the deviations between the three equations are marginally small, similar results are expected for other angles. The evolution of the primary spectral index with time is shown in Fig. 3.10. The primary spectrum becomes harder with increasing boost factor and therefore also with time. Thus, as the synchrotron spectrum (${E_\gamma}^{\alpha_\gamma}$) softens, the primary spectrum hardens. This is expected due to the inverse correlation of E_γ and E_p, $E_\gamma \cdot E_p = \mathrm{const}$ (see Section 1.2.2). Table 3.1 summarizes the results for Γ and α_p as they are calculated in this section.

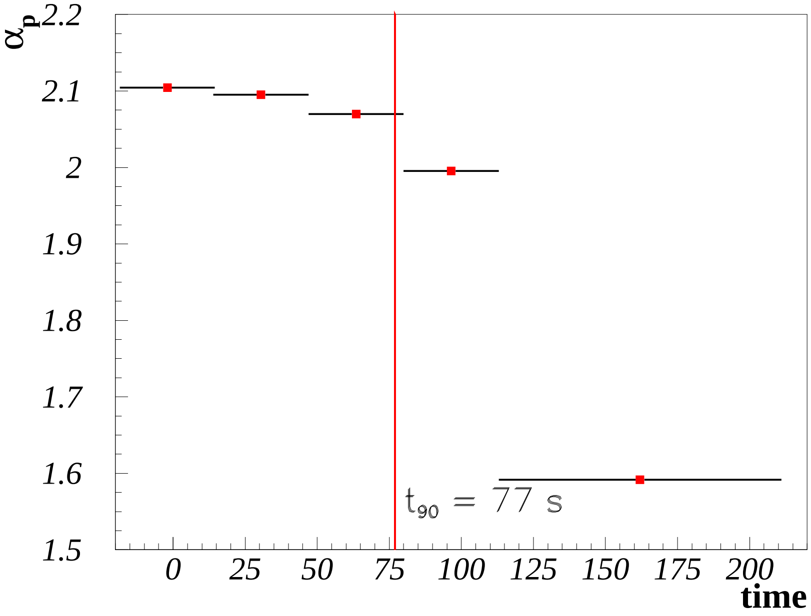

Figure 3.10: Evolution of the primary spectral index α_p with time.

time interval	ϵ_γ^b [MeV]	α_γ	Γ	α_p
−18 to 14	0.697	−0.84	144	2.104
14 to 47	0.585	−0.79	157	2.095
47 to 80	0.377	−1.08	195	2.070
80 to 113	0.377	−1.45	307	1.995
113 to 211	0.017 (E_{peak} fixed)	−1 (fixed)	912	1.592

Table 3.1: Summary of the fit values ϵ_γ^b and α_γ for GRB941017. The boost factor of the shock Γ and the primary spectral index α_p have been determined according to the description in the text.

3.4.3 BATSE variability sample

In order to investigate the primary spectral behavior of GRBs, a large sample of GRBs needs to be considered. It is essential in this case to know the break energy of the photon spectrum for each burst, since this allows for the determination of the primary spectral index. Therefore, the variability sample of BATSE bursts is used here as it is described in Chapter 2. This sample is well-suited, since the fits are given for a broken powerlaw. The SWIFT and KONUS samples only provide single powerlaw fits. The lag sample is smaller than the variability sample. The variability sample is thus considered here, since it offers the best properties of all samples available. The boost factor has been determined in [G$^+$04], using Equations (3.5) and (3.6), depending on the value of the break energy as described in Section 3.4.1. The primary spectral index is then determined using Equ. (3.4). The distribution of primary indices is shown in Fig. 3.11. No values above $\alpha_p = 2.2$ are present, since the linear correlation fitted in Section 3.3, gives $\Gamma \leq 0$ for $\alpha_p \geq 2.2$, which is unphysical. This is also the reason why the mean value ($\overline{\alpha}_p = 1.89 \pm 0.28$) is shifted towards lower energies as compared to the peak of the distribution. The given error is the root mean square of the distribution. The mean value is close to what is typically expected from first order Fermi acceleration, in sub-relativistic shocks with an adiabatic index of $\gamma_g = 5/3$, i.e. $\alpha_p = 2$. Some primary spectra seem to be extremely flat ($\alpha_p < 0$), but most bursts concentrate in a small interval of $1.5 < \alpha_p < 2.2$. These values are reasonable to expect for particle spectra from highly-relativistic shocks.

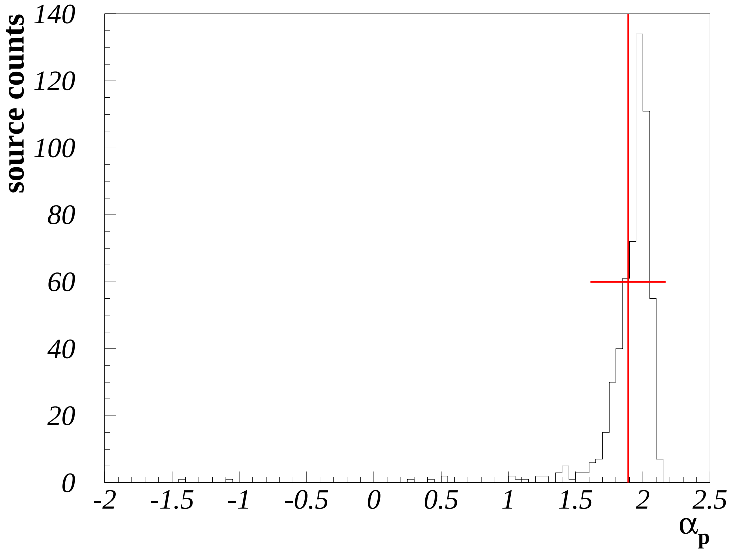

Figure 3.11: Distribution of primary spectral indices α_p.

The first spectral index in the observed photon spectrum is believed to arise from synchrotron radiation of primary electrons, see e.g. [Pir05a]. The correlation between synchrotron emission and the primary population is discussed in Section 1.1.3. According to the theory, the correlation between the spectral indices should be $\alpha_p = 2 \cdot s + 1$ with $\alpha_\gamma = -s - 1$. Figure 3.12 shows a scatter plot of the two spectral indices α_p and α_γ for the 568 bursts. The solid line represents the theoretical estimate. The dashed line is referred to as the *line of death* [P⁺98]. Above these values, the synchrotron emission model fails, since the total photon spectrum cannot be flatter than the synchrotron spectrum of a single electron, $\alpha_{\max} = -2/3$. It has been pointed out in [P⁺98] that some bursts exceed the line of death and therefore, a pure synchrotron model cannot explain the whole spectrum of GRBs. These results show deviations from the theoretical predictions as well. Most likely, these arise from absorption and scattering effects of synchrotron photons. Also, the primary electron spectrum could deviate from the energy distribution of protons. These effects need to be considered when correlating the two indices. A more detailed examination of this matter is planned in the future, but is not examined within the scope of this thesis.

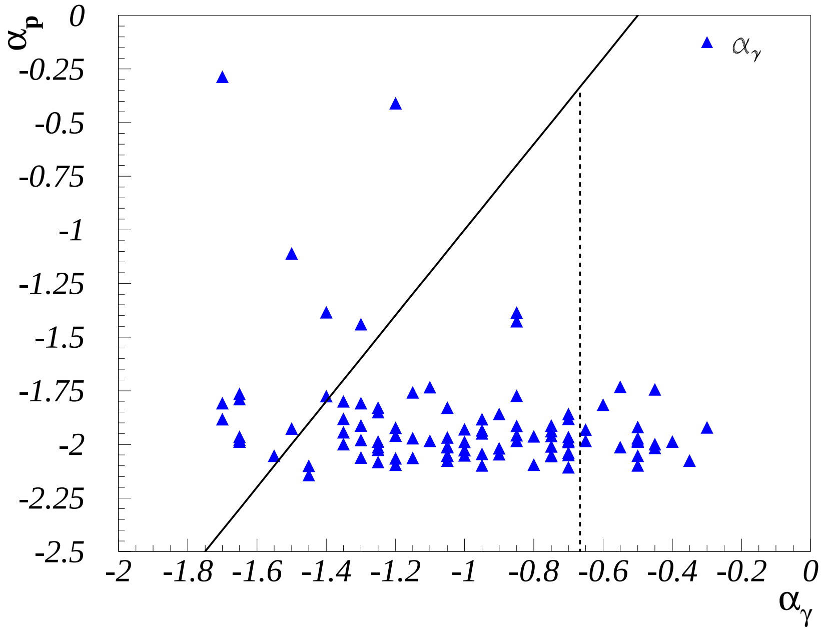

Figure 3.12: Correlation between proton and photon index for 568 GRBs from the BATSE sample. The proton index is derived using the phenomenological correlation between Γ and α_p.

3.5 Diffuse particle spectra from GRBs and AGN

In the previous section, energy spectra of sources with different boost factors have been presented. These source spectra can be translated into an expected diffuse signal from certain astrophysical sources by folding the spectrum with the spatial distribution of the sources. In this ansatz, Active Galactic Nuclei (AGN) and Gamma Ray Bursts (GRBs) are used as potential sources, since these are the sources with the highest observed boost factors.

3.5.1 From shock acceleration spectra to a diffuse spectrum

The diffuse spectrum as measured at Earth depends on several factors:

- *Single source spectra at the source* $d\Phi/dE_p$: these are the spectra for different Γ as calculated in Section 3.3. Here, the redshift evolution of the energy needs to be considered as $E_p(z) = E_p \cdot (1+z)$. Here, $E_p(z)$ is the energy as observed at a source at redshift z. E_p is the corresponding energy observed at Earth.

- *Fraction of AGN to GRBs*: To which amount do GRBs and AGN contribute to the total spectrum? - It is assumed that the total amount of the observed CR spectrum above the ankle comes from no other sources but AGN and GRBs. The fraction of the contribution from AGN and GRBs is $0 < x < 1$. It is assumed that all AGN have shocks with $\Gamma = 10$, so that the single source spectrum of all AGN is

  $$\frac{d\Phi_{AGN}}{dE_p} := d\Phi/dE_p(\Gamma = 10)\,. \tag{3.9}$$

  In the case of GRBs, boost factor variations between $100 < \Gamma < 1000$ are possible with a mean value of $\Gamma \sim 300$. Therefore, a step-function is applied, where it is assumed that 10% of the sources have $\Gamma = 100$, further 10% exist with $\Gamma = 1000$ and the majority of 80% have $\Gamma = 300$:

  $$\frac{d\Phi_{GRB}}{dE_p} := 0.1 \cdot \frac{d\Phi}{dE_p}(\Gamma = 100) + 0.8 \cdot \frac{d\Phi}{dE_p}(\Gamma = 300) + 0.1 \cdot \frac{d\Phi}{dE_p}(\Gamma = 1000)\,. \tag{3.10}$$

- *Source evolution* $g(z)$: It is assumed that both AGN and GRBs follow the Star Formation Rate (SFR) concerning the number density evolution with comoving volume, see for example [HMS05] in the case of AGN and [P$^+$00] in the case of GRBs. A large sample of radio quiet AGN selected at X-ray wavelengths was investigated in [HMS05]. The comoving density $dn/dV(z)$ is given as

  $$\frac{dn}{dV}(z) \propto \begin{cases} (1+z)^m & \text{for } z < z_1 \\ (1+z_1)^m & \text{for } z_1 < z < z_2 \\ (1+z_1)^m \cdot 10^{k\cdot(z-z_2)} & \text{for } z > z_2 \end{cases} \tag{3.11}$$

with the parameters $m = 5.0$, $z_1 = 1.7$, $z_2 = 2.7$ and $k = -0.43$. The total redshift evolution $g(z)$ further includes the comoving volume dV/dz and a factor $1/(4\,\pi\,d_L^2)$ to account for the decrease of the flux L with the distance d_L,

$$g(z) = \frac{dn}{dV}(z) \cdot \frac{dV}{dz} \cdot (4\,\pi\,d_L^2)^{-1}\,. \tag{3.12}$$

For simplicity, this model is used for both AGN and GRBs. Although deviations in the SFR scenarios of AGN and GRBs are expected, the approximation that both follow the distribution of radio quiet X-ray AGN is reasonable: the deviations are expected to be negligible with respect to general uncertainties arising from assumptions about the acceleration region.

- *Absorption of protons at the highest energies*: protons at $E_p > 5 \cdot 10^{19}$ eV are absorbed due interactions with the cosmic microwave background as it is described in Section 1.1. Therefore, the diffuse spectrum as it results from the propagation of the single source spectra is modified by a further factor $\exp[-E_p/(5 \cdot 10^{19}\text{ eV})]$ to account for the effect.
- *The normalization of the diffuse spectrum*: since the calculated particle spectra are given in arbitrary units, the normalization of the overall spectrum as measured at Earth is done using observational facts.
  - In the case of superluminal sources, the normalization of the expected signal is done using the most restrictive upper limit on the neutrino signal from extraterrestrial sources given by the AMANDA experiment (see [H$^+$06a]),

    $$E_\nu^2\,\frac{dN_\nu}{dE_\nu} < 8.8 \cdot 10^{-8}\frac{\text{GeV}}{\text{s sr cm}^2}\,.$$

    With an E^{-2} spectrum for both neutrinos and protons, the spectra are connected by assuming that the expected neutrino energy fluence is a fraction q of the proton spectrum,

    $$\int \frac{dN_\nu}{dE_\nu}\,E_\nu\,dE_\nu = q \cdot \int \frac{dN_p}{dE_p}\,E_p\,dE_p$$

    with $q = 1/40$, since only 20% of the proton flux goes into pion production via the Delta resonance, 1/2 of the remaining flux goes into the charged pion component of which 1/4 goes into neutrinos.
  - In the case of subluminal sources, using neutrino flux limits leads to a major violation of the observed spectrum of charged Cosmic Rays. In this case, the measured part above the 'ankle' of the CR spectrum is used for an estimate of the contribution from subluminal sources. The Cosmic Ray energy flux above the knee is given as [WB97, WB99]

    $$j_E(E_{\min} = 3 \cdot 10^{18}\text{ eV}) := \int_{3\cdot 10^{18}\text{eV}} \frac{dN_p}{dE_p}\,E_p\,dE_p \tag{3.13}$$

    $$\approx 10^{-7}\,\text{GeV cm}^{-2}\,\text{s}^{-1}\,\text{sr}^{-1}\,. \tag{3.14}$$

> It is expected that this contribution comes from a combined signal from AGN and GRBs with a fraction of $0 < x < 1$.

Thus, the total spectrum as observed at Earth is given as

$$\frac{dN_p}{dE_p} = A_p \int_{z_{\min}}^{z_{\max}} \left(x \cdot \frac{d\Phi_{AGN}}{dE_p}(E_p(z)) + (1-x) \cdot \frac{d\Phi_{GRB}}{dE_p}(E_p(z)) \right) \cdot g(z)\, dz \,. \qquad (3.15)$$

The minimum redshift is set to $z = 0.03$ to exclude the supergalactic plane, building on the assumption that many distant sources make up the spectrum rather than a few nearby ones. The maximum redshift is taken to be $z_{\max} = 7$.

3.5.2 The resulting diffuse spectrum

The diffuse spectrum as measured at Earth is shown in Fig. 3.13. Data points represent measurements from a selection of experiments, giving the Cosmic Ray spectrum with the features described in Section 1.1. The calculated spectra for super- and subluminal shocks are displayed as the dashed resp. the solid lines.

In the superluminal case, the only possible contribution to the Cosmic Ray spectrum is around the knee of the measured Cosmic Ray spectrum. It is expected, however, that the effective flux is actually even lower, since the normalization is based upon the assumption that the contribution cannot be more than the current neutrino flux limits omit. In this case, the fraction of AGN protons to GRB protons has been chosen to be $x = 0.5$, assuming that 50% of the signal is produced by AGN and 50% comes from GRBs.

The subluminal case has been investigated for different scenarios. The upper (blue) line represents a spectrum which would be produced by AGN only ($x = 1$). The middle line assumes that 50% are made up by AGN and the remaining 50% come from GRBs. The lower line represents a pure GRB spectrum ($x = 0$). The flux is too low to explain the observed component above the ankle if a significant contribution comes from GRBs. The flatness of the GRB spectra causes this. The flat spectra have too high contributions at the highest energies and do not fit observations. Thus, within this framework, AGN are the favored sources for the production of UHECRs.

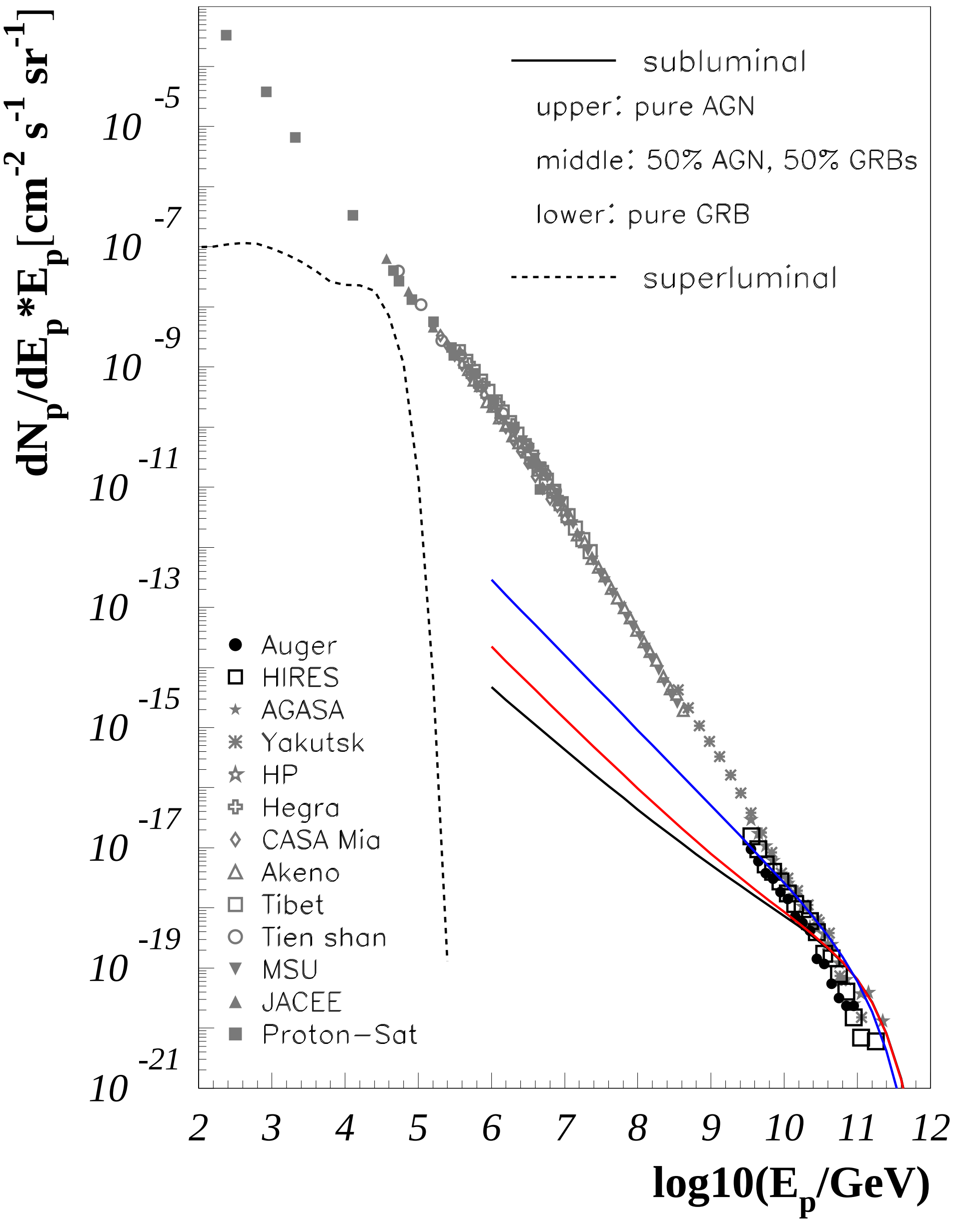

Figure 3.13: The maximum predicted diffuse flux from GRBs and AGN with superluminal shock fronts (dashed line) and subluminal shocks (solid lines). For subluminal sources, the upper line is a pure AGN-produced spectrum ($\Gamma = 10$), the lower line represents a pure GRB spectrum (10% of the sources with $\Gamma = 100$ and $\Gamma = 1000$, the remaining 80% with $\Gamma = 300$. The flux is compared to the measured Cosmic Ray Spectrum [Sta06]. In the case of superluminal sources, 50% is assumed to come from each GRBs and AGN.

3.6 Summary & conclusions

In this Chapter, relativistic, super- and subluminal shocks have been discussed as they may occur in extragalactic accelerators like AGN and GRBs. While superluminal shocks are only efficient up to $E_p \sim 10^5$ GeV, subluminal shocks are able to accelerate particles up to $E_p \sim 10^{21}$ eV, as discussed in Section 3.1).

In Section 3.3, the spectral behavior of the particle spectra are discussed. Superluminal particle spectra show spectral indices around $\alpha_p \sim 2$. In the case of subluminal sources, a correlation between the spectral index and the boost factor Γ of the shock is found. The spectra flatten with increasing Γ as

$$\alpha_p = 2.2 - 0.9 \cdot 10^{-3} \cdot \Gamma \,. \tag{3.16}$$

This implies that GRB particle spectra, arising from relativistic shocks with boost factors between $100 < \Gamma < 1000$ have spectral indices around $\alpha_p \sim 1.5$. The results have been compared to observed, prompt GRB spectra. These can be interpreted as synchrotron spectra from shock accelerated electrons. The spectral index of the primaries is therefore correlated to the synchrotron radiation spectral index s as $\alpha_p = 2 \cdot s + 1$ as discussed in Section 1.1.

This model is applied in Section 3.4 to two examples. The temporal behavior of GRB941017 is examined in Section 3.4.2. Observations reveal the hardening of the spectrum with time, the break energy in GRB spectra is shifted towards lower energies. This in turn implies the growth of the boost factor Γ and a hardening of the spectrum, as described in Section 3.4.1. As a second example, a large GRB sample from the BATSE catalog is investigated. Broken powerlaw fits for prompt GRB spectra of 568 bursts are given in [G$^+$04]. The break energies are used to calculate the boost factor Γ which can in turn be used to calculate the primary spectral indices. The correlation as expected from synchrotron theory between primary and synchrotron spectral index cannot be verified. This underlines the hypothesis that the observed spectrum is not necessarily a pure synchrotron spectrum, but modified by absorption and scattering.

In Section 3.5, a possible contribution of AGN and GRBs to the UHECR flux is discussed. For superluminal sources, such a contribution can be excluded, using current neutrino flux limits to normalize the spectrum to the highest possible contribution. In the case of subluminal sources, the spectrum is normalized to the Cosmic Ray flux above the ankle, $E_{\min} = 5 \cdot 10^9$ GeV. Using only AGN ($\Gamma = 10$), the spectrum fits the data quite well. With a significant contribution from GRBs ($100 < \Gamma < 1000$), however, the total spectrum becomes too flat and cannot explain the lower part of the spectrum around $E_p \sim 5 \cdot 10^9$ GeV anymore.

The results from above show that particle spectra can become very flat. Spectra up to $\alpha_p = 1.5$ are possible. In future investigations, observed GRB spectra will be examined in more detail in order to explain the apparent deviations from the synchrotron index-primary index correlation.

CHAPTER 4

Permanent ν sources: predictions & detection rates

The most luminous, permanent objects in the sky are Active Galactic Nuclei. Neutrino flux models from different AGN sub-classes have been derived as discussed in Chapter 1. For each sub-class, mean source properties were assumed to derive the contribution to the diffuse neutrino flux from the examined source class. In the first section of this chapter, Section 4.1, the neutrino flux from FR-II galaxies is investigated in more detail with respect to variations of the single source spectra. In Section 4.2, the different neutrino flux models are used to estimate event rates in next generation neutrino detectors. Here, both AGN neutrino models and GZK neutrino fluxes are examined. Event rates expected in IceCube are compared to acoustic and radio detection arrays.

4.1 Neutrinos from FR-II galaxies and FSRQs

The total diffuse neutrino spectrum from a certain source class at Earth is given by the single source spectrum $d\Phi_\nu/dE_\nu$ convoluted with the redshift and luminosity dependent source number. A factor $1/(4\pi\, d_L^2)$ is applied to account for the decrease of the source flux with the luminosity distance d_L. The number of sources is given by the product of the Radio Luminosity Function (RLF) of AGN, $dn/dL/dV$, and the comoving volume dV/dz. Thus, the total diffuse neutrino flux dN_ν/dE_ν can be written as

$$\frac{dN_\nu}{dE_\nu}(E_\nu^0) = \int_z \int_L dz\, dL\, \frac{d\Phi_\nu}{dE_\nu}(E_\nu^0, L, z) \cdot \frac{dn}{dL\, dV}(L, z) \cdot \frac{dV}{dz} \cdot \frac{1}{4\pi\, d_L(z)^2}\,. \qquad (4.1)$$

A shift of the neutrino energy at the source E_ν to lower energies at the detection site due to the expanding Universe, $E_\nu^0 = E_\nu/(1+z)$, is taken into account. A simple cosmology of $\Omega_m = 1$ and $\Omega_\Lambda = 0$ will be used, since the spatial distributions of the source samples are given according to this cosmology. The changes in the normalization of the result when using the experimentally confirmed model of $\Omega_m \sim 0.3$ and $\Omega_\Lambda \sim 0.7$ [S+07] should be negligible, as pointed out in [DP90].

4.1.1 Normalization of single source spectra

The diffuse neutrino flux from FR-II galaxies using average parameters has been presented in [BBR05]. For the derivation of a source spectrum, it is assumed that the neutrino spectrum follows the proton spectrum in first order approximation. Effects from multi-pion production are neglected. The changes to the spectrum due to this effect would be negligible with respect to other remaining uncertainties in the calculation, such as the lack of knowledge of the sources' optical depth. For the normalization of the spectrum, it is assumed that the neutrino output of a single AGN is proportional to the total power of the jet, which is given by the disk luminosity L_{disk},

$$\int \frac{d\Phi_\nu}{dE_\nu} E_\nu \, dE_\nu = x_{\nu/disk} \cdot L_{disk} \,, \tag{4.2}$$

with $x_{\nu/disk} = 1/60$ as described in [BBR05]. The disk luminosity is linked to the radio output L_{radio} via the *jet-disk symbiosis* approach which has been developed in [FB95, FMB95, Fal96]. In the case of FR-II galaxies, the correlation between disk and radio luminosity is

$$L_{disk} = 4.29 \cdot 10^{17} \cdot (1+z)^{-1/2} \left(\frac{L_{radio}}{\text{erg/s}}\right)^{2/3} \text{ erg/s} \,. \tag{4.3}$$

4.1.2 AGN samples

Two different source samples of AGN sub-classes are taken into account for the calculation of the diffuse neutrino flux. The source samples are described in more detail in Section 2.1.1.

- The first one consists of 356 steep spectrum sources selected by Willott et al. [W+01]. For this source type, two models are presented:
    1. The spectral index of the proton spectrum and thus of the neutrino flux, α_p ($d\Phi_\nu/dE_\nu \propto {E_\nu}^{-\alpha_p}$), can be expressed through the synchrotron spectral index s, as described in Section 1.1.3, $\alpha_p = 2 \cdot s + 1$ with the measured radio flux $S \propto \nu^{-s}$. This approach will be referred to as *model 1* in the following.
    2. In *model 2*, $\alpha_p = 2$ will be assumed following the derivation of particle spectra from diffuse shock acceleration.

- The second sample contains 171 flat spectrum sources as is presented by Dunlop & Peacock [DP90]. In this case, the observed photon spectrum is an overlap of all emitted synchrotron radiation in the AGN jets, since these sources point their jets directly towards Earth. In this case, model 1 cannot be applied and calculations will be presented for $\alpha_p = 2$ according to the model of shock acceleration. The spatial distribution functions of the two source types are given in [W$^+$01] and [DP90] respectively.

4.1.3 Average diffuse spectra

A prediction of a diffuse neutrino flux can be made by using the radio luminosity functions as they have been developed for the two source samples (see [DP90] for flat spectrum sources and [W$^+$01] for steep spectrum sources). In the case of an average spectrum, the spectral index is assumed to be the same for each source in a sample. Model 1 uses $\alpha_p = 2.6$ for steep spectrum sources which is based on a mean synchrotron spectral index of $\overline{s} = 0.8$. Model 2 uses $\alpha_p = 2$ for both samples as predicted by diffuse shock acceleration. The resulting diffuse flux is shown in Fig. 4.1 (left panel: model 1, right panel: model 2). Using model 1, it can be seen that the flux is very low, but that the ${E_\nu}^{-2}$ spectrum in model 2 even exceeds the most recent limit of AMANDA. The implications will be discussed in Chapter 6.

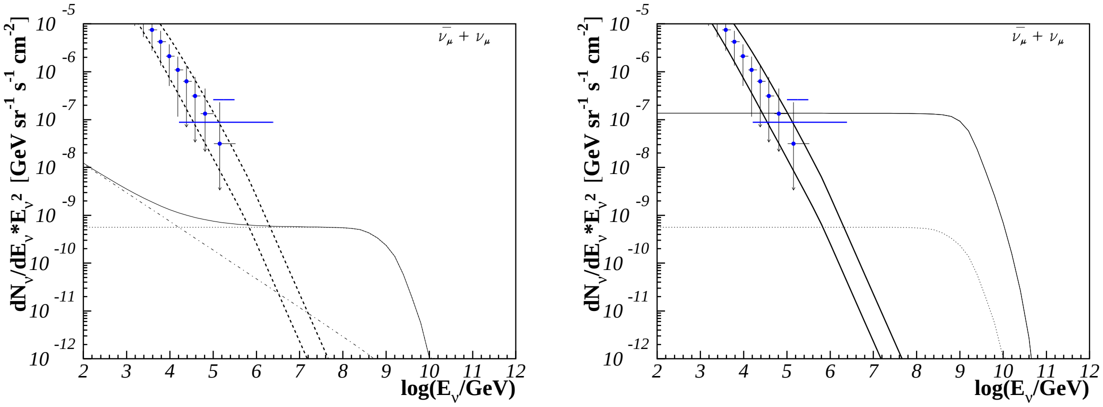

Figure 4.1: AGN $\nu_\mu + \overline{\nu}_\mu$ neutrino spectrum. *Left panel:* $\alpha_p = 2.6$ for steep spectrum sources and $\alpha_p = 2.0$ for flat spectrum sources (model 1). The steep spectrum sources (dotted line) make up most of the spectrum at lower energies ($E_\nu < 10^5$ GeV). The flat spectrum sources (dot-dashed line) dominate the total spectrum (solid line) at energies of $E_\nu < 10^5$ GeV. A signal that exceeds the atmospheric contribution is expected starting at $E_\nu > 10^7$ GeV. *Right panel:* $\alpha_p = 2$ (model 2). The flat spectrum sources (dot-dashed line) do not contribute significantly compared to the steep spectrum population - the solid line represents the sum of flat and steep spectrum sources which does not differ from the result for steep spectrum sources. The data points result from unfolding the AMANDA-II neutrino spectrum. They follow the conventional atmospheric neutrino spectrum (dashed lines) and an upper limit is derived as is indicated in the figure, see [M$^+$05d] for details.

4.1.4 Single source parameters for diffuse predictions

A more precise way of determining the total flux of a specific source sample is to use specific source parameters to determine the single source spectra and calculate the coincident flux for these sources. A sub-sample of 114 FR-II sources from the steep spectrum sample [W$^+$01] has been used to analyze the differences between an average prediction and a source property based estimate. Of the 356 sources, 114 have given spectral indices, redshifts and radio fluxes. This allows for the determination of individual spectra within model 1. The radio flux S is converted into the radio luminosity as

$$L_{radio} = 4\,\pi\,d_l^2 \cdot S \tag{4.4}$$

and the spectral radio index s is used to determine the proton spectral index for each case individually, $\alpha_p = 1 \cdot s + 1$. The neutrino flux normalization A_ν for each individual source at Earth is then given by dividing the result by $4\,\pi\,d_l^2$,

$$A_\nu = x \cdot L_{disk}/(4\pi\,d_l^2)\,. \tag{4.5}$$

The single source normalization versus the primary spectral index is shown in Fig. 4.2. The normalization is given at $E_\nu = 1$ GeV. There is a strong correlation showing that flat neutrino spectra are stronger than steep ones. The total diffuse spectrum of the 114 sources is then calculated by summing up the single source spectra,

$$\left.\frac{dN_\nu}{dE_\nu}\right|_{114} = \sum_i A_\nu^i \cdot {E_\nu}^{\alpha_p^i} \tag{4.6}$$

with $i = 1, 2, \ldots, 114$. The sample of 114 sources is small compared to the total number of FR-II galaxies which is $N_{FR-II} \sim 10^5$ using the RLF of Willott. Thus, an estimate of the maximum total diffuse flux from FR-II galaxies is given by dividing the result from Equ. (4.6) by the number of sources in the used sample, 114, and then multiplying by the total number of sources,

$$\frac{dN_\nu}{dE_\nu} = 10^3 \cdot \sum_i A_\nu^i \cdot {E_\nu}^{\alpha_p^i}\,. \tag{4.7}$$

Figure 4.3 shows the resulting spectrum when using the radio fluxes S, the spectral indices s and the redshifts z as given in the S1-S5 catalogs [P$^+$72, PK72, P$^+$78, K$^+$81]. It can clearly be seen that the coincidence spectrum is much flatter than the average prediction,

$$dN_\nu/dE_\nu \propto E_\nu^{-2.2}\,. \tag{4.8}$$

Using the mean spectral index $\overline{s} = 0.8$ results in a much steeper spectrum due to the correlation between the normalization A_ν and the spectral index α_p.

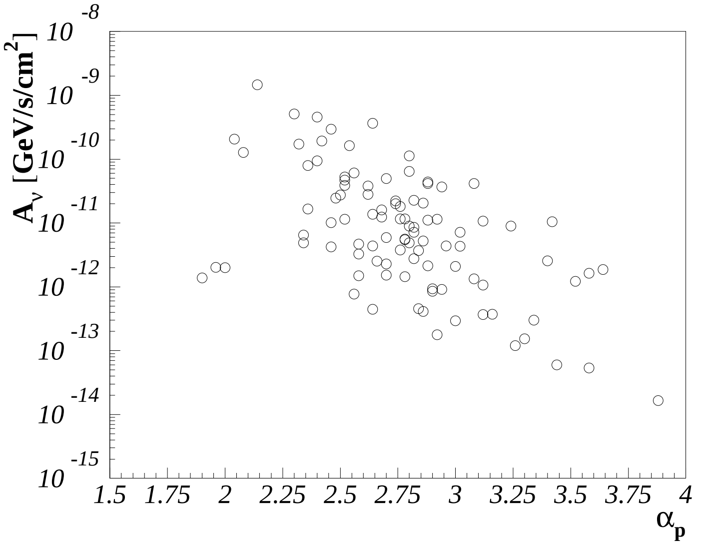

Figure 4.2: Correlation between the neutrino flux normalization and the particle spectral index α_p. While the majority of sources is concentrated around $A_\nu \sim 10^{-11}$ GeV/s/cm^2 and $\alpha_p \sim 2.6$, a strong correlation between A_ν and α_p is visible - bright sources are typically flatter.

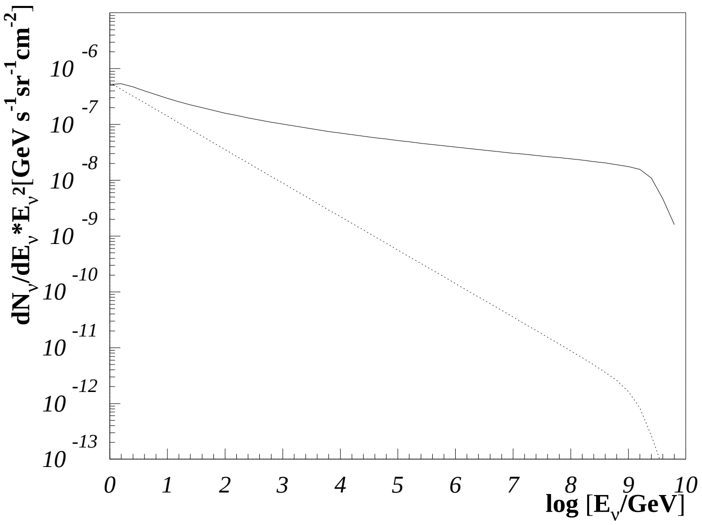

Figure 4.3: Total flux of steep spectrum sources, the coincidence spectrum of 114 sources (solid line). It can clearly be seen that the behavior of the spectral index differs significantly from the average prediction.

4.1.5 Summary & conclusions

Figure 4.4 shows the neutrino spectra derived in this chapter in the context of the measured diffuse spectrum and other predictions. The prediction in model 1, labeled BBR-I, is very low, since the average FR-II galaxy shows a steep neutrino spectrum, $dN_\nu/dE_\nu \propto {E_\nu}^{-2.6}$. In model 2 (BBR-II, line (3)), FR-II galaxies dominate the spectrum with a spectral behavior of $dN_\nu/dE_\nu \propto {E_\nu}^{-2}$. Modeling the spectra individually for those sources with given properties S, z and s shows that the average spectrum in the BBR-I configuration results in a much too steep spectrum. In reality, the spectral shape comes close to $dN_\nu/dE_\nu \propto {E_\nu}^{-2.2}$. The reason is that there is a correlation between the single source normalization and the steepness of the spectrum. The flatter the spectrum, the more luminous the sources.

In this section, it could be shown that individual sources can alter the expected diffuse neutrino spectrum significantly. Using average values can in some cases lead to the misinterpretation of the results. The difficulty with the method of normalizing single source spectra rather than using average values is threefold:

1. typically, only a fraction of all detected sources are provided with measured spectral indices,
2. not all sources are detected and the total number can only be estimated,
3. the correlation between the radio spectral index and the proton index does not necessarily hold. Electron spectra can deviate from proton spectra, and in some cases, the observed radio spectrum may be altered by other effects than synchrotron emission.

The single source properties of Gamma Ray Bursts will be investigated in Chapter 5. It will be shown that there are similar effects which can influence the diffuse neutrino flux from those transient sources.

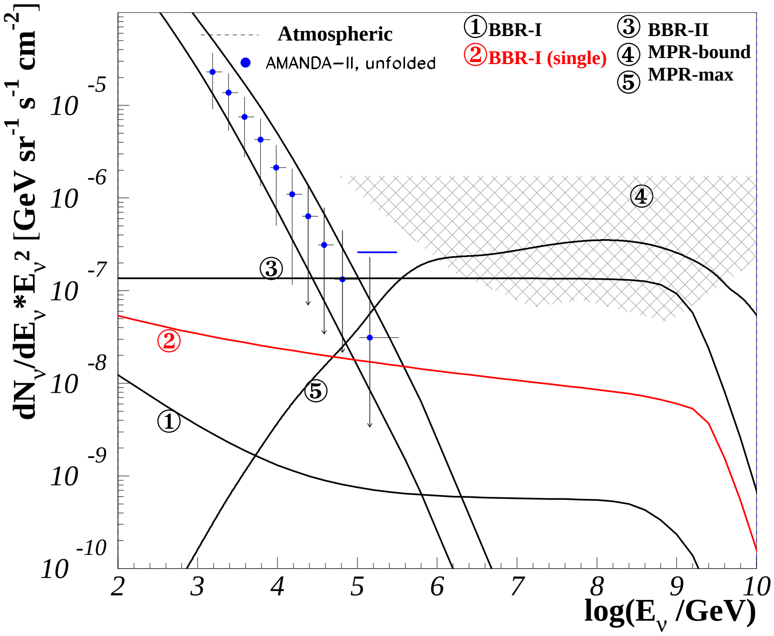

Figure 4.4: Combined figure of various UHE neutrino flux predictions. Data are taken from AMANDA-II, see [M$^+$05d], dashed lines represent the atmospheric prediction from [Vol80]. Lines (1), (2) and (3) are the predictions presented here: (1) applies the connection of the synchrotron radiation index for steep spectrum sources for the average FR-II source, $\alpha_p = 2.6$ (BBR-I). In (2), the normalization and spectral index is determined for each source individually (BBR-I (single)). Model (3) uses a spectral index of $\alpha_p = 2$ following diffuse shock acceleration for both source types (BBR-II). The shaded area (labeled (4)) is the corresponding upper bound, given sources with high optical depth for neutron-photon interactions ($\tau_{n\gamma} \gg 1$ upper straight line) and low optical depth ($\tau_{n\gamma} \ll 1$ lower part of shaded area). Model 5 is the maximum prediction of the diffuse neutrino flux from blazars given (MPR-max).

4.2 Event rates in next generation detectors

Current neutrino experiments are able to measure the atmospheric neutrino spectrum up to 100 TeV without observing a significant contribution from extragalactic sources [M$^+$05d]. Successor experiments like IceCube aim at the detection of neutrinos from 100 TeV up to 100 PeV. The detection of a signal at even higher energies is restrictedly also possible with IceCube, but to achieve a good detection possibility of the cosmogenic neutrino flux, new methods are being developed which are complementary to optical detection. Acoustic and radio neutrino detection aims at the measurement of neutrinos at Extremely High Energies (EHE), i.e. $E > 10^7$ GeV. In this section, different neutrino flux models will be discussed with respect to their detection probability for the three detection methods.

Figure 4.5 shows neutrino flux predictions with a relatively high contribution at EHEs. The models discussed are listed below:

1. Mannheim, Protheroe and Rachen (MPR) [MPR01] predict a maximum flux from blazar sources for proton-photon interactions. This model is reviewed in Section 1.3.2.

2. The model discussed in the previous section will be used in its most optimistic representation, BBR-II, where an ${E_\nu}^{-2}$ spectrum is assumed.

3. Yoshida & Teshima (YT) [YT93] calculate the neutrino flux resulting from CR interactions with the cosmic microwave background as discussed in Section 1.3.5. The spectrum is normalized to the CR spectrum, based on the GZK prediction. The source distribution ρ is assumed to be

   $$\rho \propto (1+z)^m \cdot \Theta(z_{\max} - z) + (1+z_{\max})^m \cdot \Theta(z - z_{\max}) \,. \tag{4.9}$$

   The shaded region in Fig. 4.5 represents the uncertainties in the model due to the evolution function, using $(m,\, z_{\max}) = (4,\, 5)$ as an upper limit and $(m,\, z_{\max}) = (2,\, 2)$ as a lower one. In the following, this model will be referred to YT$(m,\, z_{\max})$: YT(2, 2), YT(4, 4) and YT(4, 5). The evolution model should match the measured distribution of AGN in space, since AGN follow the star formation rate and are believed to be responsible for a significant fraction of the EHE proton flux. Comparing the models with the AGN distribution function given in [MHS00] shows that model $(m,\, z_{\max}) = (4,\, 4)$ seems to fit the data most effectively of all given scenarios, and thus it will be used as the standard GZK prediction with errors given according to the maximum prediction with $(m,\, z_{\max}) = (4,\, 5)$ and the minimum expectation of $(m,\, z_{\max}) = (2,\, 2)$. Note that $(m,\, z_{\max}) = (2,\, 2)$ is a very pessimistic evolution scenario which is far from the observed evolution, even at relatively low redshifts.

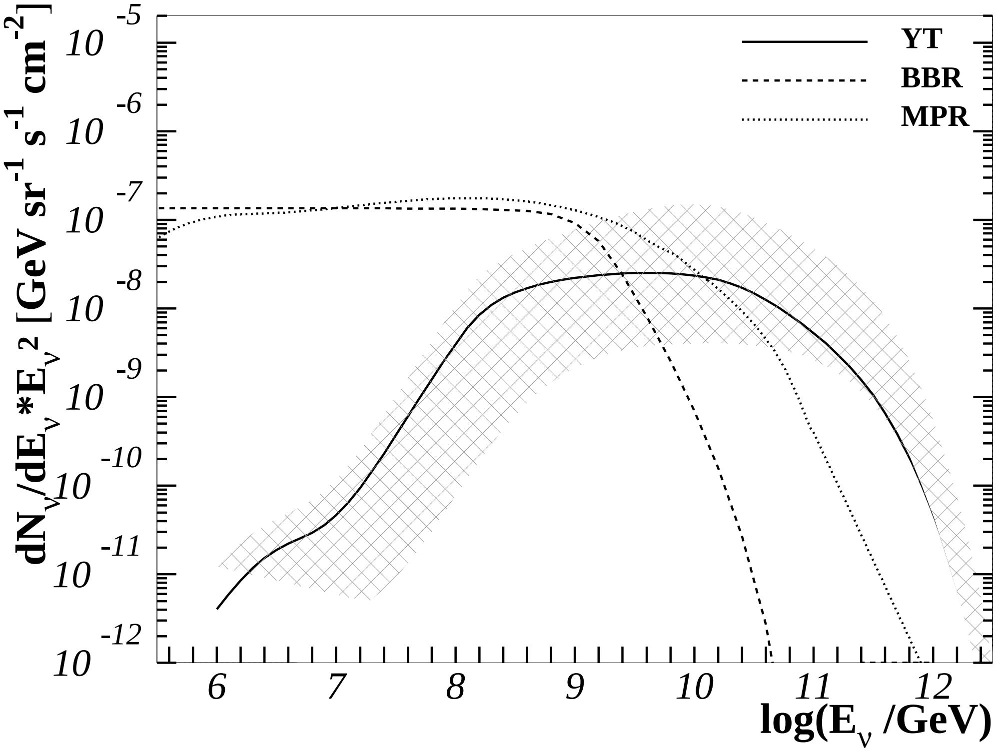

Figure 4.5: Diffuse neutrino flux models at EHE energies: Solid line: YT(4, 4). The hatched area shows deviations from YT(4, 4) due to the source evolution scenario, YT(4, 5) giving the upper limit, YT(2, 2) the lower one. The dashed line represents the BBR-II model and the dotted lines shows the MPR model of AGN.

4.2.1 Event rate calculation

The number of neutrinos per area and time unit is given as the convolution of the initial flux $dN_\nu/dE_\nu(E_\nu, \theta)$ with the probability of detecting a neutrino,

$$R(E_{\min}, \theta) = \int_{E_{\min}} P_{\nu_l \to X}(E_\nu, E_{\min}) P_{shadow} \frac{dN_\nu}{dE_\nu}(E_\nu, \theta)\, dE_\nu \,. \tag{4.10}$$

This probability is the product of the Earth shadow factor P_{shadow} that considers neutrino absorption in the Earth and of the probability that the neutrino induces a cascade within the range of the detector. In Fig. 4.6, the shadow factor for electron neutrinos (solid lines) and anti-electron neutrinos (dashed lines) depending on zenith angle and energy is shown. The dependence on the thickness X is exponential. The analytical expression for the shadow factor in terms of the thickness

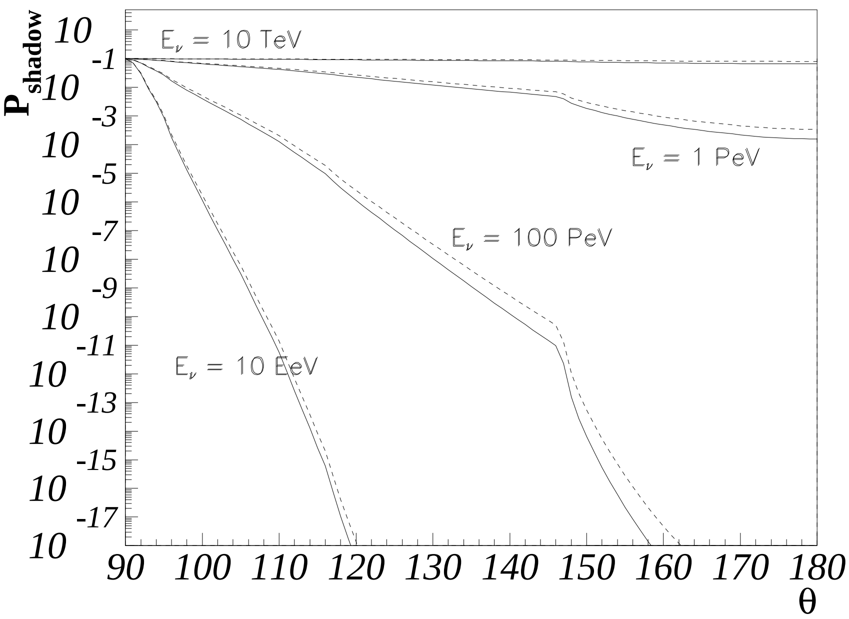

Figure 4.6: The probability that an electron neutrino (solid line) or anti-neutrino (dashed) survives without interacting on its way through Earth to the detector.

is given in Section 1.3.6. The thicknesses of the Earth and of the atmosphere are displayed in Fig. 4.7. It can be seen that the thickness of the atmosphere is very small compared to the Earth's thickness. However, changes in the thickness alter the probability exponentially. At energies above the EeV range, the Earth filters most of the neutrino signal and thus, the rates will be calculated assuming a $2\,\pi$ detection field above the horizon.

The probability of inducing a cascade can be approximated using a constant effective range, r_{eff}, of the cascades, assuming that the neutrino is detected when it induces a cascade within the range of the detector. In this case, Equ. (1.67) in Section 1.3.6 reduces to

$$P_{\nu_l \to X} = \rho' \cdot N_A \cdot \sigma(E_\nu) \cdot r_{eff}\,. \tag{4.11}$$

In this expression, N_A is Avogadro's constant and σ is the total cross section (see Fig. 4.8), including charged and neutral current interactions. In the case of anti-electron neutrinos, Glashow resonant scattering is considered as well. The density of the material changes the probability by the factor $\rho' := \rho/\rho_{H_2O}$. This factor is of the order unity for ice and water detectors, for an array in a salt dome, it is $\rho' \sim 2.3$. The probability that an electron neutrino induces a cascade in a 1 km^3 ice or water detector is shown in Fig. 4.9.

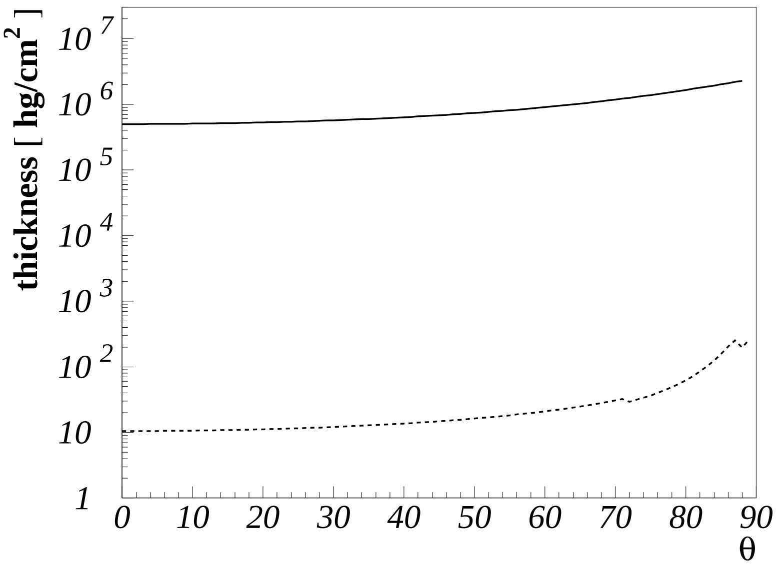

Figure 4.7: Absorption length of a neutrino, depending on the zenith angle. The solid line represents absorption in the Earth, the dashed line shows the absorption length in the atmosphere.

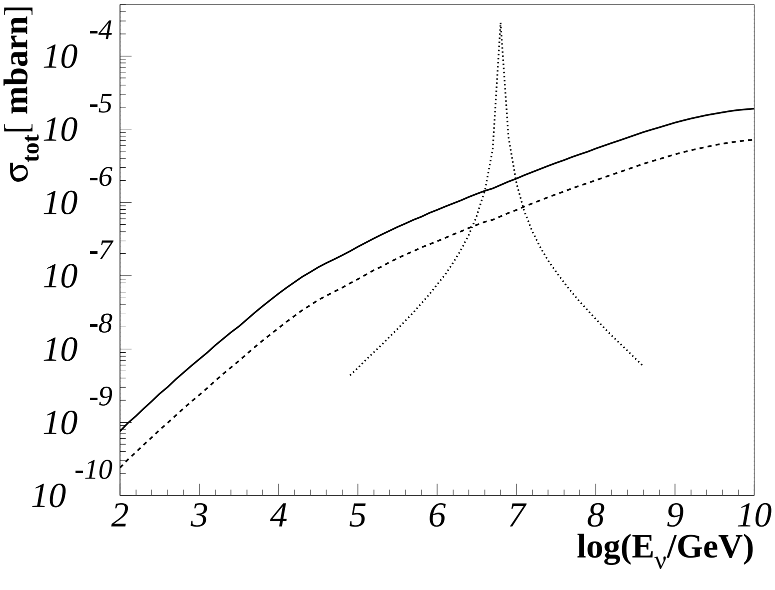

Figure 4.8: $\sigma_{\nu_e N}$ cross section (CC - solid line; NC - dashed line). $\overline{\nu}_e\, e$ cross section (*Glashow resonance*) indicated by dot-dashed line.

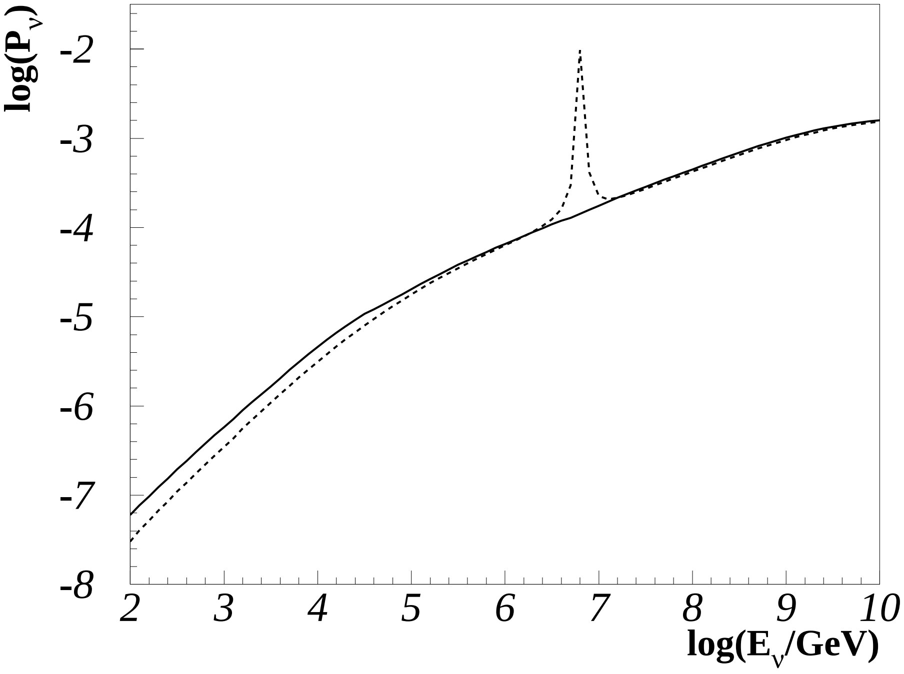

Figure 4.9: Probability that an electron neutrino induces a cascade (solid line). The dashed line represents anti-neutrino scattering, which includes resonant scattering of $\overline{\nu}_e$ with electrons in the material.

4.2.2 Comparison of event rates

The search for a neutrino-induced acoustic or radio signal aims at the detection of extragalactic neutrinos at EHE. The energy threshold for such an experiment is of the order of $\sim$ EeV. Currently, there exists an array of underwater acoustic sensors, SAUND, because of which it was possible to derive a limit on the extragalactic neutrino flux at EHE, see [VGL05]. However, a much larger array of acoustic sensors is needed in order to detect a significant extraterrestrial neutrino signal.

In the following, the expected neutrino rates in such a detector will be calculated. For that purpose, four detector properties have to be considered:

1. the *threshold energy* $E_{\min}$ of the detector determines the total integral neutrino rate per year and km^2. The threshold energy will be varied between $E_{\min} = 10^7$ GeV and $E_{\min} = 10^{10}$ GeV in the following.

2. The *depth* of the detector below the Earth's surface d determines the thickness.

3. Another important parameter is the *effective range* of neutrino-induced cascade, r_{eff}. It is determined by the size of the detector, since the cascade has to be induced within the detection array in order to be seen. Results will be given per km^3, giving the detection rate for $r_{eff}^{\mathrm{1km}} := r_{eff}/1$ km=1,

   $$R = R_0 \cdot r_{eff}^{\mathrm{1km}} \cdot \rho' \, . \tag{4.12}$$

   The increase of the detector volume is then simply given by multiplying the rate by the geometric volume in units of km^3.

4. Furthermore, the *density* of the detector material, $\rho' = \rho/\rho_{H_2O}$ has to be considered as well. The density will be given in terms of $\rho' = 1$, assuming water or ice as the detector medium. For detection arrays in salt, the result can be multiplied by a factor 2.3 in order to receive the corresponding event rates.

The event rates induced by (anti-)electron neutrinos are shown in Fig. 4.10. The four neutrino flux models discussed above are presented as well. The angle integration over the upper hemisphere ($2\,\pi$) has been performed, since at these energies, no contribution from the lower hemisphere due to absorption is expected. The result is given in units of yr^{-1} km^{-3} GeV^{-1}. Because the predicted neutrino fluxes decrease as a power law, the event rate decreases rapidly with increasing threshold energy.

Since the cross sections for nucleon neutrino interactions do not change significantly with neutrino flavor, the results are basically the same for both flavors.

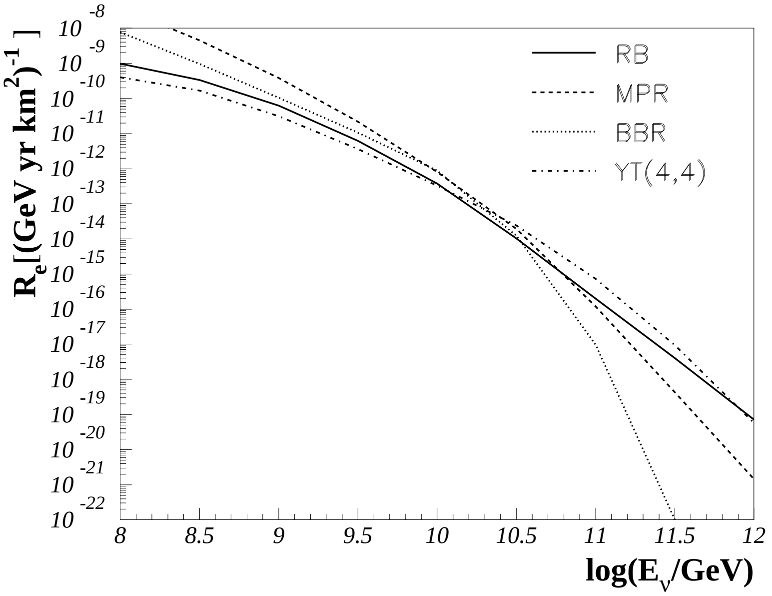

Figure 4.10: Electron and anti-electron neutrino induced event rate per year, square kilometer and GeV. Downgoing events have been considered, i.e. $\theta = 0° - 90°$ and $\phi = 0 - \pi$.

In this chapter, the results are presented for electron neutrinos, while the same figures and tables are listed for muon neutrinos in appendix B.

Figure 4.11 shows the integrated electron neutrino rates depending on the threshold energy of the detector for the four different neutrino flux predictions. A standard depth of $d = 0.5$ km has been assumed for these calculations. The results for $E_{\rm min} = 10^7$, 10^8, 10^9 GeV are presented in table 4.1, where the contribution from atmospheric neutrinos as listed as well. The ratio of the predicted fluxes and the atmospheric contribution ranges from 10^5 up to 10^{11}. This result shows that the atmospheric neutrino flux does not contribute significantly to any background signal.

The two predictions of a cosmogenic neutrino flux (YT and RB) result in a flux of $\sim$ 0.1 events per year and cubic kilometer for a threshold energy of $E_{\rm min} = 10^7$ GeV. The two AGN neutrino flux predictions (MPR and BBR-II) yield an event rate of the order 10/yr/km^3. The cosmogenic flux is considered to as a guaranteed flux, since a neutrino production is enforced by interactions of CR protons with the CMB, resulting in the GZK cutoff in the CR spectrum [Gre66]. The two models predicting a flux from AGN sources (BBR-II and MPR) depend on the opacity of the sources. The MPR model is an upper limit of the expected neutrino flux. The prediction by BBR-II is assuming an E^{-2} neutrino spectrum. This result shows that these models include parameters that are not yet completely restricted and that these fluxes should be considered as optimistic upper limits. The most recent AMANDA limit on the muon neutrino flux at TeV-PeV energies even indicates that the fluxes need to be a factor of $\sim 2-3$ lower, implying that the event rates at high energies also decrease by the same factor. Each model results in a detection rate of several events per year and cubic kilometer for $E_{\min} = 10^7$ GeV, which indicates that the expected event rates should lie in the range of $0.1 - 25$ events/yr/km^3. For a detection volume of approximately ~ 100 km^3, as it is proposed for an array of radio and acoustic antennae connected to the IceCube array, between ~ 10 and ~ 200 events per year considering both neutrino flavors can be expected. Here, a reduction of the fluxes by a factor of 2 has been assumed due to the limit given by AMANDA. If salt is used as detector medium instead of water, the event rate would additionally be increased by a factor of 2.3, yielding $\sim 20 - 440$ events/yr/km^3, with a detector depth of 0.5 km.

Table 4.2 shows how the event rate for electron neutrinos changes with the depth of the detector below the Earth's surface. Results for three different depths, $d = 0.5, 1.5, 2.5$ km, are shown for a threshold energy of $E_{\min} = 10^7$ GeV. The rate decreases with the depth, so that it is reduced by a factor of two when the detector is built at 1.5 km depth instead of 0.5 km. For threshold energies of $E_{\min} > 10^7$ GeV as they are expected for radio and acoustic detection, the background of atmospheric muons and neutrinos is small. Therefore, it is not necessary to deploy the detector deep into the Earth to reduce any background and a detector has the best detection potential at shallow depths.

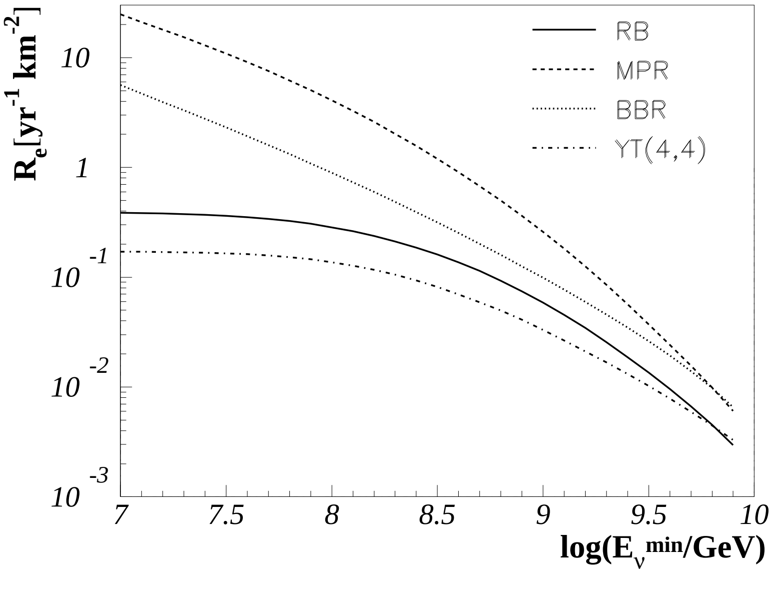

Figure 4.11: Integrated neutrino rate, representing the number of detected electron neutrino induced cascades above a certain energy $E_{\min}$.

	R_0	[km^{-3}yr^{-1}]		R_0/R_0(atm)		
$E_{\rm min} =$	10^7 GeV	10^8 GeV	10^9 GeV	10^7 GeV	10^8 GeV	10^9 GeV
BBR-II	5.6	0.89	0.099	$6 \cdot 10^6$	$4 \cdot 10^8$	$5 \cdot 10^{10}$
MPR	25	4.1	0.36	$3 \cdot 10^7$	$2 \cdot 10^9$	$2 \cdot 10^{11}$
RB	0.39	0.28	0.059	$4 \cdot 10^5$	$1 \cdot 10^8$	$3 \cdot 10^{10}$
YT	0.17	0.14	0.033	$2 \cdot 10^5$	$7 \cdot 10^7$	$2 \cdot 10^{10}$
Atmos.	$1 \cdot 10^{-06}$	$2 \cdot 10^{-09}$	$2 \cdot 10^{-12}$	1	1	1

Table 4.1: Number of electron neutrino-induced events for a 1 km^3 ice or water detection array. The numbers have been calculated for various detector threshold energies, i.e. $E_{\rm min} = 10^7$, 10^8, 10^9 GeV. The ratio of the event numbers for different models and the atmospheric rate is also quoted. The depth of the detection array below the Earth's surface is assumed to be $d = 500$ m.

	R_0	[km^{-3} yr^{-1}]	
$d =$	0.5 km	1.5 km	2.5 km
BBR-II	5.6	3.7	2.7
MPR	25	16	12
RB	0.39	0.17	0.098
YT	0.13	0.054	0.029

Table 4.2: Electron neutrino event rates for different detector depths, $d = 0.5, 1.5, 2.5$ km. The detector threshold energy is $E_{\rm min} = 10^7$ GeV. The rate decreases with the depth, since neutrinos are absorbed in the Earth.

4.2.3 Event rates for a specific detector configuration

Effective volumes for a detector configuration of radio antennae and hydrophones in the Antarctic ice around IceCube have been calculated in [V$^+$05a, BI$^+$05]. In their simulations, a geometry of a hexagonal 10×10 km^2 array of 91 strings equipped with radio and acoustic receivers has been assumed. The acoustic effective volume ranges from ~ 100 km^3 at the threshold energy $E_{\rm min} = 10^{9.5}$ GeV, while the detection threshold of a radio signal starts already at $E_{\rm min} = 10^{8.5}$ GeV, with 1 km^3, increasing to ~ 100 km^3 in one order of magnitude, at $E_\nu = 10^{9.5}$ GeV. The effective volumes differ from geometric ones, since the detector and cascade properties at different energies reduce or enlarge the detection probability. For details of the simulations, see [V$^+$05a, BI$^+$05]. In this section, the effective volumes are folded with the neutrino flux models as described above in order to investigate possible detection rates quantitatively.

Figure 4.12 shows the depth dependence of the detection rate at the example of the standard cosmogenic flux YT(4, 4). The number of observed events decreases significantly with the depth of the array below the Earth's surface. Figure 4.13 shows that the rate is about constant with respect to the lower energy integration limit $E_{\rm min}$ for acoustic detection, since the effective volume does not allow any significant detection below $\sim 10^9$ GeV. Between $10^{9.5} - 10^{10.5}$ GeV, however, the rate decreases about an order of magnitude with the threshold energy for the three models being discussed. Table 4.3 summarizes the rates for the discussed flux models with a threshold energy of $10^{7.5}$ GeV. BBR-II does not yield a significant contribution at these high energies and is a better candidate at lower energies. The main reason for this result is the exponential cutoff of the spectrum at $E_\nu \sim 10^{9.5}$ GeV. The maximum neutrino flux from blazars gives the best results with several tens of events per year. It should, however, be kept in mind that this is an upper limit on the flux of these sources, so that the event rate may in reality be even lower. The flux of GZK neutrinos leads to a significant rate of several events and is a guaranteed source. Therefore, we conclude that the detection possibilities for acoustic and radio methods are very promising.

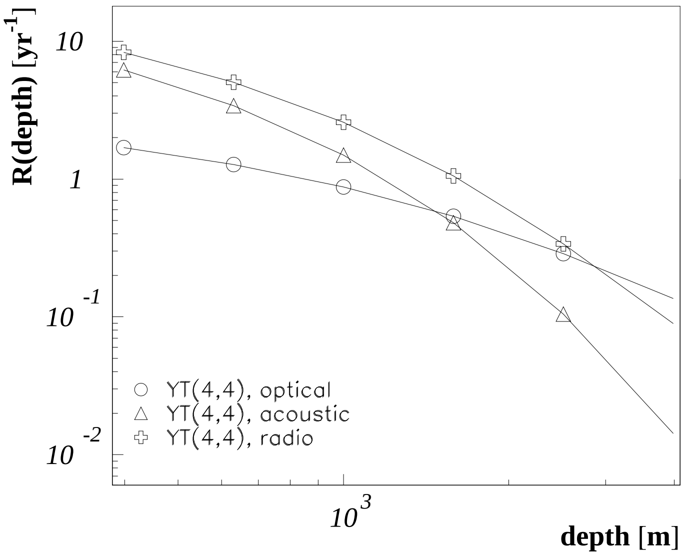

Figure 4.12: Depth dependence of a possible signal shown at the example of YT(4, 4).

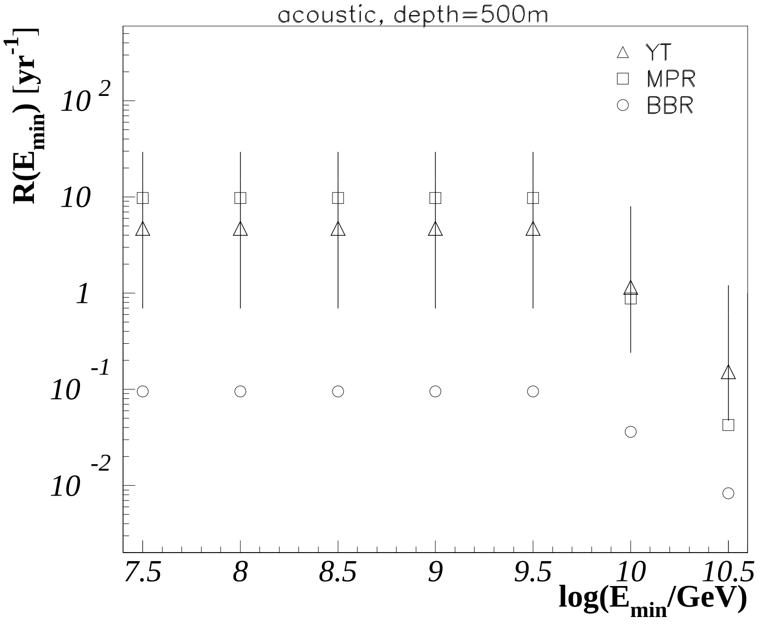

Figure 4.13: Threshold energy dependence of the total rate for an acoustic array and for various flux models. The depth of the detector is set to a depth of $d = 500$ m.

Rate/yr	MPR	YT	BBR-II
optical	19	$1.4^{+4.6}_{-1.3}$	0.05
acoustic	5	$4.7^{+24.3}_{-4.0}$	0.05
radio	13	$6.6^{+25.4}_{-5.7}$	0.1

Table 4.3: Total rate at a threshold energy of $E_{\text{min}} = 10^{7.5}$ GeV for the three detection methods: YT has been calculated for $(m, z_{\text{max}}) = (4,\ 4)$ with an absolute lower and upper limit given for $(m, z_{\text{max}}) = (2,\ 2)$ and $(m, z_{\text{max}}) = (4,\ 5)$ respectively. The rates for BBR-II and MPR have been reduced by a factor 2 due to restrictions of the models by the current AMANDA neutrino flux limit.

4.2.4 Summary & conclusions

In Section 4.2, the event rates for the EHE detection of neutrino-induced hadronic and electromagnetic showers have been discussed. Here, threshold energies of $E_{\text{min}} = 10^7$ GeV up to $E_{\text{min}} = 10^9$ GeV have been used. In Section 4.2.3, the simulated effective volumes from [V$^+$05a, BI$^+$05] have been used for the event rate calculation. It becomes clear that the detection threshold for acoustic and radio detection is close to $E_{\text{min}} \sim 10^9$. Arrays of ~ 100 km^3 are sufficient for the detection of $1 - 10$ events per year. In particular, cosmogenic neutrinos are not detectable by optical arrays like IceCube. In comparison, an acoustic array in connection with a radio array as suggested in [V$^+$05a, BI$^+$05] is very well suited for the detection of cosmogenic neutrinos, but not necessarily for AGN neutrinos. The hybrid array also gives the opportunity to study events detected in both the radio and the acoustic channel in order to get a better reconstruction of the showers and a better understanding of any systematics in the detection.

The calculations from above show that new detection methods at the highest energies in combination with optical detection yield detection rates which give the possibility to study both AGN models and models of the cosmogenic neutrino flux in detail, and thereby both restrict model parameters and detect a first signal excess.

CHAPTER 5

Transient ν sources - Gamma Ray Bursts

The presumption that UHECRs are connected to the prompt emission of GRBs is a strong support of the theory of neutrino production in Gamma Ray Bursts. An overview of the different emission scenarios connected to precursors, prompt and afterglow emission of GRBs is already given in Chapter 1. This chapter serves the basic purpose to examine fluctuations of the generic spectrum of prompt GRB emission, firstly by looking at sub-GRB classes and systematic changes in the neutrino spectra, and secondly by examining fluctuations within the same burst class. In Chapter 4, potential sources of neutrino emission with long lifetimes, i.e. AGN and GZK neutrinos, have been discussed with the prospect of detection using different methods. In this Chapter, we refer to transient neutrino sources if the neutrino flux arises from non-permanent phenomena. AGN neutrino fluxes in Chapter 4 always assume continuous emission and do not consider temporal variations. However, neutrinos from AGN flares certainly classify as transient sources, as well as SGR flares etc. This chapter focuses on the neutrino emission which is expected in coincidence with the prompt emission from Gamma Ray Bursts (GRBs). Single source neutrino spectra for two different sets of long bursts from the BATSE catalog are examined as well as the KONUS catalog of short GRBs [M^{+}05a]. Both single source spectra and the resulting total spectrum of all bursts will be discussed.

A crucial parameter in neutrino flux calculations is the redshift. The long burst samples are based on the determination of burst redshifts using the redshift estimators variability (568 bursts) and lag (292 bursts). Furthermore, 188 long and 13 short bursts detected by SWIFT are presented. Here, a large fraction of bursts have measured redshifts. For the additional long bursts, $z = 2$ has been used. SWIFT is much more sensitive to high redshift GRBs which is why the mean redshift is shifted to a relatively high value. Since there is no estimator yet for short GRBs, a generic redshift of $z = 0.1$ is assumed, since the few short bursts with measured redshifts seem to arise from binary mergers in relatively nearby galaxies around $z \sim 0.1$, see e.g. [H^{+}05, V^{+}05c, G^{+}06b].

5.1 GRB neutrino spectra

The neutrino spectrum, dN_ν/dE_ν, can be derived assuming that the proton spectrum follows the electron spectrum of the source. Furthermore, it needs to be assumed that electron losses can be neglected. The neutrino flux in turn follows the proton spectrum in a first order approximation, since it can be connected to the observed synchrotron spectrum of the sources. The resulting neutrino spectra for three different fit models for the synchrotron radiation are presented below. All variables are given in the observer's frame. An improvement of the calculations is generally possible by calculating the electron losses [De 06]. Here, we neglect this effect and take the result as a lower limit for the neutrino flux.

Protons accelerated in astrophysical shocks can interact with the source's photon field and produce a $\Delta-$resonance which in turn leads to neutrino production. Proton and neutrino energy are directly proportional, $E_\nu = E_p/20$. The product of proton and photon energy remains constant, since the energy of the Δ mass has to be produced in the center of mass system, $E_p \cdot E_\gamma = const.$ Hence, photon and neutrino energy are inversely proportional, $E_\nu \propto {E_\gamma}^{-1}$.

- *Model 1:*
  The neutrino spectrum is approximated as a powerlaw using the correlation between neutrino and photon energy, $E_\nu \propto E_\gamma^{-1}$:
  $$E_\nu^2 \frac{dN}{dE_\nu} \propto \begin{cases} E_\nu^{-\beta_\nu} & \text{for } E_\nu > \epsilon_\nu^b \\ 1 - \exp(-E_\nu/\epsilon_\nu^b) & \text{for } E_\nu < \epsilon_\nu^b\,. \end{cases} \tag{5.1}$$
  with $\beta_\nu = \alpha_\gamma + 1$. The part of the spectrum in which the exponential decay dominates, $E_\nu < \epsilon_\nu^b$, is assumed as an exponential decrease with decreasing energy.

- *Model 2:*
  In this case, Equation (5.1) can be used as well. The cutoff is set at the upper energy threshold of the detector-fit.

- *Model 3:*
  $$\frac{dN_\nu}{dE_\nu} E_\nu^2 = A_\nu \cdot \begin{cases} (E_\nu/\epsilon_\nu^b)^{-\alpha_\nu} & \text{for } E_\nu < \epsilon_\nu^b \\ (E_\nu/\epsilon_\nu^b)^{-\beta_\nu} & \text{for } \epsilon_\nu^b < E_\nu \leq \epsilon_\nu^s\,. \end{cases} \tag{5.2}$$

The photon spectral indices can be used to describe $\alpha_\nu = \beta_\gamma + 1$ and $\beta_\nu = \alpha_\gamma + 1$.

A second break at $E_\nu = \epsilon_\nu^s$ appears in the neutrino spectrum which is caused by synchrotron radiation of the neutrino-producing pions. Pions with sufficiently high energies suffer synchrotron losses before decaying and do not produce neutrinos. Thus, the high energy tail of the neutrino spectrum is steepened by two powers and for all three models,

$$\frac{dN_\nu}{dE_\nu} E_\nu^2 \propto (E_\nu/\epsilon_\nu^b)^{-\beta_\nu} (E_\nu/\epsilon_\nu^s)^{-2} \text{ for } E_\nu \geq \epsilon_\nu^s\,. \tag{5.3}$$

The spectrum is normalized to the γ-ray fluence F_γ which is assumed to be proportional to the neutrino luminosity,

$$x \cdot F_\gamma = \int_{E_{\min}}^{E_{\max}} \frac{dN_\nu}{dE_\nu}\, dE_\nu \approx \ln(10) \cdot A_\nu \,. \tag{5.4}$$

All parameters occurring in the following calculations are listed in table 5.1. The factor x is given by the product of the energy transferred to the pions, f_π, a factor 1/8 since half of the photo-hadronic interactions result in four neutrinos and a factor $1/f_e$ to account for the fraction of total energy in electrons compared to protons in the jet [G$^+$04]. The normalization constant A_ν is therefore given as

$$A_\nu = \frac{1}{8}\frac{1}{f_e}\frac{F_\gamma}{\ln(10)} f_\pi \,. \tag{5.5}$$

In the following, the normalization of a single burst will be modified to a quasi-diffuse normalization by multiplying A_ν with the number of bursts per year (1000 bursts per year, of which $\eta = 2/3$ are long and $\eta = 1/3$ are short) and dividing the result by $4\,\pi$ sr,

$$A'_\nu = \eta \cdot \frac{1000}{\text{yr } 4\,\pi \text{ sr}} A_\nu \,. \tag{5.6}$$

The total number of 1000 bursts per year is chosen to be consistent with calculations given by Waxman and Bahcall in [WB97, WB99]. A estimate of ~ 700 bursts per year, however, is a more reasonable number when looking at the BATSE catalog [P$^+$99]. In that case, all the following results could simply be weighted by another factor of 2/3.

The first break energy in the spectrum, ϵ_ν^b, is related to the break energy in the photon spectrum by

$$\epsilon_\nu^b = \frac{(m_\Delta^2 - m_p^2)\cdot\Gamma^2}{4\cdot(1+z)^2} \cdot \left(\epsilon_\gamma^b\right)^{-1} \text{ GeV} \,. \tag{5.7}$$

It is determined through the minimal energy necessary to produce a Δ-resonance in the shock fronts of the bursts. The numerical values given in [YP$^+$06] for the proton mass, $m_p = 0.94$ GeV, and the Δ mass, $m_\Delta = 1.23$ GeV, lead to

$$\epsilon_\nu^b = 7 \cdot 10^5 \cdot (1+z)^{-2}\, \frac{\Gamma_{2.5}^2}{\epsilon^b_{\gamma,MeV}} \text{ GeV} \tag{5.8}$$

in the observer's frame.

The second break energy is connected to the pion's synchrotron loss time. It depends on the neutrino flavor and for muon neutrinos, it is given as

$$\epsilon_\nu^s = \sqrt{\frac{3\,\pi\,\epsilon_e}{4\,\tau_\pi^0\,\sigma_T\,\epsilon_B\,L_\gamma}} \cdot \frac{c^4\,t_v}{(1+z)\cdot m_e}\,\Gamma^4 \,. \tag{5.9}$$

For electron and anti-muon neutrinos the break energy ϵ_ν^s is about an order of magnitude lower, since these neutrinos result from the muon decay. The muon lifetime is about a factor of 100 higher than the pion lifetime, which gives a lower energy threshold for synchrotron losses. The derivation of the second break energy can be found in [G$^+$04]. Here, ϵ_b and ϵ_e are the fractions of the burst's internal energy going into the magnetic field, respectively into electrons. The equipartition fractions have been set to $\epsilon_e = 0.1$ and $\epsilon_b = 0.1$. There is no good way of determining the equipartition fractions theoretically, yet. However, afterglow observations indicate values on the order of 0.1 [WKF98]. The remaining parameters in Equ. (5.9) are listed in table 5.1, with the values as used in the following calculations. Inserting all numerical values gives

$$\epsilon_\nu^s = \frac{10^8}{1+z} \epsilon_e^{1/2} \, \epsilon_b^{-1/2} \, \Gamma_{2.5}^4 \, t_{v,-2} / \sqrt{L_\gamma^{52}} \mathrm{GeV} \,. \tag{5.10}$$

A detailed derivation of the neutrino spectrum as presented above is given in [WKF98].

5.1.1 The fixed parameters

The parameters in the neutrino flux calculations have been adjusted according to the different classes of GRBs. A summary of the mean values of the used parameters is given in table 5.1, for Gamma Ray Bursts, X-Ray Flashed, Short Hard Bursts (SHBs) and Short High Energy (SHE) bursts. The different source classes are discussed in section 5.2. Here, we focus on classical GRBs and Short Hard Bursts, since these are examined quantitatively in the following paragraphs.

The boost factor Γ is constrained to $100 < \Gamma < 1000$ for regular GRBs, since for boost factors less than 100, the medium would be optically thick to photons and for $\Gamma > 1000$, protons lose most of their energy to synchrotron radiation [HaHo02]. The possibility of fluctuating Γ using the photon break energy is given as demonstrated in [G$^+$04], but there are several arguments for using a constant value: bursts can be misaligned which would lead to a misinterpretation of the boost factor. Also, varying the break energy for each single burst might implicitly already include boost factor fluctuations. Therefore, a constant boost factor of $\Gamma = 300$ is used in following calculations.

In previous publications, e.g. [G$^+$04], a variation of the energy going into pions f_π has been discussed. Such a variation would further increase the width of the distribution of the neutrino spectrum normalization. The burst luminosity, the boost factor, the photon break energy and the variability time influence f_π, as they are correlated as

$$f_\pi \sim 0.2 \cdot \frac{L_\gamma^{52}}{\Gamma_{2.5}^4 \, t_{v,-2} \, \epsilon_{\gamma,MeV}^b} \,. \tag{5.11}$$

Parameter	Symbol	GRB	XRF	SHB	SHE
γ fluence	F_γ [erg/cm^2]	10^{-5}	10^{-5}	10^{-5}	10^{-5}
Redshift	z	2	2	0.1	0.1
Lumi. dist.	d_l [Gpc]	15	15	0.45	0.45
γ energy	E_γ [keV]	$(10, 300)$	$(0.1, 100)$	$(10^2, 10^3)$	$(10^3, 10^4)$
ν energy	E_ν [GeV]	$(10^3, 10^7)$	$(10^3, 10^7)$	$(10^2, 10^7)$	$(10^2, 10^7)$
Equipartition fractions	ϵ_b	0.1	0.1	0.1	0.1
	ϵ_e	0.1	0.1	0.1	0.1
Electron-proton total energy ratio	f_e	0.1	0.5	0.1	0.1
Energy transferred to π	f_π	0.2	10^4	0.2	0.2
Burst luminosity	L_γ [erg/s]	10^{52}	10^{52}	10^{51}	10^{51}
	$L_\gamma^{52} := L_\gamma/(10^{52}$ erg/s$)$	1	1	0.1	0.1
Boost factor	Γ	300	30	300	3000
	$\Gamma_{2.5}$	1	0.1	1	10
Spectral indices	α_ν	-1	-1	0	0
	β_ν	0	0	1	1
γ break energy	ϵ_γ^b [MeV]	1	0.1	1	> 1
	$\epsilon_{\gamma,MeV}^b := \epsilon_\gamma^b/\mathrm{MeV}$	1	0.1	1	> 1
ν break energies	ϵ_ν^b [GeV]	10^5	10^6	10^5	10^5
	$\epsilon_{\nu,GeV}^b := \epsilon_\nu^b/\mathrm{GeV}$	10^5	10^6	10^5	10^5
	ϵ_ν^s [GeV]	10^7	10^3	10^{11}	10^{11}
	$\epsilon_{\nu,GeV}^s := \epsilon_\nu^s/\mathrm{GeV}$	10^7	10^3	10^{11}	10^{11}
Time variability	t_v [ms]	10	10	1	1
	$t_{v,-2} := t_v/(10^{-2}$ s$)$	1	1	0.1	0.1
Burst duration	t_{90} [s]	40	40	0.2	0.2
Pion mass	m_π	140 MeV			
Thomson cross section	σ_T	$0.665 \cdot 10^{-24}$	cm^2		
pion lifetime at rest	τ_π^0	$2.6 \cdot 10^{-8}$ s			

Table 5.1: Parameters for neutrinos flux calculations. The numbers quoted as typical values for GRBs, XRFs, Short Hard Bursts (SHBs) and Short High Energy (SHE) bursts are to be taken as rough bench marks, since all of these parameters fluctuate strongly as emphasized in the text. The calculation of the luminosity distance at a redshift between $z = 1 - 2$ for long bursts and $z = 0.1$ for short events is done using cosmological parameters of $\Omega_m = 0.3$, $\Omega_\Lambda = 0.7$ and $h = 0.72$.

In the following calculations, this fraction will be kept at a constant value of $f_\pi \sim 0.2$ for classical GRBs for the following reasons:

1. f_π strongly depends on the boost factor Γ which will be used as a constant as discussed before. The dependence on the other three parameters is only linear. The variation of Γ is more striking, since it is amplified by the Γ^4 behavior.

2. The main uncertainties in the current calculations result from the lack of knowledge of the parameters ϵ_e and ϵ_B as well as from uncertainties in the redshift relation which leads to uncertainties in L_γ. These three parameters are all important in the determination of the spectral normalization and thus a constant value is favorable.

In the case of SHBs, the variability time is smaller, $t_{v,-2} \sim 0.1$ and also the luminosity is about an order of magnitude lower, $L_\gamma^{52} \sim 0.1$. Thus, the pion energy constant stays the same and is assumed to be $f_\pi = 0.2$ for SHBs as well.

X-Ray Flashes (XRFs) will produce very high pion efficiencies due to their low boost factors and break energies. $f_\pi \sim 10^4$ indicates an optically thick source in comparison to a classical GRB and yields a good target for neutrino production. The striking disadvantage for such spectra is, however, the synchrotron loss of pions at very low energies as will be discussed later.

The variability time is kept at a constant value. Apart from the arguments already mentioned for the normalization of the spectrum, the effect of varying t_v here would not be very significant in the detection rates, because the dominant contribution seen in the detector comes from the energy region of the first break.

The prediction of the diffuse neutrino flux derived from the model above is given in [WB97, WB99], where the authors use average parameters to determine the shape of the spectrum. Cosmological evolution of the sources has been considered in that model by taking into account the redshift evolution of GRBs. It is assumed that GRBs follow the star formation rate, since they appear to be connected to supernova-Ic explosions. The final result of this work will be compared to this standard flux. To do this, the diffuse Waxman-Bahcall flux has to be weighted by a factor $\eta = 2/3$ or $\eta = 1/3$ for long and short burst samples respectively.

A different approach to predicting the neutrino flux from GRBs is to look at each burst individually and add up the individual spectra to make a prediction of the total flux from these sources. An approach of using individual spectra as discussed by Guetta et al. [G$^+$04] will be used here to get an estimate of the flux that can be expected to be observed by coincident measurements of AMANDA. In addition, a prediction for a diffuse flux will be made using the mean values of the parameter distributions that are given or can be derived from BATSE data.

5.2 Different classes - different spectra

As discussed in Chapter 1, GRBs can be divided into different sub-classes, such as long and short events and a further division of long bursts into XRR bursts, XRF and regular GRBs. While short and long bursts differ in duration and in the hardness of the spectrum, XRR/XRFs and regular GRBs differ in the energy range of prompt emission. A further class of short bursts is predicted with a high energy component, which has not be observed yet, but which would be observable with GLAST.

The photon spectral properties are reflected in the neutrino spectra. A schematic representation of the neutrino spectra of the four different classes is shown in Fig. 5.1. Due to a low boost factor of $\Gamma \sim 30$, XRR and XRFs have a lower break energy in the photon spectrum, which leads to higher neutrino break energy ($\epsilon_{\nu}^{b} \sim 10^{6}$ GeV for XRR/XRFs (b) compared to 10^{5} GeV for regular GRBs (a)). However, due to the low boost factor, the pion synchrotron losses happen at extremely low energies and the second break energy is in this case three orders of magnitude lower than the first one. Thus, these events are only observable below energies of $E_{\nu} < 10^{3}$ GeV. At these energies, the signal is about four orders of magnitude higher than for regular GRBs, since the pion efficiency is $f_{\pi} \sim 10^{4}$ due to the low boost factor and the small photon break energy.

The photon spectra of short bursts are typically harder than long ones leading to a much softer neutrino spectrum of $\sim E_{\nu}^{-2}$ below the break energy and $\sim E_{\nu}^{-3}$ above the break energy (see Fig. 5.1 (c)). The class of high energy short bursts would produce a neutrino spectrum as displayed in Fig. 5.1 (d). There is, however, no experimental evidence yet that such a class exists. While the photon spectrum would be observed at > 10 MeV energies, the corresponding neutrino spectrum is supposedly visible at lower energies as indicated in the figure.

The reflections above show that the assumption of a (2:1) ratio of long to short bursts and a (1:1:1) ratio of (GRB:XRR:XRF) would result in a modified spectrum which can look significantly different from the spectrum which has so far been classified as the typical neutrino GRB spectrum.

Apart from spectral fluctuations between different burst classes, there are relatively large variations within the classes themselves. This is discussed in the following section.

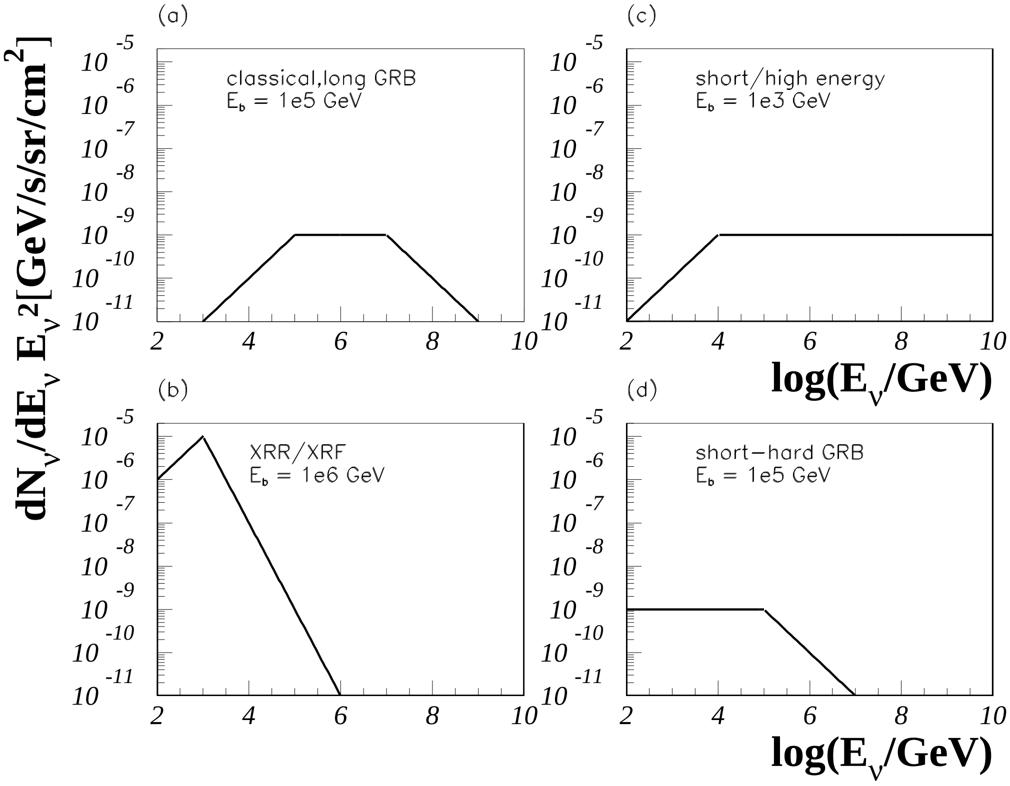

Figure 5.1: Prompt emission neutrino spectra from (a) a classical, long GRB as opposed to an XRR/XRF event (b) and from (c) short, high energy bursts which are not observed yet compared to short, regular bursts as observed by KONUS, SWIFT, etc (d).

5.3 Calculation of single source spectra

5.3.1 The burst samples

Due to the necessity of detailed afterglow observations for the determination of GRB redshifts, only a small fraction of GRBs have measured redshifts as of today. Most of the redshift measurements are connected to SWIFT observations. Because of the low statistics of bursts with directly observed redshifts, different redshift estimators have been developed. Note that these methods apply only to *long duration bursts*. Although first measurements of short duration burst redshifts succeeded recently, see e.g. [H$^+$05, V$^+$05c, G$^+$06b], there are not enough statistics for short bursts yet, and therefore for short GRBs, a generic redshift of $z = 0.1$ is assumed.

Two samples of long GRBs from the BATSE catalog will be used in the following sections, as well as different estimator methods for the redshift determination. Both burst sets are subsamples of the BATSE catalog.

A subsample of 568 bursts with redshifts determined using the variability of GRBs to estimate redshifts is given by Guetta et al. [G$^+$04]. Throughout the chapter, it will be referred to as the *variability sample*. Additionally, a sample of 292 bursts with redshifts determined by connecting temporal lag between the signal in BATSE's different energy channels, is given by [GSF05], based on the work of [Nor02] and [B$^+$97b]. Band fits have been applied to fit these spectra. We will refer to this set of GRBs as the *lag sample*.

The KONUS catalog of short GBRs [M$^+$05a] provides 99 short GRBs with spectral parameters and it will be examined with respect to the potential neutrino output independently.

The SWIFT team provides single powerlaw fits for most of their bursts shortly after detection on their web-page [Swi06a]. A sample of 188 long bursts and 13 short GRBs is used, including all bursts up to March 12, 2007. Redshifts are provided for a large fraction of bursts. For the remaining long bursts without redshift information, $z = 2$ is used to account for the sensitivity to high redshift bursts.

The possibility of analyzing bursts with respect to their neutrino signal is only given for a small set of bursts because of constraints from the running UHE neutrino experiments. During BATSE's operation time, the AMANDA experiment was one of the most interesting neutrino detectors for GRB analysis: there are 105 bursts in the BATSE catalog that can potentially be examined using the AMANDA experiment [StA04]. None of these bursts is given in the lag sample, but there are 82 bursts of the variability sample which are in the set of the 105 bursts as well. These bursts will be discussed separately in this section. In the following, we will refer to these bursts as the AMANDA *subsample* for simplicity.

	# (GRBs)	#loc. GRBs	$\log(A'_\nu)$	α_ν	β_ν	$\log \epsilon^b_{\nu,GeV}$	$\log \epsilon^s_{\nu,GeV}$
BV	568	568	-8.8 ± 0.6	-0.89 ± 0.44	-0.17 ± 0.37	5.0 ± 0.8	7.0 ± 0.9
BL	292	292	-9.0 ± 0.7	-1.62 ± 0.56	0.63 ± 0.62	5.4 ± 0.5	7.3 ± 0.7
BA	105	105	-8.9 ± 0.5	-0.93 ± 0.45	-0.24 ± 0.37	4.8 ± 0.8	6.8 ± 1.0
KS	99	34	-9.7 ± 0.5	0.47 ± 0.73	1.3 ± 0.5	6.0 ± 0.5	8.2 ± 0.3
SwS	13	9	-11.4 ± 0.7	-	-0.15 ± 0.33	6.0 ± 0.2	8.7 ± 0.7
SwL	188	165	-9.9 ± 0.6	-	-0.61 ± 0.46	5.4 ± 0.2	8.3 ± 0.6
WB	1000/yr	-	-8.7	-1	0	5	7

Table 5.2: Mean neutrino spectra parameters for the the different samples, BATSE variability (568 bursts - BV), BATSE lag (292, BL) and the variability subsample (82 bursts, BA) as well as the sample of KONUS short bursts (99 GRBs, KS), SWIFT long and short bursts (13 short GRBs - SwS and 188 long bursts - SwL). The standard deviation to the mean values has been calculated as an error estimate. The values used by Waxman-Bahcall (WB) are given as reference values. The neutrino flux normalization A'_ν is given in diffuse units, GeV $\text{cm}^{-2}\,\text{s}^{-1}\,\text{sr}^{-1}$.

In this section, the parameter distributions of the burst samples will be discussed. Each individual set of bursts will be used to make a prediction of the flux from the given source sample. Additionally, average values will be determined by calculating the weighted mean value of each distribution as

$$\overline{p} = \frac{\sum_{i=1}^{n} w(p_i) \cdot p_i}{\sum_{i=1}^{n} w(p_i)} \tag{5.12}$$

with 1σ errors,

$$\sigma^2(p) = (\overline{p})^2 - \overline{p^2} \tag{5.13}$$

Here, p_i is the corresponding parameter value of a certain bin i, and $w(p_i)$ is the number of entries in that bin. Here, n is the total number of bins. In each of the following parameter distributions, the average values are indicated as vertical lines. The horizontal lines show the 1σ deviation from the average. The set of average parameters of each sample are summarized in table 5.2.

It should be noted that the mean values for fit parameters like the spectral indices of the photon spectra, α_γ and β_γ as well as the break energy in the photon spectrum, ϵ^b_γ, vary between different samples. The reason is that the three parameters are correlated. Fixing the break energy, for example, at a certain energy would influence the values of the spectral indices etc. Different properties of the observing experiment, e.g. energy range, field of view etc., can also influence the results.

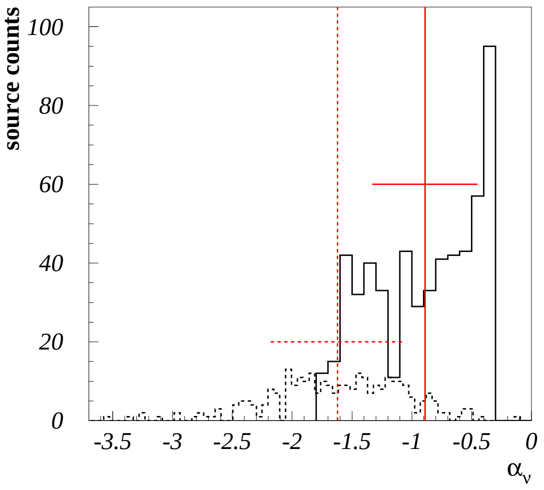

Figure 5.2: Distribution of the first neutrino spectral index α_ν. Solid line: variability sample; Dashed line: lag sample. Mean values with 1σ errors are indicated for each distribution.

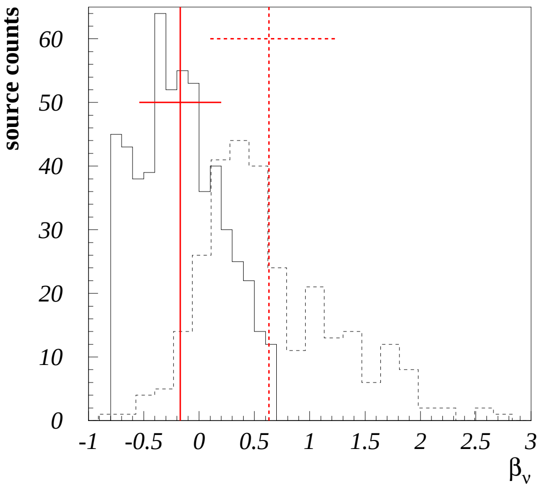

Figure 5.3: Second neutrino spectral index, β_ν, of the neutrino spectrum for bursts in the variability (solid line) and lag sample (dashed line). Mean values with 1σ errors are indicated for each distribution.

Lag and variability samples from the BATSE catalog

The expected neutrino spectrum from individual bursts can be estimated from the parameters of the photon spectrum as discussed in section 5.1. The distribution of the neutrino spectra's indices follows the one of the photon spectrum with $\alpha_\nu = \beta_\gamma + 1$ and $\beta_\nu = \alpha_\gamma + 1$. The distributions of the neutrino spectral indices α_ν and β_ν are displayed in Fig. 5.2 and 5.3. In all following figures, the solid line represents the distribution of the variability sample, while the dashed line shows the lag sample distribution. The distributions of the first spectral index differs between the two samples: while the lag sample shows a Gaussian behavior, the variability sample distribution does not seem to give a particular pattern. The distribution seems to be more randomly scattered. The mean values for the first spectral index are $\overline{\alpha}_\nu^{var} = -0.89 \pm 0.44$ and $\overline{\alpha}_\nu^{lag} = -1.62 \pm 0.56$. The distributions of the second spectral index also show different mean values for the two samples, i.e. $\overline{\beta}_\nu^{var} = -0.17 \pm 0.37$ and $\overline{\beta}_\nu^{lag} = 0.63 \pm 0.62$.

The neutrino break energies depend on the luminosity, redshift and the boost factor of the burst. The redshift distribution is displayed in Fig. 5.4. The variability sample has a significant contribution at higher redshifts ($0.8 < \log z < 1.5$), compared to the lag sample. Both distributions have their maxima around $\log z \sim 0 - 1$. The boost factor is set to a constant value of $\Gamma = 300$, as discussed above.

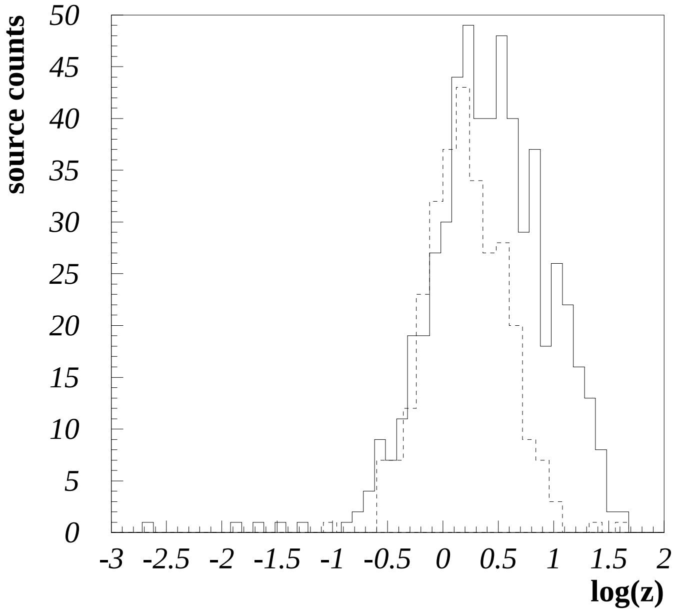

Figure 5.4: Redshift distribution of the sources, solid line: variability sample; dashed line: lag sample.

The resulting break energies are shown in Figures 5.5 and 5.6. Both samples scatter widely in both break energies, so that the errors in the average values, $\overline{\log\epsilon^{b}_{\nu,GeV}}^{var} = 5.0 \pm 0.8$ and $\overline{\log\epsilon^{b}_{\nu,GeV}}^{lag} = 5.4 \pm 0.5$ as well as $\overline{\log\epsilon^{s}_{\nu,GeV}}^{var} = 7.0 \pm 0.9$ and $\overline{\log\epsilon^{s}_{\nu,GeV}}^{lag} = 7.3 \pm 0.7$ allow a deviation of about up to an order of magnitude from the mean values. Scatter plots of ϵ^{b}_{ν} and ϵ^{s}_{ν} also show that there is a relatively strong correlation between the first and the second break energy in both samples with $\epsilon^{b}_{\nu} \propto \epsilon^{s}_{\nu}$, see Fig. 5.7.

Fig. 5.8 shows the neutrino flux normalization of the variability (solid line) and lag spectra (dashed line). The distribution of the variability sample shows a peak with a mean value at $\log[A'_{\nu}/\mathrm{GeV\ s^{-1}\ sr^{-1}\ cm^{-2}}] \sim -8.8 \pm 0.6$, while the maximum for the lag sample is slightly lower, $\log[A'{}_{\nu}/\mathrm{GeV\ s^{-1}\ sr^{-1}\ cm^{-2}}] \sim -9.0 \pm 0.7$.

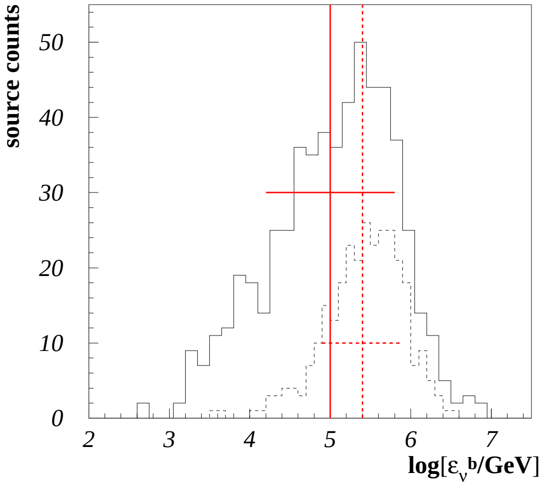

Figure 5.5: Distribution of the predicted first break energy. Solid line: variability sample; Dashed line: lag sample.

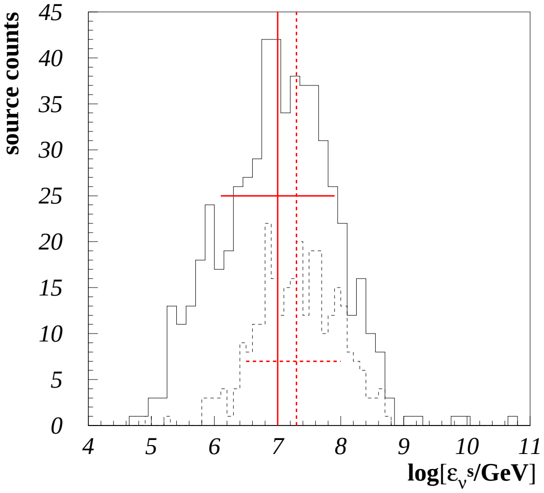

Figure 5.6: Distribution of the predicted second break energy. Solid line: variability sample; Dashed line: lag sample.

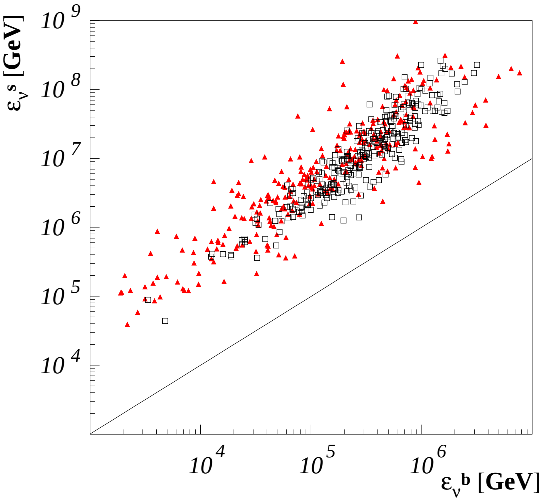

Figure 5.7: ϵ_ν^b versus ϵ_ν^s. A correlation between the two break energies is present due to a correlation of Equ. (5.8) and (5.10). Black squares represent the correlation for the lag sample, red triangles represent values for the variability sample. The black line shows $\epsilon_\nu^b = \epsilon_\nu^s$.

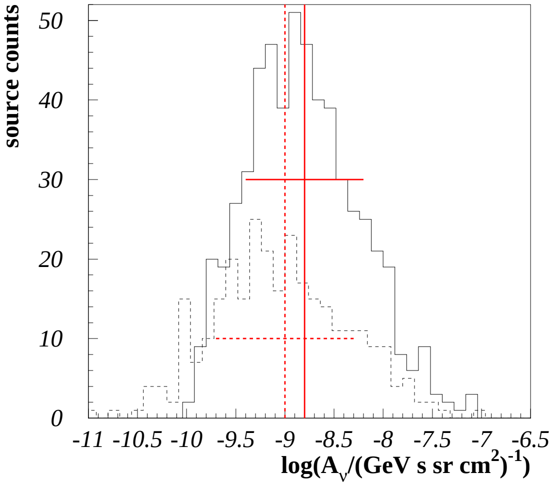

Figure 5.8: Distribution of the predicted neutrino flux normalization for the single burst neutrino spectra, solid line: variability sample; dashed line: lag sample.

In the search for an optimal spectrum for neutrino detection with a large volume neutrino Cherenkov telescope, the most interesting bursts in the presented sample are those with low first neutrino break energies. These are the bursts with a neutrino spectrum that decreases with a relatively hard neutrino spectral index α_ν up to high energies, $E_\nu > 10^5$. Furthermore, strong bursts, $A'_\nu > \overline{A}'_\nu$ will have a strong influence on the shape of the coincidence spectrum. The coincidence spectra are being discussed in Section 5.3.2.

Subsample from variability for AMANDA data analysis

The last four years of BATSE operation time, 1997-2000, coincide with the beginning years of the AMANDA experiment. That implies the possibility of an examination of the neutrino signal from a BATSE subsample. 105 BATSE bursts lie within AMANDA's field of view ($\sim$ northern hemisphere) as is examined in [StA04]. Since the lag sample only contains bursts from before 1997, it cannot be used to examine any AMANDA burst. The variability sample, however, contains 82 of the 105 bursts. The parameter distributions of these bursts will not be discussed in more detail, but they are displayed in appendix C.1.

Sample of short GRBs

The KONUS catalog of short duration bursts from 1994 to 2002 consists of 130 bursts, see [M$^+$05a]. Energy spectra have been fitted for 99 of them.

There are 99 of 130 bursts with given spectral parameters. Of the 99 bursts, 70 are described by model 1 and 12 have been fitted using model 2. These 82 bursts have only one spectral index. A Band fit is used for the description of the photon spectra in 17 cases. Here, a broken powerlaw approximation is used for the description of the neutrino spectra as a first order approximation. The first index of the neutrino spectrum is thus only given for the 17 sources which have been fitted by a Band function. The parameter distribution is shown in Fig. 5.9. The distribution of the second spectral index, $\beta_\nu = \alpha_\gamma + 1$, for all 99 sources is shown in Fig. 5.10. The photon spectrum for short duration bursts are much harder than for long duration bursts, which leads to steep neutrino spectra.

For short GRBs, some parameters differ from those used for the long bursts. The variability time, $t_v = t_{v,-2} \cdot 0.01$ s, is in this case given by the burst duration: short duration bursts do not last longer than $10 - 2000$ ms and usually consist of only one spike which therefore defines the variability time. The redshift has been assumed to be $z = 0.1$, which is supported by observations of about half a dozen bursts as of March 2006, see e.g. [H$^+$05, V$^+$05c, G$^+$06b]. These bursts all show low redshifts around $z \sim 0.1$. All other fixed parameters are given according to table 5.1 and have already been discussed in Section 5.1.1.

The break energy distributions are displayed in Fig. 5.11 (ϵ_ν^b) and 5.12 (ϵ_ν^s). The distribution of the first break energy shows a tail of sources at low values for ϵ_ν^b compared to a symmetric distribution. This is due to the fact that 12 sources are described by a simple powerlaw and that an artificial cutoff in the spectrum at the upper energy threshold for the particular bursts has been used. This upper energy threshold for the photon spectra translates into a lower limit for the neutrino break energy (see Equ. (5.8)). The break energies depend on the redshift of the sources, which is not known in any case. Three different distributions have been calculated to show the influence of the redshift. The solid line represents $z = 0.1$ which is used in all calculations. In comparison, the dashed line shows the energies when using a redshift of $z = 1$ and the dotted line represents calculations for $z = 2$. The break energies depend on z such that the values decrease generally with increasing redshift. This effect is most striking for the second break energy, because the change of redshift influences the absolute luminosity of the GRB which is an important parameter in the calculation of the second break energy.

The fifth and last parameter is the neutrino flux normalization of the single bursts, the distribution is shown in Fig. 5.13.

The mean values of the neutrino parameters are

$$\overline{\alpha}_\nu = 0.5 \pm 0.7 \tag{5.14}$$

for the 17 sources with a Band fit and for all 99 sources,

$$\begin{aligned}
\overline{\beta}_\nu &= 1.3 \pm 0.5 & (5.15)\\
\overline{\log(\epsilon_\nu^b/\mathrm{GeV})} &= 6.0 \pm 0.5 & (5.16)\\
\overline{\log(\epsilon_\nu^s/\mathrm{GeV})} &= 8.2 \pm 0.3 & (5.17)\\
\overline{\log(A_\nu/\mathrm{GeV\ cm}^2)} &= -3.6 \pm 0.5\,. & (5.18)
\end{aligned}$$

As expected from the hard photon spectra of short GRBs, the value of β_ν is about an order of magnitude higher than in the case of long duration bursts. Thus, the neutrino spectrum of short GRBs is steeper than the one of long bursts.

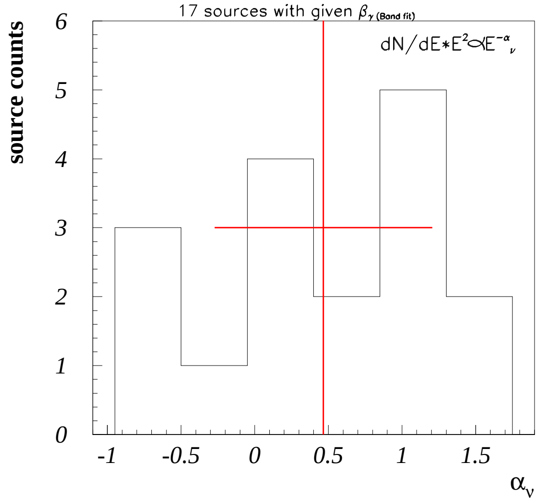

Figure 5.9: A first neutrino spectral index differing from β_ν is given for model 3, 17 sources are described by this model.

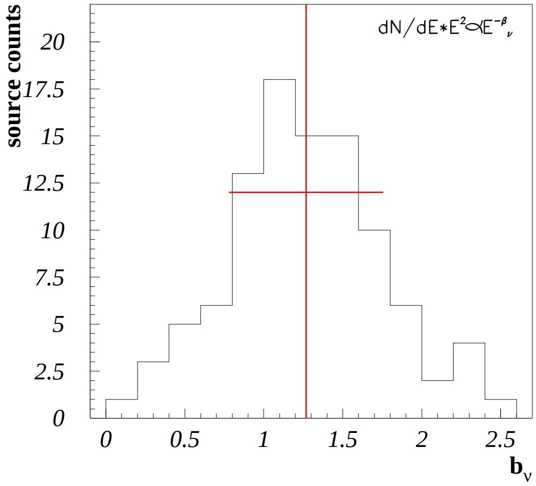

Figure 5.10: Second Neutrino index, given for 99 sources.

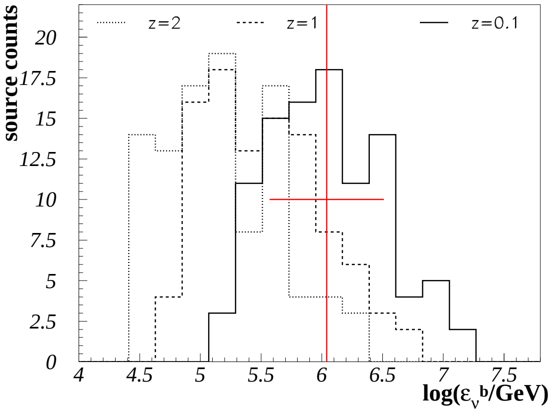

Figure 5.11: Energy ϵ_ν^b for three different redshifts, solid: $z = 0.1$, dashed: $z = 1$ and dotted: $z = 2$. The vertical and the horizontal line represent mean value and error for $z = 0.1$.

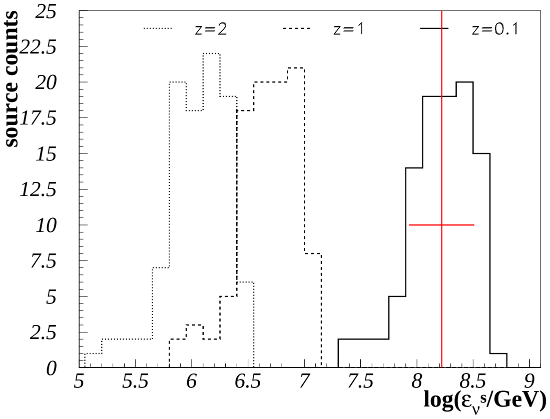

Figure 5.12: Energy ϵ_ν^s for three different redshifts, solid: $z = 0.1$, dashed: $z = 1$ and dotted: $z = 2$. The huge differences in the break energies result from the variation of the luminosity.

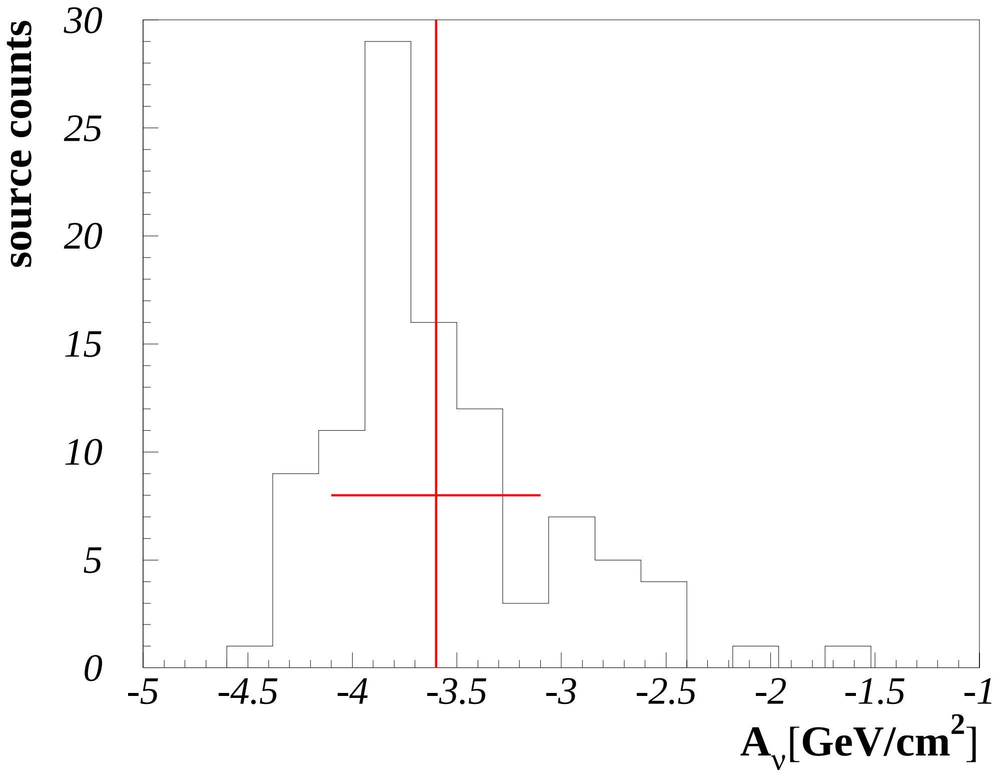

Figure 5.13: Neutrino flux normalization A_ν for Konus short GRBs.

Sample of SWIFT bursts

The sample of SWIFT-detected bursts has increased to 228 bursts as of March 12, 2007. Of these 228 GRBs, there are 201 with given spectral information. These 201 GRBs divide into 188 long and 13 short GRBs. Single powerlaw fits to the photon spectra are given on the SWIFT web page [Swi06a]. The spectrum represents the lower energy part of the Band function which corresponds to the upper part in the neutrino spectrum. SWIFT is relatively sensitive to high redshift GRBs. In the case of unknown redshifts, $z = 2$ has been assumed.

While BATSE covered a very wide energy range up to MeV energies, SWIFT detections usually cover energies only up to $\sim 150 - 350$ keV. The single powerlaw fits therefore represent the lower part of the photon spectrum with a spectral index of α_γ. Thus, the second part of the neutrino spectrum is covered by the spectral fits, yielding the second neutrino spectral index β_ν. The distribution of β_ν for the 201 SWIFT bursts is shown in Fig. 5.14 with a mean value of $\beta_\nu = -0.6$ for the 188 long bursts (solid line) and $\beta_\nu = -0.16$ for the 13 short bursts. The latter value shows that the few short GRBs detected by SWIFT are not necessarily hard bursts. The reason for the softness of these events may lie in the bias of the SWIFT detector due to the narrow energy band. The ratio of long to short bursts is about 18:1. The short hard events may simply be missed, since for hard spectra, the major emission occurs at high energies, $E_\gamma > 350$ keV and thus above the SWIFT detection threshold.

The distribution of neutrino normalization factors for the single sources is shown in Fig. 5.15. The total detected flux as detected by SWIFT is much lower than for the long bursts, an indication that the main signal may have been emitted outside of the energy detection band of SWIFT.

The break energy distributions are shown in Figures 5.16 and 5.17. For the first break energy, the major peak at $\sim 10^{5.4}$ GeV results from the fixing of the redshift at $z = 2$ for bursts without redshift information.

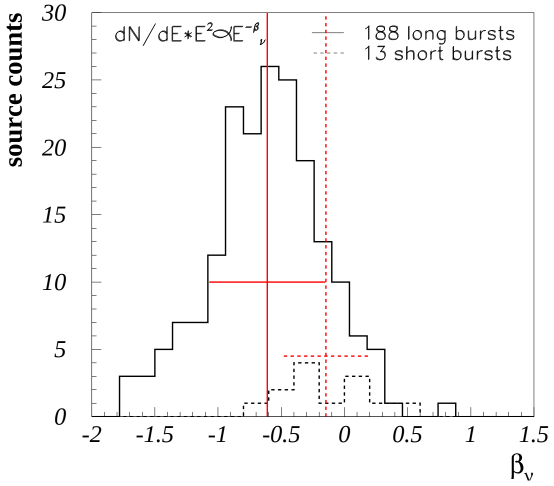

Figure 5.14: Neutrino spectral index for 188 long (solid line) and 13 short (dashed line) SWIFT bursts.

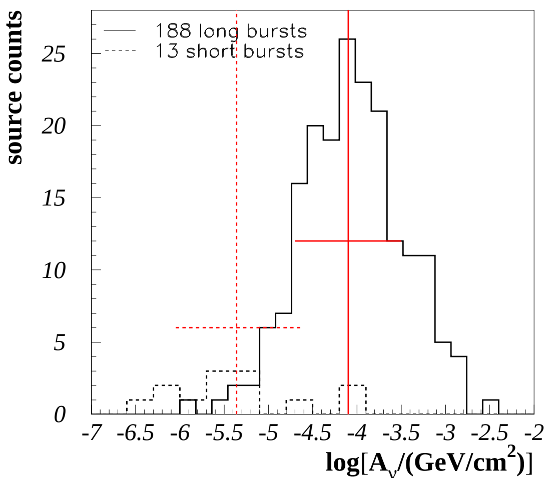

Figure 5.15: Neutrino flux normalization A_ν of SWIFT bursts, the solid line representing the 188 long bursts and the dashed line showing the 13 short events.

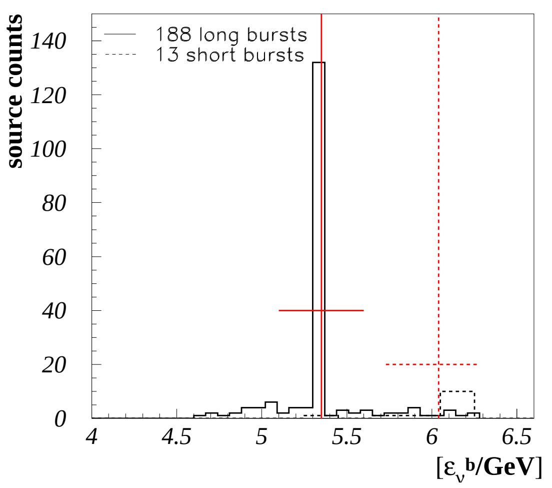

Figure 5.16: First break energy of SWIFT GRBs.

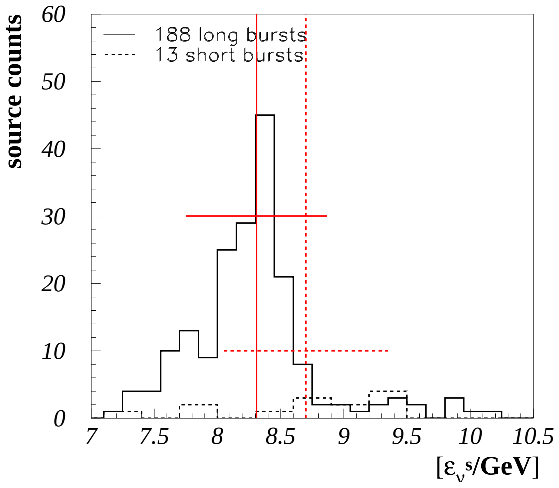

Figure 5.17: Second break energy of SWIFT GRBs.

5.3.2 Between coincidence and average predictions

For each burst i in a sample of n GRBs, a prediction of the prompt neutrino flux, Φ_i, from this source can be made as described above. With a large volume neutrino telescope like AMANDA, a large number of bursts can be analyzed simultaneously in order to increase the detection significance. By stacking many bursts, the signal is increased more than the background. This makes it interesting to look at a coincident spectrum of burst samples, i.e. a quasi-diffuse flux. The total flux Φ is given as

$$\Phi = \frac{\sum_i^n \Phi_i}{n}\,. \tag{5.19}$$

In this section, the coincidence spectra of each examined sample are described in more detail. The four samples of long bursts and the KONUS sample of short bursts are examined with respect to their coincidence and mean spectra and finally, a comparison between the samples is done. Neither the sample of short SWIFT bursts nor the AMANDA subsample will be considered here due to the small total number of bursts.

Figure 5.18 shows the expected energy spectrum for the variability sample, the solid line representing the coincidence spectrum, the dotted line displaying the average spectrum calculated from the mean parameters as given in table 5.2. There are large differences between the two spectra, especially concerning the spectral indices at low and high energies. The differences between coincidence and average spectrum in the lag sample are in the normalization rather than in the shape of the spectra, see Fig. 5.19. The reason for these deviations lies in the contribution of individual burst parameters far from the average. These bursts are not considered in average calculations at all, but can be responsible for a significant change in the spectral shape and normalization. The average and coincidence flux for the AMANDA subsample is shown in Fig. 5.20. Both versions of the energy spectra follow the larger sample with smaller deviations, because the distributions of the subsample show a similar behavior as the whole sample.

The mean and the coincidence spectrum for long SWIFT bursts is shown in Fig. 5.21. The differences between the two spectra are striking. The mean spectrum is much flatter in the middle energy part, following $dN_\nu/dE_\nu \sim {E_\nu}^{-1.4}$, rather than a quasi diffuse coincident distribution which follows an ${E_\nu}^{-2}$-spectrum. The reason for this is most likely that the average parameters have been determined independently. However, parameters like spectral shape and break energies are interconnected and this can lead to larger differences in mean and coincidence spectra as seen in Fig. 5.21.

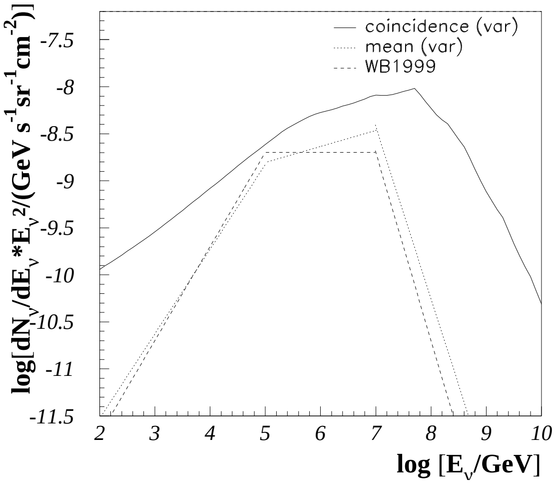

Figure 5.18: Comparison of coincidence and average spectrum (variability).

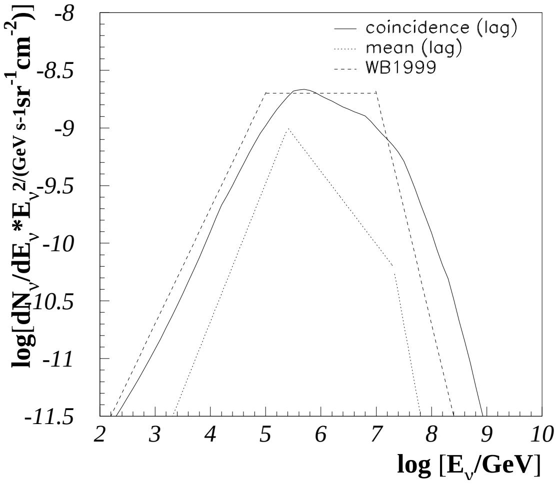

Figure 5.19: Comparison of coincidence and average spectrum (lag).

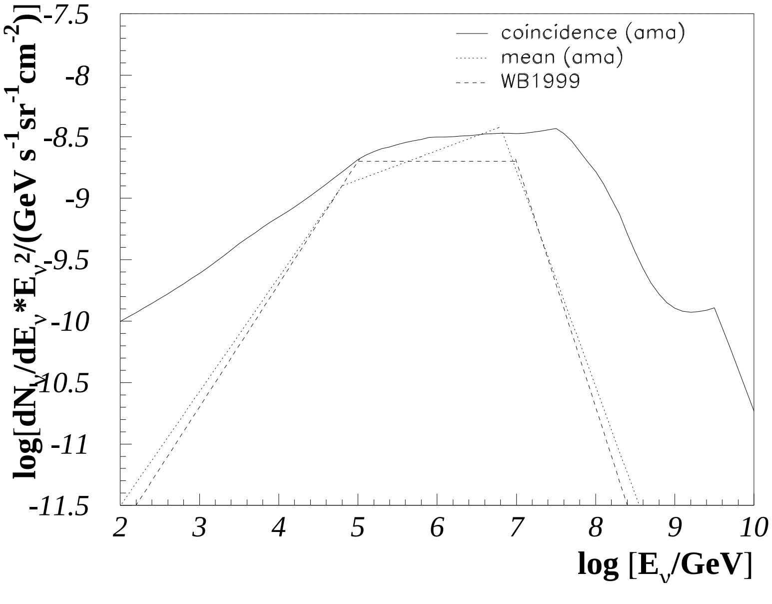

Figure 5.20: Comparison of coincidence and average spectrum (AMANDA-variability subsample).

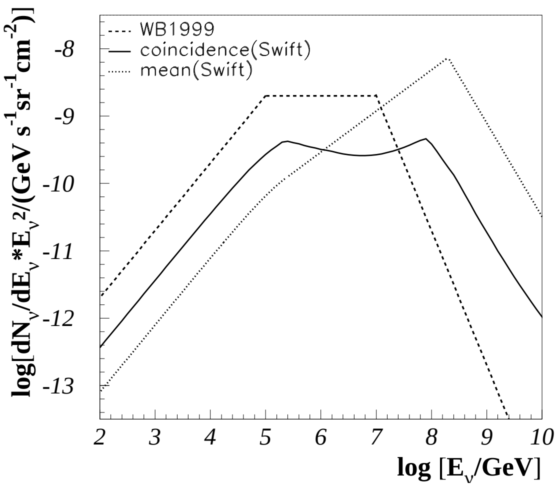

Figure 5.21: Comparison of coincidence and average spectrum (SWIFT sample).

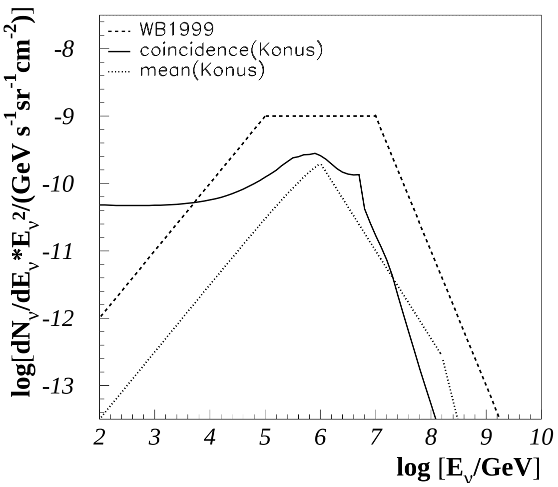

Figure 5.22: Comparison of coincidence and average spectrum (KONUS sample of short bursts).

Similar differences occur for KONUS short bursts. The muon neutrino spectra are compared in Fig. 5.22. Here, the main deviations are seen in the low energy part of the spectrum. The dominating reason here is that while 17 bursts have broken powerlaw spectra for the individual bursts, the mean spectrum is calculated for the single powerlaw parameters only. This graph emphasizes that a considerable fraction of the neutrino flux may be neglected due to restrictions from the keV-photon observing satellite. Only 17 of 99 sources have measured data at high energies, leading to the prediction of the low energy part of the neutrino spectrum. For all other bursts, an exponential cutoff towards lower energies has been assumed. However, the 17 bursts contributing at low energies already increase this part of the spectrum by several orders of magnitude as compared to a pure exponential cutoff spectrum.

To compare the different samples to each other, the coincidence fluxes of all samples are shown in Fig. 5.23. The flux numbers given in the figure refer to the following models:

1. BATSE variability sample,
2. BATSE lag sample,
3. KONUS sample of short bursts,
4. SWIFT sample of long bursts.

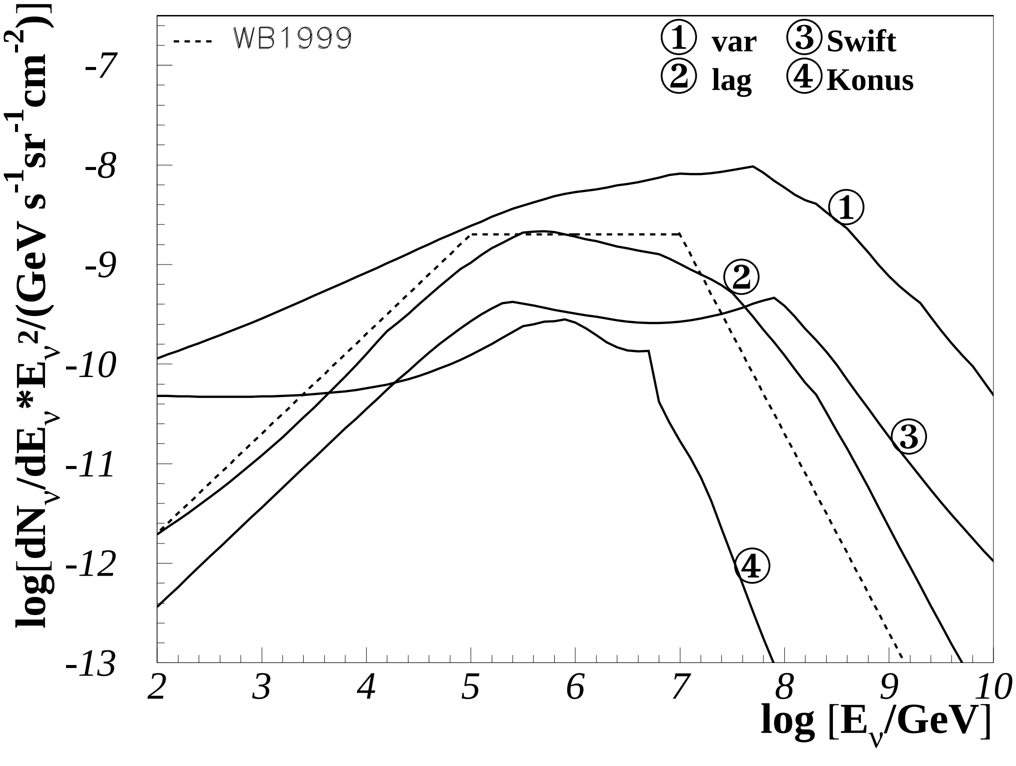

Figure 5.23: Summary of the coincidence spectra of all samples. Major differences can be seen between the variability (sample 1) and lag sample (sample 2), mostly due to differences in the second spectral index and normalization. The short bursts (sample 4) are generally very weak and produce a steep spectrum, while SWIFT-detected bursts (sample 3) have a flat spectrum and a high second break energy. All calculated mean spectra differ significantly from the average diffuse prediction made by Waxman and Bahcall (dashed line).

At first glance, the differences between the samples are obvious. Three major conclusions can be drawn from the comparison of coincidence spectra.

- While the spectral shape for the three samples of long bursts are *relatively* comparable, even small differences in the spectral indices result in order of magnitude deviations in certain parts of the spectrum. The main, systematic difference between the samples is the low normalization of the SWIFT sample. Here, the reason lies in the properties of the BATSE and SWIFT experiments. While BATSE had a wide field of view and could observe about 2π sr, its sensitivity was not as good as the one of SWIFT. This fact leads to the observation of a large number of strong GRBs for BATSE (~ 1 per day) compared with a lower number (~ 100 per year) of bursts with lower fluence for SWIFT. Consequently, the neutrino flux which is proportional to the photon fluence is also lower. The differences in the field of view are corrected by assuming a GRB rate of 1000/yr for all of the samples. The coincidence spectra of the two BATSE-samples are more than two orders of magnitude intenser than the SWIFT sample only due to the fact that the increased number of bursts in the SWIFT sample is not due to a large field of view but due to a good sensitivity. There are fewer strong bursts but a large number of low-intensity ones which reduces the total contribution of the signal. Such a bias from experimental data will be present in all of the experiments, since the results in each case will be dependent on properties such as energy range, sensitivity, field of view etc.

- The energy spectrum for short bursts is about one power steeper than the general flux for long bursts. This is a general conclusion and not specific to the investigated samples. The reason lies in the hardness of the photon spectra. Since the short keV photon spectra are typically much harder than the long burst spectra, neutrino spectra for short bursts tend to be softer (γ and ν energies are inversely proportional). This underlines that long and short bursts have to be treated separately.

- For all samples both average and coincidence spectrum differ from the spectrum that is considered as the standard diffuse spectrum. The differences between diffuse and lag spectrum are quite small, but the spectrum of the variability sample has significantly different features compared to the diffuse spectrum.

Figure 5.24 compares the mean spectra of the four different samples, underlining the conclusions which have been drawn above. In particular, the steepness of the short burst spectrum can be seen. The key point of the graph is the deviation of each of the mean spectra from the typically assumed Waxman-Bahcall flux. The examination of the three different samples of long bursts show that a mean spectrum is always dependent on the instrument as well as on the subsample used. It is thus important for a neutrino analysis of GRBs to consider the individual parameters and spectra. Even if not all energy spectra are known, the mean spectrum should be determined by looking at the parameter distribution of the sample and determine the mean spectrum according to the measured values rather than taking a generic spectrum. This fact will further be underlined in the next section where the neutrino detection rate will be examined for the individual bursts.

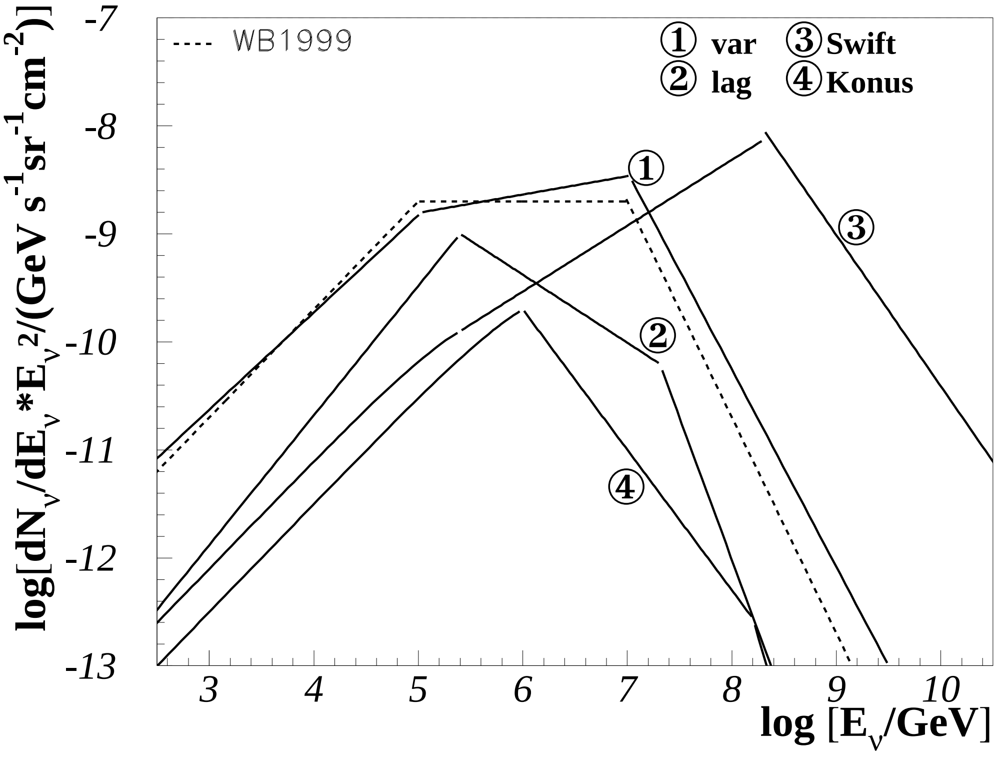

Figure 5.24: Neutrino prediction for mean neutrino fluxes of different burst samples. Two samples from the BATSE catalog 568 bursts from variability method (sample 1), 292 bursts (lag, sample 2) are presented as well as a sample of long SWIFT bursts and a sample of short KONUS bursts. All samples differ from the standard WB spectrum (dashed line, normalized to long GRBs). In particular, the SWIFT-detected bursts yield a much lower flux and the KONUS sample produces a steeper spectrum.

5.3.3 Estimate of neutrino detection rate

The rate of neutrinos as detected in neutrino Cherenkov telescopes like AMANDA and ICECUBE, is determined as described in Section 1.3.6. Here, the focus lies on the examination of single GRB rates and the variations of such a rate due to the individual properties of the single GRBs in *one* sample as well as the variations between the *different* samples. In addition, potential deviations of the individual GRB rates and deviations of mean and coincidence spectra from the generic Waxman-Bahcall spectrum will be discussed. Figure 5.25 shows the distribution of detection rates for single GRBs in the variability (solid line) and lag (dashed line). The thick line represents detection rates for single source spectra modeled as described above, while the thin, blue line shows the rates assuming a

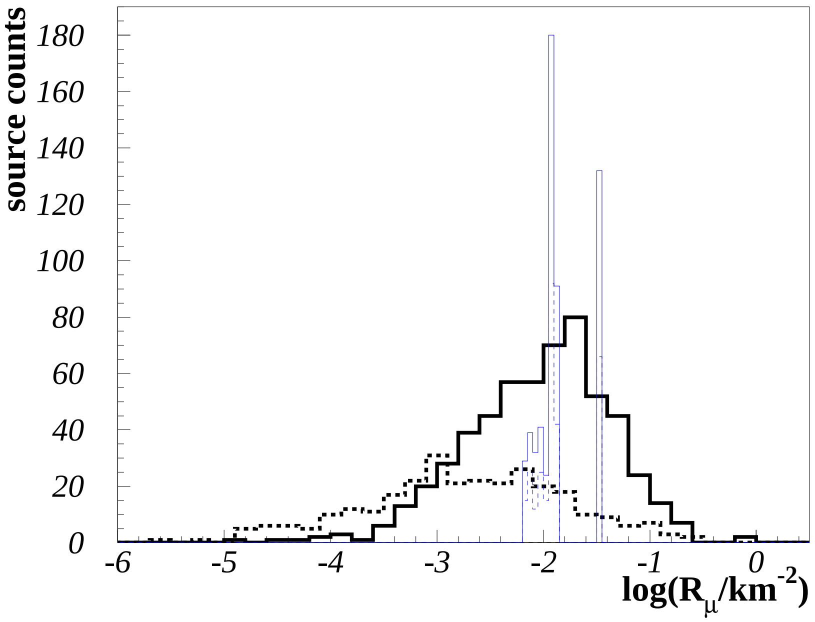

Figure 5.25: Muon neutrino rates for the single bursts using a threshold energy of $E_{\min} = 100$ GeV (thick lines). The rates are given per burst and per square kilometer. On average, the neutrino flux rates determined in the lag sample are lower than the ones for the variability sample ($\log(R_\mu^{lag}/\text{km}^{-2}) = -2.73 \pm 0.94$ compared to $\log(R_\mu^{var}/\text{km}^{-2}) = -2.05 \pm 0.67$). The thin, blue lines represent the same burst samples (solid: variability; dashed: lag) with the Waxman-Bahcall spectrum as input flux. All parameters except the incoming angle of the neutrino are fixed as described above.

Waxman-Bahcall spectrum. The only varying parameter in the latter case is the localization of the bursts. Focusing on the first case of varying GRB spectra, it can be seen that these scatter widely over almost six orders of magnitude. There are a few bursts with close to one event per km^2, while the mean of the distribution rather lies around $R \sim 0.01$ yr^{-1}. The exact values of the mean for each sample are given in table 5.3. The lag sample yields slightly lower values than the variability sample on average. Comparing the single burst parameter distribution with the distribution of Waxman-Bahcall spectrum shows clearly why a single source modeling is necessary. The strong variations are completely missed by the WB parameterization.

The latter conclusion can also be drawn for the short bursts detected by KONUS which are displayed in Fig. 5.26.

	mean ν_μ rate/GRB [km^{-2}]	total number of ν_μ [km^{-2}]
variability	$10^{-2.05\pm0.67}$	14
WB [var. sample]	$10^{-1.86\pm0.23}$	9.1
AMANDA subsample	$10^{-2.05\pm0.59}$	1.5
lag	$10^{-2.73\pm0.94}$	3.6
WB [lag sample]	$10^{-1.86\pm0.23}$	4.7
Konus	$10^{-2.76\pm0.69}$	0.28
WB [Konus sample]	$10^{-2.36\pm0.17}$	0.17
Swift(long)	$10^{-2.72\pm1.35}$	3.4
WB [Swift(long) sample]	$10^{-1.95\pm0.17}$	2.0
Swift(short)	$10^{-4.42\pm0.87}$	0.16
WB [Swift(short) sample]	$10^{-1.7750\pm0.0003}$	0.13

Table 5.3: Mean neutrino spectra parameters for the three samples, variability (568 bursts, single burst parameters and WB), lag (292, single burst parameters and WB) and the variability subsample of AMANDA bursts (82 bursts). In addition, the result for 99 short bursts detected by Konus is shown, as well as for 13 short and 188 long bursts in the Swift sample. The standard deviation to the mean values has been calculated as an error estimate.

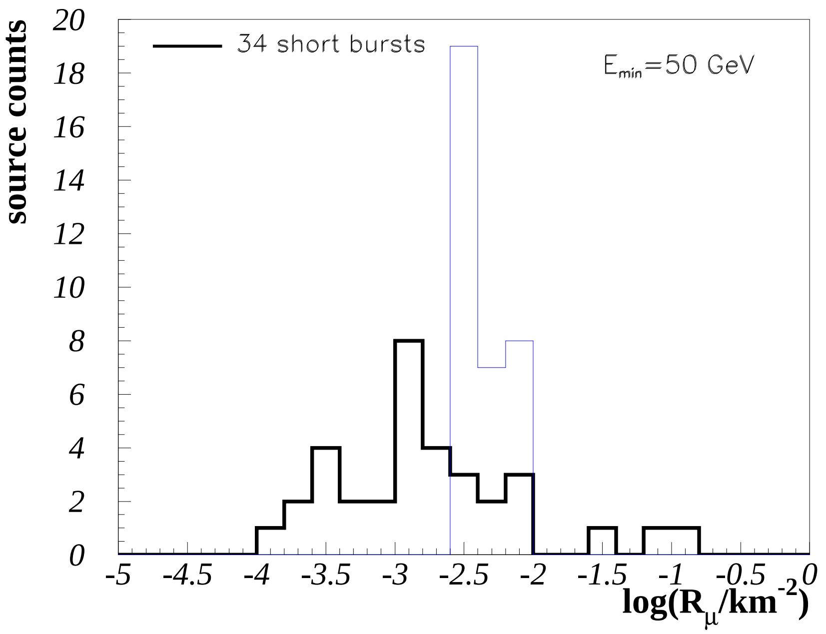

Figure 5.26: Konus single short bursts - muon neutrino rate for a threshold energy of $E_{\text{min}} = 50$ GeV. The thick, black line shows the rates using individual source spectra. The thin, blue line represents the same samples, but using a standard WB spectrum.

Only 34 of the 99 sources with spectral information in the KONUS satellite are well-localized by the IPN3, so that the detection rates are only given for these 34 events. The single source parameterization causes a much wider scattering than the WB rates. Also, the mean detection rate is about half an order of magnitude lower in the case of single source parameterization (see table 5.3). The main reason lies in the steepness of the actual GRB spectra. These are typically about one power steeper than assumed in the WB spectrum and have a relatively low flux at the main detection energy range in neutrino Cherenkov telescopes ($E_\nu > 10^4 - 10^5$ GeV). This demonstrates again that at least systematic differences in the spectra need to be taken into account.

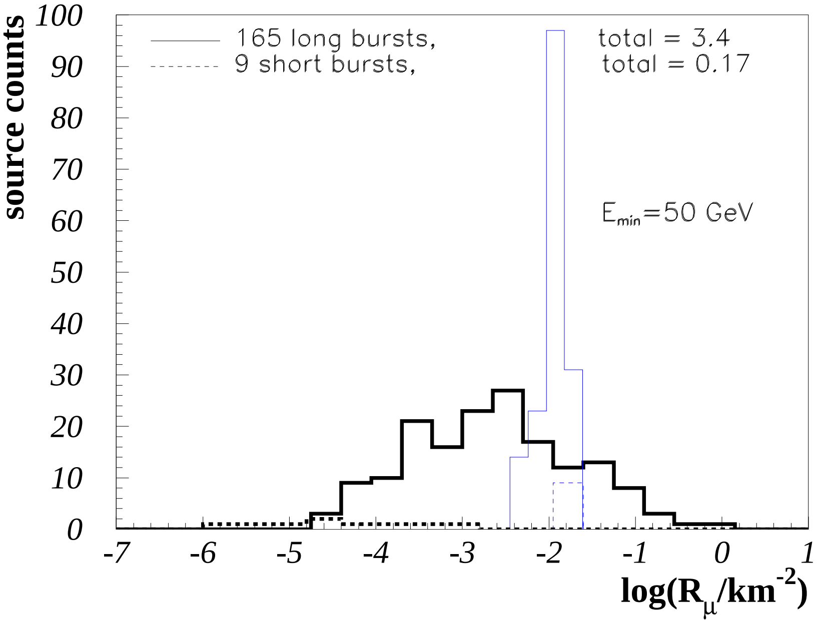

Figure 5.27: Muon neutrino rates for the SWIFT single bursts using a threshold energy of $E_{\mathrm{min}} = 50$ GeV. The thick, black lines show the rates using individual source spectra, the solid line representing long SWIFT bursts, the dashed line showing the 9 short ones. The thin, blue lines show the same samples, but using a standard WB spectrum. The only thing which is varied is the incoming direction of the neutrino with respect to the nadir angle.

Figure 5.27 shows the distribution of 165 long SWIFT bursts with given localization (solid line) and 9 short bursts. Due to the low statistics for short bursts, no general conclusion can be drawn for this class. In the case of the long bursts, the results from previous samples can be confirmed. Here, the systematic shift between WB rate and single source parameterization comes from the lower normalization of SWIFT bursts.

It is obvious from all of the samples that a single burst detection will be difficult even with instrumented arrays of one cubic kilometer like the ones planned for ICECUBE or KM3NET: the most intense bursts in the detector have a detection probability of < 1 neutrino event per km^2 effective area. The brightest bursts of ~ 1 event per burst and km^2 are very rare. In the case of SWIFT, there is one burst in two years of measurement yielding one event for neutrino detection. One bright burst every second year can be expected to be seen in either ICECUBE or KM3NET. For the individual experiments, it is only one bright burst every fourth year, since only half a hemisphere is visible with each of the telescopes.

GRB analyses as done by AMANDA usually make use of the temporal and spatial information from the GRB satellites. GRB030329 has been analyzed and it turns out that the single source sensitivity in this case is indeed several orders of magnitude above the predicted flux [S$^+$05b]. The burst has been analyzed adjusting the spectrum to the observed properties of the GRB, similar to how it is described above. An alternative approach like the one done by AMANDA, is the stacking of all bursts in a sample using the WB spectrum for all of the bursts. By stacking data from the sample of neutrino-induced muons [AI$^+$06d] or cascades [AI$^+$06c] according to the arrival direction and their arrival time, the sensitivity to a diffuse flux from GRBs according to WB can be determined. As Figures 5.25, 5.26 and 5.27 demonstrate, it is reasonable in the case of a Waxman-Bahcall like spectrum to use all bursts, since the detection rates are comparable. As shown here, however, the bursts have much wider scattered neutrino rates. This implies that bursts with very low detection rates (e.g. $< 10^{-4}/\text{km}^2$) could even decrease the sensitivity. This makes it interesting to consider the stacking of only the strongest bursts in a sample. A stacking analysis of the strongest sources of a class of objects in the sky has been done for the case of Active Galactic Nuclei already [AI$^+$06e, AI$^+$06a]. Here, in most cases, the optimum number of sources was ~ 10, depending on the luminosity distribution. The sources were stacked according to the photon wavelength, since the basic assumption is that the neutrino signal is proportional to the photon output.

In the case of GRBs, there are two striking differences. Firstly, it is expected that it will be necessary to stack many more than only 10 GRBs to have the optimal sensitivity. The reason is that GRB searches are almost background free, since data within a very small time window are selected per GRB. The case of signal stacking for AGN relies on pure spatial cuts and the background is therefore about 5 orders of magnitude higher. A detailed analysis is necessary to find out the optimal number of GRBs for such a stacking analysis. The second difference between the two analyses is that while for AGN, sources can be selected directly according to their signal strength in photons, GRBs need to be sorted by the actual neutrino detection rate. Figure 5.28 shows a scatter plot of the neutrino detection rate and the normalization of the neutrino spectrum. The latter is

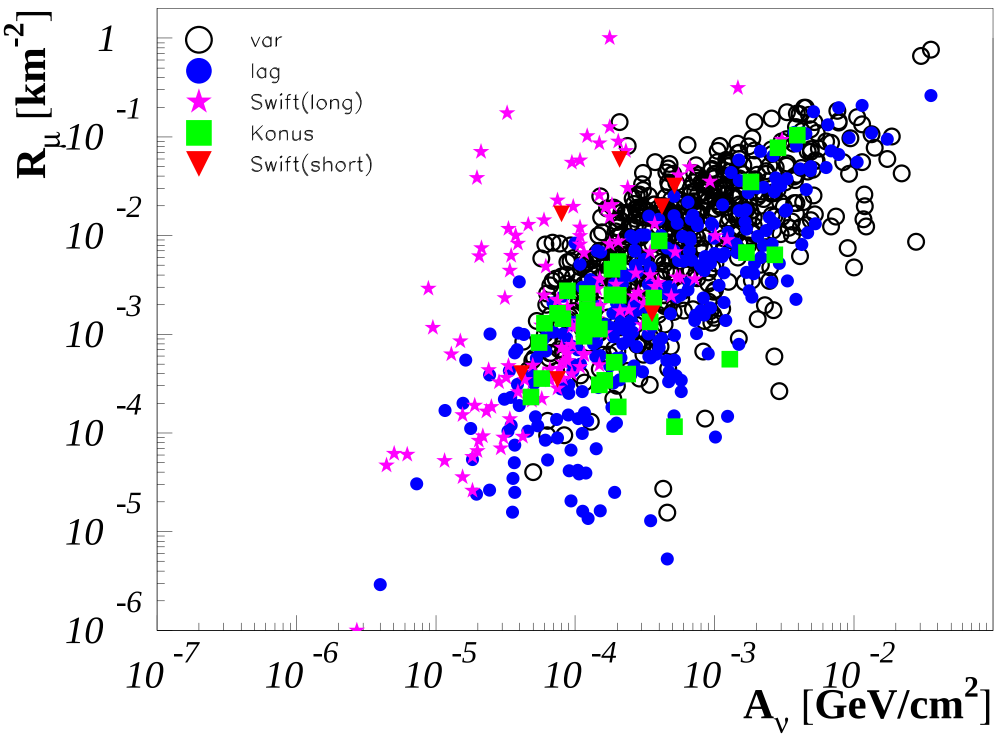

Figure 5.28: Muon neutrino detection rate R_μ vs. neutrino spectrum normalization A_ν for five different GRB samples using a threshold energy of $E_{\min} = 50$ GeV. Empty circles: variability sample; filled circles: lag sample, stars: SWIFT sample of long bursts; filled squares: KONUS short bursts; triangles: SWIFT short bursts.

directly proportional to the photon output. While a strong correlation is seen for all samples, there are still bursts off the main axis. These bursts can be crucial for the stacking selection.

Figures 5.29, 5.30, 5.31 and 5.32 show the striking differences in the selection process for the lag and variability sample as well as for short bursts and SWIFT long bursts. The panels in each of the figures shows the total number of neutrinos (solid line) and the total neutrino spectral normalization for a number of bursts. The rate and normalization constant is given per total number/normalization of all bursts in the sample in each case, so that the maximum value is one. In the case of the left panels, the sources are sorted by the strength of the spectrum, while in the right panel, the sorting is done by the actual signal strength in the detector.

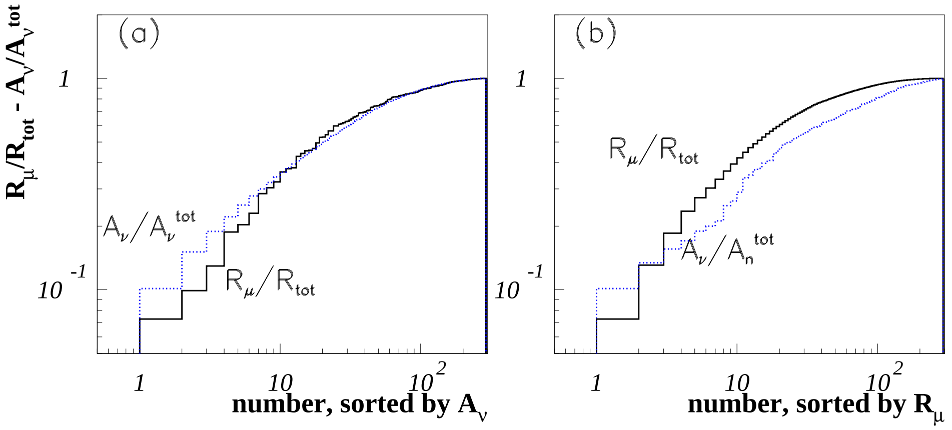

Figure 5.29: BATSE (lag) sample - total number of neutrinos and total neutrino normalization versus number of bursts (maximum: 292 bursts). The solid, black line shows the summation of the neutrino rate and the dotted, blue line displays the normalization. In (a), bursts are sorted according to the neutrino flux normalization. In (b), the sorting is done by the number of neutrinos in the detector. The comparison of the two graphs shows that it makes a big difference whether the bursts are selected by neutrino rate or spectral normalization.

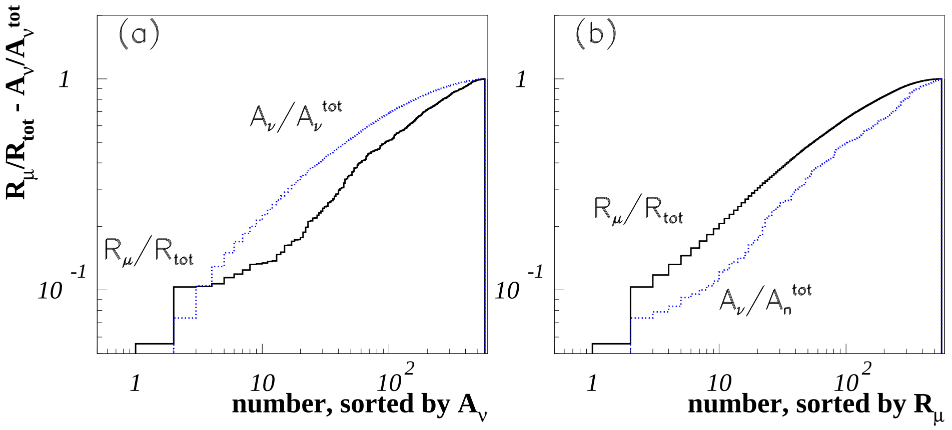

Figure 5.30: BATSE (var) sample - total number of neutrinos and total neutrino normalization versus number of bursts (maximum: 568 bursts). The solid, black line shows the summation of the neutrino rate and the dotted, blue line displays the normalization. In (a), bursts are sorted according to the neutrino flux normalization. In (b), the sorting is done by the neutrino rate strength. The comparison of the two graphs shows that it makes a big difference whether the bursts are selected by neutrino rate or spectral normalization.

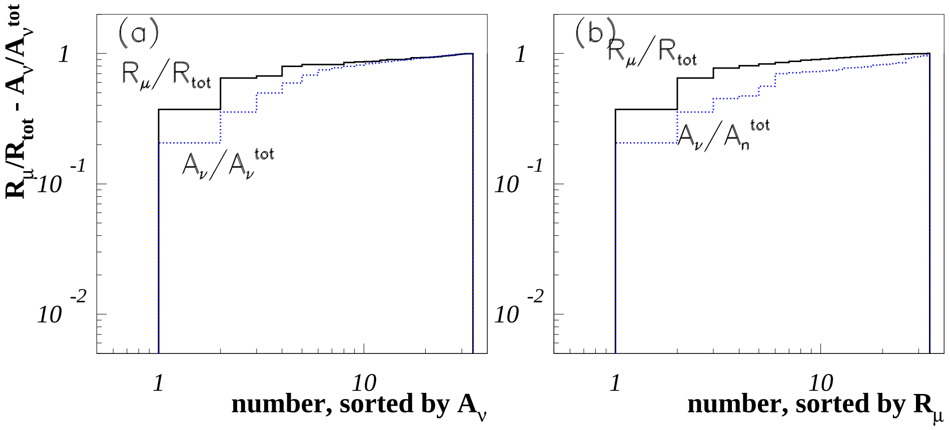

Figure 5.31: KONUS total number of neutrinos and total neutrino normalization versus number of bursts (maximum: 34 bursts). The solid, black line shows the summation of the neutrino rate and the dotted, blue line displays the normalization. In (a), bursts are sorted according to the neutrino flux normalization. In (b), the sorting is done by the neutrino rate strength. The comparison of the two graphs shows that it makes a big difference whether the bursts are selected by neutrino rate or spectral normalization.

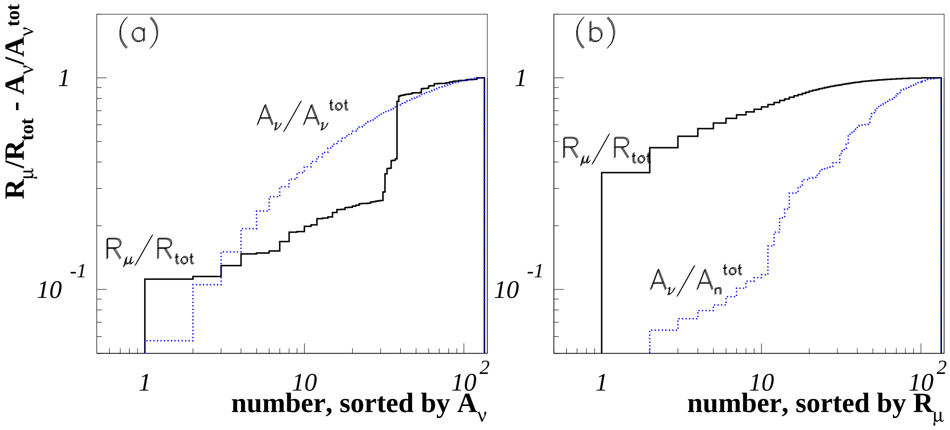

Figure 5.32: SWIFT total number of neutrinos and total neutrino normalization versus number of bursts. The solid, black line shows the summation of the neutrino rate and the dotted, blue line displays the normalization. In (a), bursts are sorted according to the neutrino flux normalization. In (b), the sorting is done by the neutrino rate strength. The comparison of the two graphs shows that it makes a big difference whether the bursts are selected by neutrino rate or spectral normalization.

The lag and the variability sample (Fig. 5.29 and 5.30 respectively) show only small, but still visible differences in the selection process. If the two lines agree, the selection can be done either way. In case of stronger disagreement, it is necessary to select the bursts by rate and not by spectral strength. Further, a flat curve with an early saturation level is better-suited for stacking, since this suggests that the first part of the curve suffices for an analysis. In the case of a slowly increasing curve, generally speaking more bursts need to be stacked.

For the short bursts detected by KONUS, the signal selection looks similar in the two cases. This can already be gathered from Figure 5.28: there are a few GRBs with relatively low rates compared to the normalization. All other bursts are on the main axis of the normalization-rate correlation. While low rates at high normalizations only make a difference in the steepness of distributions, as shown in Fig. 5.31, low normalizations at high rates have a large impact in the behavior of the summation. This is the case for long SWIFT bursts, where a few bursts have high rates relative to the normalization as seen in Fig. 5.28. Figure 5.32 shows the summation of rate and normalization with respect to the number of bursts, again, the left panel with bursts sorted according to the normalization, the right panel sorting the bursts according to their signal strength in the detector. There are extreme differences in the two sorting processes. The correct way to stack the bursts is shown in the right panel.

Even with little or no differences in the behavior of the two panels as it is the case for KONUS short bursts in Fig. 5.31, the behavior between summing the normalization or the rate is still not the same. The summation of the rates leads to a much flatter distribution than using the normalization.

Even though the distributions of all four samples are very different, the conclusion is the same in all of the cases: it is necessary to sort the bursts according to their neutrino detection rate and not according to the normalization of the spectrum. The reason lies in variations of the spectral indices and the break energies of the spectra, but also in the differences of the incoming angle of the neutrinos.

5.4 Summary & conclusions

This chapter deals with the neutrino flux properties of single GRBs and with differences in the single source spectra as well as variations between different samples. Primarily, it is shown that the variation of single source spectra changes both the spectral behavior and also the expected neutrino rate in a detection array, significantly. Here, the variations simply rely on using the actual spectral information from different satellites, BATSE, KONUS and SWIFT, while the WB spectrum is based on average parameters as known from the BATSE time. The investigation of the theoretical detection rates for single bursts show that the event rates scatter between 10^{-5} events/km^2 and ~ 1 event/km^2 using single burst predictions, but that event rates are fixed within a factor of ~ 3 when using a generic WB spectrum.

In addition to single burst variations, significant differences in the burst samples are observed. These arise mostly from the selection effects for each of the samples: the class of short bursts has a steeper spectrum than the typical WB spectrum for long bursts. Short burst photon spectra are usually harder than their long equivalents. The hardness in photons translates into a spectral softness for neutrinos. Therefore, the strong deviation from KONUS short bursts from the mean WB spectrum relies on intrinsically different properties between short and long bursts.

The sample of SWIFT long bursts yields a much lower quasi-diffuse neutrino flux than the BATSE samples and also lower than the WB flux suggests: while BATSE had a very large field of view ($\sim 2\pi$ sr), SWIFT sees about 2 sr of the sky, but with a much higher sensitivity. This results in the observation of more and more weak bursts compared to the BATSE sample. Since the photon intensity as observed at Earth translates directly into the neutrino flux normalization, the quasi-diffuse neutrino flux from the SWIFT sample is bound to be much lower than the BATSE coincidence flux.

From the absolute values of the GRB neutrino rates it can be seen that single bursts are generally unlikely to be detected in 1 km^3 arrays like ICECUBE or KM3NET. The most intense bursts still yield < 1 event per km^2. The observation of a whole source class, however, is more likely. A stacking analysis of all GRBs in the northern hemisphere has already been done with AMANDA. The sensitivity does not reach the predicted flux level yet, and is still about an order of magnitude higher than the WB flux [AI$^+$06d]. The limit is set by assuming a WB like spectrum, while here, we suggest to use single source spectral predictions as discussed above. Also, the significance is likely to be optimal already for a small number of bursts, namely the ones with the strongest signal in the detector. A similar analysis has been done with classes of Active Galactic Nuclei, where the optimal number of sources was found to be ~ 10 per source class [AI$^+$06e, AI$^+$06a]. In the case of GRBs, the background is reduced significantly compared to the AGN search, since the time window of analyzed neutrino data lies in the order of $\sim$ 50 s. The AGN classes have been considered to permanently emit neutrinos. In that case the background is much higher. The number of GRBs to be stacked is expected to be much larger than 10, but still smaller than the maximum number of sources.

In addition, we conclude that it is necessary to distinguish between bursts from different satellite experiments. As explained above and shown in detail in previous sections, different satellites are sensitive to different kinds of bursts. These are experimental selection effects, due to variations from satellite to satellite in the energy band, field of view, sensitivity and more.

In the years between 2000 and 2004, this was not possible BATSE was not taking data anymore, and SWIFT was only launched in November 2004. Between 2000 and 2004, many different satellites contributed to collecting a relatively large sample of GRBs. However, most of these satellites were not launched primarily for GRB detection, but were built for different purposes. This results in a relatively low number of GRBs per satellite and the single samples can barely be used for an analysis of GRB neutrino spectra. Many satellites launched before the SWIFT era are able to give the duration and sometimes the fluence of the bursts, but there is only very little spectral information during that time. Therefore, an average spectrum like the WB flux has to suffice in this case. Using the knowledge of the systematically different short burst spectrum, only long bursts can be included in such an analysis: the signal expectation deviates too much for short events.

In the case of burst samples with missing spectral information for several bursts, it is reasonable to use average parameters as calculated from the bursts with given spectral information. In the case of muon neutrino searches, the complete sample is larger than the number of bursts to be used in the analysis, since only the northern hemisphere can be used to ensure that the detected muons are neutrino-induced. For a statistical analysis of the mean parameters for the given satellite properties, the investigation of the complete sample is useful.

With the launch of SWIFT, the picture is more complete. Most bursts detected by SWIFT have spectral information and preliminary values are given on the SWIFT web-page [Swi06a] already shortly after the burst. In addition, redshift measurements have been made more frequently since the launch of SWIFT. The relation between peak and break energy seems to become a reliable redshift estimator, so that GRBs could in the future serve as standard candles.

CHAPTER 6

Astrophysical implications of high energy neutrino limits

Second generation high energy neutrino telescopes are being built to reach sensitivities of neutrino emission from galactic and extragalactic sources. Current neutrino detectors are already able to set limits which are in the range of some emission models. In particular, the so far most restrictive limit on diffuse neutrino emission have been presented by the AMANDA Collaboration [H$^+$06a]. Stacking limits which apply to AGN point source classes rather than to single point sources [AI$^+$06e] are given as well. In this chapter, the two different types of limits will be used to draw conclusions about different emission models. An interpretation of stacking limits as diffuse limits to the emission from considered point source class is presented. The limits can for instance be used to restrict the predicted correlation of EGRET-detected diffuse emission and neutrino emission. Also, the correlation between X-ray and neutrino emission is restricted. Further results for source classes like TeV blazars and FR-II galaxies are presented. Starting from the source catalogs so-far examined for the stacking method, we discuss further potential catalogs and examine the possibilities of the second generation telescopes IceCube and KM3NeT by comparing catalogs with respect to northern and southern hemisphere total flux.

6.1 The Olbers paradox for neutrinos

As has been well known for hundreds of years, the sky would be infinitely bright in optical light, if all space were homogeneously full of stars, and space were infinitely extended without any change in properties [Olb26]. This reasoning can be applied to stars as well as to galaxies. This argument can also be applied to electromagnetic emissions and just as well to neutrino emission. The solution to Olbers paradox is that space is not homogeneously full of identical distributions of stars or galaxies, and that the Universe evolves quite strongly. This implies that the integral over the optical light of all galaxies has a finite sum, which does not exceed an observable level. Clearly, given a proper sampling of galaxies, it is possible to determine this level. In some cases, there is a unique relationship between the optical light and the emission at some other wavelength. Starting from this correlation, the summed emission from all galaxies over all history can be deduced and it is a simple function of the sum at optical wavelengths. The optical emission can certainly be replaced with the emission at some other electromagnetic wavelength, such as X-rays. Equally, the correlated wavelength can be neutrino emission. If we now do not know what the sum of the emission is at the electromagnetic wavelength, but have limits, then a limit for the neutrino emission can be deduced. Vice versa, if a limit for the neutrino emission is given, a corresponding limit for the electromagnetic emission can be derived. In either case, it might happen, that a known background is present, and it can be deduced whether this specific class of sources could possibly explain all background at the other "wavelength". In this chapter, this argument is started with neutrinos, for which a limit can be set, and then a limit for the electromagnetic background is derived. Alternatively, the electromagnetic background can be used for a start, and then a limit for the neutrino emission can be set. So we have the *Olbers paradox for neutrinos.* This is the key point of this chapter.

More concretely, the interpretation of different AMANDA neutrino flux limits is done for different classes of Active Galactic Nuclei (AGN). In the case of a stacking analysis in which the strongest sources from the same class are selected, a method for the interpretation of these limits as limits to the diffuse flux from the given source class is developed. Additionally, future possibilities of second generation neutrino telescopes like IceCube and KM3NeT are examined. Different source classes are discussed with respect to their distribution in the sky, i.e. which sources are in the northern and which are in the southern hemisphere. The field of view for IceCube respectively KM3NeT is the northern respectively the southern hemisphere and their view of the sky is complementary.

This chapter is organized as follows: Current neutrino flux limits are investigated in Section 6.2. A general ansatz for the interpretation of stacking limits as diffuse limits is presented here. In Section 6.3, the method is applied to AMANDA limits which have been derived by stacking AGN according to their electromagnetic output. The question which stacking limits apply to which normalization scenario is discussed in Section 6.4 and it is examined how the limits restrict different models. In Section 6.5, further source classes are examined according to the possibility of applying the stacking method for high energy neutrinos, i.e. $E_\nu >$ TeV. In addition, a comparison of the contribution from the northern and southern hemisphere is done for various source classes in order to compare the capabilities of next generation's telescopes IceCube and KM3NeT. The results are summarized in Section 6.6.

6.2 Neutrino flux limits

The conversion of stacking limits into stacking diffuse limits is the main topic of this section. Basically the contribution of the identified sources to the integrated background is used at a chosen electromagnetic wavelength to estimate by way of a physical model the corresponding ratio for neutrinos: What fraction of identified neutrino source candidates goes towards the integrated background? It is important to note here that conservative estimates are used in order to obtain absolute, reliable upper limits. As limits to the flux of identified source classes we use the sample of AGN classes from the AMANDA stacking analysis which is described in [AI$^+$06e, AI$^+$06a].

To avoid any confusion of the notation, a paragraph on the limit conventions precedes the actual discussion of the limits.

6.2.1 Limit conventions

Throughout this chapter, several types of neutrino flux limits will appear. Limits are usually given in the form ${E_\nu}^2 \cdot dN_\nu/dE_\nu$ with dN_ν/dE_ν as the differential neutrino flux at Earth and E_ν as the neutrino energy.

Throughout the chapter, the limits will be denoted as follows:

- Φ^{DL}: Diffuse Limit (DL) derived by using data from the complete northern hemisphere. It is given in units of GeV $\mathrm{cm}^{-2}\,\mathrm{s}^{-1}\,\mathrm{sr}^{-1}$.
- Φ^{SL}: Stacking Limit (SL) in units of GeV $\mathrm{cm}^{-2}\,\mathrm{s}^{-1}$, obtained for the point source flux from a certain class of AGN. The principle is indicated schematically in Fig. 6.1. As an example, three source classes, FR-I and FR-II galaxies as well as blazars, are displayed. The stacking limits are obtained by stacking the most luminous sources of the same class in the sky, indicated by sources with filled circles. Weaker sources (empty circles) are not included.
- Φ^{SDL}: Stacking Diffuse Limit (SDL), derived from the stacking limit in the same units as the diffuse limit, GeV $\mathrm{cm}^{-2}\,\mathrm{s}^{-1}\,\mathrm{sr}^{-1}$. It is determined by taking into account the contribution from weaker sources as well as yet unidentified sources, present in a diffuse background.

A similar convention is used to denote the corresponding sensitivities:

- Φ^{DS}: Diffuse Sensitivity (DS), giving the sensitivity of AMANDA towards a diffuse signal from the northern hemisphere. Units are GeV $\mathrm{cm}^{-2}\,\mathrm{s}^{-1}\,\mathrm{sr}^{-1}$.
- Φ^{PS}: the sensitivity to a single point source in AMANDA. Units are GeV $\mathrm{cm}^{-2}\,\mathrm{s}^{-1}$.

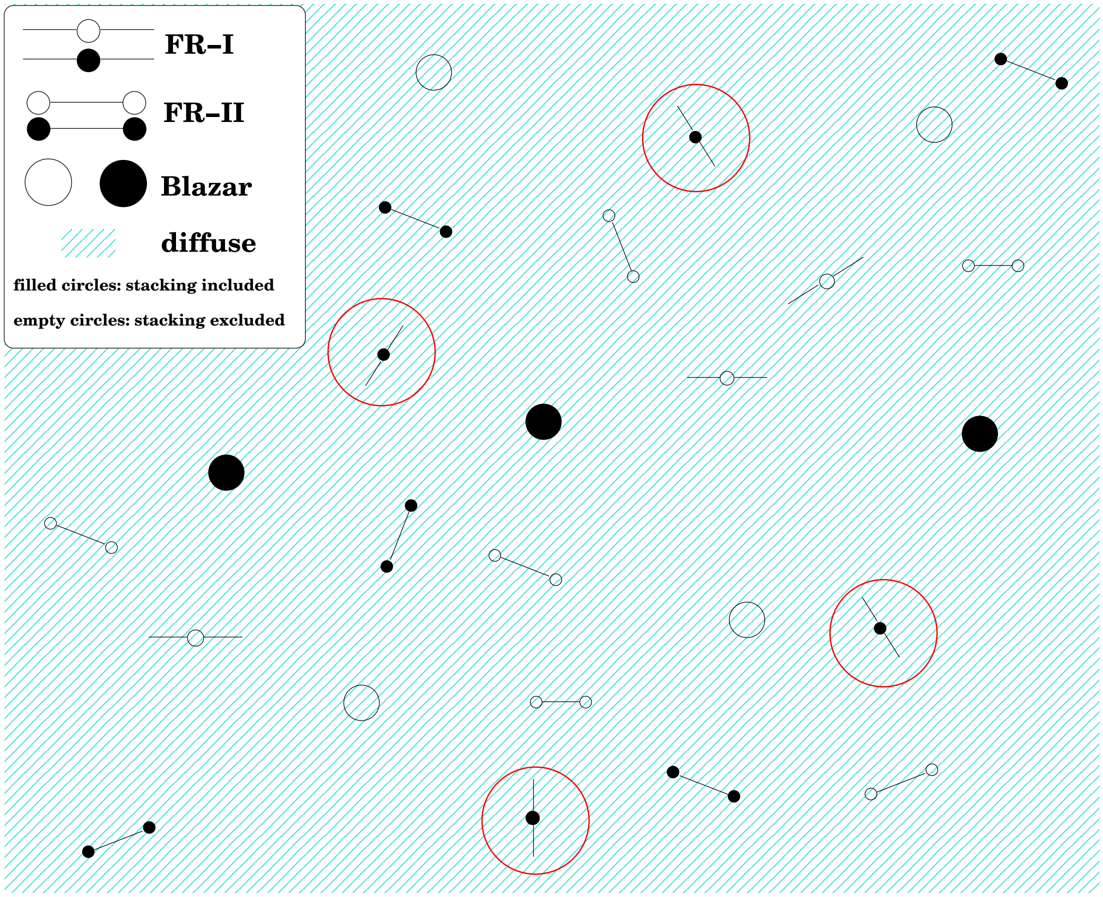

Figure 6.1: Schematic figure of the principle of source stacking. Objects are classified into source classes (here: FR-I and FR-II galaxies as well as blazars). Under the signal hypothesis that photons in a certain bandpass are directly correlated to neutrinos, the sources are selected according to their strength in the corresponding bandpass. The most intense sources are then stacked for an analysis of a neutrino signal from the source class. This is indicated for the case of FR-I galaxies as circles around the objects. Only the strongest sources are used in the stacking analysis (filled circles), while weaker objects are not used (empty circles). An estimate of the remaining source signal is needed as well as knowledge about unresolved sources, possibly seen as diffuse background in order to interpret the stacking neutrino limits as diffuse upper bounds to the given source class. The diffuse background varies with the source class.

6.2.2 Limits on the total diffuse neutrino flux

The unfolded spectrum of the diffuse neutrino flux as observed by the AMANDA experiment is indicated in e.g. Fig. 6.8. It can be seen that the measured flux follows the prediction of the atmospheric neutrino spectrum and no extragalactic contribution is observed [M$^+$05d]. The unfolded spectrum is derived using data from the year 2000. The current limit on the diffuse muon neutrino flux from extragalactic sources is given for four years of data (2000-2004) [H$^+$06a],

$$\Phi^{\mathrm{DL}} = 8.8 \cdot 10^{-8} \mathrm{GeV\,cm^{-2}\,s^{-1}\,sr^{-1}} \tag{6.1}$$

in the energy range of $10^{4.2}$ GeV to $10^{6.4}$ GeV.

In addition to a diffuse search, a possible signal from single sources is examined. No signal excess above the atmospheric background was observed yet. To maximize the significance of the signal to background expectation, a stacking method has been applied examining different source classes of AGN [AI$^+$06e]. This method is commonly used in cases where a single source is not likely to have a significant signal above background, see e.g. [M$^+$96]. Given the limit for a certain source class, Φ^{SL}, the differential flux renormalized to a diffuse signal is

$$\Phi^{\mathrm{SDL}} = \epsilon \cdot \xi \cdot \frac{\Phi^{\mathrm{SL}}}{2\pi \mathrm{sr}}\,. \tag{6.2}$$

The transition from point source to diffuse flux is done by dividing the source limits by the field of view of AMANDA, $2\,\pi$ sr. The stacking factor ϵ is the ratio of the total photon signal in the sample and the photon signal which is included in the analysis. Figure 6.1 gives a schematic representation. The stacking factor corrects for all sources with empty circles in the diffuse limit, since the signal from these sources is not included in the stacking analysis. The diffusive factor ξ represents the ratio of the total diffuse flux to the contribution of resolved sources. Sources which have not been resolved yet have to be considered as potentially contributing to the total diffuse neutrino signal as they contribute to the isotropic photon signal. In Fig. 6.1, this is indicated by the diffuse background which is different for each source class. This background is identified in a few cases by looking at the luminosity function of the objects, in others by measurements of the diffuse component. A detailed view on ϵ and ξ will be given in Section 6.3.

6.3 Point source limits on AGN neutrino fluxes

Recently, a stacking analysis has been published for the first time for a neutrino signal from Active Galactic Nuclei for which eleven AGN source classes have been defined. The source classes have been defined and selected as follows. The catalogs below have been selected in [AI$^+$06e].

1. GeV blazars detected by EGRET (*GeV*).
2. Unidentified GeV sources observed by EGRET (*unidGeV*). Sources of possible galactic origin have been excluded.
3. Blazars that have been observed at infrared wavelengths (*IR*).
4. Blazars that have been observed at keV wavelengths by the experiment HEAO-A (*keV(H)*).
5. keV blazars observed by the ROSAT experiment (*keV (R)*).
6. The class of blazars with observed TeV emission (*TeV*).
7. Compact Steep Sources (CSS) and GHz peaked sources (GPS) (*CSS/GPS*) as selected by O'Dea [OB97].
8. Low luminosity Faranoff Riley galaxies (FR-I) with M-87 included (*FR-I(M)*).
9. FR-I galaxies excluding M-87 (*FR-I*). These two different cases are necessary to consider, since M-87 is the closest AGN (distance $\sim$ 20 Mpc) and dominates the total signal of all FR-I galaxies.
10. High luminosity Faranoff Riley galaxies (*FR-II*).
11. Quasi Stellar Objects (*QSO*).

References to the corresponding catalogs as well as a detailed description of the analysis methods are given there. In brackets, the abbreviations for the source classes are given as they appear in Fig. 6.2.

The limits on the neutrino flux from the given source classes are displayed in Fig. 6.2. They are compared to the single source sensitivity of AMANDA of $\Phi^{\mathrm{PS}} = 5.9 \cdot 10^{-8}\,\mathrm{GeV\,cm^{-2}\,s^{-1}}$ to point out the improvement that has been achieved in the stacking approach. In the following, the stacking factor ϵ and the diffusive factor ξ will be discussed. It will be shown that seven of the eleven samples can effectively be used to determine a diffuse limit on the neutrino flux from the given class.

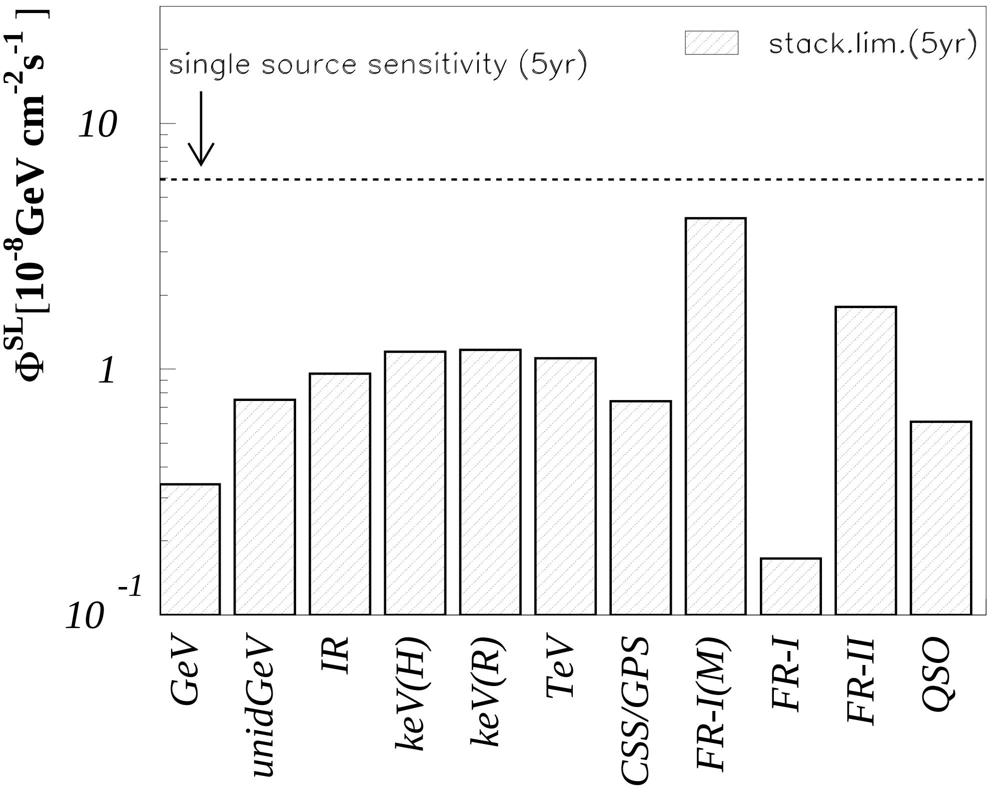

Figure 6.2: Limits on the neutrino flux for a given source class [AI^{+}06a]. Limits in this representation are given per source. The source classes are labeled with the abbreviation indicated in the list of the samples above.

6.3.1 The stacking factor

The number of sources in a sample that is included in the stacking analysis is determined by optimizing the expected significance for signal and background. Subsequently, the amount of the total photon signal of the analyzed sources is determined by the number of included objects. This is shown schematically in Fig. 6.1. The strongest FR-I galaxies (filled circles) are included in the stacking analysis. The stacking process for FR-I galaxies is indicated by circles around the stacked objects. FR-I galaxies having a too weak signal (empty circles) are not part of the stacking and have thus to be included in the *stacking factor* ϵ. Quantitatively, the ratio of the total photon signal and the signal of the sources that are used in the stacking approach is represented by ϵ. The precise values of ϵ for each class are given in table 6.1.

Source class	selected wavelength	ϵ	ξ	Φ^{SL}	possible diffuse limit?
EGRET GeV	> 100 MeV	1.4	< 12	2.71	yes
unid. EGRET	> 100 MeV	1.3	1	31.7	yes
infrared	$60\,\mu$m	1	-	10.6	no
keV (HEAO-A)	$(0.25, 25)$ keV	1	-	3.55	no
keV (ROSAT)	$(0.2, 2)$ keV	1.2	1.43	9.71	yes
TeV blazars	> 100 GeV	1	-	5.53	no
CSS/GPS	178 MHz, 2.7 GHz,5 GHz	1.3	model dep.	5.94	yes
FR-I w. M-87	178 MHz	-	-	4.11	no
FR-I w/o M-87	178 MHz	1.1	model dep.	2.91	yes
FR-II	178 MHz	2.65	< 160	30.4	yes
QSOs	UV	1.3	model dep.	6.70	yes

Table 6.1: Table of the source class limits obtained with the stacking method. Five years of data, 2000-2004, have been used for the analysis with AMANDA in [AI$^+$06a]. Listed are the source class, the selection wavelength, the stacking and diffusive factors, the stacking limit Φ^{SL} in units of $10^{-8}\,\mathrm{GeV\,cm^{-2}\,s^{-1}}$ and the possibility of interpreting the stacking result as a diffuse limit.

Some of the stacking classes cannot be used for a diffuse interpretation. Firstly, the number of sources needs to be sufficiently high. An indication for an insufficient number of sources would be the use of all the sources in a sample in the stacking analysis. Secondly, the luminosity function should be moderately falling: if only very few sources in our vicinity dominate the signal, no conclusions about the overall diffuse contribution can be justified.

The complete sample was used for stacking in several cases due to the low number of detected sources in the given wavelength interval. In particular, these source classes are the infrared and HEAO-A sources as well as the TeV blazars. Since all twelve observed infrared sources have been used and only three sources are reported from HEAO-A, a diffuse limit to the source class cannot be derived for these samples. There are five sources in the stacking sample of TeV blazars. Due to the small number, this class cannot be used for a diffuse interpretation. Due to the strong absorption of the TeV signal in photons, the contribution of a neutrino flux from TeV-resolved photon sources is expected to be much lower than the total flux. This is discussed in detail in Section 6.4.

Apart from the three classes already excluded, the class of FR-I galaxies including M-87 is not suitable for an interpretation of a stacking limit as a diffuse limit: M-87 makes up most of the photon signal from all FR-I galaxies. This is also the reason why the stacking limit is very close to the single point source sensitivity. This result must therefore rather be interpreted as a point source result of M-87. The FR-I sample without M-87 on the other hand is applicable for the diffuse interpretation.

6.3.2 The diffusive factor

Apart from the contribution of resolved sources to a diffuse background, a component of unresolved sources has to be considered. The ratio of the total diffuse signal to the signal of resolved sources is called the *diffusive factor* ξ in the following. In Fig. 6.1, this is indicated as the diffuse photon background of unidentified sources. A truly diffuse contribution from e.g. dark matter decays is discussed as a component of the diffuse photon background [BK06], but it will be considered as negligible here. Any contribution of a diffuse component not connected to any source population would improve the limits accomplished.

70% of the diffuse X-ray background has been identified as AGN in the ROSAT data sample [BH05]. Thus, the diffusive factor ξ, which is the inverse of the fraction of resolved sources, for the keV ROSAT data sample is given as $\xi_{ROSAT} = 1.43$. Note that today, XMM-NEWTON and CHANDRA provide values of $\sim 95\%$ resolved sources. But since both the neutrino flux predictions are based on and the stacking limit has been derived from ROSAT data, a fraction of 70% resolved sources is used.

For EGRET sources, it could be shown that only 1/12 of the total diffuse background can be made up by resolved sources, as derived by Chiang and Mukherjee [CM98]. The claim from Chiang & Mukherjee that about 25% of the diffuse background of blazars is made up by resolved AGN, while the remaining contribution is from unresolved sources which are not blazars, would reduce ξ significantly to $\xi_{EGRET} \approx 4$. However, Stecker & Salamon [StSa01] point out that this estimate is based on assumptions that do not hold for EGRET blazars. Thus, $\xi_{\max} = 12$

will used as a conservative number in the following. With the launch of GLAST, the question of the contribution from resolved blazars will most likely be settled.

For the remaining source classes, there is no explicit estimate of the contribution of resolved sources to a diffuse background. In this case, an estimate of ξ can be possible for source populations where there is an estimate of the weakest sources in the sky. In this case, the luminosity evolution of the population has to be considered. In the Euclidean case, sources evolve as $N(>S) \propto S^{-3/2}$ with S as the observed flux and $N(>S)$ as the number of sources for fluxes greater than S. In such a case, the integral of the distribution diverges for a vanishing minimal source strength, $N(S_{\min} \rightarrow 0) \rightarrow 0$. For cosmological sources, the behavior is not Euclidean and in some cases, it is possible to determine a lower threshold for the flux, see e.g. [Lon98]. For instance, such determination can be done in the case of FR-II galaxies which are high luminous AGN with a defined luminosity limit of $L_{radio} \sim 10^{43}$ erg/s [FR74].

The determination of a lower luminosity limit enables the calculation of the total number of sources in a population N_{tot}. The total number of sources is given by integrating the number per flux interval, dN/dS over the flux:

$$N_{tot} = \int_{S_{\min}}^{\infty} \frac{dN}{dS}\, dS\,. \tag{6.3}$$

For the case of divergence for $S_{\min} \rightarrow 0$, the lower integration limit is essential to know as mentioned before. This is not trivial, since measurements for most source classes do not reveal the low luminosity cutoff. The lowest luminosities identified for X-ray AGN, for instance, lie at 10^{39} erg/s [ESK84]. The luminosity functions of different AGN classes at $z = 0$ are shown in Fig. 6.3. In this case, the diffusive factor can be estimated by assuming that sources which are not in the catalog are not stronger than the weakest source in the catalog. Thus, the flux of any additional source S^i_{add} is smaller than the flux of the weakest source, S_{weak}, $S^i_{add} < S_{weak}$ for all non-resolved sources i. The total flux not considered in the calculation is thus

$$S^{add}_{tot} = \int \frac{dN}{dS}\, S\, dS < S_{weak} \cdot N_{add}\,. \tag{6.4}$$

Here, $N_{add} = N_{tot} - N_{cat}$ is the number of additional sources which is calculated from the total number of sources expected in the sky, N_{tot}, subtracting the number of sources in the catalog, N_{cat}. ξ is then calculated to

$$\begin{aligned} \xi &= \frac{S^{cat}_{tot} + S^{add}_{tot}}{S^{cat}_{tot}} && (6.5)\\ \xi_{\max} &= \frac{S^{cat}_{tot} + S_{weak} \cdot N_{add}}{S^{cat}_{tot}}\,, && (6.6) \end{aligned}$$

where S^{cat}_{tot} is the total flux in the catalog.

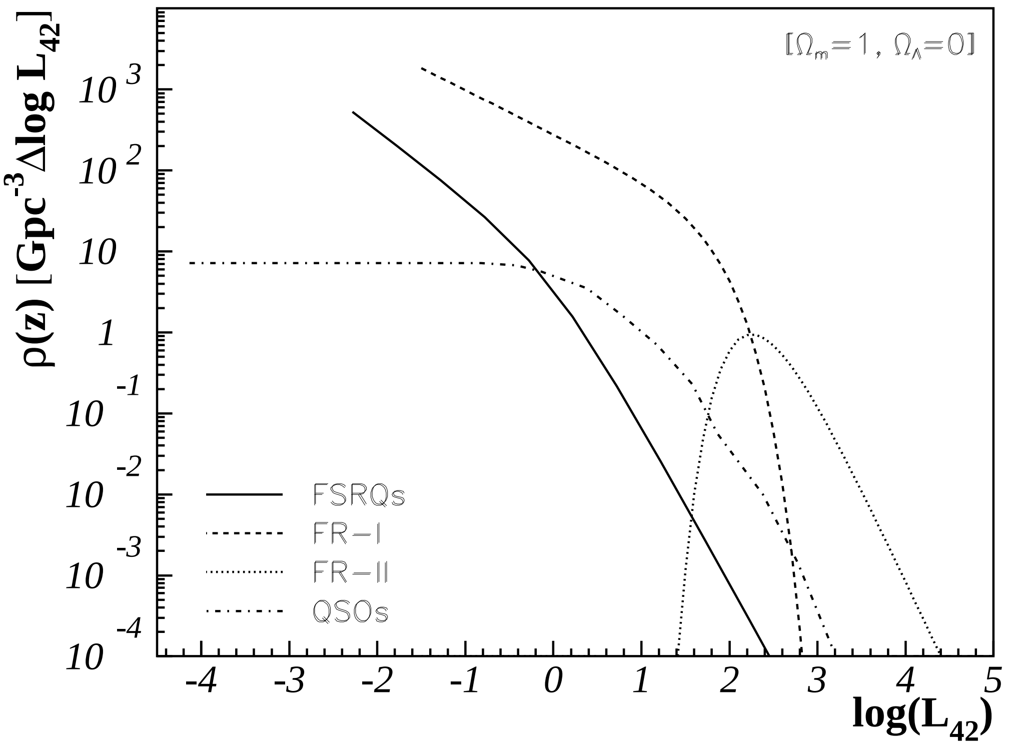

Figure 6.3: Radio Luminosity Functions at $z = 0$ for Flat Spectrum Radio Quasars (FSRQs, solid line) [DP90], FR-I and FR-II galaxies (dashed and dotted lines) [W+01], as well as for QSOs (dot-dashed line) [Sch72]. Density units are $1/\text{Gpc}^3 \cdot \Delta \log L$ and luminosity units are $L_{42} := L/(10^{42}\ \text{erg/s})$. Only FR-II galaxies show a cutoff at low luminosities. All other source classes show an increasing or constant population with decreasing luminosity.

Figure 6.4 shows the behavior of the maximum value of the diffusive factor $\xi_{\max}$ according to Equ. (6.6) at the example of EGRET sources. The figure emphasizes the challenge in such a representation. It is essential to have an estimate of the total number of sources in the class to get a good estimate for $\xi_{\max}$. This implies the necessity of the knowledge of the absolute lower luminosity limit. For FR-II galaxies, this is relatively simple, since the number of sources decreases for low luminosities [W+01]. FR-I galaxies on the other hand have a high number of low luminosity sources and it is not known at which luminosity the function turns. In such a case, the diffusive factor can be quite large, since a high contribution from low luminosity sources is expected. ξ has thus explicitly been determined according to the neutrino flux model which is tested by the limits. For FR-II galaxies,

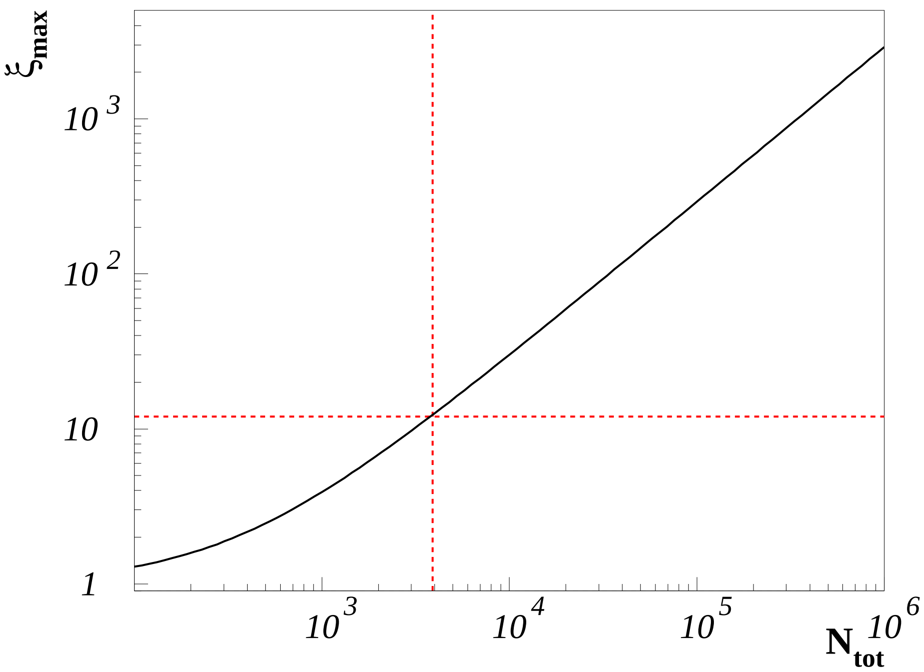

Figure 6.4: Maximum diffusive factor ξ_{max} versus total number of $>$ 100 MeV-emitting sources for EGRET sources. With $\xi_{\text{max}} = 12$, the lower limit of the total number of sources contributing to the diffuse EGRET background is $N_{tot} > 3.9 \cdot 10^3$.

the investigated neutrino flux model presented in [BBR05] uses the luminosity function by Willott et al. [W$^+$01], labeled "FR-II" in Fig. 6.3. In this case, a total number of $\sim 10^5$ sources is expected and the maximum diffusive factor is determined to $\xi_{\text{max}} = 160$. For the remaining source classes, FR-I galaxies, GPS/CSS and QSOs, the value of ξ_{max} will not be given, since no explicit neutrino model for these source classes is examined here. Note that ξ_{max} gives an absolute upper limit: every source not included in the stacking analysis is assumed to have the flux of the weakest included source, S_{weak}. This results in an overestimate of ξ, since it is likely that only a small fraction of the sources has such a high flux.

For EGRET sources, Equ. (6.6) can be used to determine a lower limit of sources contributing to the diffuse EGRET background. Figure 6.4 shows the dependence of the maximum value of ξ on the total number of sources in the source class of blazars emitting at > 100 MeV. Using a diffusive factor of $\xi = 12$, the total number of sources contributing to the total diffuse EGRET background is $N_{tot}^{EGRET} > 3.9 \cdot 10^3$.

6.3.3 Stacking diffuse limits and overall diffuse results

Figure 6.5 shows the diffuse limits that could be derived from the stacking approach for each source class. It is compared to the diffuse limit of AMANDA (solid line) for the operation time considered (2000-2003),

$$\Phi^{\mathrm{DL}} = 8.8 \cdot 10^{-8}\,\mathrm{GeV\ cm^{-2}\,s^{-1}\,sr^{-1}}\,, \tag{6.7}$$

given in [H$^+$06a]. Several stacking diffuse limits are more restrictive than the general diffuse limits. The exact numbers are given in table 6.2, where the stacking limit, the diffuse bound derived from the stacking method and the ratio of the latter and the general diffuse limit are compared. Note that in the case of CSS/GPS, QSOs and FR-I galaxies, the diffusive factor still has to be applied.

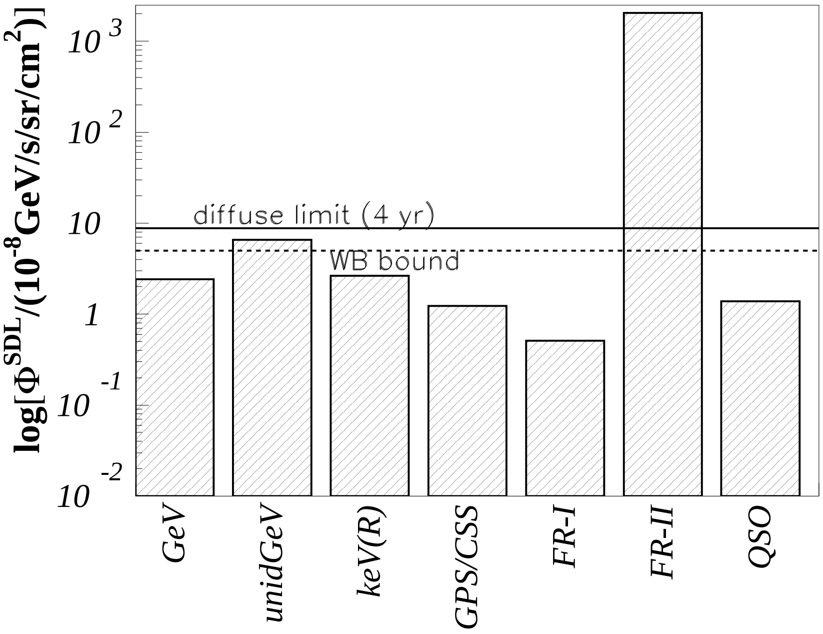

Figure 6.5: Diffuse limits of seven different AGN classes. The solid line represents the total diffuse limit of AMANDA [H$^+$06a]. Several of the stacking diffuse limits are more restrictive than the general diffuse limit. The dashed line indicates the Waxman/Bahcall (WB) bound which gives a theoretical estimation of the maximum contribution of AGN to the diffuse neutrino flux.

Figure 6.5 also indicates the Waxman/Bahcall bound (WB bound, dashed line). This bound gives a theoretical estimate of the maximum contribution to be expected in neutrinos from Active Galactic Nuclei [WB97, WB99]. This bound is

Source class	Φ^{SL}	Φ^{SDL}	$\Phi^{\mathrm{DL}}/\Phi^{\mathrm{SDL}}$	models
EGRET GeV	2.71	7.25	1.21	[MPR01], [Man95], [M$^+$03b]
unid. EGRET	31.7	6.56	1.34	-
infrared	10.6	EXCL.:	too few	-
keV (HEAO-A)	3.55	EXCL.:	too few	-
keV (ROSAT)	9.71	2.65	3.32	[StSa96], [NMB93], [AM04]
TeV blazars	5.53	EXCL.:	too few*	[MPR01], [M$^+$03b], [Man95]
CSS/GPS	5.94	$1.23 \cdot \xi_{model}$	$7.16/\xi_{model}$	-
FR-I incl. M-87	4.11	EXCL.: M87	dominant	-
FR-I excl. M-87	2.91	$0.51 \cdot \xi_{model}$	$17.3/\xi_{model}$	-
FR-II	30.4	$2.05 \cdot 10^3$	$4.29 \cdot 10^{-3}$	[BBR05]
QSOs	6.70	$1.39 \cdot \xi_{model}$	$6.35/\xi_{model}$	-

Table 6.2: Table of the source class limits obtained with the stacking method. Five years of data, 2000-2004, have been used for the analysis with AMANDA in [AI$^+$06a]. The stacking limit is given in units of $10^{-8}\,\mathrm{GeV\,cm^{-2}\,s^{-1}}$ while the stacking diffuse limits is given in units of $10^{-8}\,\mathrm{GeV\,cm^{-2}\,s^{-1}\,sr^{-1}}$. *While the class of TeV blazars cannot be used to determine a stacking diffuse limit, the general diffuse limit gives an upper limit to the contribution of TeV-observable blazars to the total diffuse flux as it is shown in Section 6.4.

valid for optically thin sources at an energy of $E_\nu \sim 10^{17}$ eV, where it is most restrictive. The description for all energies is given in [MPR01]. Five of the seven source class limits lie below the indicated WB bound. This shows that the sensitivity reached with this method in AMANDA is already extremely high. Next generation's neutrino telescopes such as IceCube and KM3NeT which will have a cubic kilometer of ice resp. water instrumented will therefore be able to provide more information either by giving very strong restrictions on prevailing models or by confirming a positive neutrino signal.

Note that the class of TeV blazars is on the other hand an optimal candidate for a general diffuse search. The contribution of photon-observable TeV blazars is very small, since many sources are hidden in photons due to the strong absorption, while they would still be visible in neutrinos. This will be discussed in Section 6.4.

6.4 Direct implications for AGN ν flux models

The diffuse limits discussed in Sections 6.1 and 6.3 restrict some of the currently discussed neutrino flux models. However, it is known that these models bear different uncertainties in both normalization and spectral shape due to a lack of knowledge of the conditions at the source.

In this section, the neutrino flux models having been discussed in Section 1.3 will be examined with respect to the limits obtained.

6.4.1 TeV blazars

The detection of TeV photon emission from distant sources is limited due to the absorption of high energy photons by the Extragalactic Background Light (EBL), see e.g. [SdS92, K^+04c]. The absorption factor η describes the ratio of the total emitted TeV photon flux from HBLs and the TeV flux from HBLs up to a redshift $z_{\max}$. It is a measure of the absorption of TeV photons. The ratio of a diffuse neutrino signal from photon-observable TeV blazars will be calculated using the general diffuse limit and taking into account the absorption factor for TeV photons. Only a relatively small fraction of all TeV blazars can be identified in TeV photons, since sources at high redshifts are hidden due to the strong absorption.

In this paragraph, the absorption factor and the general diffuse neutrino limit are used to derive the maximum contribution of TeV photon-observable sources to the total diffuse neutrino flux.

The absorption factor η

In the case of TeV blazars, the absorption factor η is much greater than unity due to the strong absorption of TeV photons by the EBL. HBLs seem to have no or even a slightly negative evolution, see e.g. [B^+03, B^+98, L^+99b].

For a no-evolution scenario as it is discussed for BL Lacs, the co-moving density $\rho(z)$ is considered to be constant with redshift, $\rho(z) = \text{constant}$. Using a negative evolution with less than $(1+z)^{-0.2}$ does not change the results significantly. Also, the positive source evolution is neglected which has to be present up to a certain redshift z^*: both effects positive evolution up to z^* and negative evolution at higher redshifts are believed to cancel. Each effect for itself alters the result less than 10% in opposite directions.

The normalization of the co-moving density is not important in this calculation, since only ratios of concrete values of ρ are considered and the constant of proportionality cancels.

The neutrino flux from sources up to a certain redshift $z_{\max}$ is given by

$$\frac{dN_\nu}{dE_\nu} = \phi_0 \cdot \int_{z=0}^{z_{\max}} E'(z)^{-2} \cdot \rho(z) \frac{dV_c}{dz}\, dz\,, \tag{6.8}$$

where $E'(z) = (1+z) \cdot E$ is the energy of the neutrino at the source. The E^2-weighted flux is thus given as

$$E_\nu{}^2 \frac{dN_\nu}{dE_\nu} = \phi_0 \cdot \zeta(z_{\max})\,. \tag{6.9}$$

Here, $\zeta(z_{\max}) = \int_{z=0}^{z_{\max}} (z+1)^{-2} \cdot \rho(z)\, dV_c/dz\, dz$ is the evolution factor depending on the upper redshift integration limit $z_{\max}$. If all present sources are considered, $z_{\max} \approx 7$ is a reasonable value. Recent searches for luminous galaxies at redshifts between $z = 6 - 8$ imply that only few ultra-luminous objects only exist beyond $z = 7$ [I$^+$06, BI06]. At higher redshifts, no galaxies are observed, leading to the conclusion that only smaller galaxies can be present. Also, the results to not change significantly when going up to higher redshifts: the major contribution comes from redshifts of $z < 3$.

The absorption factor η is given by the ratio of the total flux and the contribution that is observed by TeV-photon experiments:

$$\eta(z_{\max}) = \frac{\zeta(7)}{\zeta(z_{\max})}\,. \tag{6.10}$$

Here, $z_{\max}$ is the maximum redshift at which TeV photon sources can be identified by present IACTs. TeV sources have up to today been observed up to a redshift of z=0.186 - 1ES1101-232 [AhH$^+$06e]. As a conservative upper limit, the maximum redshift of observation with IACTs is taken to be $z_{\max} = 0.3$, since an upper bound is derived from these values. The absorption factor depending on $z_{\max}$ is shown in Fig. 6.6. At $z_{\max} = 0.3$, the numerical value is

$$\eta(z_{\max} = 0.3) = 54\,. \tag{6.11}$$

It is important to note that for a lower energy threshold (e.g. ~ 30 GeV), IACTs could be able to detect sources up to $z_{\max} \sim 1$. This would lead to a much lower absorption factor of

$$\eta(z_{\max} = 1) = 4.6\,. \tag{6.12}$$

An upper limit to the contribution from photon-observable TeV blazars

Using the above reflections, one can argue that a diffuse limit can be used to estimate the maximum diffuse signal from HBLs resolved in TeV photons. From the existing general diffuse limit, it is known that no source type and,

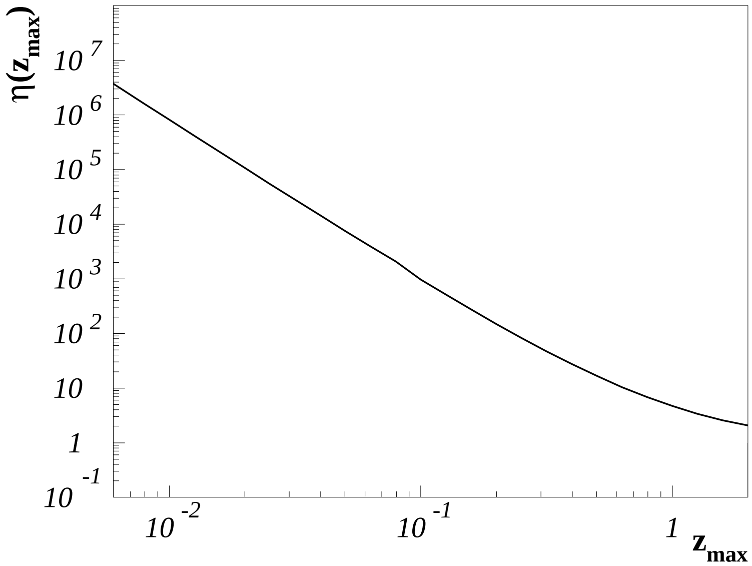

Figure 6.6: Absorption factor η versus maximum redshift z_{max}. For TeV sources, the most distant source observed is 1ES1101-232 at z=0.186 [AhH+06e]. $\eta(z_{\mathrm{max}} = 0.3) = 54$ is used for TeV sources.

thus particularly also not the class of TeV blazars, can contribute more than $\Phi^{\mathrm{DL}} = 8.8 \cdot 10^{-8}\,\mathrm{GeV\,cm^{-2}\,s^{-1}\,sr^{-1}}$:

$$E_\nu{}^2 \left.\frac{dN_\nu}{dE_\nu}\right|_{TeV} < \Phi^{\mathrm{DL}} . \tag{6.13}$$

An upper limit to the normalization constant ϕ_0 of the neutrino flux can be derived by inserting Equ. (6.9) with $z_{\mathrm{max}} = 10$ in Equ. (6.13):

$$\phi_0 < \frac{\Phi^{\mathrm{DL}}}{\zeta(10)} . \tag{6.14}$$

The contribution of sources at $z < z_{\mathrm{max}}$ is given as

$$E_\nu{}^2 \left.\frac{dN_\nu}{dE_\nu}\right|_{TeV} (z_{\mathrm{max}}) = \phi_0 \cdot \zeta(z_{\mathrm{max}}) < \frac{\zeta(z_{\mathrm{max}})}{\zeta(10)} \Phi^{\mathrm{DL}} \tag{6.15}$$

with the final result of

$$E_\nu{}^2 \left.\frac{dN_\nu}{dE_\nu}\right|_{TeV} (z_{\mathrm{max}}) < \eta(z_{\mathrm{max}})^{-1} \cdot \Phi^{\mathrm{DL}} . \tag{6.16}$$

The upper limit on the neutrino flux up to z_{max} is shown in Fig. 6.7. The curve shows the no-evolution scenario.

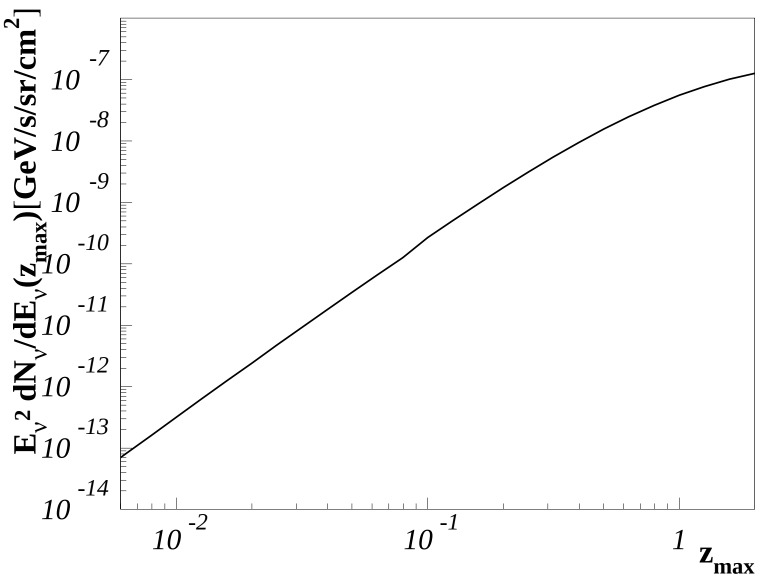

Figure 6.7: Upper limit on the contribution of photon-observable TeV blazars for the no-evolution scenario for HBLs.

The contribution of photon-observable TeV blazars to the diffuse neutrino flux is therefore limited to

$$E_\nu{}^2 \left.\frac{dN_\nu}{dE_\nu}\right|_{TeV} (z_{\max} = 0.3) < 1.67 \cdot 10^{-9}\,\mathrm{GeV\ cm^{-2}\,s^{-1}\,sr^{-1}}\,, \tag{6.17}$$

where $\eta(z_{\max} = 0.3) = 53$ is used as a lower limit. The contribution of sources observed by IACTs is thus about three orders of magnitude lower than the possible total contribution. This is displayed in Fig. 6.8 together with the general diffuse limit. The limit to the maximum contribution from photon-observable TeV blazars is shown (*obs. TeV*) as well. The contribution is a factor of $\eta^{-1} \approx 0.019$ lower than the diffuse limit. This indicates that a diffuse analysis of TeV sources is most effective with an overall diffuse approach, since most of the TeV sources are hidden due to the strong absorption at such high photon energies. The stacking of the strongest sources in the sky in comparison only comprise a small fraction of the total diffuse flux as these calculations show. This result stands in contrast to the other sources samples where the selection of the strongest sources yields stronger restrictions than a general search for a diffuse signal, see following paragraphs.

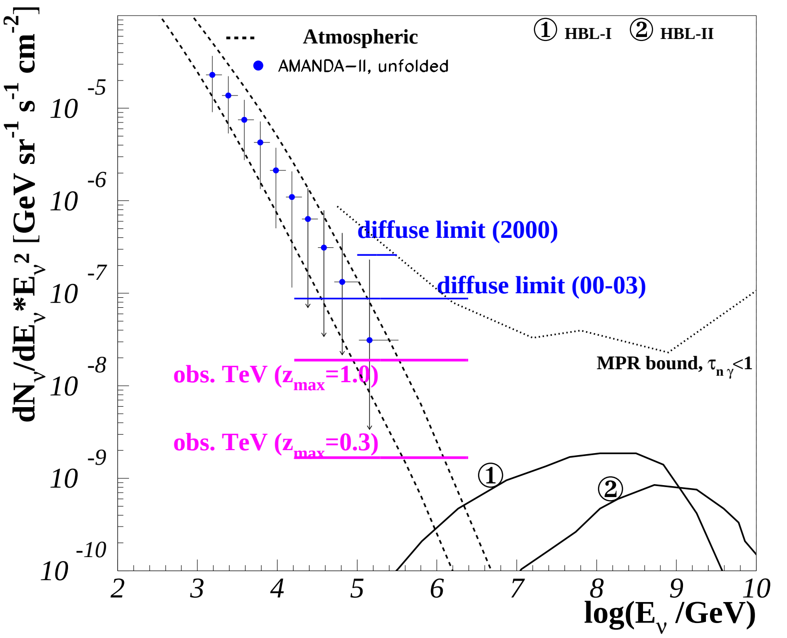

Figure 6.8: Neutrino predictions for optically thin sources. TeV photons from decaying pions escape together with neutrons which make up charged CRs by decaying in the vicinity of the source in protons. All models have been corrected for oscillations. The *MPR-bound* derivation is described in [MPR01]. Predictions for the contribution from HBL sources (*HBL-I* and *HBL-II*) depend on the extension of the acceleration region and the jet frame target photon density. Model 1 and 2 represent two different parameter settings, see [M$^+$03b]. The general diffuse limit is shown as well as the limit to photon-observable TeV blazars (*obs.TeV*), indicating that the major contribution to the diffuse neutrino signal from TeV blazars is expected to come from hidden TeV photon sources for two different maximum redshifts, $z = 0.3$ and $z = 1$.

The importance of reaching down to low energies with IACTs is demonstrated in this calculation, since lowering the energy threshold to observe sources up to $z = 1$ would already include sources with a one order of magnitude higher maximum neutrino flux of

$$E_\nu{}^2 \left.\frac{dN_\nu}{dE_\nu}\right|_{TeV} (z_{\max}) < 1.90 \cdot 10^{-8}\,\mathrm{GeV\ cm^{-2}\,s^{-1}\,sr^{-1}}\,. \tag{6.18}$$

6.4.2 Optically thick cases: MeV and GeV γ emission

If the sources are optically thick to photon-neutron interactions, $\tau_{\gamma n} \gg 1$, the photon signal which is emitted from the sources lies in the MeV to GeV range. Thus, EGRET and COMPTEL diffuse cosmic photon fluxes are used to determine the expected neutrino contribution.

EGRET blazars

Figure 6.9 shows neutrino flux predictions in connection with EGRET data and the derived stacking diffuse limits for a neutrino signal from EGRET sources. Since the indicated models are all normalized to the EGRET diffuse spectrum, the limit of identified EGRET blazars applies. The gray line between 1 TeV and $10^{2.8}$ TeV indicates the most conservative calculation where it is assumed that the total diffuse background as measured by EGRET it produced by AGN ($\xi = 12$). The limit falls short of the MPR bound and also touches the maximum prediction for the source class predicted by MPR and it is possible to reach sensitivities at the level of predictions concerning a neutrino signal from blazars. The same is valid for the prediction by Mannheim (M(95), A). The proton-proton contribution from optically thick blazars can be constrained even though the atmospheric flux exceeds the prediction at these energies. With an overall diffuse analysis, it would not be possible to extract any information on this low-energy part of the spectrum from AGN.

The contribution from LBL within the proton-blazar model dominates the total observable flux at ultra high energies. With the current data, it is not possible to get to any reliable conclusion from the stacking method, since it is valid at energies $E <$ PeV while the flux is present at much higher energies. A stacking analysis of cascade events with second generation telescopes such as IceCube would be an option to explore regions of energies at $>$ PeV. A stacking approach for cascades is, however, accompanied by the challenge of getting a reasonable directional reconstruction of the neutrino events, since the cascade signal is generally not as boosted as a signal from neutrino-induced muons.

COMPTEL blazars

A stacking analysis using COMPTEL blazars has not been done yet. The option is discussed in Section 6.5. Current diffuse neutrino flux limits are still about a factor of 2 or more above the predictions. The hypothesis of an avalanched TeV signal down to MeV energies will be tested by IceCube.

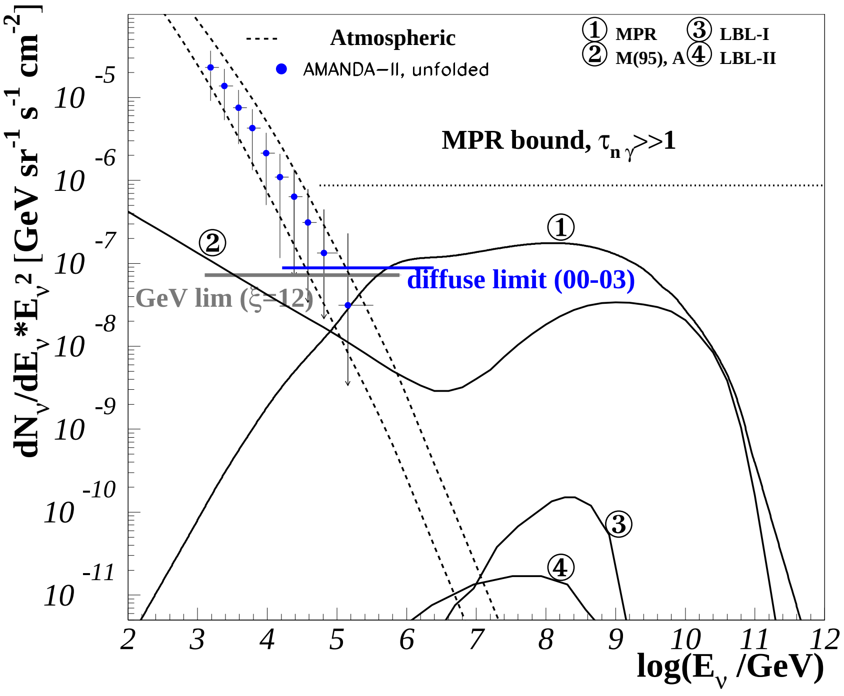

Figure 6.9: Neutrino flux predictions for optically thick sources, normalized to the diffuse EGRET flux above 100 MeV. Model 1 (*MPR*) represents the maximum contribution from blazars within the framework of Mannheim, Protheroe and Rachen [MPR01] in which the *MPR bound* for optically thick sources (dashed line) is derived. Model 2 (*M95,A*) - gives the neutrino spectrum from proton-proton and proton-photon interactions in blazars determined in [Man95]. Models 3 and 4 (*LBL-I* and *LBL-II*) represent the prediction of neutrinos from LBLs given two different parameter settings, see [M$^+$03b]. The stacking diffuse limit for the class of identified EGRET sources is indicated with $\xi = \xi_{\max} = 12$ where it is assumed that AGN produce the complete diffuse EGRET signal.

6.4.3 The diffuse X-ray background and radio weak AGN

The X-ray component of radio weak AGN can be correlated to the emission of neutrinos at the foot of the jet. This has been investigated in calculations of Nellen, Mannheim & Biermann (NMB) [NMB93], Stecker & Salamon (StSa96) [StSa96] as well as Alvarez-Muñiz & Mészáros (AM) [AM04]. All models are restricted by the current general diffuse AMANDA limit. The resolved ROSAT sources which have been used to determine the stacking limit are radio loud and thus, the limit is not as easily applicable to these predictions. If the same production mechanism is assumed in radio loud as in radio weak sources, the stacking diffuse limit of ROSAT sources would apply in this case.

However, the limit to radio weak objects $\Phi^{\mathrm{SDL}}{}_{rq}$ is about a factor of 10 higher than the calculated limit for radio loud sources $\Phi^{\mathrm{SDL}}{}_{rl}$, since radio loud objects are about a factor of 10 less frequent than radio weak sources,

$$\Phi^{\mathrm{SDL}}{}_{rq} \lesssim 10 \cdot \Phi^{\mathrm{SDL}}{}_{rl} = 1.72 \cdot 10^{-7}\,\mathrm{GeV\ cm^{-2}\,s^{-1}\,sr^{-1}}\,.$$

The more restrictive limit in this case is therefore the general diffuse limit.

Figure 6.10 shows the prediction of neutrinos being produced coincidentally with X-rays at the foot of AGN jets. The diffuse ROSAT-measured background has been used in two models, NMB and StSa96, to normalize the neutrino spectrum. In the third case presented by AM, the luminosity evolution function of radio quiet AGN has been used so that the result also applies to the correlation with the X-ray diffuse background.

In the case of the prediction by NMB, diffuse neutrino flux limit of AMANDA lies an order of magnitude below the flux. Stecker et al. updated their calculation by normalizing to the diffuse flux as measured by COMPTEL [Ste05]. This is discussed in the context of the MeV photon emission in correlation with neutrinos in Section 6.4.2. The absence of neutrinos from ROSAT-detected sources implies strongly that the X-ray emission from AGN cannot be directly correlated to neutrino emission. While the missing emission of neutrinos disfavors a hadronic scenario for the X-ray emission from AGN, it is consistent with Inverse Compton (IC) models for the X-ray emission and underlines leptonic models for the production of X-rays in AGN.

Calculations by StSa96 show a flux peaking at higher energies compared to the prediction from NMB. The main reason is that NMB use a more conservative estimate of the maximum energy and a simpler approach for the spectral behavior. The spectrum of the model by StSa96 is not exactly $E_\nu{}^{-2}$-shaped, while the AMANDA limits are typically derived assuming an $E_\nu{}^{-2}$ spectrum. The modeling of different spectral shapes, including StSa96, has been done recently, see [H$^+$06b]. The curved blue line indicates the limit modeled according to the model of StSa96. The limit lies half an order of magnitude below the prediction.

While the previously described models normalize the diffuse spectrum by using ROSAT data, calculations by AM use the radio luminosity function for radio quiet AGN and a single source normalization. Further differences with respect to model 1 and 2 are the maximum energy and the break in the neutrino spectral shape. The underlying idea is the same by assuming proton-proton and proton-photon interactions at the foot of AGN jets, leading to X-rays in coincidence with neutrinos. This model overproduces neutrinos as well as the previous ones.

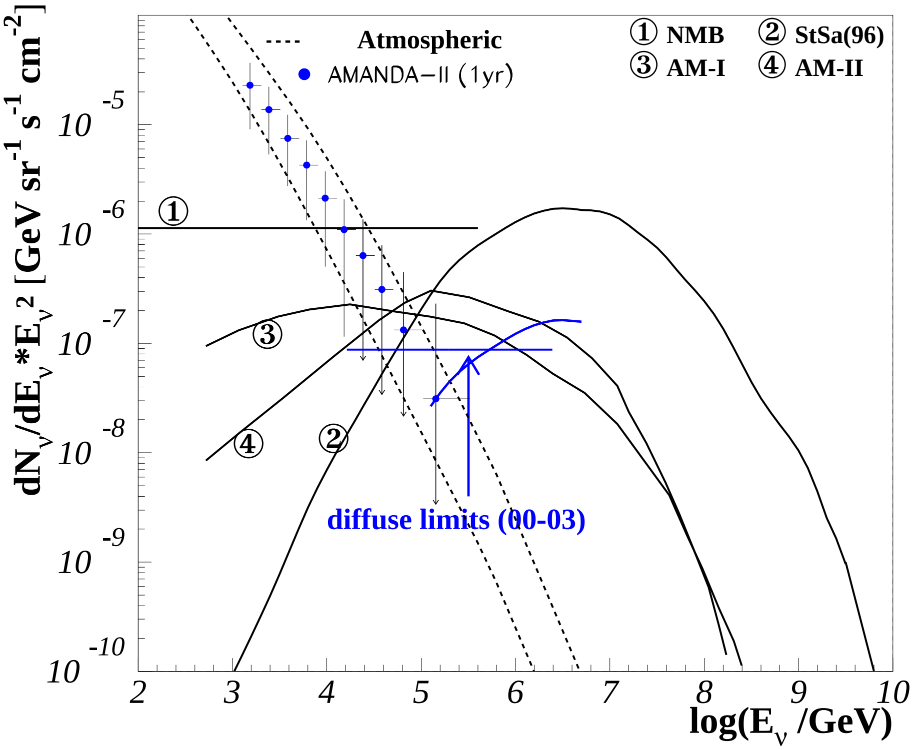

Figure 6.10: Stecker&Salamon [StSa96] (*StSa96*, model 2) predict a large contribution of neutrinos from radio weak sources using ROSAT data to normalize the spectrum. [NMB93] (*NMB*, model 1) use the same normalization method. Model 3 and 4 (*AM-I* and *AM-II*, [AM04]) use the luminosity function of radio quiet AGN and normalize the single source spectrum. While the black hole mass is varied in model 3, model 4 varies the accretion rate. All these models have been corrected for neutrino oscillations. All models are excluded in their published form by the diffuse limit of AMANDA. The typical ${E_\nu}^{-2}$ limit is represented by the blue horizontal line. The curved blue line, crossing the ${E_\nu}^{-2}$-limit represents the AMANDA limit for the years 2000-2003 calculated for a flux shaped as the model presented in [StSa96] and [Ste05].

Three independent calculations on the correlation of X-ray emission from radio quiet AGN and neutrino emission have been examined. The absence of neutrino emission from the foot of relativistic jets implies that the particles there are not accelerated to high energy, and then interact. However, the concept that the innermost ring of the accretion disk, just underneath the jet, turns into an

Advection Dominated Accretion Flow (ADAF) with a very high temperature, see e.g. [FMB95, BSF95, RMB95, DB96, Mah98], is consistent with the results. This implies that the spin parameter of the black hole is high, above 0.95, and that hadronic interaction at weakly relativistic temperatures produce charged pions, which decay and provide an energetic particle seed population for further acceleration downstream for the radio emission of the jet [GBW04]. This is then consistent with an Inverse Compton explanation of the X-ray emission [MSR95], and predicts that there should be a large production of energetic neutrinos at an energy commensurate with the pion mass.

6.4.4 Radio galaxies

The radio emission of Active Galactic Nuclei is likely to be directly correlated to neutrino emission in the jet. This has been discussed in [BBR05] (BBR) using the example of FR-II radio galaxies and flat spectrum radio quasars (FSRQs). In both cases, the normalization of the neutrino spectrum depends on many different intrinsic factors, i.e. the correlation between radio and disk luminosity and the parameterization of the maximum proton acceleration energy. The jet-disk correlation of AGN has been worked out in [FMB95, FB95, FB99]. Although the model includes several parameters, all are fixed by the comparison with the data except the accretion rate. Within that model, it is shown that the parameters reach extreme values and are not strongly scattered. The jet-disk symbiosis model has been proven for different source types, reaching from microquasars to quasars.

A parameter in the calculation of the neutrino flux is the optical depth of the source which is unknown. BBR define the effective optical depth of the source, τ_{eff}, as the product of the proton-photon optical depth $\tau_{p\gamma}$ and a reduction factor due to contributions from Bethe-Heitler production η',

$$\tau_{eff} = \tau_{p\gamma} \cdot \eta' \,. \tag{6.19}$$

It can be derived from the solution of the transport equation, the neutrino flux is proportional to $\tau_{eff}/(1-\exp(-\tau_{eff}))$. Consider a homogeneous region of length x_{max}, with a constant density of energetic particles with a production ϵ of photons; the absorption coefficient of these photons is κ. The intensity of the stream of photons is Φ_γ. Then the transport equation is

$$\frac{d\Phi_\gamma}{dx} = -\kappa\Phi_\gamma + \epsilon \,. \tag{6.20}$$

The optical depth for photon absorption is $\tau := x \cdot \kappa$ and

$$\frac{d\Phi_\gamma}{d\tau} = -\Phi_\gamma + \frac{\epsilon}{\kappa} \,. \tag{6.21}$$

The solution of the differential equation is

$$\Phi_\gamma = \frac{\epsilon}{\kappa}\left(1-\exp(-\tau)\right) \tag{6.22}$$

In the limit of small optical depth this is

$$\Phi_\gamma \; = \; \frac{\epsilon}{\kappa}\tau \tag{6.23}$$

The corresponding intensity of neutrinos Φ_ν and their production $\epsilon^\star$, the transport equation for neutrinos is

$$\frac{d\Phi_\nu}{dx} \; = \; \epsilon^\star \, , \tag{6.24}$$

since neutrinos do not get absorbed under these circumstances. Therefore,

$$\Phi_\nu \; = \; \frac{\epsilon^\star}{\kappa}\tau \, , \tag{6.25}$$

where τ is the optical depth for photon absorption, and κ is the absorption coefficient for photons. Dividing the two resulting equations gives then

$$\frac{\Phi_\nu}{\Phi_\gamma} \; = \; \frac{\epsilon^\star}{\epsilon}\,\frac{\tau}{(1-\exp(-\tau))} \, . \tag{6.26}$$

For very small optical depth for photon absorption this second factor reduces to unity, while for very large photon optical depth it is just the optical depth itself, and so obviously gets very large.

The effective optical depth has been chosen to be $\tau_{eff} = 1$ in [BBR05]. The optical depth of proton-photon interactions is determined by the product of the photo-hadronic cross section $\sigma_{p\gamma}$ and the photon density in the source, n_γ. These in turn depend on the disk luminosity L_{disk} and the extent r of the source such as

$$\tau_{p\gamma} = 800\frac{L_{46}}{r_{17}} \, , \tag{6.27}$$

with $L_{46} := L_{disk}/10^{46}$ erg/s and $r_{17} := r/10^{17}$ cm. This shows that the photo-hadronic optical depth itself uncertain, since low values around unity are possible as well as extremely high numbers. AMANDA limits will be used to derive limits on the optical depth of FR-II galaxies and FSRQs.

Note that the determination of τ_{eff} happens only within the specific model of neutrino production as it is described above. The difficulty of drawing more general conclusions lies in the uncertainty of the spectral index. This highly depends on the original spectral behavior of the protons. This can only be simulated and is not directly observable.

FR-II radio galaxies

Using a generic ${E_\nu}^{-2}$ spectrum for the neutrino flux from FR-II galaxies, the flux normalization has been derived to be

$$\Phi = 1.43 \cdot 10^{-7}\,\mathrm{GeV\ cm^{-2}\,s^{-1}\,sr^{-1}} \, . \tag{6.28}$$

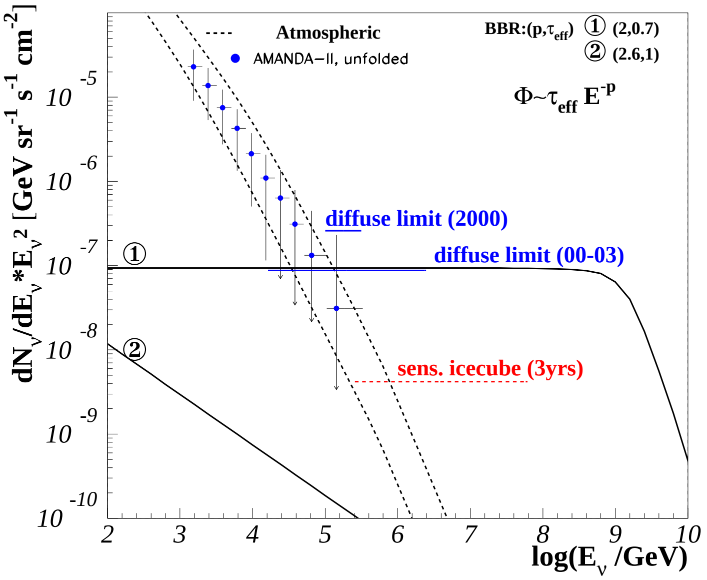

Figure 6.11: Contribution to the diffuse neutrino background from FR-II radio galaxies. For an ${E_\nu}^{-2}$ spectrum, it is constrained to an optical depth of $\tau_{eff} < 0.7$. A steeper spectrum ${E_\nu}^{-2.6}$ (model 2) is consistent with the current limit. A flux of $\sim {E_\nu}^{-2.2}$ would still be consistent with the limit.

Comparing the normalization in Equ. (6.28) with the diffuse limit shows that a flux with the chosen parameter settings is not detected. An upper limit to the optical depth can be derived from the limit yielding

$$\tau_{eff} < 0.7\,. \tag{6.29}$$

Within three years of IceCube, it will be possible to explore sources with $\tau_{eff} > 0.029$.

Figure 6.11 shows the the prediction of a neutrino flux from FR-II radio galaxies. Model (1) is the original calculation of BBR modified by a factor τ_{eff}=0.7. This is the maximum contribution for an ${E_\nu}^{-2}$ signal from those sources not violating the diffuse limit of AMANDA. However, there is another production scenario which leads to a significant reduction of a contribution from FR-II galaxies. The synchrotron spectral index of FR-II galaxies α is correlated to the neutrino spectral index p by $p = 2\cdot\alpha+1$, see e.g. [RL79]. The mean synchrotron spectral index is $\alpha \approx 0.8$ for large scale emission and therefore, the neutrino spectrum can be as steep as ${E_\nu}^{-2.6}$. This prediction is shown in Fig. 6.11 as model (2). In that case, the contribution is very low and does neither violate the current diffuse limit, nor is it within reach of IceCube's sensitivity for three (or even five) years of operation [H$^+$06a]. In such a case, an observation of a neutrino signal from FR-II galaxies would be very difficult. If the spectrum were this steep for real, then all Ultra High Energy Cosmic Ray (UHECR) arguments would fail and so it may be more appropriate to assume a flatter spectrum. The radio spectral index of the hot spots are usually about $\alpha \sim 0.6$ and so correspond to a particle spectral index of about $p \sim 2.2$. Using Fig. 6.11 it can be estimated that a spectrum with an index of 2.2 could already be explored by the three year sensitivity of ICECUBE.

Flat Spectrum Radio Quasars

Using a similar correlation between radio and neutrino flux as for FR-II galaxies, the contribution from FSRQs to the diffuse neutrino flux can be calculated to

$$E_\nu{}^2 \frac{dN_\nu}{dE_\nu} = 1.70 \cdot \tau_{eff} 10^{-9}\,\mathrm{GeV\ cm^{-2}\,s^{-1}\,sr^{-1}}\,. \tag{6.30}$$

The flux lies well beyond the current diffuse limit and even below the sensitivity of ICECUBE for an optical depth around $\tau_{eff} = 1$. Equivalent as for the case of FR-II radio galaxies, the upper limit to the optical depth in FSRQs can be determined to be

$$\tau_{eff} < 52 \tag{6.31}$$

by using the diffuse AMANDA limit.

The effective optical depth is quite uncertain in the case of Flat Spectrum Radio Quasars. Just as an example, a sub-class of FSRQs are GPS, which are compact AGN where it is assumed that the jet runs into dense matter, yielding a high potential for proton-photon interaction which results in a high optical depth. However, other sources like TeV blazars contribute to the source class, being at the other end with a very low optical depth.

With ICECUBE, it will be possible to examine sources with $\tau_{eff} > 2.5$. Consequently, neutrino emission in coincidence with the radio signal from FSRQs will only be observable in the near future, if the optical depth of FSRQs is significantly higher than the one for FR-II galaxies.

6.5 Examination of source class capabilities

In the previous sections it has been shown that the stacking method can be used to increase the diffuse sensitivity of high energy neutrino telescopes to certain source classes.

Further catalogs published recently which are not yet part of the stacking search in AMANDA will be discussed in this section. The references for the catalogs are given throughout the text. They will be examined with respect to the potential neutrino signal and the effectiveness of the method.

Also, a diffuse component from unresolved sources is expected to show deviations from a purely isotropic flux, since it is expected to follow the source distribution in the sky. The total signal from a certain source class to be observed by a neutrino telescope is highly dependent on the detector's field of view. We will generically examine source classes concerning the total flux from the northern respectively from the southern hemisphere. This gives a qualitative examination of the capabilities of IceCube and KM3NeT which is planned to observe the southern hemisphere. The local supercluster for example is observable from the northern hemisphere and so in some cases, a significant fraction of the total flux in a sample comes from that hemisphere. It is shown, however, that there are classes with the dominant contribution in the southern sky. A further constraint is the limitation of the source catalogs themselves. Radio data are mainly given for the northern hemisphere and there are only a few southern identified sources in the case of very sensitive radio-selected samples. Here, high energy photon catalogs which are mostly provided by satellite experiments are much more complete in the sense of directionality.

6.5.1 Additional source catalogs

This subsection gives an overview of four additional source catalogs which yield high capabilities for neutrino searches with the stacking approach. The point source sensitivity is likely to be increased in all the cases, diffuse limits can be derived in two of the cases. A summary of the basic properties of these catalogs is given in table 6.3. The maximum diffusive factor for the examined catalogs can be determined as described in Section 6.3, Equ. (6.6), assuming that the total number of sources in that class can be determined. This is quite challenging, since a lower luminosity limit is difficult to determine. Figure 6.12 shows the increase of the diffusive factor with N_{tot} for the whole sky for all four examined catalogs. Table 6.4 reviews the parameters used for the four catalogs.

Catalog	energy range	Reference	Underlying ν model
COMPTEL	< 100 MeV	[K$^+$96]	[Man95, Ste05]
INTEGRAL	hard X-ray	[B$^+$06]	-
INTEGRAL	soft γ-ray	[B$^+$06]	-
Starburst	FIR	-	[LW06b]

Table 6.3: Summary of source catalogs interesting to examine with respect to the neutrino output of the sources.

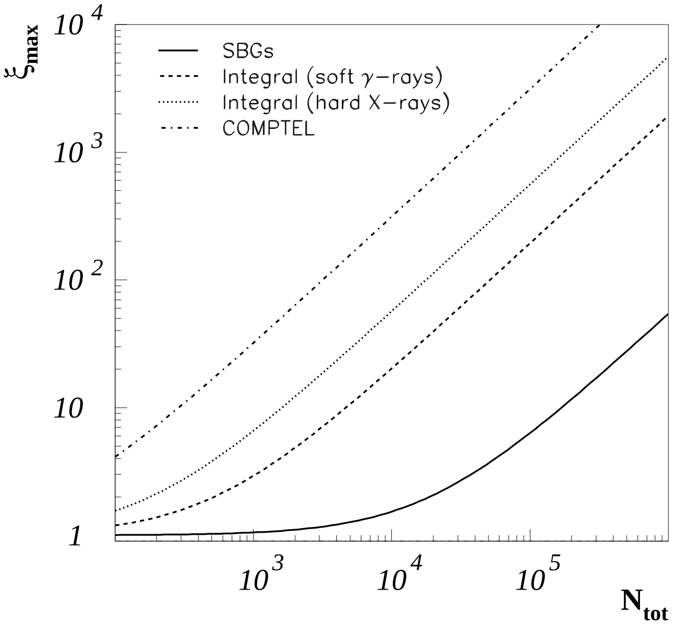

Figure 6.12: Behavior of the maximum diffusive factor with the total number of sources in the source class. Only a fraction of the total number of sources is included in the catalog, dependent on the instrument's sensitivity.

Catalog	#(*sources*) south/north	S_{tot}^{cat}	S_{weak}
COMPTEL	11 5/6	0.638×10^{47}erg/s/Gpc^2 0.326/0.311	0.0199×10^{47}erg/s/Gpc^2 0.0384/0.0199
INTEGRAL (hard X-rays)	15 10/5	175×10^{-11} erg/s/cm^2 130.08/45.1	0.98×10^{-11} erg/s/cm^2 0.98/4.34
INTEGRAL (soft γ rays)	42 23/19	441×10^{-11} erg/s/cm^2 265/176	0.85×10^{-11} erg/s/cm^2 1.31/0.85
Starburst (FIR)	199 46/153	17000 mJy 2260/9480	0.906 mJy 1.52/0.906

Table 6.4: Summary of the main parameters in the source catalogs. The total number of sources in a catalog is given, #(*sources*). S_{tot}^{cat} is the integrated flux in the catalog and S_{weak} is the measured flux of the weakest source in the sample. Units are given for each individual source class. The second row for each class shows the same properties for north and south (south/north).

Sources of MeV emission

Neutrino flux predictions using the diffuse background as measured in hard X-rays by COMPTEL are based on the assumption that the cosmic diffuse photon flux below 100 MeV is directly correlated to the neutrino flux. About 10 blazars could be resolved by COMPTEL underlining the assumption that intrinsically weaker AGN are responsible for the diffuse signal. No neutrino stacking analysis of the resolved COMPTEL blazars has been done yet. Using the same assumptions as in [Man95] (*M95-B*) and in [Ste05] (*StSa05*) would challenge such an analysis. The derivation of a diffuse limit from a stacking limit would, however, be difficult at this stage, since only a negligible fraction of the sources potentially responsible for a diffuse signal is resolved into sources. Thus, the major fraction of the diffuse signal would not be included in a stacking analysis and the limit would not apply to diffuse predictions. The planned launch of satellites such as GLAST [GM99] and MEGA [K$^+$04a] encourages to pursue the examination of this source class, since it gives the prospect of increased statistics of resolved sources in the considered energy range.

Soft and hard X-rays

As mentioned before, the limit to a neutrino flux from ROSAT-detected sources would be improved significantly by selecting radio-weak sources instead of radio strong ones. A significant neutrino flux would not be expected as discussed in Section 6.4, but the improvement of the limit would underline the fact that X-ray emission from the foot of the jet is not correlated with a neutrino signal.

In hard X-rays, 15 sources have been identified in the INTEGRAL survey by JEM-X [B$^+$06] and could be interesting to examine. With the current analysis, HEAO-A results were used, while the more recent measurements by INTEGRAL are bound to be more accurate. Since a direct correlation between hard X-ray sources as detected by INTEGRAL and soft X-ray sources as seen by ROSAT does not seem to exist, an independent analysis would be reasonable. The emission of hard X-rays is likely to be correlated with TeV photon emission at least via the up-scattering of synchrotron photons by Inverse Compton scattering. Therefore, under the assumption of a correlated emission of hard X-rays and TeV photons, an analysis of the hard X-ray signal gives an indication of the flux from high frequency peaked BL Lacs.

Soft γ-rays

A catalog of 42 AGN with emission in soft γ-rays, (20, 100) keV has been released by INTEGRAL [B$^+$06]. Here, some of the sources detected by OSSE in the energy range of (50, 150) keV could be confirmed, others were not seen. We suggest to use INTEGRAL data to define a source class for the stacking of potential neutrino sources.

Starburst galaxies

The emission of neutrinos from Starburst galaxies has been suggested by Loeb & Waxman [LW06b] (LW). It is assumed that

1. Relativistic protons are accelerated along with relativistic electrons,
2. the observed radio emission results from pion-induced electrons. The same pions produce neutrinos,
3. protons lose all their energy in proton-photon interactions before reaching the diffusion time.

It has been pointed out by [Ste07] that LW overestimate the fraction of the diffuse far infrared (FIR) flux coming from Starbursts. While it is $\sim 23\%$ on average, LW assume that 100% of the detected signal comes from Starbursts. On the whole, the diffuse flux from Starbursts is presumable much lower than predicted: LW assume that Starbursts are loss dominated, which means that most primaries interact and do not escape the source. This enhances the neutrino flux, since basically all protons lose their energy in proton-photon or proton-proton interactions and produce neutrinos. Observations of the spectral radio index of the sources ($S \sim \nu^{-0.8}$) indicate, however, that Starbursts are in the diffusion limit, indicating that a negligible fraction of protons interact and only few neutrinos are produced. This contribution cannot be expected to be observed by IceCube.

There is another possibility to expect enhanced neutrino emission from Starbursts. In the past few years, it could be shown that long GRBs are typically connected to the explosion of Wolf-Rayet stars into a supernova Ic. These occur preferably in star forming regions. Thus, a diffuse flux of GRBs similar to the prediction of [WB97, WB99] should originate from the direction of these galaxies. There are two different ways to normalize the diffuse GRB spectrum. One method is to assume that the observed keV-photon flux is proportional to the neutrino flux. In that case, the normalization is dependent on the number of observed GRBs per year. This number is strongly dependent on the instrument and the number is not very exact. Under the assumption that GRBs accelerate protons up to the highest energies, $E_p \sim 10^{21}$ eV, the neutrino spectrum can also be normalized to the flux of ultra high energy cosmic rays (UHECRs). In this case, the normalization is independent of GRB observations. It should be kept in mind that the spectral index of the spectrum still varies from burst to burst - in the model of Waxman&Bahcall, an average spectral index has been used.

It is possible to look for a neutrino signal from GRBs by stacking Starburst galaxies. This method has one advantage over a triggered-GRB search: it is a systematic search, since independent of GRB data. A disadvantage is that only nearby events are included, since the sample of Starbursts only reaches out to redshifts of $z = 0.07$. It should, however, be possible to use IRAS data to identify Starburst galaxies at higher redshift. The search for a GRB signal from Starbursts should be considered as a systematic search for choked and undetected GRBs. The sources can be selected according to their FIR-flux, since this is a measure of the SN rate in a Starbursts. A higher FIR flux indicates a high star formation rate, thus more SNe and therefore, also more GRBs.

General approach to optimize stacking for diffuse interpretation

In order to get diffuse limits from source stacking, it is important to choose source classes which have information on both resolved sources and diffuse background. That way, the parameters ϵ and ξ are easily and correctly determined. A good example is the EGRET catalog, where both diffuse and resolved emission could be proven to be correlated. Alternatively, the determination of an upper limit to ξ is possible when working with a relatively complete catalog of the strongest sources in the sky by using a generic number of total sources in the source class as it is described in Section 6.3, Equ. (6.6). The diffuse interpretation of source classes like TeV blazars on the other hand is difficult, since IACTs can barely look for diffuse emission and the sensitivity of all-sky monitors such as MILAGRO is not high enough yet to detect extragalactic diffuse emission. Future Projects like HAWC experiment as a successor of MILAGRO [SSM05, S^{+}06] and CTA[1] following in the footsteps of H.E.S.S. and MAGIC, but aiming at a large field of view, see e.g. [Tes06, CTA06], will help enhancing the completeness of the sample.

In the first approach of AGN stacking in order to examine a potential excess in neutrinos, the number of used sources was determined by optimizing the significance in the detector. The optimal number of sources was in that case typically around ~ 10. In order to achieve the best stacking diffuse limit it is interesting to optimize the number of sources by taking into account ξ as well. It needs to be tested if, by reducing ξ as much as possible and taking the penalty of a possibly increased point source stacking limit instead, the diffuse limit can be increased. Also, it needs to be considered carefully if an optimization to a possible detection or to a limit is the most reasonable choice.

6.5.2 Source class evolution

For the standard analysis of muon neutrino signatures in high energy neutrino detectors, the field of view is $2\,\pi$ sr. The two experiments IceCube and KM3NeT will be observing the northern respectively the southern hemisphere in the near future and whole sky coverage is achieved by the combination of the two experiments.

---

[1] **C**herenkov **T**elescope **A**rray

Previously, in the stacking analysis of AMANDA data, sources with $\delta < 10°$ were excluded due to the decreasing sensitivity and high muon background towards the horizon. Here, all sources are included, for both northern and southern hemisphere down to $\delta = 0°$, expecting a much better sensitivity and better muon rejection near the horizon for both IceCube and KM3NeT due to improved directional reconstruction.

In this section, the different source classes discussed above will be examined with respect to their luminosity evolution. The total sample will be compared to the contribution from the northern and from the southern sky. For each sample, two figures will be discussed. The differential source counts are shown in (a), $\log N(> S)$ versus the logarithm of the flux S. In (b), the integral source evolution with the total flux of N sources is displayed. Here, the sources are organized according to their strength, starting with the brightest one. Open (black) sources display in both cases the whole sky. Red stars consider only the southern hemisphere and blue triangles show the northern hemisphere contribution.

Optically thick blazars - MeV to GeV emission

Figure 6.13 shows the luminosity evolution of EGRET sources, for the whole sky as well as for the northern and southern populations. The three most luminous sources in the EGRET sky are in the southern hemisphere. That is why the main contribution from GeV γ rays is located in the southern hemisphere where the neutrino signal contribution is thus expected to be much higher. Given the restrictive limit which could already be derived from AMANDA data, this source sample is interesting for IceCube. Considering the source distribution in the sky, the class of GeV blazars is particularly interesting for KM3NeT given the high total flux.

The COMPTEL Catalog of sources with $E < 100$ MeV is displayed in Fig. 6.14. In this case, the main contribution lies in the northern hemisphere. The small number of only 11 identified COMPTEL sources make a diffuse interpretation of a possible limit difficult. Satellites like MEGA would make the investigation even more interesting. The 11 identified sources are still useful to investigate with respect to a point source signal. The maximum diffusive factor lies around $\xi_{\max} \sim 300$ for 10,000 sources and $\xi_{\max} \sim 3000$ for 100,000 sources in the class. Depending on the steepness of the evolution function, this factor can be significantly smaller, so that doubling the number of sources could already help to draw a conclusion about a diffuse limit.

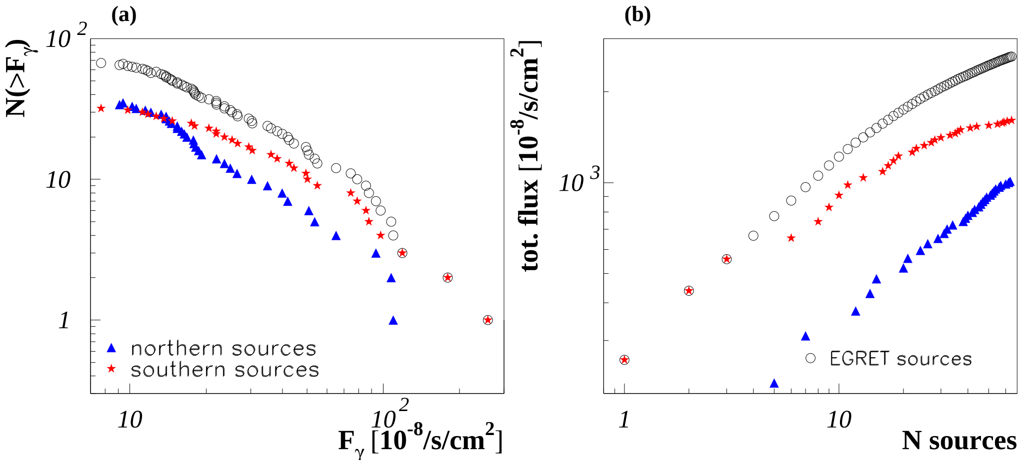

Figure 6.13: (a): Number of sources in the EGRET catalog with a flux $> F_\gamma$. The complete catalog is shown as open circles. The sample has been divided into a sub-class of sources at the northern (triangles) and southern (stars) hemisphere. (b): Total luminosities of all sources $< N$, starting to sum up with the strongest source and successively adding the next luminous source.

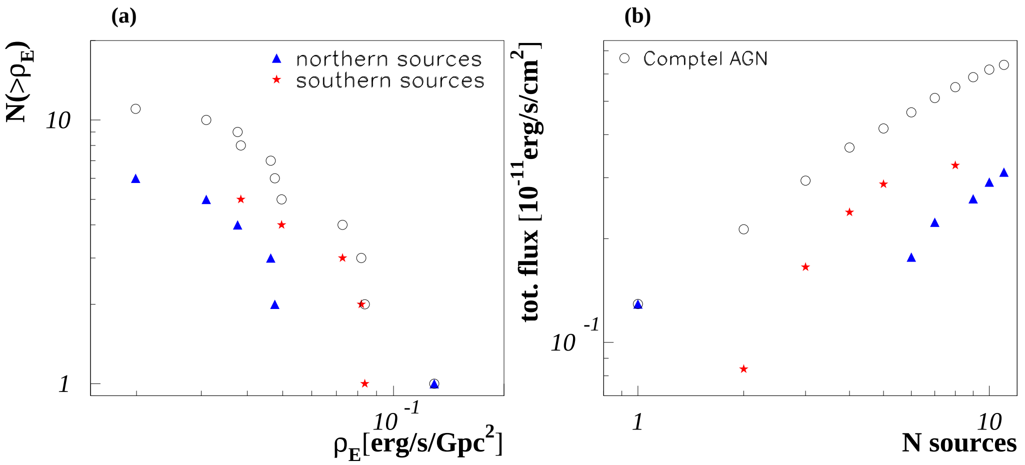

Figure 6.14: (a): Number of sources in the COMPTEL catalog with an energy density $> \rho_e$. (b): Total energy density of all sources $< N$, starting to sum up with the strongest source and successively adding the next luminous source.

Soft γ-rays

A catalog of soft γ-ray-detected AGN is given by INTEGRAL [B^+06]. There are 19 of 42 sources in the northern sky. The three most luminous sources are among the 23 southern blazars. The catalog is a good candidate for diffuse interpretation of the neutrino results, given the relatively high number of sources. The luminosity evolution is displayed in Fig. 6.15. It can be seen that the evolution is still rising and that there is still a significant fraction of signal missing. This is mirrored in the numerical value of the maximum diffusive factor which is calculated to $\xi_{\max} \sim 20$ for $N_{tot} = 10,000$ sources and $\xi_{\max} \sim 200$ for $N_{tot} = 100,000$ sources. These relatively large numbers increase a potential limit on the neutrino flux from INTEGRAL sources by about one order of magnitude[2].

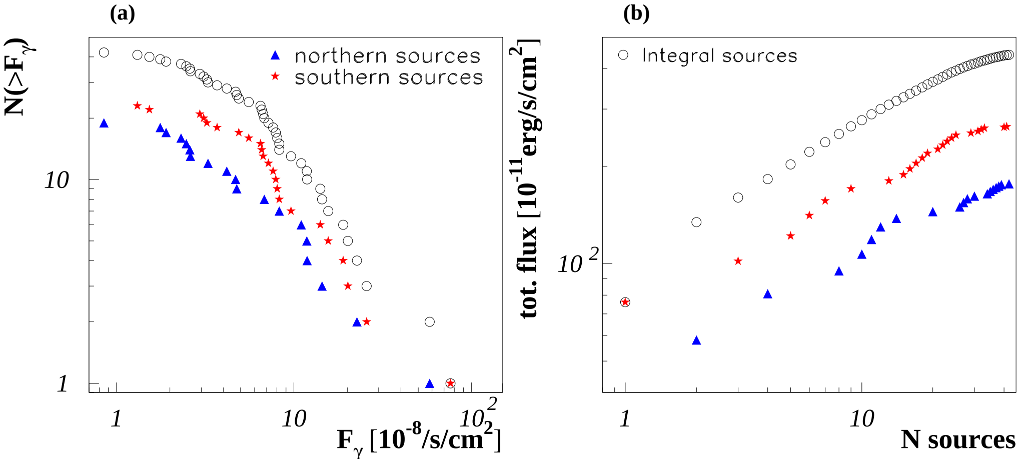

Figure 6.15: (a): $\log N(>S) - \log S$-plot for INTEGRAL sources - total catalog (circles), only northern sources (triangles) and only southern sources(stars). (b): Integral flux versus number of contributing sources.

---

[2] In Section 6.3 it is already discussed that even with a source class of 10^5 sources, the strongest 10^4 AGN make up the dominant contribution. Thus, $\xi_{\max} = 20$ is the more realistic value in this case.

Soft and hard X-rays

Figure 6.16 shows the luminosity evolution for ROSAT-detected sources. There are 84 sources in the sample, of which 35 are northern and 49 are southern sources. The three most luminous sources are in the northern hemisphere. However, these are objects which have such a large flux, since they are extremely close to Earth and not because of their high intrinsic luminosity. This is why these sources were excluded in the stacking analysis as described in [AI$^+$06e]. Without these sources, the contributions from both hemispheres are comparable.

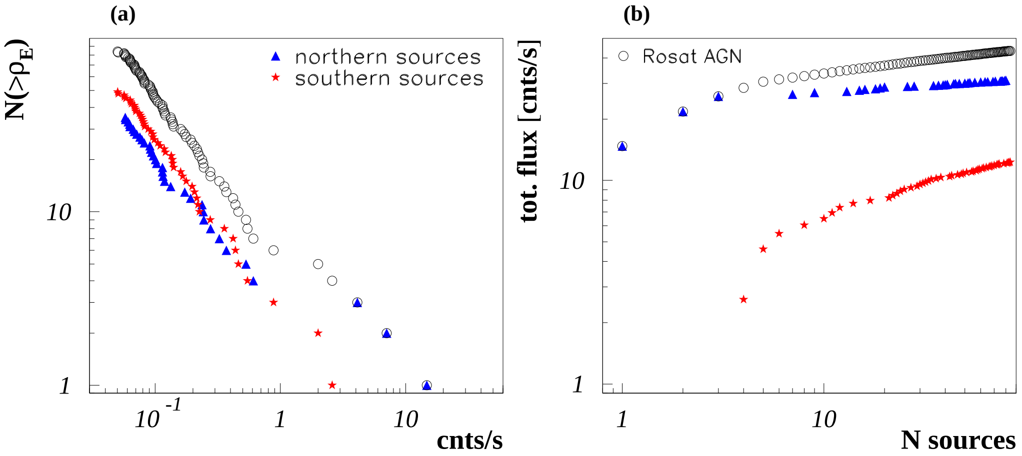

Figure 6.16: (a): Number of sources in the ROSAT catalog with an energy density $> \rho_e$. (b): Total energy density of all sources $< N$, starting to sum up with the strongest source and successively adding the next luminous source.

A sample of hard X-ray AGN is available from the INTEGRAL satellite, see Fig. 6.17. INTEGRAL detected 15 sources in the energy band of 2 keV to 10 keV. Among the 10 sources in the southern hemisphere are the two strongest sources in the sample. There are only 5 northern sources and the main contribution comes from the southern hemisphere. The INTEGRAL sample can improve the stacking analysis of hard X-ray sources which has been done with HEAO-A information. Only three northern sources were reported from HEAO-A. For a diffuse interpretation, there are still too few sources in the sample, though.

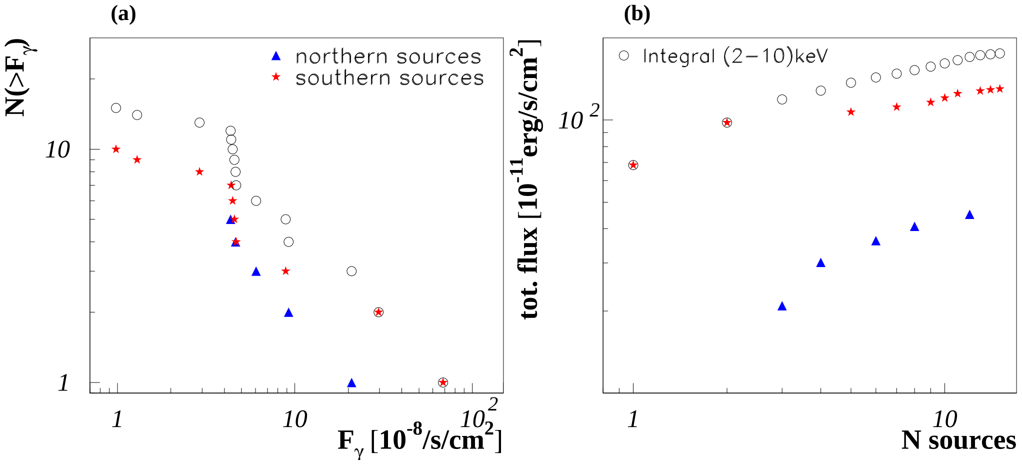

Figure 6.17: (a): $\log N(>S) - \log S$-plot for INTEGRAL sources in hard X-rays (2, 10) keV - total catalog (circles), only northern sources (triangles) and only southern sources (stars). (b) total flux of N contributing sources, starting with the brightest sources and going to weaker fluxes with higher N.

FR-I/FR-II

The catalog FR-I and FR-II sources is restricted to values of $\delta > -10°$. Therefore, only few southern sources (7 FR-I and 14 FR-II galaxies) are in the complete sample which is seen in Fig. 6.18 for FR-I galaxies and in Fig. 6.19 for FR-II galaxies. The flux is totally dominated by the northern hemisphere.

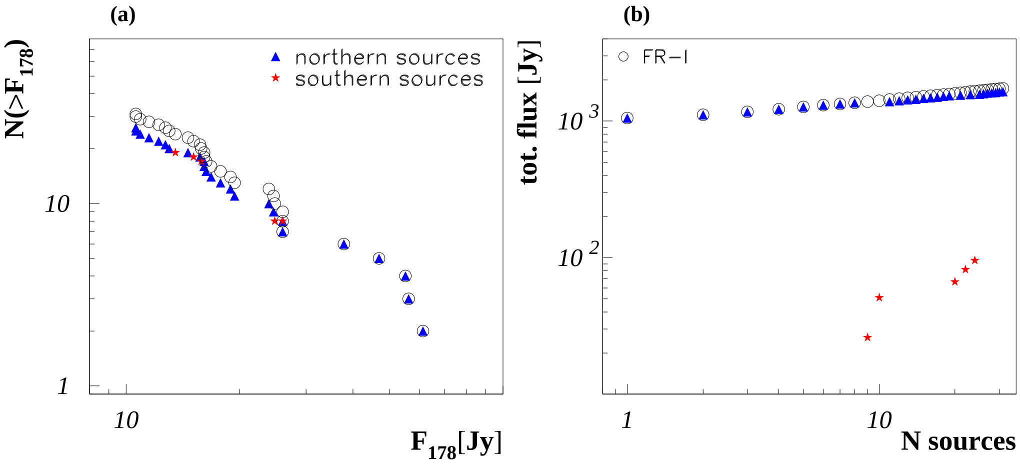

Figure 6.18: (a): Number of sources $> S$ for FR-I galaxies. (b) Total flux vs. N..

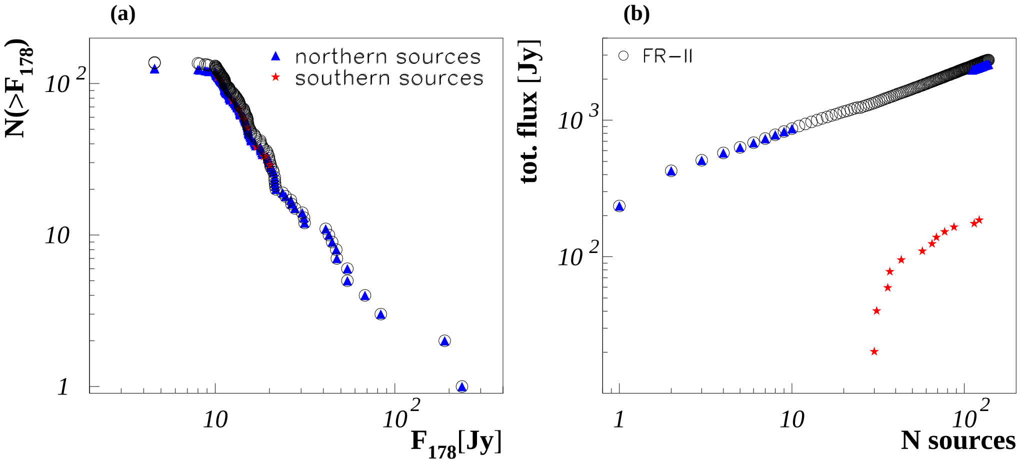

Figure 6.19: (a): Number of sources $> S$ for FR-II galaxies. (b) Total flux vs. N.

CSS/GPS

The problem for the catalog of CSS and GPS sources is similar to the situation of the FR-I and FR-II catalog. CSS have been selected at $\delta > 10°$, while GPS include data with $\delta > -25°$. Therefore, there are no southern sources in the case of CSS. Figure 6.20 shows the GPS sample. 8 southern and 20 northern sources have been identified with the main contribution from the northern hemisphere.

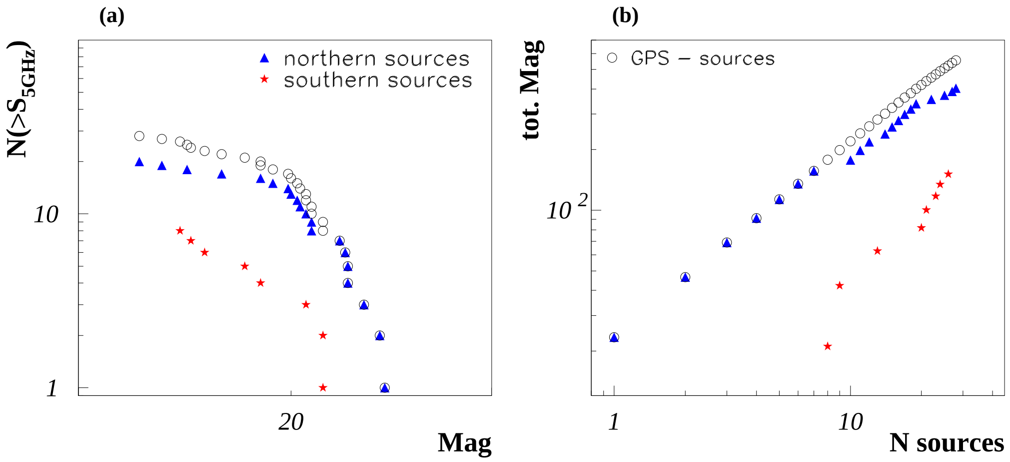

Figure 6.20: Giga-Hertz-Peaked Sources (GPS) [OB97], (a) is the differential flux evolution, (b) shows the total flux versus number of sources N.

QSOs

In the sample of QSOs as presented in [S+89], there are only 3 sources in the southern hemisphere with a measured flux at the selection wavelength, 60 μm. The sample selection of the sample was done for $\delta > -15°$, which only leaves a small window on the southern sky. While this source class is well-suited for the analysis of the northern hemisphere, there is too little data available in the southern hemisphere.

Starburst galaxies

The catalog of Starburst galaxies includes 199 sources. While the most luminous sources are in the southern, the total flux is higher in the northern hemisphere, since 153 of 199 sources are located north. A stacking analysis has good potential for both hemispheres.

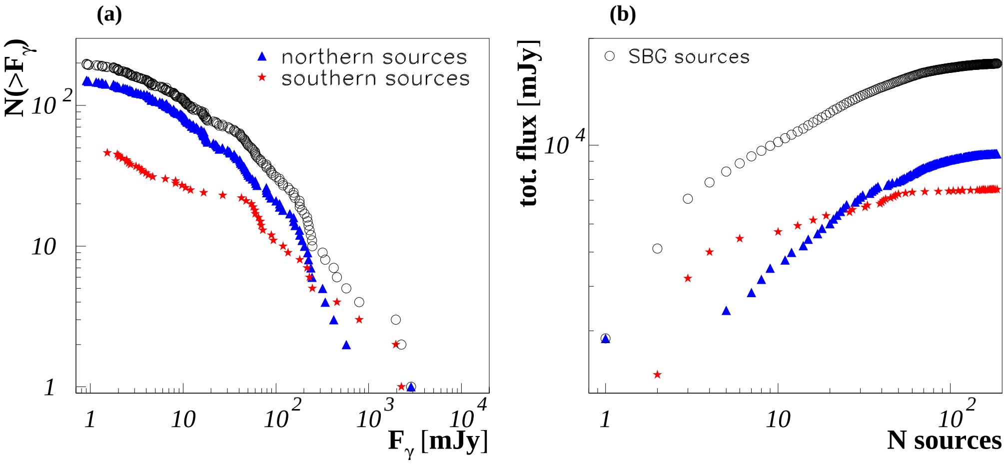

Figure 6.21: (a): Number of sources in the Starburst catalog with a flux $> F_\gamma$. (b): Total flux of all sources $< N$, starting to sum up with the strongest source and successively adding the next luminous source.

6.6 Summary & conclusions

In this chapter, limits to the diffuse flux from seven different AGN source classes could be derived from point source stacking limits from AMANDA. There is in many cases an additional constraint on flux models at the lowest energies: while the general diffuse limit is restricted to the energy band of $10^{4.2}$ GeV to $10^{6.4}$ GeV, the stacking limits reach down to 10^3 GeV. In many cases, the diffusive factor can conservatively only be estimated. It is expected, that the additional diffuse component is much smaller than the values derived here as upper limits. A reduction of the diffusive factor would result in the improvement of the stacking diffuse limits.

Neutrino flux predictions normalized to the diffuse EGRET signal above 100 MeV use the assumption that the diffuse component is produced by unresolved AGN, see [MPR01, Man95, M$^+$03b]. Thus, the EGRET stacking limit applies to such calculations. The limit falls short of the outline of two of the models, [MPR01, Man95]. The model of proton-proton interactions normalized to the EGRET diffuse measurements violates the limit at low energies around 10^3 GeV. At the highest energies, the stacking diffuse limit is more restrictive than the general diffuse limit and reaches below sensitivities of the maximum contribution from proton-photon interactions. A detection of a flux from optically thick blazars should be visible with second generation neutrino telescopes such as IceCube.

The neutrino flux models from X-ray detected AGN and from FR-II galaxies can be restricted by the general diffuse limit.

In the case of X-ray AGN, the limit strongly disfavors a hadronic model. It is an order of magnitude below the flux predictions. According to the strongly restrictive limit, neutrinos are not produced at the foot of AGN jets in coincidence with X-rays. Thus, the diffuse emission as measured by ROSAT is likely to be due to Inverse Compton radiation.

Analyzing the correlation between the radio and neutrino emission from FR-II galaxies and blazars, the limit was used to restrict the optical depth of the sources. For FR-II galaxies, $\tau_{eff} < 0.7$ could be derived, while the upper limit for blazars is given as $\tau_{eff} < 52$. Thus, the detection potential for such a source class in IceCube is very high, since within three years, IceCube is sensitive to sources of optical depth with $\tau_{eff} > 0.029$ (FR-II) resp. $\tau_{eff} > 2.5$ (blazars).

It was shown that a general diffuse analysis gives a high discovery potential for hidden TeV sources: While TeV photons are absorbed at high redshifts, neutrinos propagate freely. An upper limit to the neutrino flux from photon-resolved TeV blazars is determined to be

$$\Phi^{\mathrm{DL}}{}_{resolvedTeV} = 1.67 \cdot 10^{-9}\,\mathrm{GeV\ cm^{-2}\,s^{-1}\,sr^{-1}}\,. \tag{6.32}$$

The considerations above show that an investigation of a neutrino signal can be used to help determining different intrinsic parameters of the source type considered. It could be shown that a stacking analysis yields valuable information on the diffuse contribution from theses sources. The detection probability is enlarged significantly in such an approach and there is a high detection potential with IceCube and KM3NeT. A cascade stacking analysis by these neutrino detection arrays should be considered in order to increase the sensitivity to ultra high energy neutrino fluxes as they are described in [M^+03b].

Apart from the catalogs which have already been used in the stacking analysis of AMANDA, further source classes are investigated here. The possibility of a stacking analysis of COMPTEL sources is discussed in this chapter as a first approach to examine optically thick sources with photon emission of $E < 100$ MeV. Although no stacking diffuse limit can be derived yet due to the small percentage of resolved sources, future experiments such as GLAST at an energy range of (0.02, 300) GeV [GM99] and MEGA at (0.4, 50) MeV [K^+04a] give hope to resolve many more sources in the MeV range. Another interesting source class is the catalog of Starburst galaxies. With the correlation between starforming regions and long duration gamma ray bursts, an enhanced neutrino signal from Starbursts can be expected. The prospects of IceCube and KM3NeT are different considering source stacking. Most catalogs show a bias to one of the hemispheres. Both neutrino detection arrays can be used to extract complementary information about the different source classes.

The upper limits derived in this chapter restrict several prevailing neutrino flux models. This underlines the necessity of calculation on the basis of new developments within astroparticle physics and numerical approaches. A unified model concerning acceleration processes in AGN would give the opportunity to examine a potential neutrino signal with respect to different AGN classes within the same framework. The numerical results could be applied to individual sources and to diffuse flux measurements. The interaction between the observation of resolved sources and diffuse photon and proton components of CRs is of high significance with respect as it could be shown in this chapter.

CHAPTER 7

Final conclusions and outlook

> 'Hey - If you'd been listening, you'd know that Nintendos pass through everything.'
>
> Stargate SG1- The Crystal Skull (season 3:21)

The primary, and most general aim of this thesis is the connection of experimental and theoretical results for the three astrophysical messengers, the proton, the photon and the neutrino. This has been achieved in three basic steps: the investigation of primary proton spectra, the examination of neutrino emission from extragalactic sources and the connection to current neutrino flux limits. The main results are reviewed for each part in this Chapter.

1. Primary particle spectra for highly relativistic, oblique shocks have been examined with respect to their evolution with increasing boost factor (Chapter 3). A correlation between the spectral index and the boost factor is found. For higher boost factors, the spectra become flatter, and the correlation is found to be linear. The model is applied to GRB941017, which is a Gamma Ray Burst with spectral information on the temporal evolution of the photon energy spectrum. The spectrum of primary protons is shown to become harder with time, since the boost factor increases significantly from $\Gamma = 100$ to $\Gamma = 1000$. The diffuse spectrum resulting from the calculated spectra has been estimated, assuming that the Cosmic Ray spectrum above the knee is produced by AGN and GRBs. It turns out that the best correspondence to the spectrum is a pure AGN spectrum. In addition, the diffuse flux produced by GRBs is too flat and deviates from the measurements at high energies. In the future, the implications of the correlation between boost factor and spectral index of the primary spectra need to be investigated in more detail. Here, observations of GRB photon spectra and of AGN need to be used.

2. In Chapters 4 and 5, neutrino flux models for extragalactic sources have been investigated with respect to single source variations. Both FR-II galaxies and Gamma Ray Bursts show very strong, individual fluctuations. The neutrino flux from FR-II galaxies in the case of individually modeled sources

evolves as $\sim E^{-2.2}$, while the mean spectrum is much steeper, $E^{-2.6}$. In the case of Gamma Ray Bursts, the coincidence spectra strongly depend on the investigated burst catalog. Each catalog shows a strong individual bias concerning the detector properties. For instance, BATSE bursts are extremely strong in comparison to SWIFT-detected bursts. The results from the two chapters show that it is useful to model each object individually in order to get a better understanding of the signal strength of each source in the detector. The detection rates in high energy neutrino detectors have been estimated for GRBs, different AGN models and the flux of GZK neutrinos. In the case of GRBs, the strongest bursts yield ~ 1 event per burst in a detector like ICECUBE. One neutrino event, however, may not be significant, and therefore it is suggested to stack the most luminous bursts in order to increase the signal count. In the case of AGN and GZK neutrinos, the event rates for future detection methods like the measurement of neutrino-induced acoustic and radio signals have been estimated. For a threshold energy of 10^9 GeV, an event rate of ~ 0.01 event per km^2 and year for GZK neutrinos is expected. Planned arrays have a surface of about 100 km^2, resulting in a significant rate in only a few years. The detection rates are shown to vary with the depth of the detector in the medium, since the absorption of neutrinos by matter above the detector is significant at high energies, i.e. $E_\nu >$ EeV.

3. In Chapter 6, neutrino flux predictions are investigated with respect to current neutrino flux limits. The most restrictive limits at high energies come from the AMANDA experiment. A limit on the diffuse flux is given by AMANDA as well as point source limits to AGN classes. In this thesis, a method of interpreting the point source limits as diffuse limits to the given source class is presented. It is applied in the case of EGRET sources, for which the AMANDA limit starts to restrict predictions at energies of $E \sim 1$ TeV. The general limit to a diffuse flux restricts those models most stringently, which assume a correlation between neutrino emission and the diffuse background of X-rays from AGN. Three models exceed the AMANDA limit. Therefore, it is concluded in this thesis that X-ray emission from AGN is not connected to a significant neutrino flux. This in turn indicates that it comes from leptonic phenomena rather than hadronic acceleration processes. Other sources, on the other hand, like GeV to TeV photon emitters, are still good candidates for neutrino emission. As an outlook for the prospects of ICECUBE and KM3NET, AGN source catalogs are investigated. While ICECUBE will be sensitive to northern hemisphere sources, KM3NET mostly observes southern hemisphere objects. For instance, it is shown that much of the total signal from AGN in the EGRET catalog comes from the southern hemisphere, while FR galaxies from the 3CRR catalog are mostly located in the northern hemisphere.

In this thesis, the Olbers paradox for neutrinos has been introduced to emphasize the importance of experimental limits in the context of theoretical predictions. Once a limit contradicts the prediction, the underlying model needs to be revised. This has been done here by using AMANDA limits. Currently, the IceCube detector is under construction at the geographic South Pole. As of March 2007, 22 strings have been deployed, which corresponds to an instrumentation of about 25% of the total detector. With IceCube, it will be possible to further restrict neutrino flux predictions or to confirm a positive signal. In this thesis, possible sources and source classes are proposed, and indications of the strongest sources in the different classes are given. It is shown that there are good preconditions for the detection of both single sources and of a diffuse contribution from various source classes, if theoretical predictions are used as a basis for data selection. Such analysis strategies in turn allow for the interpretation of the theoretical results, either by confirming or restricting them.

Schlußfolgerungen und Ausblick

Das primäre und allgemeinste Ziel der vorliegenden Arbeit ist die Untersuchung der Verbindung von experimentellen und theoretischen Resultaten für die drei astrophysikalischen Botenteilchen, die Protonen, die Photonen und die Neutrinos. Der Zusammenhang wurde im Rahmen dieser Arbeit in drei grundsätzlichen Schritten analysiert: der Untersuchung von primären Protonspektren, der phänomenologischen Bestimmung von Neutrinoflüssen extragalaktischer Quellen und der Berechnung des Zusammenhangs der Photonflüsse mit den aktuellen oberen extraterrestrischen Neutrinoflußgrenzen. Die wichtigsten Resultate werden in diesem Kapitel zusammengefaßt.

1. Primäre Teilchenspektren hochrelativistischer, schiefer Schocks wurden in Hinsicht auf ihre Entwicklung in Abhängigkeit vom Lorentzfaktor betrachtet (Kapitel 3). Eine Korrelation zwischen dem Spektralverhalten der Quellen und dem Lorentzfaktor wurde festgestellt. Für hohe Lorentzfaktoren werden die Spektren flacher und es besteht ein linearer Zusammenhang zwischen den beiden Größen. Dieses theoretische Ergebnis wurde auf GRB941017 angewendet. Es handelt sich hier um einen Gamma Ray Burst, für den Informationen über die zeitliche Entwicklung des Energiespektrums vorliegen. Das Spektrum der Primärteilchen wird mit der Zeit flacher, weil der Lorentzfaktor des GRBs während der Entwicklung der Schocks signifikant von $\Gamma = 100$ auf $\Gamma = 1000$ erhöht wird. Zudem wurde das diffuse Teilchenspektrum, welches aus den theoretisch berechneten Spektren resultiert, unter der Annahme abgeschätzt, daß das Spektrum der kosmischen Strahlung oberhalb des Knies von Aktiven Galaktischen Kernen (AGN) und Gamma Ray Bursts produziert wird. Es wurde gezeigt, daß die Vorhersage am ehesten dem beobachteten Spektrum der kosmischen Strahlung entspricht, wenn ein reines AGN-Spektrum angenommen wird. Der diffuse Teilchenfluß, der von GRBs erzeugt werden würde, ist zu flach, um das beobachtete Spektrum erklären zu können. Ausgehend von diesen Ergebnissen soll in Zukunft die Korrelation zwischen Lorentzfaktor und Spek-

tralindex der Quellspektren verwendet werden, um sie mit beobachteten Photonspektren von AGN und GRBs zu vergleichen.

2. In den Kapiteln 4 und 5 wurden Neutrinoflußmodelle im Hinblick auf die Variation von Einzelquellspektren untersucht. Sowohl FR-II Galaxien als auch Gamma Ray Bursts zeigen sehr starke, individuelle Fluktuationen. Der Neutrinofluß von FR-II Galaxien folgt einem $\sim E^{-2.2}$-Energieverhalten im Fall von individuell modellierten Spektren, während das Spektrum unter Verwendung von mittleren Parametern ein $E^{-2.6}$-Spektrum ergibt. Im Fall von Gamma Ray Bursts ist das koinzidente Spektrum stark abhängig von dem untersuchten Quellkatalog. Jeder Katalog beinhaltet eine starke Beeinflussung der Ergebnisse durch die Detektoreigenschaften des Experiments. So sind zum Beispiel BATSE-detektierte Bursts extrem stark im Vergleich zu SWIFT-detektierten. Die Ergebnisse der beiden Kapitel verdeutlichen die Notwendigkeit, Neutrinospektren individuell zu modellieren, um ein besseres Verständnis der Signalstärke jeder einzelnen Quelle im Detektor zu erreichen. Die Detektionsraten bei Hochenergie-Neutrinodetektoren wurden für GRBs, verschiedene AGN-Modelle und GZK-Neutrinos abgeschätzt. Im Fall von Gamma Ray Bursts ergibt der stärkste Burst eine Rate von ~ 1 Ereignis pro Burst in einem Detektor wie ICECUBE. Ein einzelnes Signalereignis ist jedoch vermutlich nicht signifikant, da die Wahrscheinlichkeit, daß es sich um ein atmosphärisches Neutrino handelt, nicht Null ist. Das Überlagern des potentiellen Signals der stärksten Bursts ist daher sinnvoll, um die Signalstärke zu maximieren. Im Fall von AGN- und GZK-Neutrinos wurden die Ereignisraten für zukünftige Detektionsmethoden wie die akustische Detektion und die Messung eines Neutrino-induzierten Radiosignals berechnet. Für eine Schwellenergie von 10^9 GeV wird eine Ereignisrate von ~ 0.01 Ereignissen pro km^2 und Jahr von GZK-Neutrinos erwartet. Die Detektion von Neutrino-induzierten akustischen Signalen und Radioereignissen wird für ein mit akustischen Sensoren und Radioantennen ausgestattetem Array von ca. 100 km^2 geplant. Dies wiederum impliziert, daß das durch GZK-Neutrinos erzeugte Signal schon nach wenigen Jahren nachweisbar sein sollte. Die Berechnungen zeigen eine Variation der Detektionsraten mit der Tiefe des Detektors in der Erde, da die Absorption von Neutrinos durch Materie oberhalb des Detektors bei solch hohen Energien ($E_\nu >$ EeV) signifikant ist.

3. In Kapitel 6 wurden Neutrinoflußvorhersagen in Hinsicht auf aktuelle Neutrinoflußgrenzen untersucht. Das momentan sensitivste Experiment bei hohen Energien ist das AMANDA-Teleskop. Eine obere Grenze für den diffusen Fluß wird von AMANDA ebenso festgelegt wie Grenzen an Punktquellenklassen, insbesondere AGN-Klassen. In der vorliegenden Arbeit wurde eine Methode zur Interpretation der Punktquellengrenzen als Grenzen für den diffusen Fluß der entsprechenden Quellklasse präsentiert. Diese wurde dann im Fall der EGRET Quellen angewendet. Neutrinoflußmodelle,

> die auf einer Korrelation zwischen GeV Photonen und Neutrinos beruhen, werden von der berechneten Grenze oberhalb von $E_\nu \sim 1$ TeV teilweise eingeschränkt. Des weiteren schränkt die allgemeine Grenze bezüglich des diffusen Flusses jene Modelle stark ein, die einen Zusammenhang zwischen Neutrinoemission und dem diffusen Röntgenhintergrund von AGN annehmen. Drei dieser Modelle sagen einen Neutrinofluß vorher, der oberhalb der experimentellen Neutrinoflußgrenze von AMANDA liegt. Daraus kann geschlossen werden, daß die beobachtete Röntgenemission nicht mit einer signifikanten Neutrinoemission zusammenhängt. Das bedeutet wiederum, daß hier ein leptonisches Beschleunigungsszenarium wahrscheinlicher ist, als ein hadronisches. Andere Quellklassen, wie Aktive Galaktische Kerne, die hochenergetische Photonen im GeV- bis TeV-Bereich aussenden, sind immer noch gute Kandidaten für die Emission von Neutrinos. Um einen Ausblick auf die Möglichkeiten von IceCube und KM3NeT zu geben, wurden AGN-Quellkataloge bezüglich ihrer Quellverteilung am Himmel betrachtet. Während IceCube die nördliche Hemisphäre im Blick haben wird, erfaßt KM3NeT hauptsächlich die südliche Hemisphäre. Weiterhin wurde gezeigt, daß ein Großteil des totalen Signals von Aktiven Galaktischen Kernen, die im EGRET Katalog verzeichnet sind, in der südlichen Hemisphäre lokalisiert ist, während FR Galaxien aus dem 3CRR Katalog zum Großteil in der nördlichen Hemisphäre zu finden sind.

In der hier präsentierten Arbeit wurde das Olbers Paradoxon für Neutrinos eingeführt, um die Wichtigkeit experimenteller Grenzen in bezug auf theoretische Vorhersagen zu diskutieren. Sobald eine Grenze der Flußvorhersage widerspricht, muß das zugrundeliegende Modell bezüglich seiner grundlegenden Annahmen verändert werden. Dies konnte hier mit Hilfe der mit AMANDA bestimmten Flußgrenzen geschehen. Momentan ist der IceCube Detektor am geographischen Südpol im Aufbau. Bisher wurden 22 Stränge, bestückt mit Lichtverstärkern, im antarktischen Eis installiert, was bereits 25% des totalen Detektorvolumens von 1 km^3 entspricht. Mit IceCube wird es möglich sein, Neutrinoflußvorhersagen weiter einzuschränken oder Signale zu beobachten. In der vorliegenden Arbeit wurden mögliche Einzelquellen und Quellklassen als Beobachtungsobjekte vorgeschlagen, und es wurde untersucht, wo die stärksten Quellen einer Klasse liegen. Es wurde gezeigt, daß sowohl die Suche nach Einzelquellen wie auch nach einem diffusen Signal verschiedener Quellklassen sehr vielversprechend ist, wenn theoretische Vorhersagen als Grundlage zur Datenselektion verwendet werden. Umgekehrt lassen wiederum die experimentellen Ergebnisse sowohl bei Ausschluß wie auch bei Bestätigung des Modells Rückschlüsse auf die Physik der Quellen zu.

APPENDIX A

How to read this thesis

Figure A.1 shows a scheme of how to read this thesis if you are interested in a specific chapter. The scheme gives suggestions what parts of the introductory chapters are significant for the given chapter. Of course, you are welcome to read the thesis from the beginning to the end!

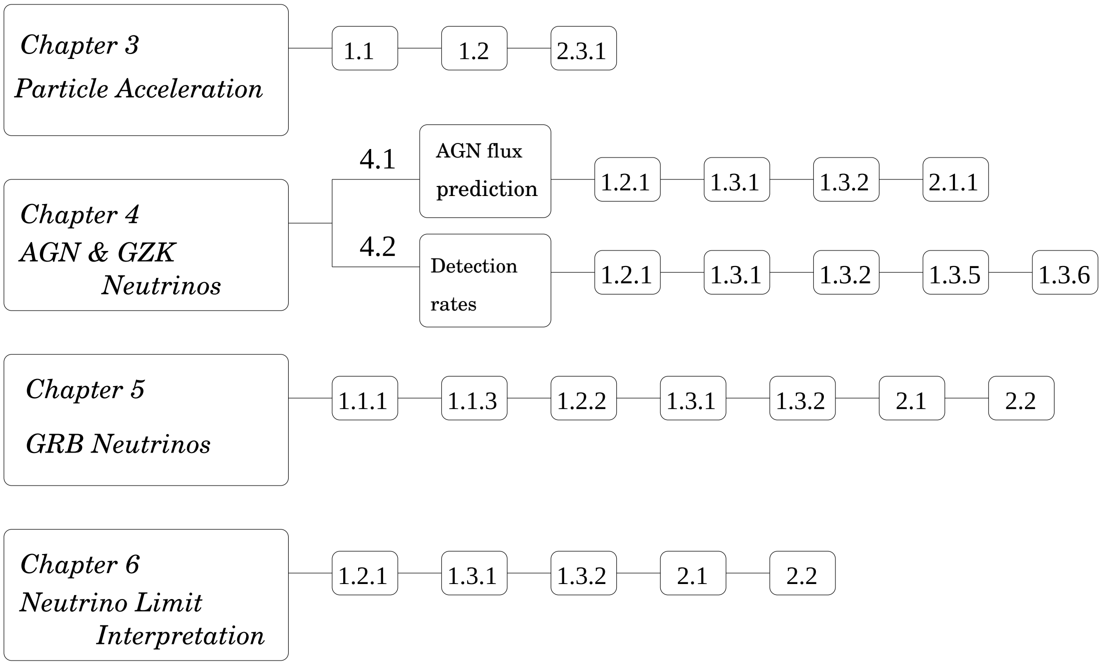

Figure A.1: Organization scheme.

APPENDIX B

Neutrino detection rates - muon neutrinos

While Chapter 4 presents neutrino detection rates for electron neutrinos, the results for muon neutrinos are presented here. The rates for muon and electron neutrinos are comparable. The incident neutrino flux at Earth is the same for most models and the interaction probability varies very little between the two flavors.

	R_0	[km^{-3}yr^{-1}]		R_0/R_0(atm)		
$E_{\rm min}$ =	10^7 GeV	10^8 GeV	10^9 GeV	10^7 GeV	10^8 GeV	10^9 GeV
BBR-II	5.6	0.89	0.099	$6 \cdot 10^6$	$4 \cdot 10^8$	$5 \cdot 10^{10}$
MPR	25	4.1	0.36	$3 \cdot 10^7$	$2 \cdot 10^9$	$2 \cdot 10^{11}$
RB	0.39	0.28	0.059	$4 \cdot 10^5$	$1 \cdot 10^8$	$3 \cdot 10^{10}$
YT	0.17	0.14	0.033	$2 \cdot 10^5$	$7 \cdot 10^7$	$2 \cdot 10^{10}$
Atmos.	$1 \cdot 10^{-06}$	$2 \cdot 10^{-09}$	$2 \cdot 10^{-12}$	1	1	1

Table B.1: Number of muon neutrino-induced events for a 1 km^3 ice or water detection array. The numbers have been calculated for various detector threshold energies, i.e. $E_{\rm min} = 10^7$, 10^8, 10^9 GeV. The ratio of the event numbers for different models and the atmospheric rate is also quoted. The depth of the detection array below the Earth's surface is assumed to be $d = 500$ m.

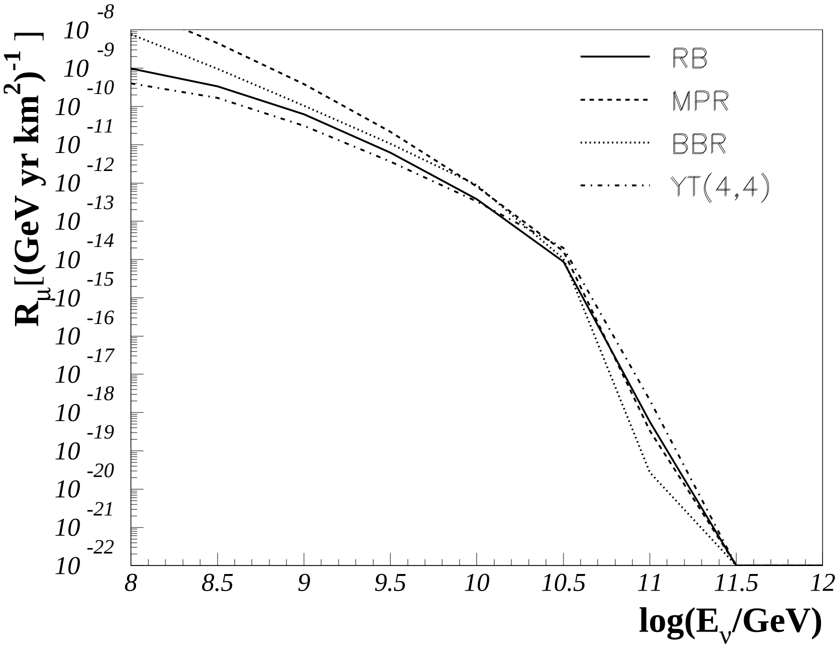

Figure B.1: Muon and anti-muon neutrino induced event rate per year, square kilometer and GeV. Downgoing events have been considered, i.e. $\theta = 0^\circ - 90^\circ$ and $\phi = 0 - \pi$.

	R_0	$[\mathrm{km}^{-3}\,\mathrm{yr}^{-1}]$	
$d =$	0.5 km	1.5 km	2.5 km
BBR-II	5.6	3.7	2.7
MPR	25	16	12
RB	0.39	0.17	0.098
YT	0.13	0.054	0.029

Table B.2: Muon neutrino event rates for different detector depths, $d = 0.5, 1.5, 2.5$ km. The detector threshold energy is $E_{\min} = 10^7$ GeV. The rate decreases with the depth, since neutrinos are absorbed in the Earth.

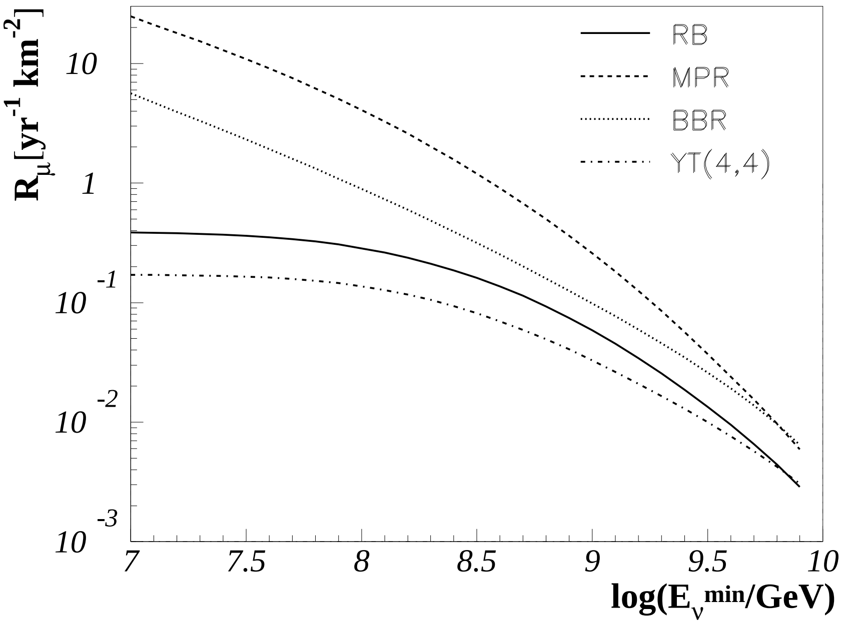

Figure B.2: Integrated neutrino rate, representing the number of detected muon neutrino induced cascades above a certain energy E_{min}.

APPENDIX C

GRBs

C.1 Parameter distribution of the AMANDA subsample (82 bursts)

In this section, the parameters for the 82 bursts in the BATSE sample, which occurred during the operation of AMANDA, are shown.

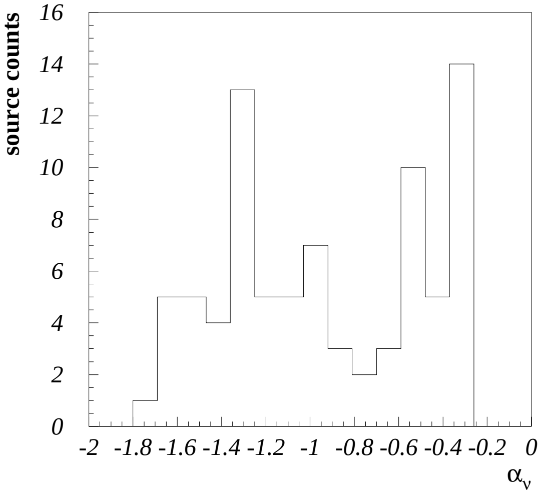

Figure C.1: α_ν: first spectral index of the neutrino spectrum.

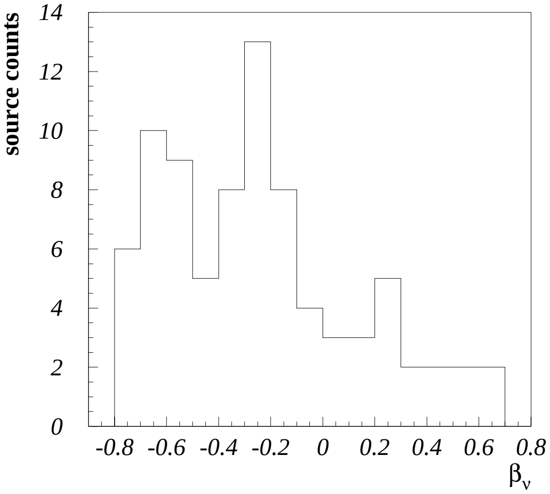

Figure C.2: β_ν: second spectral index of the neutrino spectrum.

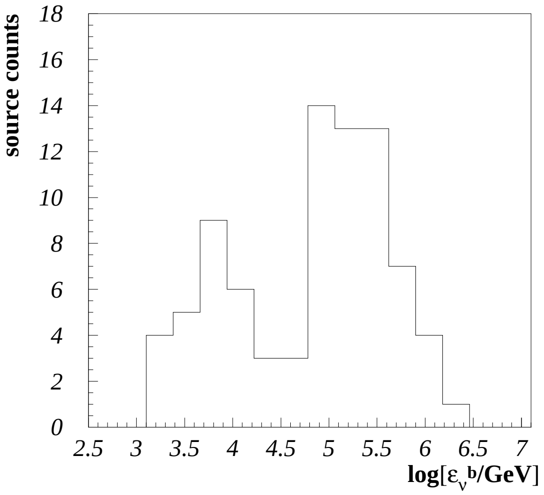

Figure C.3: First break energy, AMANDA bursts.

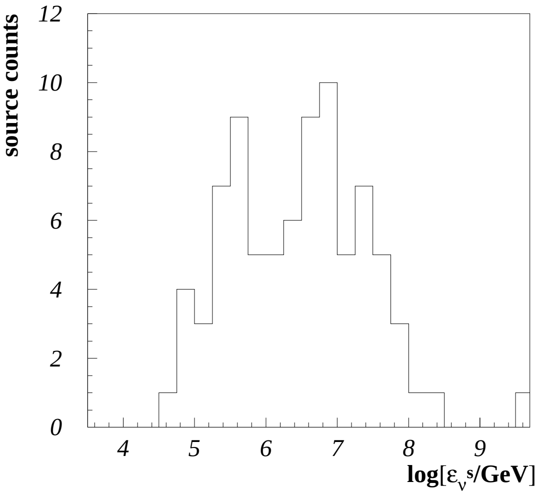

Figure C.4: Second break energy, AMANDA bursts.

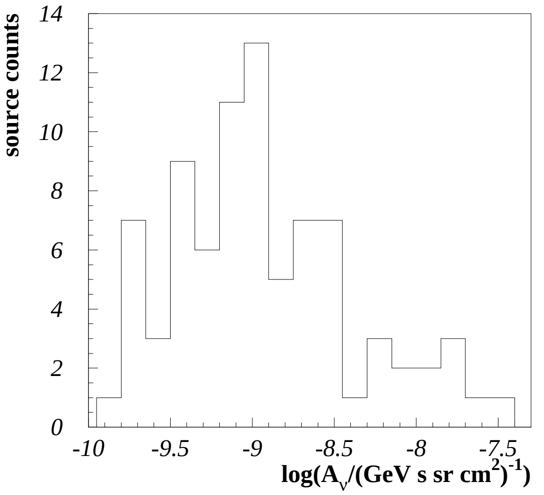

Figure C.5: Normalization A_ν of the neutrino spectrum (AMANDA subsample).

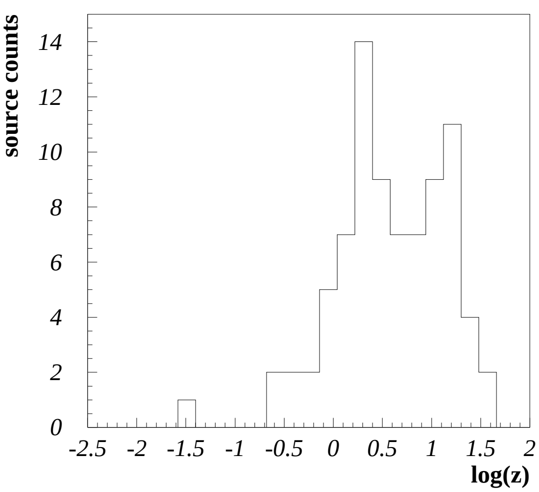

Figure C.6: Redshift distribution (AMANDA subsample)

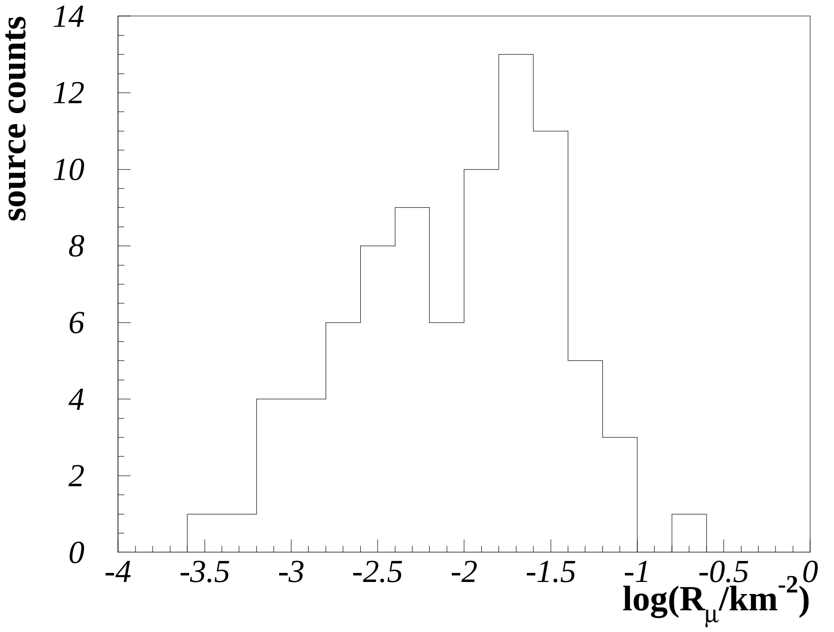

Figure C.7: Rate distribution for the 82 bursts in the AMANDA subsample.

C.2 Single source spectra

The coincidence spectra for different GRB samples as presented in Chapter 5 have been calculated using the single source spectra which are shown for each sample in this section.

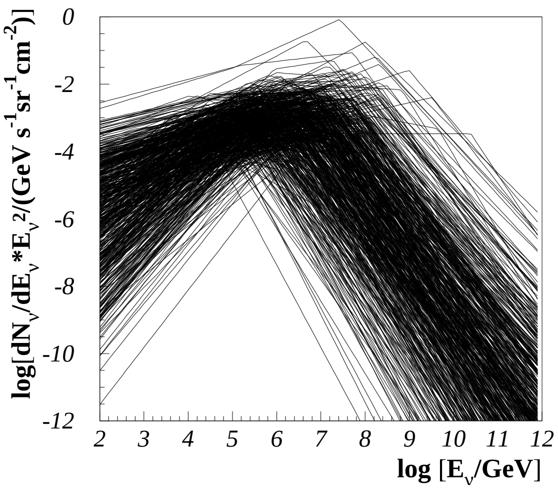

Figure C.8: Single burst neutrino spectra for 568 BATSE bursts, redshifts determined via the variability method.

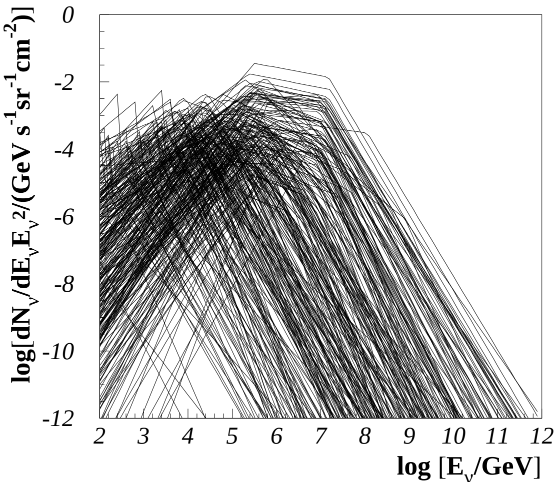

Figure C.9: Single burst spectra for 292 BATSE bursts with lag-determined redshifts.

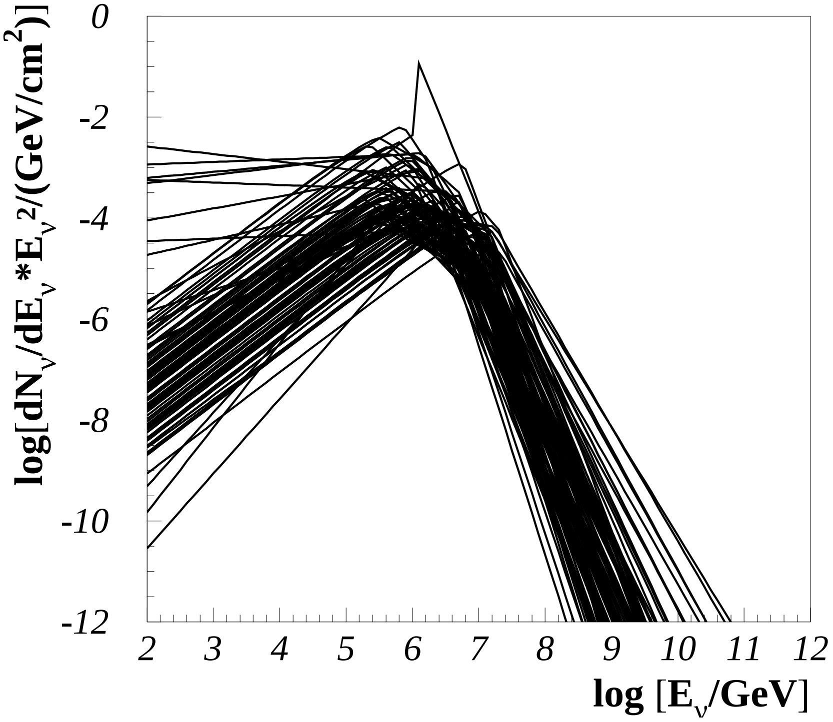

Figure C.10: Single burst spectra for 99 KONUS short bursts.

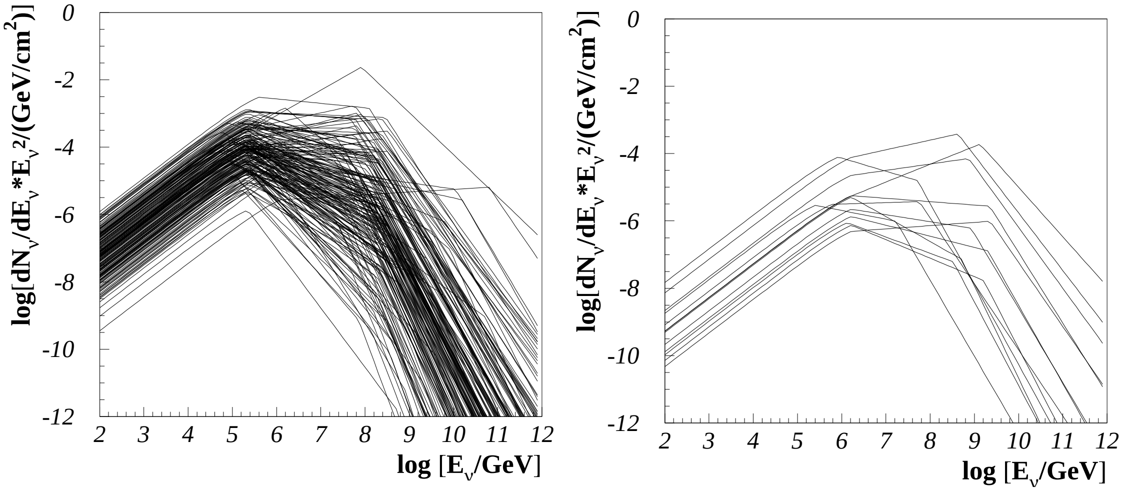

Figure C.11: Single burst spectra for 188 long SWIFT bursts.

Figure C.12: Single burst spectra for 13 short SWIFT bursts.

APPENDIX D

Glossary

D.1 Flux definitions

	spectrum	units
	At the source	
Differential proton flux	$d\Phi/dE_p \propto E_p^{-\alpha_p}$	arbitrary
Integral neutrino flux	Φ_ν	arbitrary
Differential neutrino flux	$d\Phi_\nu/dE_\nu$	arbitrary
Integral photon flux	Φ_γ	arbitrary
Electromagn. luminosity	L	erg/s
Luminosity at a certain frequency	L_ν	W/Hz
	At Earth	
Differential flux of charged CRs	$dN_{CR}/dE_{CR} \propto E_{CR}^{-\alpha_{CR}}$	$\mathrm{GeV}^{-1}\,\mathrm{cm}^{-2}\,\mathrm{s}^{-1}\,\mathrm{sr}^{-1}$
Differential proton flux	$dN_p/dE_p \propto {E_p}^{-\alpha_p}$	$\mathrm{GeV}^{-1}\,\mathrm{cm}^{-2}\,\mathrm{s}^{-1}\,\mathrm{sr}^{-1}$
Differential neutrino flux	$dN_\nu/dE_\nu \cdot {E_\nu}^2 \propto E_p^{-\alpha_\nu}$	$\mathrm{GeV\ cm}^{-2}\,\mathrm{s}^{-1}\,\mathrm{sr}^{-1}$
Photon fluence	F_γ	$\mathrm{erg/cm}^2$
Differential photon flux	$dN_\gamma/dE_\gamma \propto {E_\gamma}^{\alpha_\gamma}$	arbitrary
Total synchrotron power	$P_{tot} \propto \omega^{-s}$	arbitrary
Photon flux density	$S \propto \nu^{-s}$	arbitrary
Cosmic Ray energy density	$j_E = \int_{E_{\min}} dN_p/dE_p\, E_p\, dE_p$	$\mathrm{GeV\ cm}^{-2}\,\mathrm{s}^{-1}\,\mathrm{sr}^{-1}$
CR luminosity	$L_{CR} = \frac{4\,\pi}{c} \cdot j_E(E_{\min}) \cdot \frac{V_{GD}}{\tau_R}$	erg/s
(galactic)	τ_R: CR residence time	
	V_{gd}: volume galactic disk	
CR luminosity	$L_{CR} = \frac{4\,\pi}{c} \cdot j_E(E_{\min}) \cdot \frac{dV}{dz} t_H$	erg/s
(extragalactic)	dV/dz : comoving volume	
	t_H: Hubble time	
	Neutrino flux limits	
Point source limit	Φ^{PS}	$\mathrm{GeV\ cm}^{-2}\,\mathrm{s}^{-1}$
Stacking limit	Φ^{SL}	$\mathrm{GeV\ cm}^{-2}\,\mathrm{s}^{-1}$
Diffuse limit	Φ^{DL}	$\mathrm{GeV\ cm}^{-2}\,\mathrm{s}^{-1}\,\mathrm{sr}^{-1}$
Stacking diffuse limit	Φ^{SDL}	$\mathrm{GeV\ cm}^{-2}\,\mathrm{s}^{-1}\,\mathrm{sr}^{-1}$

D.2 Physical constants and units

	General	
Gravitational constant	[YP+06]	$G = 6.6742 \cdot 10^{-11}$ m^3 kg^{-1} s^{-2}
Speed of light	[YP+06]	$c = 2.998 \cdot 10^8$ m/s
	Particle Physics	$(c = \hbar = 1)$
Avogadro constant	[YP+06]	$N_A = 6.022 \cdot 10^{23}$ mol^{-1}
Thomson cross section	[YP+06]	$\sigma_T = 0.665 \cdot 10^{-24}$ cm^2
W boson mass	[YP+06]	$M_W = 80.403$ GeV
Z boson mass	[YP+06]	$M_Z = 91.188$ GeV
Proton mass	[YP+06]	$m_p = 0.9383$ GeV
Neutron mass	[YP+06]	$m_n = 0.9396$ GeV
Mass Δ^+	[YP+06]	$m_\Delta = 1.232$ GeV
Mass π^+	[YP+06]	$m_\pi^+ = 0.1396$ GeV
Mass π^0	[YP+06]	$m_\pi^0 = 0.1394$ GeV
Muon mass	[YP+06]	$m_\mu = 105.7$ MeV
Electron mass	[YP+06]	$m_e = 5110$ keV
Fermi constant	[YP+06]	$G_F = 1.166 \cdot 10^{-5}$ GeV^{-2}
Weak mixing parameter	[YP+06]	$x_W = \sin^2 \theta_W = 0.2315$
	Astronomy	(cgs)
Astronomical Unit	[CO96]	1 AU= $1.4960 \cdot 10^{13}$ cm
lightyear	[CO96]	1 ly= $9.4605 \cdot 10^{17}$ cm
parsec	[CO96]	1 pc= $3.0857 \cdot 10^{18}$ cm
	[CO96]	= 3.2616 ly
erg	[CO96]	$= 10^{-7}$ J
	[CO96]	= 0.624 TeV
Earth radius	[CO96]	$R_\oplus = 6378$ km
Solar Mass	[CO96]	$M_\odot = 1.989 \cdot 10^{33}$ g
Solar Luminosity	[CO96]	$L_\odot = 3.826 \cdot 10^{33}$ erg/s
Solar Radius	[CO96]	$R_\odot = 6.9599 \cdot 10^{10}$ cm
	Cosmology	
Hubble parameter	[S+07]	$h = 0.72$
Matter density	[S+07]	$\Omega_m = 0.24$
Cosmological constant	[S+07]	$\Omega_\Lambda = 0.76$
Schwarzschild radius	[CO96]	$r_s = \frac{2GM}{c^2} \approx 3 \cdot \frac{M}{M_\odot}$ km

D.3 Astroparticle physics experiments

AGASA	**A**keno **G**iant **A**ir **S**hower **A**rray	[Y$^+$95]
AGILE	**A**stro-rivelatore **G**amma a **I**mmagini **LE**ggero	[PTA06]
AMADEUS	ANTARES **M**odules for **A**coustic **DE**tection **U**nder the **S**ea	[N$^+$06]
AMS	**A**lpha **M**agnetic **S**pectrometer	[Cri03]
AMANDA	**A**ntarctic **M**uon **A**nd **N**eutrino **D**etector **A**rray-II	[AI$^+$06a]
ANITA	**AN**tarctic **I**mpulsive **T**ransient **A**ntenna Experiment	[BA$^+$06]
ANTARES	**A**stronomy with a **N**eutrino **T**elescope and **A**byss environmental **RES**earch	[Mon03] [AA$^+$97]
ARIANNA	**A**ntarctic **R**oss **I**ceshelf **AN**tenna **N**eutrino **A**rray	[Bar06]
Auger	Pièrre **Auger** Observatory	[DA$^+$06]
AURA	**A**skaryan **U**nderice **R**adio **A**rray	[GME93]
Baikal	The experiment is localized in lake **Baikal**	[Wis06]
BATSE	**B**urst **a**nd **T**ransient **S**ource **E**xperiment	[P$^+$99]
BeppoSax	**Beppo** stands for Guiseppe Occhialini, SAX=**S**atellite per **A**stronomia **X**	[WRM97]
BESS	**B**alloon **B**orne **E**xperiment with a **S**uperconducting Solenoidal **S**pectrometer	[M$^+$05c]
Chandra	Short for **Chandra**sekhar	[K$^+$04b]
CGRO	**C**ompton **G**amma **R**ay **O**bservatory	[CGR07]
COMPTEL	**COM**pton **TEL**escope	[K$^+$96]
CTA	**C**herenkov **T**elescope **A**rray	[Tes06]
EGRET	**E**nergetic **G**amma **R**ay **E**xperiment **T**elescope	[S$^+$98]
Fréjus	the experiment is located near the French town **Fréjus**	[Ber87]
GLAST	**G**amma-Ray **L**arge **A**rea **S**pace **T**elescope	[GM99]
HAWC	**H**igh **A**ltitude **W**ater **C**herenkov	[SSM05]
HEAO-A	**H**igh **E**nergy **A**stronomy **O**bservatories-**A**	[SD78]
HETE-II	**H**igh **E**nergy **T**ransient **E**xplorer-II	[S$^+$05a]
HEGRA	**H**igh **E**nergy **G**amma-**R**ay **A**stronomy	[Aha04b]
H.E.S.S.	**H**igh **E**nergy **S**tereoscopic **S**ystem	[Vas05]
HiRes	**Hi**gh **Res**olution Fly's Eye Detector	[HiR04]
IceCube	-	[AI$^+$04]
IMP-6	**I**nterplanetary **M**onitoring **P**latform	[IMP07]
INTEGRAL	**INTE**rnational **G**amma-**R**ay **A**strophysics **L**aboratory	[Win04]
IPN3	Third **I**nter**P**lanetary **N**etwork	[IPN07]
IRAS	**I**nfra**R**ed **A**stronomical **S**atellite	[S$^+$03]

Kamiokande	**KAMIOKA** **N**ucleon **D**ecay **E**xperiment where the experiment is located	[FK^{+}98]
KASCADE	**KA**rlsruhe **S**hower **C**ore and **A**rray **DE**tector	[A^{+}05]
KASCADE-Grande	see KASKADE	[HK^{+}03]
KM3NeT	-	[KM3a]
Konus Wind	-	[M^{+}05a]
Kosmos-461	-	[M^{+}75]
LOFAR	**LO**w **F**requency **A**rray	[F^{+}06]
LOPES	**LO**FAR **P**rototyp**E** **S**tation	[FL^{+}05]
LUNASKA	**L**unar **U**ltra-high-energy **N**eutrino **A**strophysics using **SKA**	[LUN07]
MAGIC	**M**ajor **A**tmospheric **G**amma **I**maging **C**herenkov Telescope	[AM^{+}06b]
Mars Odyssey	-	[Mar07]
MEGA	**M**edium **E**nergy **G**amma-ray **A**stronomy	[K^{+}04a]
MILAGRO	**M**ultiple **I**nstitution **L**os **A**lamos **G**amma **R**ay **O**bservatory	[GM^{+}06]
NEMO	**NE**utrino **M**editerranean **O**bservatory	[Sap06]
NESTOR	**N**eutrino **E**xtended **S**ubmarine **T**elescope with **O**ceanographic **R**esearch	[AN^{+}05]
OSSE	**O**riented **S**cintillation **S**pectrometer **E**xperiment	[J^{+}97]
OSO-7	**O**rbiting **S**olar **O**bservatory-**7**	[OSO07]
PAMELA	A **P**ayload for **A**ntimatter **M**atter **E**xploration and **L**ight-nuclei **A**strophysics	[P^{+}06]
Planck	after Max **Planck**	[MVV02]
RHESSI	**R**amaty **H**igh **E**nergy **S**olar **S**pectroscopic **I**mager	[KH04]
RICE	**R**adio **I**ce **C**herenkov **E**xperiment	[K^{+}03]
ROSAT	**RO**entgen **SAT**ellite	[BHI94]
RXTE	**R**ossi **X**-ray **T**iming **E**xplorer	[R^{+}04]
SalSA	**Sal**t dome **S**hower **A**rray	[V^{+}05b]
SAUND	**S**tudy of **A**coustic **U**ltra-high-energy **N**eutrino **D**etection	[VGL05]
SKA	**S**quare **K**ilometre **A**rray	[SKA07]
SNO	**S**udbury **N**eutrino **O**bservatory	[SNO02]
SPATS	**S**outh **P**ole **A**coustic **T**est **S**etup	[B^{+}05b]
SuperKamiokande	**S**uper **KAMIOKA** **N**ucleon **D**ecay **E**xperiment	[FK^{+}98]
Suzaku	named after a red sparrow-like bird in Chinese mythology	[M^{+}07]
Swift	-	[Chi06]
Ulysses	-	[H^{+}92]
UMRAO	**U**niversity of **M**ichigan **R**adio **A**strophysical **O**bservatory	[UMR07]
Vela Satellites	-	[KSO73]
Whipple	named after Fred Lawrence **Whipple**	[Kre98]
WMAP	**W**ilkonson **M**icrowave **A**nisotropy **P**robe	[S^{+}07]
VERITAS	**V**erv **E**nergetic **R**adiation **I**maging **T**elescope **A**rray **S**ystem	[Hol06]
VLA	**V**ery **L**arge **A**rray	[VLA07]
WSRT	**W**esterbork **S**ynthesis **R**adio **T**elescope	[HB74]
XMM-Newton	**X**-ray **M**ulti-**M**irror Mission **Newton**	[J^{+}01]

LIST OF FIGURES

LIST OF TABLES

Danke an/Thanks to...

☺ ...Wolfgang Rhode - Vielen, herzlichen Dank für die langjährige, exzellente Betreuung und die vielen Möglichkeiten - zu Konferenzen und Schulen zu fahren, den Dialog mit anderen Wissenschaftlern zu pflegen, für tolle Lehraufgaben und Weiterbildungsmöglichkeiten!

☺ ...Peter Biermann - Danke für die intensiven Gespräche und die tolle Betreuung, sei es in Dortmund, Bonn, Bloomington oder sonstwo auf der Welt.

☺ ...Francis Halzen - All discussions on astroparticle physics and more have been and are always a great pleasure!

☺ ...Kirsten Münich - Vielen, lieben Dank für die wissenschaftliche und freundschaftliche Unterstützung durch die Jahre - im Büro und außerhalb. Ciao, ich bin raus!

☺ ... die gesamte Arbeitsgruppe Dortmund - Vielen Dank, Jens Dreyer, Matthias Bartelt, Andreas Gross, Wolfgang Wagner, Dominik Leier, Jan Lünemann, Michael Backes, Marijke Haffke, Frank Refflinghaus, Tanja Kneiske, Vanessa Cirkel, Timo Messarius, Matthias Domke und Eva Lorenz - für die verschiedensten Dinge, sei es wissenschaftliche Diskussionen, Computer-Beratungen und -Reparaturen, administrative Dinge, Kaffeepausen und vieles mehr!

☺ ... Lynn Suter and Cat Lewis - for their work and support during their RISE internship in summer 2006 here in Dortmund.

☺ ... the Madison IceCube group - particularly to Mike Stamatikos and Paolo Desiati for their friendship and help.

☺ ... the entire IceCube collaboration - for all scientific discussions and a good atmosphere throughout the years.

☺ … the MAGIC collaboration - for good and extensive scientific discussions.

☺ … Athina Meli and John Quenby - Thanks for the great collaboration and the opportunity to learn about acceleration mechanisms from both of you. Particularly, I would like to thank you, Athina, for providing primary particle spectra for this work.

☺ … Reinhard Schlickeiser, Karl Mannheim, Eli Waxman, Valentin Pal'shin, Werner Collmar, Pauline Harris, Floyd Stecker, Todor Stanev, Marina Kaufman and many more - for improving this work in many ways, through extensive and fruitful discussions.

☺ … Peter Schneider, Konny Eschbach und Patricia Pielage - u.a. dafür daß Ihr Euch die Zeit genommen habt, die Arbeit Korrektur zu lesen.

☺ … Horst Mühlhaus - Ein großes Dankeschön - ohne den Spaß, der im Oberstufen-Unterricht vermittelt wurde, wäre dies wohl eine Arbeit ganz anderer Natur geworden ☺.

☺ … an meine Familie - für Eure andauernde Unterstütung. Vielen Dank, Mama Ingrid und Papa Norbert, Bruder K, Schwester N und Bruder S, sowie Oma und Opa Mral. Alles, was ich bin, bin ich durch Euch.

BIBLIOGRAPHY

Note: *Please note that the references are organized according to their acronym, and not according to the first author.*

[A$^+$02] L. Amati et al. *Astron. & Astroph.*, 390:81, 2002.

[A$^+$05] T. Antoni et al. *Astropart. Phys.*, 24:1, 2005.

[AA$^+$97] J. A. Aguilar, (ANTARES Coll.), et al. astro-ph/9707136, 1997.

[AB$^+$06] V. Aynutdinov, (Baikal Coll.), et al. *Nucl. Instr. & Methods in Phys. Res. A*, 567:423, 2006.

[Aha04a] F. Aharonian. *Very High Energy Cosmic Gamma Radiation.* World Scientific Publishing, 2004.

[Aha04b] F. Aharonian et al. *Astron. & Astroph.*, 421:529, 2004.

[AhH$^+$06a] F. Aharonian, (H.E.S.S. Coll.), et al. *Science*, 314:1424, 2006.

[AhH$^+$06b] F. Aharonian, (H.E.S.S. Coll.), et al. *Astron. & Astroph.*, 457:899, 2006.

[AhH$^+$06c] F. Aharonian, (H.E.S.S. Coll.), et al. *Astron. & Astroph.*, 460:743, 2006.

[AhH$^+$06d] F. Aharonian, (H.E.S.S. Coll.), et al. *Nature*, 439:695, 2006.

[AhH$^+$06e] F. Aharonian, (H.E.S.S. Coll.), et al. *Nature*, 440:1018, 2006.

[AI$^+$04] Ackermann, (IceCube Collaboration), et al. *Astropart. Phys.*, 20:507, 2004.

[AI$^+$05] A. Achterberg, (IceCube Coll.), et al. IceCube contributions to *ICRC 2005*, 2005. *astro-ph/0509330.*

[AI$^+$06a] A. Achterberg, (IceCube Coll.), et al. *astro-ph/0611063*, 2006. submitted to *Phys. Rev. D.*

[AI$^+$06b] A. Achterberg, (IceCube Coll.), et al. In *Journal of Physics*, Conference Series, 2006. *astro-ph/0611597*; http://www.icecube.wisc.edu/tev/.

[AI$^+$06c] A. Achterberg, (IceCube Coll.), et al. submitted to *Astrophys. Journal*, 2006. *astro-ph/0702265.*

[AI$^+$06d] A. Achterberg, (IceCube Coll.), et al. The Search for Muon Neutrinos from Gamma-Ray Bursts with AMANDA. in preparation, 2006.

[AI$^+$06e] A. Achterberg, (IceCube Coll. and P. L. Biermann), et al. *Astropart. Phys.*, 26:282, 2006.

[AI$^+$07] A. Achterberg, (IceCube Coll.), et al. Search for neutrino-induced cascades from gamma-ray bursts with AMANDA. *astro-ph/0702265*, 2007. submitted to ApJ.

[Alb07] Albert, J. and (MAGIC Coll.) and others. *astro-ph/0703084*, 2007. submitted to ApJL.

[ALS78] W. I. Axford, E. Leer, and G. Skadron. In *15th International Cosmic Ray Conference*, page 132, 1978.

[AM04] J. Alvarez-Muñiz and P. Mészáros. *Phys. Rev. D*, 70(12):123001, 2004.

[AM$^+$06a] J. Albert, (MAGIC Coll.), et al. *Science*, 312:1771, 2006.

[AM$^+$06b] J. Albert, (MAGIC Coll.), et al. Signal Reconstruction for the MAGIC Telescope. *ArXiv Astrophysics e-prints*, 2006. submitted to NIM-A.

[AN$^+$05] G. Aggouras, (Nestor Coll.), et al. *Astropart. Phys.*, 23:377, 2005.

[ANT07] http://antares.in2p3.fr, 2007. ANTARES web-page.

[Arg00] S. Argiro. *The fluorescence detector of the Pierre Auger Cosmic Ray Observatory and its readout electronics.* PhD thesis, Universita degli Studi di Milano, 2000.

[Ask62] G. A. Askaryan. *JETP*, 14:441, 1962.

[Att03] J.-L. Atteia. *Astron. & Astroph.*, 407:L1, 2003.

[B$^+$93] D. Band et al. *Astroph. Journal*, 413:281, 1993.

[B$^+$97a] G. Boella et al. *Astron. & Astroph. Supplement*, 122:299, 1997.

[B$^+$97b] J. T. Bonnell et al. *Astroph. Journal*, 490:79, 1997.

[B$^+$98] N. Bade et al. *Astron. & Astroph.*, 334:459, 1998.

[B^+03] V. Beckmann et al. *Astron. & Astroph.*, 401:927, 2003.

[B^+05a] M. Błażejowski et al. *Astroph. Journal*, 630:130, 2005.

[B^+05b] S. Böser et al. In R. Nahnhauer and S. Böser, editors, *Acoustic and Radio EeV Neutrino Detection Activities*. World Scientific Publishing, 2005.

[B^+06] V. Beckmann et al. *Astroph. Journal*, 638:642, 2006.

[BA^+06] S. W. Barwick, (ANITA Coll.), et al. *Phys. Rev. Let.*, 96(17):171101, 2006.

[Bar04] M. G. Baring. *Nucl. Phys. B Proc. Suppl.*, 136:198, 2004.

[Bar06] S. Barwick. In *Journal of Physics - TeV Particle Astrophysics II, Madison*, Conference Series, 2006. http://www.icecube.wisc.edu/tev/.

[BAT06] http://www.batse.msfc.nasa.gov/batse/, 2006. BATSE web-page.

[BBR05] J. K. Becker, P. L. Biermann, and W. Rhode. *Astropart. Phys.*, 23:355, 2005.

[Bed05] W. Bednarek. *Astroph. Journal*, 631:466, 2005.

[Bel78a] A. R. Bell. *Mon. Not. of the Royal Astron. Soc.*, 182:147, 1978.

[Bel78b] A. R. Bell. *Mon. Not. of the Royal Astron. Soc.*, 182:443, 1978.

[Bep06] http://www.asdc.asi.it/bepposax/, 2006. BeppoSax web-page.

[Ber87] C. et al. Berger. 262:463, 1987.

[BH05] W. N. Brandt and G. Hasinger. *Ann. Rev. Astron. Astrophys.*, 43:827, 2005.

[BHI94] T. Belloni, G. Hasinger, and C. Izzo. *Astron. & Astroph.*, 283:1037, 1994.

[BI^+05] D. Besson, (IceCube Coll.), et al. In *29th International Cosmic Ray Conference*, page 21, 2005.

[BI06] R. J. Bouwens and G. D. Illingworth. *Nature*, 443:189, 2006.

[Bis70] G. S. Bisnovatyi-Kogan. *Astronomicheskii Zhurnal*, 47:813, 1970.

[Bis71] G. S. Bisnovatyi-Kogan. *Soviet Astron.*, 14:652, 1971.

[BK06] P. L. Biermann and A. Kusenko. *Phys. Rev. Let.*, 96(9):091301, 2006.

[BM76] R. D. Blandford and C. F. McKee. *Physics of Fluids*, 19:1130, 1976.

[BO78] R. D. Blandford and J. P. Ostriker. *Astroph. Journal Let.*, 221:L29, 1978.

[BO98] J. Bednarz and M. Ostrowski. *Phys. Rev. Let.*, 80:3911, 1998.

[BRAH07] D. Besson, S. Razzaque, J. Adams, and P. Harris. *Astropart. Phys.*, 26:367, 2007.

[BS87] P. L. Biermann and P. A. Strittmatter. *Astroph. Journal*, 322:643, 1987.

[BSF95] P. L. Biermann, R. G. Strom, and H. Falcke. *Astron. & Astroph.*, 302:429, 1995.

[BWE91] R. H. Becker, R. L. White, and A. L. Edwards. *Astroph. Journal Suppl. Series*, 75:1, 1991.

[BWH95] R. H. Becker, R. L. White, and D. J. Helfland. *Astroph. Journal*, 450:559, 1995.

[C^+87] R. Chini et al. *Astron. & Astroph.*, 181:237, 1987.

[C^+89] R. Chini et al. *Astron. & Astroph.*, 221:L3, 1989.

[C^+96] J. J. Condon et al. *Astroph. Journal Suppl. Series*, 103:81, 1996.

[C^+98] J. J. Condon et al. *Astron. Journ.*, 115:1693, 1998.

[C^+06a] S. Campana et al. *Nature*, 442:1008, 2006.

[C^+06b] B. M. Connolly et al. *Phys. Rev. D*, 74(4):043001, 2006.

[CD73] T. L. Cline and U. D. Desai. In *11th International Cosmic Ray Conference*, page 80, 1973.

[CER] CERN. *PDFLIB - User's Manual*, 8.04 edition.

[CGR07] cossc.gsfc.nasa.gov/, 2007. CGRO web-page.

[Chi06] G. Chincarini. *astro-ph/0608414*, 2006. to appear in proceedings of Vulcano Workshop 2006.

[CM98] J. Chiang and R. Mukherjee. *Astroph. Journal*, 496:752, 1998.

[CO96] B. W. Carroll and D. A. Ostlie. *An introduction to modern astrophysics.* Addison Wesley, 1996.

[Cox72] D. P. Cox. *Astroph. Journal*, 178:159, 1972.

[Cri03] M. Cristinziani. *Nucl. Phys. B Proc. Suppl.*, 114:275, 2003.

[CS74] D. P. Cox and B. W. Smith. *Astroph. Journal Let.*, 189:L105, 1974.

[CTA06] http://www.mpi-hd.mpg.de/hfm/CTA/, 2006. CTA web-page.

[D$^+$95] K. Daum et al. *Zeitschrift für Physik C*, 66:417, 1995.

[D$^+$96] J. N. Douglas et al. *Astron. Journ.*, 111:1945, 1996.

[DA81] A. M. Dziewonski and D. L. Andersson. *Physics of the Earth and Planetary Interiors*, 25(4):297, 1981.

[DA$^+$06] B. R. Dawson, (Auger Coll.), et al. In *Journal of Physics - TeV Particle Astrophysics II, Madison*, Conference Series, 2006. http://www.icecube.wisc.edu/tev/.

[DAK07] E. V. Derishev, F. A. Aharonian, and V. V. Kocharovsky. *Astroph. Journal*, 655:980, 2007.

[Dar49] C. Darwin. *Nature*, 164:1112, 1949.

[Dar06] A. Dar. *Chinese Journ. of Astron & Astrop. Suppl.*, 6:301, 2006.

[DB96] A. C. Donea and P. L. Biermann. *Astron. & Astroph.*, 316:43, 1996.

[DCB99] C. D. Dermer, J. Chiang, and M. Böttcher. *Astroph. Journal*, 513:656, 1999.

[De 06] D. S. De Young. *Astroph. Journal*, 648:200, 2006.

[DP90] J. S. Dunlop and J. A. Peacock. *Mon. Not. of the Royal Astron. Soc.*, 247:19, 1990.

[DR04] A. Dar and A. de Rújula. *Physics Reports*, 405:203, 2004.

[Dre09] J. Dreyer. PhD thesis, Universität Dortmund, 2009. paper in preparation.

[ESK84] M. Elvis, A. Soltan, and W. C. Keel. *Astroph. Journal*, 283:479, 1984.

[ESS01] R. Engel, D. Seckel, and T. Stanev. *Phys. Rev. D*, 64(9):093010, 2001.

[F$^+$06] H. Falcke et al. *astro-ph/0610652*, 2006.

[Fal96] H. Falcke. In *Jets from Stars and Galactic Nuclei*, page 19, 1996.

[FB95] H. Falcke and P. L. Biermann. *Astron. & Astroph.*, 293:665, 1995.

[FB99] H. Falcke and P. L. Biermann. *Astron. & Astroph.*, 342:49, 1999.

[Fer49] E. Fermi. *Phys. Rev.*, 75(8):1169, 1949.

[Fer54] E. Fermi. *Astroph. Journal*, 119:1, 1954.

[FK$^+$98] Y. Fukuda, (Kamiokande Coll.), et al. *Phys. Rev. Let.*, 81:1562, 1998.

[FL$^+$05] H. Falcke, (LOPES Coll.), et al. *Nature*, 435:313, 2005.

[FMB95] H. Falcke, M. A. Malkan, and P. L. Biermann. *Astron. & Astroph.*, 298:375, 1995.

[FR74] B. L. Faranoff and J. M Riley. *Mon. Not. of the Royal Astron. Soc.*, 167:31P, 1974.

[FR00] E. E. Fenimore and E. Ramirez-Ruiz. *astro-ph/0004176*, 2000. submitted to ApJ. Report number LA-UR 00-1791.

[FS96] D. Fargion and A. Salis. In C. Kouveliotou, M. F. Briggs, and G. J. Fishman, editors, *American Institute of Physics Conference Series*, page 754, 1996.

[G$^+$04] D. Guetta et al. *Astropart. Phys.*, 20:429, 2004.

[G$^+$05] P. W. Gorham et al. *Phys. Rev. D*, 72(2):023002, 2005.

[G$^+$06a] N. Gehrels et al. *Nature*, 444:1044, 2006.

[G$^+$06b] J. Gorosabel et al. *Astron. & Astroph.*, 450:87, 2006.

[GA$^+$06] P. W. Gorham, (ANITA Coll.), et al. *hep-ex/0611008*, 2006.

[Gai90] T. K. Gaisser. *Cosmic Rays and Particle Physics.* Cambridge University Press, 1990.

[GBW04] Gopal-Krishna, P. L. Biermann, and P. J. Wiita. *Astroph. Journal Let.*, 603:L9, 2004.

[GM99] N. Gehrels and P. Michelson. *Astropart. Phys.*, 11:277, 1999.

[GM$^+$06] J. A. Goodman, (MILAGRO Coll.), et al. In *Journal of Physics - TeV Particle Astrophysics II, Madison*, Conference Series, 2006. http://www.icecube.wisc.edu/tev/.

[GME93] M. E. Gangl, J. H. Middlestadt, and R. W. Eastes. In R. E. Huffman, editor, *Ultraviolet technology IV; Proceedings of the Meeting, San Diego, CA, July 20, 21, 1992 (A93-34426 13-35)*, page 50, 1993.

[Gon04] M. M. González Sánchez. *Gamma Ray Bursts, their High Energy Emission as Observed by EGRET.* PhD thesis, University of Wisconsin, Madison, 2004.

[Gre66] K. Greisen. *Phys. Rev. Let.*, 16, 1966.

[Gro06] A. Groß. *Search for High Energy Neutrinos from Generic AGN classes with AMANDA-II.* PhD thesis, Universität Dortmund, 2006.

[GRV92] M. Glück, E. Reya, and A. Vogt. *Z. Phys.*, C(53), 1992.

[GS03] D. A. Green and F. R. Stephenson. In K. Weiler, editor, *LNP Vol. 598: Supernovae and Gamma-Ray Bursters*, page 7, 2003.

[GSF05] GSFC Lag-Luminosity Database. http://heasarc.gsfc.nasa.gov/docs/cgro/analysis/lags/, 2005.

[H+92] K. Hurley et al. *Astron. & Astroph. Supplement*, 92:401, 1992.

[H+94] D. H. Hartmann et al. *Astroph. Journal Suppl. Series*, 90:893, 1994.

[H+95] M. Honda et al. *Phys. Rev. D*, 52:4985, 1995.

[H+05] J. Hjorth et al. *Astroph. Journal Let.*, 630:L117, 2005.

[H+06a] G. Hill et al. Neutrino 2006, Santa Fe, 2006.

[H+06b] J. Hodges et al. In *TeV Particle Astrophysics II*, 2006. astro-ph/ http://icecube.wisc.edu/tev/presentations.php.

[H+06c] K. Hurley et al. *Astroph. Journal Suppl. Series*, 164:124, 2006.

[Hal06] F. Halzen. *astro-ph/0611915*, 2006. proceedings contribution for multi-messenger conference in Barcelona (July 2006).

[HB74] J. A. Hogbom and W. N. Brouw. *Astron. & Astroph.*, 33:289, 1974.

[Hel87] D. Helfand. *Physics Today*, 40:24, 1987.

[Hes12] V. F. Hess. 13:1084, 1912.

[HET06] http://space.mit.edu/HETE/, 2006. HETE-II web-page.

[HaHo02] F. Halzen and D. Hooper. *Reports of Progress in Physics*, 65:1025, 2002.

[Hil84] A. M. Hillas. *Ann. Rev. Astron. Astrophys.*, 22:425, 1984.

[HiR04] HiRes Collaboration. Search for Small-Scale Anisotropy of Cosmic Rays above 10^{19} eV with HiRes Stereo. *Nuclear Physics B Proceedings Supplements*, 136:46, 2004.

[HK+03] A. Haungs, (KASCADE-Grande Coll.), et al. In *27th International Cosmic Ray Conference*, page 985, 2003.

[HKT07] J. R. Hörandel, N. N. Kalmykov, and A. V. Timokhin. *Astropart. Phys.*, 27:119, 2007.

[HLM05] F. Halzen, H. Landsman, and T. Montaruli. *astro-ph/0503348*, 2005.

[HMS05] G. Hasinger, T. Miyaji, and M. Schmidt. *Astron. & Astroph.*, 441:417, 2005.

[Hol06] J. et al. Holder. *Astropart. Phys.*, 25:391, 2006.

[Hör03] J. R. Hörandel. *Astropart. Phys.*, 19:193, 2003.

[HT50] F. de Hoffmann and E. Teller. *Phys. Rev.*, 80(4):692, 1950.

[HW64] D. S. Heeschen and C. M. Wade. *Astron. Journ.*, 69:277, 1964.

[I^+06] M. Iye et al. *Nature*, 443:186, 2006.

[IMP07] http://heasarc.gsfc.nasa.gov/docs/heasarc/missions/imp6.html, 2007. IMP-6 web-page.

[IPN07] http://www.ssl.berkeley.edu/ipn3/, 2007. Interplanetary Network (IPN3).

[J^+97] W. N. Johnson et al. In C. D. Dermer, M. S. Strickman, and J. D. Kurfess, editors, *AIP Conf. Proc. 410: Proceedings of the Fourth Compton Symposium*, page 283, 1997.

[J^+01] F. Jansen et al. *Astron. & Astroph.*, 365:L1, 2001.

[Jac06] J. D. Jackson. *Klassische Elektrodynamik*. de Gruyter, 4th edition, 2006.

[JE91] F. C. Jones and D. C. Ellison. *Space Science Rev.*, 58:259, 1991.

[K^+81] H. Kühr et al. *Astron. Journ.*, 86:854, 1981.

[K^+96] S. C. Kappadath et al. *Astron. & Astroph. Supplement*, 120:C619, 1996.

[K^+00] J. G. Kirk et al. *Astroph. Journal*, 542:235, 2000.

[K^+03] I. Kravchenko et al. *Astropart. Phys.*, 19:15, 2003.

[K^+04a] G. Kanbach et al. *New Astron. Rev.*, 48:275, 2004.

[K^+04b] D.-W. Kim et al. Chandra Multiwavelength Project. I. First X-Ray Source Catalog. *Astroph. Journal Suppl. Series*, 150:19, 2004.

[K^+04c] T. M. Kneiske et al. *Astron. & Astroph.*, 413:807, 2004.

[K^+04d] H. Krawczynski et al. *Astroph. Journal*, 601:151, 2004.

[K^+06] A. Kappes et al. *astro-ph/0607286*, 2006.

[Kar62] N. S. Kardashev. *Soviet Astron. A. J.*, 6:317, 1962.

[KH04] S. Krucker and H. S. Hudson. In R. W. Walsh, J. Ireland, D. Danesy, and B. Fleck, editors, *ESA SP-575: SOHO 15 Coronal Heating*, page 247, 2004.

[KM3a] see e.g. Proccedings of ”Very Large Volume neutrino Telescopes”, Catania (Italy), Nov 2005. KM3NeT web-page: http://www.km3net.org/publications.php.

[KM3b] http://www.km3net.org/. KM3NeT web-page.

[Koh13] W. Kohlhörster. *Phys. Z.*, 14:1153, 1913.

[Kon06] http://heasarc.gsfc.nasa.gov/docs/heasarc/missions/wind.html, 2006. Konus Wind web-page.

[Kre98] F. et al. Krennrich. *Astropart. Phys.*, 8:213, 1998.

[Kry77] G. F. Krymskii. *Akademiia Nauk SSSR Doklady*, 234:1306, 1977.

[KSO73] R. W. Klebesadel, I. B. Strong, and R. A. Olson. *Bulletin of the American Astron. Soc.*, 5:322, 1973.

[KZ68] V. A. Kuzmin and G. T. Zatsepin. In *10th International Cosmic Ray Conference*, volume 46, page 617, 1968.

[L^+99a] M. Lacy et al. *Mon. Not. of the Royal Astron. Soc.*, 308:1096, 1999.

[L^+99b] S. A. Laurent-Muehleisen et al. *Astroph. Journal*, 525:127, 1999.

[L^+05] A. Leroy et al. *Astroph. Journal*, 625:763, 2005.

[Lon98] M. S. Longair. *Galaxy Formation.* Springer, 1998.

[LRL83] R. A. Laing, J. M. Riley, and M. S. Longair. *Mon. Not. of the Royal Astron. Soc.*, 204:151, 1983.

[LUN07] http://www.physics.adelaide.edu.au/astrophysics/lunaska/index.html, 2007. LUNASKA web-page.

[LW06a] Z. Li and E. Waxman. *Astroph. Journal*, 651:328, 2006.

[LW06b] A. Loeb and E. Waxman. *Journ. of Cosm. and Astr.Phys.*, 5:3, 2006.

[M^+75] E. P. Mazets et al. *Astrophys. & Space Science*, 33:347, 1975.

[M^+90] M. Moshir et al. The faint source catalog, version 2.0. *Bulletin of the American Astronomical Society*, 22:1325, 1990.

[M^+95] K. McNaron-Brown et al. *Astroph. Journal*, 451:575, 1995.

[M^+96] K. Mannheim et al. *Astron. & Astroph.*, 315:77, 1996.

[M$^+$03a] P. A. Mazzali et al. *Astroph. Journal Let.*, 599:L95, 2003.

[M$^+$03b] A. Mücke et al. *Astropart. Phys.*, 18:593, 2003.

[M$^+$05a] E. P. Mazets et al. Konus catalog of short GRBs. http://www.ioffe.ru/LEA/shortGRBs/Catalog/, 2005.

[M$^+$05b] S. McGlyn et al. In S. S. Holt, N. Gehrels, and J.A.Nousek, editors, *Gamma-Ray Bursts in the Swift Era*, volume 838 of *AIP Conference Proceedings*, 2005.

[M$^+$05c] J. W. Mitchell et al. *Advances in Space Research*, 35:135, 2005.

[M$^+$05d] K. Münich et al. In *29th International Cosmic Ray Conference*, 2005. astro-ph/0509330.

[M$^+$07] K. Mitsuda et al. The X-Ray Observatory Suzaku. *Publ. of the Astron. Soc. of Japan*, 59:1, 2007.

[Mac98] E. Mach. Über Erscheinungen an fliegenden Projektilen. *Separatum ex. Ver. nw. Kenntn., Wien*, 1898.

[Mah98] R. Mahadevan. *Nature*, 394:651, 1998.

[Man95] K. Mannheim. *Astropart. Phys.*, 3:295, 1995.

[Mar07] http://mars.jpl.nasa.gov/odyssey/, 2007. Mars-Odyssey web-page.

[Mel06] A. Meli. Private Communication, 2006.

[Més06] P. Mészáros. In S. S. Holt, N. Gehrels, and J. A. Nousek, editors, *AIP Conf. Proc. 838: Gamma-Ray Bursts in the Swift Era*, page 234, 2006.

[MGI74] E. P. Mazets, S. V. Golenetskii, and V. N. Il'inskii. volume 19, page 77. JETP Lett., 1974.

[MHS00] T. Miyaji, G. Hasinger, and M. Schmidt. *Astron. & Astroph.*, 353:25, 2000.

[Mir06] I. F. Mirabel. *astro-ph/0610707*, 2006. proceedings contribution for multimessenger conference in Barcelona (July 2006).

[MOK06] M. Misiaszek, A. Odrzywołek, and M. Kutschera. *Phys. Rev. D*, 74(4):043006, 2006.

[Möl76] C. Möllenhoff. *Astron. & Astroph.*, 50:105, 1976.

[Mon03] T. Montaruli. In *Particle Astrophysics Instrumentation. Edited by Peter W. Gorham. Proceedings of the SPIE, Volume 4858, pp. 92-102 (2003).*, page 92, 2003.

[MPR01] K. Mannheim, R. J. Protheroe, and J. P. Rachen. *Phys. Rev. D*, 63:23003, 2001.

[MQB05] A. Meli, J. J. Quenby, and J. Becker. In *29th International Cosmic Ray Conference*, page 229, 2005.

[MR90] M. M. McGilchrist and J. M. Riley. *Mon. Not. of the Royal Astron. Soc.*, 246:123, 1990.

[MR94] I. F. Mirabel and L. F. Rodriguez. *Nature*, 371:46, 1994.

[MR97] P. Mészáros and M. J. Rees. *Astroph. Journal*, 476:232, 1997.

[MRS03] A. D. Martin, M.G. Ryskin, and A.M. Stasto. *Acta Phys.Polon.*, B34, 2003.

[MRZ04] P. Mészáros, S. Razzaque, and B. Zhang. *New Astron. Rev.*, 48:445, 2004.

[MSR95] K. Mannheim, M. Schulte, and J. Rachen. *Astron. & Astroph.*, 303:L41, 1995.

[MVV02] N. Mandolesi, F. Villa, and L. Valenziano. *Advances in Space Research*, 30:2123, 2002.

[MW84] E. Mach and J. Wentzel. *Anzeiger der Kaiserlichen Akademie der wissensch., Math. Naturw. Classe, Wien*, 21:121, 1884. Experimental setup.

[MW85] E. Mach and J. Wentzel. *Kaiserliche Akademie der wissensch., Math. Naturw. Classe, Wien*, 92:625, 1885. Experimental results.

[N$^+$06] C. Naumann et al. *Int. Journal of Mod. Phys. A*, 21:92, 2006.

[NEA06] http://near.jhuapl.edu/instruments/XGRS/, 2006. NEAR web-page.

[NEM07] http://nemoweb.lns.infn.it/, 2007. NEMO web-page.

[NES07] http://www.nestor.org.gr/, 2007. NESTOR web-page.

[NMB93] L. Nellen, K. Mannheim, and P. L. Biermann. *Phys. Rev. D*, 47:5270, 1993.

[Nor02] J. P. Norris. *Astroph. Journal*, 579:386, 2002.

[OB97] C. P. O'Dea and S. A. Baum. *Astron. Journ.*, 113:148, 1997.

[OB02] M. Ostrowski and J. Bednarz. *Astron. & Astroph.*, 394:1141, 2002.

[Olb26] H. W. M. Olbers. Über die Durchsichtigkeit des Weltraums. *Astron. Jahrb. für das Jahr 1826*, 1826. Later puplished in the collection *Olbers. Sein Leben und seine Werke*, Editor: C. Schilling, Publisher: Julius Springer, Year: 1894.

[OMK04] A. Odrzywolek, M. Misiaszek, and M. Kutschera. *Astropart. Phys.*, 21:303, 2004.

[OSO07] http://heasarc.gsfc.nasa.gov/docs/oso7/oso7.html, 2007. OSO-7 webpage.

[P^+72] I. I. K. Pauliny-Toth et al. *Astron. Journ.*, 77:265, 1972.

[P^+78] I. I. K. Pauliny-Toth et al. *Astron. Journ.*, 83:451, 1978.

[P^+98] R. D. Preece et al. *Astroph. Journal Let.*, 506:L23, 1998.

[P^+99] W. S. Paciesas et al. *Astroph. Journal Suppl. Series*, 122:465, 1999.

[P^+00] G. Pugliese et al. *Astron. & Astroph.*, 358:409, 2000.

[P^+06] P. Picozza et al. *astro-ph/0608697*, 2006.

[Pal07] V. Pal'shin. Private Communication, 2007.

[Par04] G. K. Parks. Westview Press Books, 2nd edition, 2004.

[Pea85] J. A. Peacock. *Mon. Not. of the Royal Astron. Soc.*, 217:601, 1985.

[PH06] A. Pélangeon and Hete-II Science Team. In S. S. Holt, N. Gehrels, and J. A. Nousek, editors, *American Institute of Physics Conference Series*, page 149, 2006. *astro-ph/0601150*; see http://cosmos.ast.obs-mip.fr/projet/ for online tool.

[Pir99] T. Piran. *Physics Reports*, 314:575, 1999.

[Pir05a] T. Piran. *Rev. of Mod. Phys.*, 76:1143, 2005.

[Pir05b] T. Piran. *Nuovo Cim. C Geophys. Space Phys. C*, 28:373, 2005.

[PK72] I. I. K. Pauliny-Toth and K. I. Kellermann. *Astron. Journ.*, 77:797, 1972.

[Pro98] R. J. Protheroe. In *Towards the Millennium in Astrophysics, Problems and Prospects. International School of Cosmic Ray Astrophysics 10th Course*, page 3, 1998.

[PRR95] P. Podsiadlowski, M. J. Rees, and M. Ruderman. *Mon. Not. of the Royal Astron. Soc.*, 273:755, 1995.

[PTA06] C. Pittori, M. Tavani and the AGILE Team. *Chin. Journal of Astron. &Astroph. Suppl.*, 6:373, 2006.

[PW81] J. A. Peacock and J. V. Wall. *Mon. Not. of the Royal Astron. Soc.*, 194:331, 1981.

[R$^+$04] M. Revnivtsev et al. *Astron. & Astroph.*, 418:927, 2004.

[Rac00] J. P. Rachen. In B. L. Dingus, M. H. Salamon, and D. B. Kieda, editors, *American Institute of Physics Conference Series*, page 41, 2000.

[RB93] J. P. Rachen and P. L. Biermann. *Astron. & Astroph.*, 272:161, 1993.

[Ree70] M. J. Rees. *Nature*, 227:1303, 1970.

[REL01] S. Rawlings, S. Eales, and M. Lacy. A sample of 6C radio sources with virtually complete redshifts - II. Optical spectroscopy. *Mon. Not. of the Royal Astron. Soc.*, 322:523, 2001.

[RHE06] http://hessi.web.psi.ch/;http://hesperia.gsfc.nasa.gov/hessi/index.html, 2006. RHESSI web-page.

[RL79] G. B. Rybicki and A. P. Lightman. *Radiative processes in astrophysics.* J. Wiley & Sons, Inc., 1979.

[RM98] J. P. Rachen and P. Mészáros. *Phys. Rev. D*, 58(12):123005, 1998.

[RMB95] J. Rachen, K. Mannheim, and P. L. Biermann. *Astron. & Astroph.*, 310:371, 1995.

[RMW03a] S. Razzaque, P. Mészáros, and E. Waxman. *Phys. Rev. D*, 68(8):083001, 2003.

[RMW03b] S. Razzaque, P. Mészáros, and E. Waxman. *Phys. Rev. Let.*, 90(24):241103, 2003.

[Rou00] E. Roulet. *astro-ph/0011570*, 2000. Lectures at the ICTP Summer School on Particle Physics and Cosmology.

[S$^+$89] D. B. Sanders et al. *Astroph. Journal*, 347:29, 1989.

[S$^+$98] P. Sreekumar et al. *Astroph. Journal*, 494:523, 1998.

[S$^+$01] D. Saltzberg et al. *Phys. Rev. Let.*, 86:2802, 2001.

[S$^+$03] D. B. Sanders et al. *Astron. Journ.*, 126:1607, 2003.

[S$^+$05a] T. Sakamoto et al. *Astroph. Journal*, 629:311, 2005.

[S$^+$05b] M. Stamatikos et al. In *29th International Cosmic Ray Conference*, page 21, 2005. *astro-ph/0510336.*

[S$^+$06] A. Smith et al. In *TeV Particle Astrophysics II*, 2006. http://icecube.wisc.edu/tev/presentations.php.

[S$^+$07] D. N. Spergel et al. *astro-ph/0603449*, 2007. accepted for publication in ApJ.

[Sak71] S. Sakashita. *Astrophys. & Space Science*, 14:431, 1971.

[Sal06] D. Saltzberg. In *Journal of Physics - TeV Particle Astrophysics II, Madison*, Conference Series, 2006. http://www.icecube.wisc.edu/tev/.

[Sap06] P. Sapienza. *astro-ph/0611105*, 2006. proceedings of the ECRS2006 conference.

[SaSw06] T. Sakamoto and Swift-Bat Konus-Wind Hete-II Team. In S. S. Holt, N. Gehrels, and J. A. Nousek, editors, *AIP Conf. Proc. 836: Gamma-Ray Bursts in the Swift Era*, page 43, 2006. *astro-ph/0605717*.

[Sch63] M. Schmidt. *Nature*, 197:1040, 1963.

[Sch72] M. Schmidt. *Astroph. Journal*, 176:303, 1972.

[Sch04] M. Schmidt. In M. Feroci, F. Frontera, N. Masetti, and L. Piro, editors, *Astronomical Society of the Pacific Conference Series*, page 47, 2004.

[SD78] F. A. Speer and C. C. Dailey, editors. 1978.

[SdS92] F. W. Stecker, O. C. de Jager, and M. H. Salamon. *Astroph. Journal Let.*, 390:L49, 1992.

[Sed58] L. I. Sedov. *Rev. of Mod. Phys.*, 30:1077, 1958.

[SKA07] http://www.skatelescope.org/, 2007. SKA web-page.

[SMR05] A. W. Strong, I. V. Moskalenko, and O. Reimer. In *AIP Conf. Proc. 745: High Energy Gamma-Ray Astronomy*, page 585, 2005.

[SNO02] SNO Collaboration. *Phys. Rev. Let.*, 89:11301, 2002.

[Som05] P. Sommers. In *29th International Cosmic Ray Conference*, page 387, 2005.

[SSM05] G. Sinnis, A. Smith, and J. E. McEnery. In M. Novello, S. Perez Bergliaffa, and R. Ruffini, editors, *The Tenth Marcel Grossmann Meeting. On recent developments in theoretical and experimental general relativity, gravitation and relativistic field theories*, page 1068, 2005.

[StA04] M. Stamatikos and AMANDA Collaboration. In *AIP Conf. Proc. 727: Gamma-Ray Bursts: 30 Years of Discovery*, page 146, 2004.

[Sta04] T. Stanev. *High Energy Cosmic Rays.* Springer Verlag, 2004.

[Sta06] T. Stanev. Private Communication, 2006.

[Ste05] F. W. Stecker. *Phys. Rev. D*, 72(10):107301, 2005.

[Ste07] F. W. Stecker. *Astropart. Phys.*, 26:398, 2007.

[StSa96] F. W. Stecker and M. H. Salamon. *Space Science Rev.*, 75:341, 1996.

[StSa01] F. W. Stecker and M. H. Salamon. In S. Ritz, N. Gehrels, and C. R. Shrader, editors, *AIP Conf. Proc. 587: Gamma 2001: Gamma-Ray Astrophysics*, page 432, 2001.

[Swi06a] http://swift.gsfc.nasa.gov/docs/swift/swiftsc.html, 2006. Swift web-page.

[Swi06b] http://www.swift.ac.uk/grb.shtml, 2006.

[Tes06] M. Teshima. In *Journal of Physics - TeV Particle Astrophysics II, Madison*, Conference Series, 2006. http://www.icecube.wisc.edu/tev/.

[TRM05] D. F. Torres, G. E. Romero, and F. Mirabel. *Chin. J. Astron. & Astrophys. Suppl.*, 5:183, 2005.

[Uly06] http://ulysses.jpl.nasa.gov/, 2006. Ulysses web-page.

[UMR07] http://www.astro.lsa.umich.edu/obs/radiotel/radiotel.php, 2007. UMRAO.

[V^+99] H.-H. Voigt et al. Landolt-Börnstein: Numerical Data and Functional Relationships in Science and Technology, 1999.

[V^+05a] J. Vandenbroucke et al. In R. Nahnhauer and S. Böser, editors, *Acoustic and Radio EeV Neutrino Detection Activities*. World Scientific Publishing, 2005.

[V^+05b] G. S. Varner et al. *Nucl. Instr. & Methods in Phys. Res. A*, 554:437, 2005.

[V^+05c] J. S. Villasenor et al. *Nature*, 437:855, 2005.

[Van06] J. Vandenbroucke. In *Journal of Physics - TeV Particle Astrophysics II, Madison*, Conference Series, 2006. *astro-ph/0611503*; http://www.icecube.wisc.edu/tev/.

[Vas05] G. et al. Vasileiadis. The H.E.S.S experimental project. 553:268–273, November 2005.

[VGL05] J. Vandenbroucke, G. Gratta, and N. Lehtinen. *Astroph. Journal*, 621:301, 2005.

[Vie95] M. Vietri. *Astroph. Journal*, 453:883–+, 1995.

[VLA07] http://www.vla.nrao.edu/, 2007. VLA web-page.

[Vol80] L. V. Volkova. *Soviet J. of Nuclear Physics*, 31:748, 1980.

[W$^+$73] W. A. Wheaton et al. *Astroph. Journal Let.*, 185:L57, 1973.

[W$^+$82] A. E. Wright et al. *Austr. J. of Phys.*, 35:177, 1982.

[W$^+$84] K. S. Wood et al. *Astroph. Journal Suppl. Series*, 56:507, 1984.

[W$^+$01] C. J. Willott et al. *Mon. Not. of the Royal Astron. Soc.*, 322:536, 2001.

[Wax00] E. Waxman. *Astroph. Journal Suppl. Series*, 127:519, 2000.

[WB92] R. L. White and R. H. Becker. *Astroph. Journal Suppl. Series*, 79:331, 1992.

[WB97] E. Waxman and J. N. Bahcall. *Phys. Rev. Let.*, 78:2292, 1997.

[WB99] E. Waxman and J. N. Bahcall. *Phys. Rev. D*, 59:23002, 1999.

[WB00] E. Waxman and J. N. Bahcall. *Astroph. Journal*, 541:707, 2000.

[WBM98] B. Wiebel-Sooth, P. L. Biermann, and H. Meyer. *Astron. & Astroph.*, 330:389, 1998.

[Wei93] Y. Wei. *Untersuchung der neutrinoinduzierten Myonen im Frejus-Untergrunddetektor*. PhD thesis, Bergische Universität GH Wuppertal, 1993.

[Win04] C. Winkler. *New Astron. Rev.*, 48:183, 2004.

[Wis06] R. Wischnewski. *astro-ph/0609743*, 2006. see also http://www.ifh.de/baikal/baikalhome.html.

[WKF98] E. Waxman, S. R. Kulkarni, and D. A. Frail. *Astroph. Journal*, 497:288, 1998.

[WO90] A. Wright and R. Otrupcek. *Australia Telescope National Facility*, 1990.

[Wol72] L. Woltjer. *Ann. Rev. Astron. Astrophys.*, 10:129, 1972.

[WP85] J. V. Wall and J. A. Peacock. *Mon. Not. of the Royal Astron. Soc.*, 216:173, 1985.

[WRM97] R. A. M. J. Wijers, M. J. Rees, and P. Mészáros. *Mon. Not. of the Royal Astron. Soc.*, 288:L51, 1997.

[WT04] P. M. Woods and C. Thompson. *astro-ph/0406133*, 2004.

[Y$^+$95] S. Yoshida et al. *Astropart. Phys.*, 3:105, 1995.

[Y$^+$04] D. Yonetoku et al. *Astroph. Journal*, 609:935, 2004.

[YK06] H. Yüksel and M. D. Kistler. *submitted to Phys. Rev. D*, 2006. *astro-ph/0610481.*

[YP$^+$06] W.-M. Yao, (Particle Data Group), et al. Rev. of particle physics. *Journ. of Phys. G*, 33:1, 2006.

[YT93] S. Yoshida and M. Teshima. *Progress of Theoretical Physics*, 89:833, 1993.

[Z$^+$07] B. Zhang et al. *Astroph. Journal*, 655:989, 2007.

[ZB02] C. Zier and P. L. Biermann. *Astron. & Astroph.*, 396:91, 2002.

[ZM04] B. Zhang and P. Mészáros. *Intern. J. of Modern Phys. A*, 19:2385, 2004.

Index: key words

Index: astroparticle experiments